Role of Reactive Oxygen Species in Multiphase Chemistry of Organic Aerosols in the Atmosphere

Dissertation

zur Erlangung des Grades

'Doctor rerum naturalium (Dr. rer. nat.)'

im Promotionsfach Chemie

am Fachbereich Chemie, Pharmazie und Geowissenschaften

der Johannes Gutenberg-Universität in Mainz

International Max Planck Research Schools

Andrea Mario Arangio

geb. am 11.01.1988 in Enna

Tag der Prüfung: 27 März 2017

I hereby declare that I wrote the dissertation submitted without any unauthorized external assistance and used only sources acknowledged in the work. All textual passages which are appropriated verbatim or paraphrased from published and unpublished texts as well as all information obtained from oral sources are duly indicated and listed in accordance with bibliographical rules. In carrying out this research, I complied with the rules of standard scientific practice as formulated in the statutes of Johannes Gutenberg-University Mainz to insure standard scientific practice.

Abstract

Reactive oxygen species (ROS) play a central role in both atmospheric and physiological processes. In the atmosphere, ROS are produced by photochemical and multiphase reactions, and are important species in the removal of air pollutants. In biological systems, ROS act as mediators of intracellular signaling, but they can also cause oxidative stress by damaging lipids, proteins, and DNA. At the atmosphere-biosphere interface such as biogenic aerosols and lung lining fluid, chemical interactions of ROS pose feedback loops involving the Earth system, climate, and public health. Multiphase processes of ROS are controlled by reactions and mass transport of species between gas, liquid and solid phases. Despite their importance, kinetics and chemical mechanisms that govern the interactions between atmospheric and physiological processes are not yet well understood and characterized.

Multiphase reactions of OH radicals are among the most important pathways for chemical aging of organic aerosols in the atmosphere. Reactive uptake of OH by organic compounds has been investigated extensively, but the kinetics of mass transport, chemical reactions as well as their interdependence are still not understood. The kinetic multilayer model of gas–particle interactions in aerosols and clouds (KM-GAP) resolves these processes by explicitly taking into account solubility, diffusivity and reactivity of each species involved. In this work, KM-GAP was applied to experimental data from OH exposure of coated-wall flow tube of levoglucosan (LG) and abietic acid (AA), which serve as surrogates and molecular markers of biomass burning aerosol (BBA). For both LG and AA, the bulk diffusion coefficients were found to be approximately 10^{-16} cm^2s^{-1}, reflecting their amorphous semisolid state. It was shown that the OH uptake by these films was governed by the reaction at or near the surface and could be kinetically limited by bulk diffusion of the organic reactants. Through these diffusion coefficients, the chemical half-life of LG in 200 nm diameter particles in a biomass burning plume was estimated to increase from one day to one week depending on the relative humidity. In BBA particles transported to the free troposphere, the chemical half-life of LG can exceed one month due to slow bulk diffusion at low temperature.

Ambient and laboratory-generated secondary organic aerosols (SOA) were found to form substantial amounts of OH radicals upon interaction with liquid water, which can be explained by the decomposition of organic hydroperoxides. The molar OH yield from SOA formed by oxidation of terpenes (α-pinene, β-pinene, limonene and isoprene) is 0.1 % upon extraction with pure water and increases to 1.5 % in presence of Fe^{2+} ions due to Fenton-like reaction. These findings imply that the chemical reactivity and aging of SOA particles is strongly enhanced upon interaction with water and iron. In the human respiratory tract, the inhalation and deposition of SOA particles may lead to a substantial release of OH radicals, which may contribute to oxidative stress and play an important role in the adverse health effects of atmospheric aerosols.

A wide range of particle-associated radicals were detected and quantified in size segregated atmospheric particles using electron paramagnetic resonance (EPR) spec-

troscopy. Particle samples were collected using a cascade impactor at a semi-urban site in Mainz, Germany, in May-June 2015. Concentrations of environmentally persistent free radicals (EPFR), most likely semiquinone radicals, were found to be in the range of (1-7) $\times$ 10^{11} spins μg^{-1} for particles in the accumulation mode. Coarse particles with a diameter larger than 1 μm did not contain substantial amounts of EPFR. Using a spin trapping technique, ROS formed upon extraction of the particle samples in water were determined to be (0.1-3) $\times$ 10^{11} spins μg^{-1}. By deconvolution of EPR spectra ROS released by submicron particle samples were found to include OH, superoxide (O_2^-), carbon- and oxygen-centered organic radicals. OH was instead the dominant species for coarse particles. EPR spectra derived from ambient particulate matter were compared with those of mixtures of organic hydroperoxides, quinones and iron ions. By means of the EPR spectra comparison and chemical analysis with liquid chromatography mass spectrometry (LC-MS), the particle-associated ROS were suggested to be formed by decomposition of organic hydroperoxides interacting with transition metal ions and quinones contained in atmospheric humic-like substances (HULIS).

Ambient particles were collected using a cascade impactor also in Beijing, China in January 2016 and in Nagoya, Japan in April 2016. The average EPFR concentration contained in particles with size diameter range of 100 - 560 nm was 1.3 $\times$ 10^{12} spins μg^{-1} in Beijing, which is almost one order of magnitude higher than the average EPFR concentrations in Mainz (2.3 $\times$ 10^{11} spins μg^{-1}), and in Nagoya (4.7 $\times$ 10^{11} spins μg^{-1}). The difference is remarkably high for particles with lower cut-off sizes of 320 nm. The result reflects stronger aerosol emission from biomass and coal combustion in Beijing compared to fossil fuels and traffic emissions in Nagoya and Mainz.

Identification and evaluation of chemical stability of radical adducts resulting from spin trap EPR experiments is a difficult task to accomplish. Electron Paramagnetic Resonance for Spin TrappIng Chemical Kinetics (EPR-STICK) was developed, which is a new MATLAB-based toolbox to perform EPR spectral processing, radical quantification, spectra deconvolution and kinetic modeling of radical reactions. The toolbox was applied to experimental data to investigate the kinetics of the spin trapping, efficiency and yield of radicals formed upon decomposition of tert-butyl-hydroperoxide catalyzed by iron ions.

Zusammenfassung

Reaktive Sauerstoffspezies (ROS) spielen eine zentrale Rolle in atmosphärischen und physiologischen Prozessen. In der Atmosphäre werden ROS bei photochemischen und Multiphasenreaktionen gebildet, wo sie eine wichtige Rolle bei der Entfernung von Luftschadstoffen spielen. In biologischen Systemen agieren ROS als Vermittler in intrazellulären Signalkaskaden und sind auch bei oxidativem Stress beteiligt, wodurch Lipide, Proteine und DNS geschädigt werden. An der Grenzfläche von Atmosphäre und Biosphäre, wie beispielsweise biogene Aerosole oder die Schleimhaut des Lungenepithels, nehmen ROS eine zentrale Rolle in den Rückkopplungsschleifen von Erdsystem, Klima, und Gesundheit ein. Multiphasenprozesse von ROS werden durch eine Vielzahl chemischer Reaktionen und Transportprozesse in gasförmiger, flüssiger und fester Phase bestimmt. Trotz ihrer großen Bedeutung sind die Reaktionskinetiken und chemischen Mechanismen für die Wechselwirkungen von atmosphärischen und physiologischen Prozessen bis heute unzureichend charakterisiert.

Multiphasenreaktionen von OH-Radikalen gehören zu den wichtigsten Pfaden der chemischen Alterung von organischen Aerosolpartikeln in der Atmosphäre. Die reaktive Aufnahme von OH-Radikalen durch organische Verbindungen wurde bisher zwar ausführlich untersucht, aber die Kinetik der Transportprozesse, der entsprechenden chemischen Reaktionen sowie deren gegenseitige Abhängigkeit sind nach wie vor unzureichend bekannt. Das kinetische Mehrschichtenmodell für Gas-Partikel-Interaktion in Aerosolen und Wolken (KM-GAP) kann diese Prozesse auflösen, indem es explizit Löslichkeit, Diffusion und Reaktivität aller beteiligten Spezies betrachtet. In dieser Arbeit wurde KM-GAP auf experimentelle Daten aus Studien zur OH-Exposition von dünnen Schichten puren Levoglukosans (LG) und purer Abietinsäure (AS) angewendet, welche als molekulare Marker für die aus Biomassenverbrennung entstandenen Aerosole dienen (BBA). Der Bulk-Diffusionskoeffizient wurde für LG und AS auf je ca. 10^{-16} cm^2s^{-1} bestimmt, was einem amorphen, halbfesten Zustand dieser Phasen entspricht. Es konnte gezeigt werden, dass die OH-Aufnahme der dünnen Schichten durch chemische Reaktionen auf oder nahe an der Filmoberfläche bestimmt wird und von der Bulk-Diffusion der organischen Reaktanten kinetisch gehemmt werden kann. Mit diesem Koeffiezienten ergab sich eine chemische Halbwertszeit von LG in Aerosolpartikeln mit Durchmessern von 200 nm abhängig von der relativen Feuchte von Tagen bis Wochen. Beim Transport von BBA in die freie Troposphäre kann diese sich durch die durch niedrige Temperaturen verlangsamte Diffusion auf über einen Monat erhöhen.

Durch die Interaktion von atmosphärischen sowie synthetisch hergestellten, sekundären organischen Aerosolen (SOA) mit Wasser wird eine große Menge an OH-Radikalen gebildet, was durch die Zersetzung der organischen Hydroperoxide erklärt werden kann. Die molare Ausbeute an OH-Radikalen aus SOA, welches durch die Oxidation von Terpenen (α-Pinen, β-Pinen, Limonen, Isopren) gebildet wurde, beträgt 0.1 % bei Extraktion mit reinem Wasser und steigt basierend auf Fenton-ähnlichen Reaktionen an auf bis zu

1.5 % in Gegenwart von Fe^{2+}-Ionen. Diese Ergebnisse implizieren, dass die chemische Reaktivität und das Altern von SOA-Partikeln durch die Interaktion von Wasser mit Eisen deutlich gesteigert werden. Im menschlichen Respirationstrakt könnte das Einatmen und Ablagern von SOA-Partikeln zu einem starken Anstieg an OH-Radikalen führen, der zu oxidativem Stress beitragen und die Gesundheit negativ beeinflussen kann.

Ein breites Spektrum an partikelassoziierten Radikalen wurde mit Hilfe der Elektronenspinresonanzspektroskopie (ESR) detektiert und als größenaufgelöste Aerosolpartikel quantifiziert. Die Partikelproben wurden mittels eines Kaskadenimpaktors im Mai und Juni 2015 an einem semiurbanen Standort in Mainz, Deutschland, gesammelt. Die Konzentrationen an langlebigen, freien Radikalen (Englisch: *environmentally persistent free radicals*, EPFR), vor allem Semichinon-Radikale, lag bei (1-7) $\times$ 10^{11} Spins μg^{-1} für Partikel im Akkumulationsmode, wohingegen gröbere Partikel mit einem Durchmesser größer als 1 μm keine wesentlichen Mengen an EPFR enthielten. Mit Hilfe der Spin-Trapping-Technik wurde eine ROS-Konzentration von (0.1-3) $\times$ 10^{11} Spins μg^{-1} bestimmt, die durch die Extraktion der Partikelproben in Wasser gebildet wurden. Bei der Dekonvolution von EPR-Spektren wurden ROS aus Submikron-Partikeln gefunden, die sowohl OH-, Superoxid- (O_2^-) als auch kohlenstoff- und sauerstoffzentrierte organische Radikale enthalten. Dagegen waren OH-Radikale bei groben Partikeln vorherrschend. Die EPR-Spektren von Aerosolpartikelmaterial wurden mit denen von Mischungen aus organischen Hydroperoxiden, Chinonen und Eisenionen verglichen. Dieser Vergleich und die chemische Analyse mittels Flüssigchromatographie-Massenspektrometrie (LC-MS) legen nahe, dass partikelassoziierte ROS aus der Zersetzung von organischen Hydroperoxiden entstehen, welche mit in atmosphärischen huminstoffartigen Substanzen (HULIS) enthaltenen Übergangsmetallionen und Chinonen wechselwirken.

Mit Hilfe eines Kaskadenimpaktors wurden im Januar 2016 in Beijing, China und im April desselben Jahres in Nagoya, Japan, Umgebungspartikel gesammelt. In Beijing lag die durchschnittlich enthaltene EPFR-Konzentration in den Partikeln mit einem Durchmesser von 100-560 nm bei 1.3 $\times$ 10^{12} Spins μg^{-1}, welche fast eine Größenordnung höher ist als die durchschnittliche EPFR-Konzentration in Mainz, 2.3 $\times$ 10^{11} Spins μg^{-1}, und in Nagoya 4.7$\times$ 10^{11} Spins μg^{-1}. Die Differenz für Partikel größer als 320 nm ist noch größer. Diese Ergebnisse könnten mit den starken Emissionen aus Biomassen- und Kohleverbrennung in Beijing sowie mit den fossilen Brennstoffen und Verkehrsemissionen in Nagoya und Mainz zusammenhängen.

Die Identifikation und Bewertung der chemischen Stabilität von Radikaladdukten, die aus EPR-Experimenten mit Spin-Trapping-Technik resultieren, ist nicht trivial. Hierfür wurde eine neue, MATLAB-basierte Toolbox (Electron Paramagnetic Resonance for Spin TrappIng Chemical Kinetics, EPR-STICK) zur Bearbeitung von EPR-Spektren, Quantifizierung von Radikalen, Dekonvolution von Spektren und kinetischer Modellierung von Radikalreaktionen entwickelt. Sie wurde auf experimentelle Daten angewendet, um sowohl die Kinetik von Spin-Trapping, als auch die Effizienz und Ausbeute von Radikalen zu untersuchen, die bei der durch Eisenionen katalysierten Zersetzung von Tertbutylhydroperoxid entstehen.

Acknowledgements

I am very grateful to have done my PhD in Germany and in particular at the Max Planck Institute for Chemistry, where I had many opportunities to challenge myself.

First of all I would like to thank Manabu Shiraiwa, my advisor, for the opportunity to spend these enriching years under his guidance at the MPIC, for trusting, encouraging and continuously supporting me in all situations and contexts. He gave me a lot of freedom and more importantly, the opportunity to make mistakes and learn from them, as an excellent supervisor does. We had always great discussions and I have learnt a lot from his suggestions and corrections.

I would also like to thank Ulrich Pöschl. His comments were always inspiring and very scientifically educative. I will bring with me many of his principles.

Thanks to Thorsten Hoffmann for his valuable inputs and advices at PAC meetings.

Others thanks go to my actual office mates Haijie Tong, Pascale Lakey, Joanna Socorro as well as my former office mates Thomas Berkemeier, Ying Li, Taina Yli-Juuti, Nihan Uygur and Yan Liu. Together with Christopher Kampf and Fobang Liu, I had great scientific discussions, and I have learned a lot from all of them. They helped me in many situations.

Thanks to Daniel Knopf and Jonatahan Slade (Stony Brook University), Dorothea Macholdt (MPIC), Michihiro Mochida and Tomoki Nakayama (Nagoya University), Hang Su (MPIC) and Keding Lu (Peking University) for our wonderful and successful collaborations.

The Earth System Science conference group with David Cabrera, Thomas Berkemeier (again), Christiane Schultz, Bettina Derstroff, Einar Karu, Mega Octaviani, Janek Zeuschner for this experience and for their friendship.

My work was logistically and financially supported by the International Max Planck Research School for Atmospheric Chemistry and Physics.

Last but not least, I thank the most important person in my life, Giulia. We managed to go through many difficulties even at thousands of kilometer of distance and we turn to be even stronger, thanks for trusting me all this time.

Contents

1. Introduction

1.1. The Anthropocene

Mankind is the strongest global geophysical force (Ehlers and Krafft, 2006; Crutzen, 2002). Since the industrial revolution human activity has become intense enough to induce changes in the environment on both local and global scales. Habitats which are more affected by human activity are characterized by less genetic diversity than in wilder regions (Miraldo et al., 2016), suggesting that human activity threatens biodiversity directly (e.g. overfishing) and indirectly (e.g. pollution). Mankind is introducing chemicals and materials into the environment that were not present in nature before. Extensive use of pesticides and fertilizers to support the increasing food demand is altering the global nitrogen cycle (Fox et al., 2007; Fields, 2004). Plastics are already spread and sedimented throughout the world and they have even been proposed as geological indicator for the age of man, the "Anthropocene" (Zalasiewicz et al., 2016).

The pressure that human activity is applying to the environment has accelerated since the 1950s (Steffen et al., 2015) and the human footprint index has been established to quantify it. The index takes into account several aspects including the extraction rate of natural resources, proliferation of infrastructures and conversion of natural habitats to urban territory or productive lands (Kareiva et al., 2007). The human footprint indicates that through agriculture, construction, damming of rivers, and fabrication of artificial islands mankind is completely changing the landscape and stripping away land sediments at much faster rate than erosion by natural forces (Monastersky, 2015; Ruddiman, 2013). It is worth noting that from 1993 to 2009 the world population has increased by the 23%, the world economy has grown by the 153%, but the human footprint has increased by just 9% (Venter et al., 2016), indicating an increased efficiency in the use of land resources particularly in wealthy regions.

Exploitation of Earth's resources is negatively affecting the environment in many aspects. Due to high emissions and the accumulation of greenhouse gasses such as CO_2, CH_4, N_2O, the atmospheric composition is altered and is causing global warming (Stocker, 2014). The rising global temperature induces glaciers to melt (Medwedeff and Roe, 2016), extreme weather events in terms of temperature (Cohen et al., 2014) and precipitation (Lehmann et al., 2015) to become more frequent and the risk of biological extinction for many species to increase (Urban, 2015). Concentrations of air pollutants including O_3, $PM_{2.5}$, and NO_x and related public health effects are increasing over the last 150 years and this is an increasing trend also in the next years.

More efforts are needed to reach global agreements between states to avoid to making climate changes irreversible. The necessity to achieve a global agreement is becoming

more urgent in the near future. Indeed, the world population is expected to grow even more, from the present 7.3 billion to 11.2 billion people in the next years and the addition is likely to be spread unevenly across the world, with the largest increase in the poorest regions (Bongaarts, 2016) that have also the largest footprint. Population growth can cause food crises due to affordability, increases in disease, and social and political instability (McMichael, 2014). A natural consequence of the demographic expansion are the continuous migration fluxes from poor and rural regions to cities. Since 2008 more than half of the world's population is living in cities (Population Fund, 2007) due to the expansion of urban areas to form megacities, that is, cities with populations exceeding several millions of inhabitants. Although fast and uncontrolled expansion of many cities in under development countries is already having serious consequences on environment, air quality and public health, well planned megacities can be a good opportunity to minimize the human footprint as megacities are densely populated areas where land conversion is reduced and where energy production and consumption can be organized more efficiently (Qiu, 2012). For this purpose clear regulations and agreements needs to be achieved.

1.1.1. Air Pollution and Aerosols

Air pollution is one of the biggest issues in the anthropocene and according to the World Health Organization, approximately 3 million premature deaths worldwide are attributed to it (WHO, 2016), representing the biggest environmental risk to public health. This is particularly true in megacities where a large number of pollution sources are active in densely populated area (Krzyzanowski et al., 2014; Mahowald et al., 2011).

Air pollution is a complex mixture of gases and suspended particles that can vary according to location and season and is composed of contaminants that alter the natural composition of the atmosphere. Its overall airborne mass concentrations are regulated in many countries to account for its association with increased morbidity and mortality. Diseases such as chronic obstructive pulmonary disease (COPD), acute lower respiratory illness, cerebrovascular disease, ischemic heart disease, and pulmonary cancer are correlated with air pollution and particulate matter (PM) exposure (Lelieveld et al., 2015).

Aerosols, consisting of liquid, solid or semisolid particles and the gas phase surrounding them, are considered a subset of air pollution in urban regions but they also play a central role on climate. Human activities such as production of energy and goods, transportation and land use for crop production leads to the emission of large amount of aerosols that have completely altered the aerosol emission pattern in the last 160 years (Mahowald et al., 2011). Aerosols are emitted directly as particles (primary aerosols) or formed upon oxidation and condensation of volatile organic compounds (secondary aerosols). The size distribution, number concentration, and chemical composition are all primary quantities that determine the impact of aerosols on the atmosphere. For example, the size distribution, which ranges from 1 nm to 100 μm, affects their atmospheric lifetime,

capacity to scatter sunlight and, together with number concentration (Dusek et al., 2006), their ability to form clouds. Moreover, the aerosol size distribution is indicative of the type of particles under investigation: combustion and condensation of volatile compounds produce mostly fine aerosols (with particle diameters $< 1.0\ \mu$m) whereas natural sources (desert dust, sea-spray or bioaerosols) emit mostly coarse aerosols (with particle diameter $> 1.0\ \mu$m). The chemical composition of particles strongly determines their impact on climate, biogeochemistry and public health but an accurate chemical characterization is a laborious analytical task. The composition can be rather uniform or very diverse depending on the particle size, source and the atmospheric age of the particles (Pöschl, 2005). The major chemical components are inorganic salts (NH_4^+, Na^+, SO_4^{2-}, NO_3^-, Cl^-), biological material (proteins, viruses, spores, fungi, bacteria, pollen), transition and alkaline earth metals and carbonaceous compounds (organic and black carbon). The carbonaceous fraction, or organic fraction, is produced by combustion, natural sources and secondary processes and can contain tens of thousands of different types of compounds including soot, polycyclic aromatic compounds (PACs), highly oxidized multifunctional organic compounds (HOMs) (Mutzel et al., 2015) with low and high molecular weight.

Transition metals, soot, polycyclic aromatic compounds (PACs) and allergenic proteins are considered to cause adverse health effects (Shiraiwa et al., 2012b). Although the mechanism is unclear, it is hypothesized that specific substances in PM are responsible for triggering illnesses rather than the overall mass of the particles. Identifying and quantifying these compounds and understanding the processes that impact public health can lead to preventative measures and reduce public health risks associated with PM.

1.2. Reactive Oxygen Species

Reactive Oxygen Species (ROS) are a class of ubiquitous compounds formed as intermediates of molecular oxygen reduction and play a central role in both atmospheric chemistry and biological systems. ROS include the hydroxyl radical ($^{\cdot}OH$), singlet oxygen ($^1O_2$), superoxide radical ($O_2^{-\cdot}$), hydrogen peroxide (H_2O_2), and ozone (O_3)(Ayres et al., 2008; Winterbourn, 2008). A less stringent definition of ROS encompasses a wider range of oxygen centered radicals, ions and molecules such as organic peroxyl radicals ($RO_2^{\cdot}$), alkoxy and phenoxy radicals ($RO^{\cdot}$), ozonides (OZ), organic hydroperoxides (ROOH), organic peroxides (ROOR), and hypocloride ions (OCl^-)(Pöschl and Shiraiwa, 2015; Shiraiwa et al., 2012b; Apel and Hirt, 2004).

ROS are involved in many intra and extracellular processes including redox homeostasis, inflammation, changes in the activity of cytosolic enzymes, intracellular metabolism of mitochondria, cell signaling and regulation (Ray et al., 2012; Foyer and Noctor, 2005; Turrens, 2003). Phagocytes produce ROS as a defense mechanism from foreign organisms (Bedard and Krause, 2007; Lambeth, 2004). External stimuli such as toxins, ultraviolet light and inflammatory cytokines can also trigger the formation of ROS (Finkel and Holbrook, 2000). ROS concentrations in both intra and extra cellular compartments

are controlled by a large variety of antioxidants including enzymatic scavengers such as superoxide dismutase (SOD) and catalase and low molecular mass antioxidants such as ascorbate, glutathione, NADPH, uric acid and α-tocopherol (Andriantsitohaina et al., 2012).

In the atmosphere, ROS are involved in the oxidation and self-cleaning processes of the atmosphere (Levy, 1971; World Meteorological Organization, 2011). The primary source of atmospheric ROS is gas-phase photochemistry, but secondary sources such as multiphase and heterogeneous reactions, can significantly contribute to the ROS budget and destabilize the atmospheric oxidation capacity (Montzka et al., 2011) as sinks and sources of many ROS are closely coupled by radical chain reactions (Finlayson-Pitts and Pitts, 2000). Secondary Organic Aerosol (SOA) formation and growth are initiated and controlled by reactions of ozone, OH, and NO_3 radicals with Volatile Organic Compounds (VOCs), producing a variety of compounds with a large range of oxidation degrees, reactivities and volatilities (Ziemann and Atkinson, 2012).

As illustrated in Figure 1.1, atmospheric and physiological ROS are chemically coupled and continually exchanged throughout the entire biosphere by means of several types of biological interfaces such as the human respiratory tract, skin, plant leaves, cryptogamic covers and bioaerosols (Pöschl and Shiraiwa, 2015). It has been demonstrated that exposure to environmental ROS induces oxidative stress in the pulmonary tract (Lakey et al., 2016), which is a key mechanism in the promotion of pathologic pulmonary fibrosis (Cheresh et al., 2013). Although the exact mechanism and molecular constituents of atmospheric particles that trigger the exogenous formation of ROS remains unclear, Fenton-like reactions between transition metals and H_2O_2 to form OH radicals is the main candidate as a source of ROS from atmospheric aerosols deposited in the lungs. However, fine particles generated from secondary processes contain species such as organic hydroperoxides (Krapf et al., 2016) that can provide additional sources of ROS (Tong et al., 2016). Moreover, several studies underline the presences in $PM_{2.5}$ of Environmentally Persistent Free Radical (EPFR) (Dellinger et al., 2001; Gehling and Dellinger, 2013), that is, stable radicals that generate ROS upon dissolution in water (Gehling et al., 2014; Arangio et al., 2016).

EPFRs are generally regarded as combustion generated organic radicals that have been associated with semiquinone-type radicals which can be stabilized by charge-transfer bonds with transition metals (Dellinger et al., 2000; Maskos and Dellinger, 2008; Lomnicki et al., 2008). Other processes can also generate EPFRs including the pyrolysis of lignin (Bährle et al., 2014) and heterogeneous oxidation of PACs with ozone (Shiraiwa et al., 2011b; Borrowman et al., 2016). Due to their stability in the particle phase, EPFRs can be detected and quantified by means of Electron Paramagnetic Resonance (EPR) spectroscopy directly from the filters containing the collected particles. EPR is applied to study materials containing unpaired electrons that can absorb microwave electromagnetic radiation when immersed in a magnetic field.

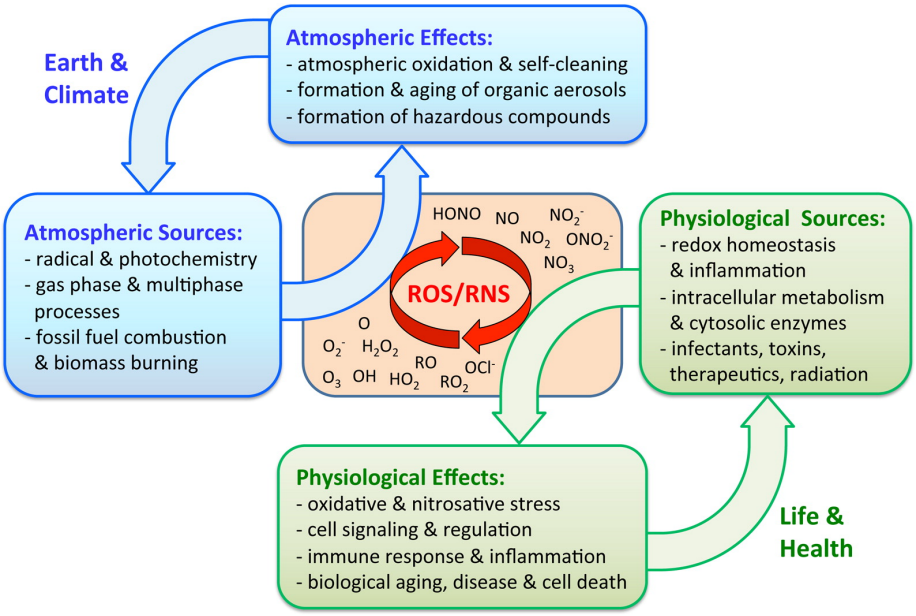

Figure 1.1.: *Reactive oxygen and nitrogen species (ROS, RNS): schematic for sources, interactions, and effects at the interface of the atmosphere and biosphere, including feedback loops involving Earth system, climate, life, and health [Pöschl and Shiraiwa (2015)]*

1.3. Multiphase Chemistry of Organic Aerosols

Organic compounds constitute 20 to 90% of fine particulate mass (Jimenez et al., 2009). Fossil fuels, biomass burning, oxidized and condensed VOCs contribute to this fraction with high temporal and spatial variability and therefore are difficult to quantify and characterize. Moreover, atmospheric aerosols are dynamic systems that evolve continuously. Gas-particle interactions including mass transport, heterogeneous and particle phase reactions can severely transform chemical composition, physical state and optical, hygroscopic and toxicological properties of particles (Pöschl, 2005; George and Abbatt, 2010).

Aerosol aging rates are controlled, among other factors, by the aerosol's physical state. Although organic aerosol particles were considered to be liquid and internally well-mixed, recent work has shown that organic particles can assume semi-solid or solid-amorphous states depending on the temperature and relative humidity (Koop et al., 2011). Solid phases are characterized by slow bulk diffusion that limits mass transport and inhibits bulk reactions causing chemical modification to be limited to the particle surface (Shiraiwa et al., 2011a; Berkemeier et al., 2013; Arangio et al., 2015; Kroll et al., 2015). At high temperature and relative humidity, and in absence of other limitations such as gas phase diffusion or gas-particle accommodation, bulk diffusion is fast enough to allow the gaseous reactant to saturate quasi-instantaneously the condensed phase and the chemical evolution proceeds in the bulk of the particle.

1.3.1. Gas Uptake and Heterogeneous Chemistry

Interaction of trace gasses with atmospheric particles is controlled by either thermodynamic factors (e.g. gas solubility in the particle phase) or kinetic factors (e.g. mass transport) (Pöschl et al., 2007). To understand which key factor control aerosol evolution, heterogeneous processes are investigated by monitoring the net reactive uptake of gases by the condensed phase. The reactive uptake γ, is defined as the ratio between the net fluxes of the reactant from the gas phase to the condensed phase, J_{net}, and the total flux of molecules that collide with the particle, J_{coll}:

$$\gamma = \frac{J_{\text{net}}}{J_{\text{coll}}} \tag{1.1}$$

where the numerator takes into account the reversible mass transport from the surface to the bulk, the gas solubility, its diffusion coefficient in the bulk and the desorption lifetime, which is the mean residence time of the adsorbed species on the particle surface. The kinetic multilayer model of gas-particle interactions in aerosols and clouds (KM-GAP) can be applied to resolve detailed kinetic information of heterogeneous processes by explicitly taking into account gas-phase diffusion, reversible adsorption of the gaseous reactant, surface-bulk exchange, bulk diffusion, and chemical reactions at the surface and in the bulk of the condensed phase (Shiraiwa et al., 2012a). Fast reactive uptake of atmospheric gasses can induce aerosol hygroscopic growth and activation of cloud condensation nuclei (Slade et al., 2015). In field campaigns and remote sensing the source strength contributions to aerosols mass concentrations are determined by applying chemical receptor-based models where source-specific molecules are quantified and assumed to be proportional to the source strength itself. This assumption implies that the marker concentration remains unchanged during transportation of aerosols from the source to the collection point. However, multiphase chemistry of atmospheric oxidants substantially affects the atmospheric chemical half-life time of biomass burning markers (Arangio et al., 2015) depending on the atmospheric conditions experienced.

1.3.2. Aqueous phase and Cloud Processing

In cases where the gas-to-particle partitioning is not limited by gas diffusion or accommodation, high bulk diffusivity in liquid particles allows gaseous reactants to saturate the condensed phase and bulk reactions proceed without being limited by mass transports. Beyond heterogeneous chemistry, aerosols with a high water content, including fog and cloud droplets, or aerosols that experience high relative humidity, are usually liquid and undergo fast chemical transformations involving several processes including gas-particle partitioning, mass transport, and complex reaction mechanisms (Finlayson-Pitts and Pitts, 2000; Seinfeld and Pandis, 2016).

Aqueous phase chemistry and cloud processing are efficient pathways to form SOA, induce particle growth and cause aging. Recent studies explicitly indicate that aqueous-

phase reactions and cloud processing of organic aerosols substantially contribute to SOA mass (Lin et al., 2014; Gilardoni et al., 2016). Although aqueous chemistry has been proven to play a role in aerosol evolution, the key chemical components and reactions remain unknown. Aerosol reactivity can be influenced by the presence of organic hydroperoxides formed during the oxidation of VOCs such as α-pinene, β-pinene, limonene and isoprene (Krapf et al., 2016; Tong et al., 2016). Upon dissolution in water, organic hydroperoxides decompose generating free radicals and ROS that subsequently trigger secondary chemistry in the bulk (Tong et al., 2016).

The presence of organic hydroperoxides could also provide an additional pathway for the production of ROS released by ambient and laboratory-generated SOA (Tong et al., 2016; Arangio et al., 2016) and might have a connection to the seasonal dependence of PM mortality indicated by epidemiological studies (Peng et al., 2005). Despite intensive research, multiphase chemistry of SOA in the atmosphere and their interactions with the human respiratory tract are not well understood and further studies are needed to characterize the particle chemical composition, identify and quantify compounds that lead to pathogenic particles and to understand the causal effects that trigger disease.

1.4. Research objectives and activities

To better understand the impact of aerosols on the atmosphere and public health, it is necessary to evaluate and characterize oxidation processes of atmospheric aerosols. The research activity described in this thesis have two main objectives: 1) to study the phase state effects on heterogeneous oxidation processes by applying the KM-GAP model by OH radicals; 2) experimental investigation of radical chemistry of ambient and laboratory generated particles to explore and quantify their ability to generate ROS. Specifically, the objectives and activities of the PhD work can be summarized as follows:

- Application of the KM-GAP model to simulate and describe the degradation of biomass burning organic markers by OH radical and the role played by the phase state of the condensed phase. The study, based on experimental data, was carried out in collaboration with Prof. D. Knopf and Dr. J. Slade from Stony Brook University, New York.

- Development and application of an analytical protocol to quantify radicals produced by laboratory-generated secondary organic aerosols (SOA) interacting with water using EPR spectroscopy and LC-MS/MS. The yields of OH radicals produced by the decomposition of SOA formed by oxidation of terpenes (α-pinene, β-pinene, limonene, isoprene) was investigated..

- Development of an analytical methodology to evaluate the concentration of Environmentally Persistent Free Radicals (EPFR) in size-segregated atmospheric particles. The methodology also includes the identification and quantification of radicals produced by atmospheric particles of different sizes upon interaction with water. The method was applied to atmospheric particles sampled in Mainz, Germany.

- Development of the Electron Paramagnetic Resonance for Spin TrappIng Chemical Kinetics (EPR-STICK), a MATLAB toolbox to process, fit and simulate EPR spectra, to perform radical quantification and kinetic studies of spin trapping EPR experiments, and to carry out routine EPR spectra analysis.
- Quantification and comparison of the size distribution of EPFR concentrations in atmospheric aerosol particles collected in urban and semi-urban sites including Beijing, China in January 2016, Nagoya, Japan in April 2016, and Mainz, Germany, May-June 2015.

2. Method

2.1. Electron Paramagnetic Resonance

Electron Paramagnetic Resonance (EPR) is a magnetic spectroscopy used to study materials with unpaired electrons. The first EPR signal was observed in 1944 by the Soviet physicist Yevgeny Zavoisky. Similarly to Nuclear Magnetic Resonance spectroscopy, the central principle of EPR spectroscopy is the interaction between the magnetic moment $\boldsymbol{\mu}$ of a spinning charged particle immersed in an external magnetic field $\boldsymbol{B}_0$ with the magnetic component $\boldsymbol{B}_1$ of an incident electromagnetic radiation. The interaction that generates the signal and the physical relations between quantities $\boldsymbol{B}_0$, $\boldsymbol{\mu}$ and $\boldsymbol{B}_1$ are mathematically described by the Zeeman effect and the hyperfine splitting.

In the paragraphs below the basics of EPR spectroscopy, including the Zeeman effect and hyperfine splitting are described, together with the spin trapping technique, an advanced methodology which is widely used to extend the application of EPR spectroscopy.

2.1.1. Zeeman Effect and Hyperfine splitting

In EPR spectroscopy, the Zeeman effect describes the splitting experienced by electronic energy levels of an atom, molecule or material immersed in an external magnetic field, $\boldsymbol{B}_0$ (Eaton et al., 2010). In the classical physical description, the energy of a magnetic dipole can be expressed as the scalar product between the external magnetic field, $\boldsymbol{B}_0$, and the intrinsic magnetic moment of the dipole, $\boldsymbol{\mu}$ (Weil et al., 2007)

$$E = - \mid \mu B_0 \mid \cos(\boldsymbol{\mu}, \boldsymbol{B}_0) \tag{2.1}$$

where $(\boldsymbol{\mu}, \boldsymbol{B}_0)$ is the angle between the magnetic moment of the dipole and the direction of the external magnetic field. According to equation 2.1, for a given $\boldsymbol{B}_0$ the minimum and the maximum energy levels $- \mid \mu B_0 \mid$ occur when the dipole is oriented respectively in parallel and anti-parallel to the direction of $\boldsymbol{B}_0$. The Zeemann effect can also be explained through the quantum mechanical theory for which the quantization of the electron spin angular moment leads to the quantization of the energy levels of an electron immersed in a magnetic field. The energy levels can be described as follow:

$$E = g_e \beta_e B_0 M_s \tag{2.2}$$

where $g_e \simeq 2.0023$ is the Zeemann splitting constant for a free electron, $\beta_e \simeq 9.274 \times 10^{-24} JT^{-1}$ is the *Bohr magneton*, and $M_s = \pm 1/2$ is the z component of the secondary

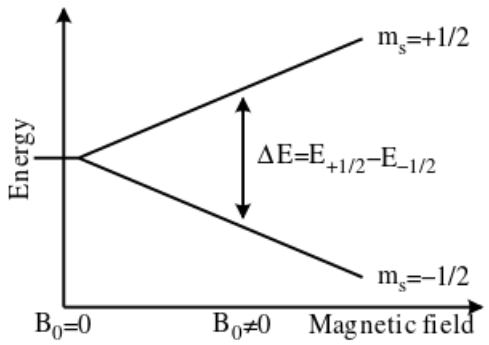

Figure 2.1.: *Schematic of the energy levels splitting for a single spin system with spin quantum number* $M_S = 1/2$ *and immersed in a external magnetic field* $\boldsymbol{B}_0$

quantum number for the electron spin angular moment. An EPR transition involves two adjacent electronic energy levels of a spin system separated by the energy, ΔE, and takes place when the spin system is irradiated by an electromagnetic radiation of frequency, ν, that meets the resonance condition:

$$\Delta E = g_e \beta_e B_0 = h\nu \tag{2.3}$$

where $|\Delta M_s| = 1$ has been omitted and ΔE increases linearly with the intensity of $\boldsymbol{B}_0$ applied (Figure 2.1).

The description above is valid only for hypothetical free electrons immersed in a magnetic field. The actual magnetic field experienced by unpaired electrons of molecules in real samples is a vectorial combination of two contributions including the external magnetic field, $\boldsymbol{B}_0$, and the local magnetic field, $\boldsymbol{B}_{loc}$, generated by magnetically active nuclei eventually present in the molecule.

$$\boldsymbol{B}_{act} = \boldsymbol{B}_0 + \boldsymbol{B}_{loc} \tag{2.4}$$

where the local field has typically two contributions: a local field induced and proportional to the external $\boldsymbol{B}_0$, and permanent local fields that depend only on their mutual orientation with respect to $\boldsymbol{B}_0$.

The spin-orbit coupling, caused by the electron spin interacting with its own motion along its orbit, generates a local field of the first type, the impact on $\boldsymbol{B}_{act}$ can be described by modifying equation 2.4:

$$\boldsymbol{B}_{act} = (1 - \sigma)\,\boldsymbol{B}_0 = (g/g_e)\,\boldsymbol{B}_0 \tag{2.5}$$

where g is the effective Zeemann factor and σ, defined as a distance from the Zeemann splitting constant is the EPR analogous to the chemical shift in NMR. The resonant magnetic field is not unique for a spin system as the resonant condition depends on instrumental parameters. The g-factor, instead, can be defined to indicate the resonant conditions unambiguously:

$$g = h\nu/\beta_e \boldsymbol{B}_0 \tag{2.6}$$

as defined in equation 2.6, the g-factor helps to distinguish and characterize paramagnetic species under investigation. It is worth noting that the spin-orbit coupling is usually weak for elements in the first row of the periodic table and strong for transition metals and heavier elements.

The most important example of the second type of local field, is the permanent local field generated by the magnetic moment associated with the nuclear-spin angular moment. Magnetically active nuclei have non-zero nuclear-spin quantum number, I, which can assume values equal to $\frac{1}{2}$, 1, $\frac{3}{2}$, 2, $\cdots$. I determines the number of nuclear spin states according to the $2I+1$ and each nuclear spin state can assume values $M_I = \pm I$. For hydrogen atoms $I = 1/2$ and $M_I = \pm 1/2$. The resulting $\boldsymbol{B}_{act}$ is:

$$\boldsymbol{B}_{act} = \boldsymbol{B'} - aM_I \tag{2.7}$$

where a is the hyperfine constant, it has most commonly the unit of magnetic field and it can be determined experimentally, whereas $\boldsymbol{B'} = h\nu/g\beta_e$ is the resonant field resulting from the perturbation due to spin-orbit interactions. The hyperfine splitting is very important for identification purposes and typically depends on the distance between the orbital carrying the unpaired electron and the magnetically active nucleus, as well as from any type of substituent that is able to affect the magnetic and electronic properties of the molecule under investigation.

During EPR experiments the resonance condition can be fulfilled by immersing the sample in a constant magnetic field B_0 and scanning the frequency of the incident radiation ν. However, it is common practice to continuously irradiate the sample with a constant frequency radiation while sweeping the magnetic field in order to change ΔE until it matches the energy of the incident radiation. The ΔE involved in EPR transitions requires frequencies of electromagnetic radiations that fall in the microwave range (about $9-10$ GHz).

2.1.2. Spin Trapping

Although, theoretically, the only requirement for a compound to be EPR active is the presence of unpaired electrons, in practice not all paramagnetic compounds give an EPR signal. Many radicals have a lifetime which is too short as they react away before they can built up to high enough concentrations to be detected during an EPR experiment. Due to their high reactivity, concentrations of such radicals in liquid solutions are very often below the instrumental detection limit (minimum detectable radical concentration is 10 nM, Church (1994)). To overcome this problem the spin trap technique is widely applied as indirect method to identify and quantify highly reactive free-radicals (Perkins, 1980; Janzen, 1980). The method is based on the reaction between a target radical and an EPR silent probe, containing a nitroso or nitrone functional group, which becomes

EPR active upon reaction, forming stable nitroxide radicals (Carmichael et al., 1984). The resulting radical-adduct that is formed is stable enough to build up in concentrations above the instrumental detection limit at room temperature.

Several spin-traps are able to form radical-adducts that generate characteristic EPR signal patterns which can be used to distinguish and quantify the type of free-radical that has been trapped. The hyperfine splitting constant is the quantity that allows spectra deconvolution and needs to be determined experimentally if it is not available in the literature. Among others, 5,5-Dimethyl-1-pyrroline N-oxide (DMPO) and 5-tert-butoxycarbonyl 5-methyl-1-pyrroline N-oxide (BMPO) are widely used spin-trap agents which can form redox stable adducts compared to other nitrone based spin-traps and they generate distinguishable EPR spectra with several N-, S-,C- and O- centered radicals (Konaka et al., 1995; Zhao et al., 2001).

3. Results and Conclusions

3.1. Overview

The results of the PhD project are described in 5 manuscripts for peer-reviewed publications in international scientific journals (4 first-author and 1 second-author paper). The manuscripts are attached in Appendix B of this thesis. Three of them have already been published, a fourth paper will to be submitted soon and a fifth is in preparation. An overview of the studies and of the connections between them is given in Figure 3.1. The main results and conclusions of each study are summarized below.

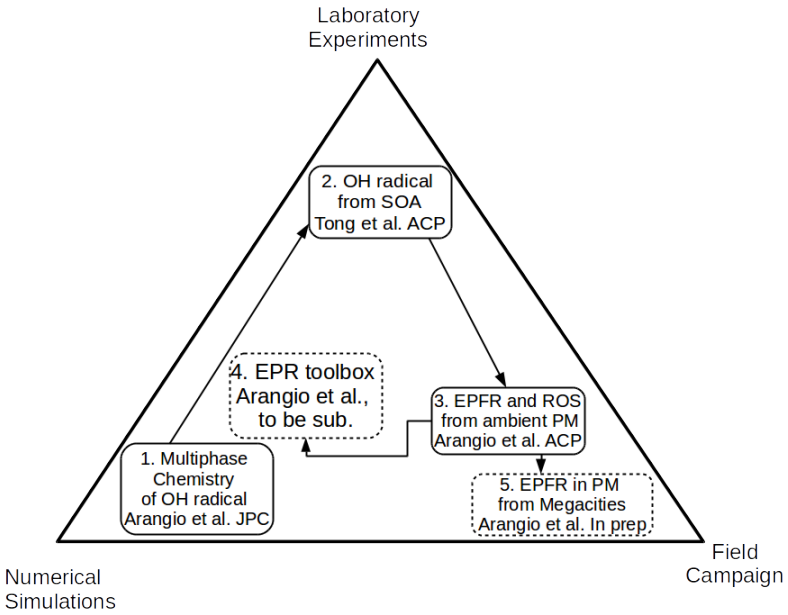

Figure 3.1.: *Structure and results of the PhD project evolving in three dimensions: numerical simulations, laboratory experiments and field campaign. Each box represents a manuscript for peer-reviewed publication in an international scientific journal. Solid frames indicate already published papers, dashed frames the manuscripts to be submitted or in preparation. Arrows show the connections between studies.*

3.2. Individual Studies

3.2.1. Multiphase chemical kinetic modeling

Multiphase reactions of OH radicals are among the most important pathways of chemical aging of organic aerosols in the atmosphere. Reactive uptake of OH by organic compounds has been investigated extensively, but the kinetics of mass transport and chemical reactions and their interdependence are still not understood. The kinetic multilayer model of gas–particle interactions in aerosols and clouds (KM-GAP) resolves these processes by explicitly taking into account solubility, diffusivity and reactivity of each species involved. In this work, KM-GAP was applied to experimental data from OH exposure in coated-wall flow tube of levoglucosan (LG) and abietic acid (AA), which serve as surrogates and molecular markers of biomass burning aerosol (BBA). For both LG and AA, the bulk diffusion coefficients were found to be approximately 10^{-16} cm^2s^{-1}, reflecting their amorphous semisolid state. It was shown that the OH uptake by these films was governed by the reaction at or near the surface and could be kinetically limited by bulk diffusion of the organic reactants. Through these diffusion coefficients, the chemical half-life of LG in 200 nm diameter particles in a biomass burning plume was estimated to increase from one day at high relative humidity to one week under dry conditions. In BBA particles transported to the free troposphere, the chemical half-life of LG can exceed one month due to slow bulk diffusion in a glassy matrix at low temperature. For details see Appendix B1: Arangio et al., J. Physics Chemistry A 2015.

3.2.2. OH generation from α-pinene Secondary Organic Aerosol

Ambient and laboratory-generated secondary organic aerosols (SOA) were found to form substantial amounts of OH radicals upon interaction with liquid water, which can be explained by the decomposition of organic hydroperoxides. The molar OH yield from SOA formed by ozonolysis of terpenes (α-pinene, β -pinene, limonene) is 0.1 % upon extraction with pure water and increases to 1.5 % in presence of Fe^{2+} ions due to Fenton-like reaction. Upon extraction of SOA samples from OH photooxidation of isoprene, OH yields were around 0.1 %, which also increases upon addition of Fe^{2+}. These findings imply that the chemical reactivity and aging of SOA particles is strongly enhanced upon interaction with water and iron. In cloud droplets under dark conditions, SOA decomposition can compete with the classical H_2O_2-Fenton reaction as source of OH radicals. Also in the human respiratory tract, the inhalation and deposition of SOA particles may lead to a substantial release of OH radicals, which may contribute to oxidative stress and play an important role in the adverse health effects of atmospheric aerosols. For details see Appendix B2: Tong et al., Atmospheric Chemistry and Physics 2015.

3.2.3. Quantification of Environmental Persistent Free Radicals and Reactive Oxygen Species from Ambient Particulate Matter

In this study, A wide range of particle-associated radicals were detected and quantified in size segregated atmospheric particles using electron paramagnetic resonance (EPR) spectroscopy. Particle samples were collected using a cascade impactor at a semi-urban site in central Europe, Mainz, Germany, in May-June 2015. Concentrations of environmentally persistent free radicals (EPFR), most likely semiquinone radicals, were found to be in the range of (1-7) $\times$ 10^{11} spins μg^{-1} for particles in the accumulation mode. Coarse particles with a diameter larger than 1 μm did not contain substantial amounts of EPFR. Using a spin trapping technique total ROS formed upon extraction of the particle samples in water were determined to be (0.1-3) $\times$ 10^{11} spins μg^{-1}. By deconvolution of EPR spectra ROS released by submicron particle samples were found to include OH, superoxide (O_2^-), carbon- and oxygen-centered organic radicals. OH was instead the dominant species for coarse particles. EPR spectra derived from ambient particulate matter were compared with those of mixtures of organic hydroperoxides, quinones and iron ions. By means of the EPR spectra comparison and chemical analysis with liquid chromatography mass spectrometry (LC-MS), the particle-associated ROS were suggested to be formed by decomposition of organic hydroperoxides interacting with transition metal ions and quinones contained in atmospheric humic-like substances (HULIS). For details see Appendix B3: Arangio et al. Atmospheric Chemistry and Physics 2015.

3.2.4. EPR-STICK, a software package for Electron Paramagnetic Resonance spectral processing, simulation and kinetic modeling of spin trapping experiments

Interpretation of Electron Paramagnetic Resonance (EPR) spectra resulting from the application of spin-trapping technique is a difficult task to accomplish. Electron Paramagnetic Resonance for Spin TrappIng Chemical Kinetics (EPR-STICK) was developed, which is a new MATLAB-based toolbox to perform EPR spectral processing, radical quantification, deconvolution of spectra from mixtures of radical-adducts and kinetic modeling of radical reactions. Based on EasySpin, a well established EPR spectra simulator, EPR-STICK was built to improve the EasySpin usability, the reproducibility of fitting and simulation procedures for non-expert users, and expand EasySpin applications with kinetic modeling of spin-trapping experiments. To illustrate the applicability of the toolbox, experiments were carried out to investigate the kinetics of spin trapping, yield and efficiency of radical-adducts formed upon Fenton-like decomposition of tert-butyl-hydroperoxide catalyzed by iron ions. The kinetic parameters such as kinetic rate

constant for radical production, trapping, and adduct decomposition reactions were determined by a global-optimization algorithm. Further details in Appendix B4: Arangio et al. *to be submitted*.

3.2.5. Comparison of Environmentally Persistent Free Radicals in Size Distributed Atmospheric Particles from different locations

Ambient particles were collected using a cascade impactor also in Beijing, China in January 2016 and in Nagoya, Japan in April 2016. The average EPFR concentration contained in particles with size diameter range of 100 - 320 nm was 1.3×10^{12} spins μg^{-1} in Beijing, which is almost one order of magnitude higher than the average EPFR concentrations in Mainz (2.3×10^{11} spins μg^{-1}), and in Nagoya (4.7×10^{11} spins μg^{-1}). The difference is remarkably high for particles with lower cut-off sizes of 320 nm, in which EPFR concentrations were 1.3×10^{12} spins μg^{-1} in Beijing and 9.9×10^{10} and 2.5×10^{11} spins μg^{-1} in Mainz and Nagoya, respectively. The result reflects stronger the aerosol emission from biomass and coal combustion in Beijing compared to fossil fuels and traffic emissions in Nagoya and Mainz.

3.2.6. Summary and Outlooks

The oxidant chemistry studies pursued in this PhD thesis stress the central role played by Reactive Oxygen Species (ROS) in promoting chemical modifications of atmospheric aerosols. Through heterogeneous processes, ROS can partially or completely oxidize biomass burning aerosols depending on the physical state of the particle. By interacting with water and transition metals, atmospheric and laboratory generated aerosols produce ROS which lead to the homogeneous oxidation of particles. The production of ROS from particles interacting with water and transition metals can also explain the negative impact of atmospheric aerosols on public health. Several pulmonary diseases are indeed associated with oxidative stress promoted by ROS.

In this thesis, EPFRs contained in atmospheric aerosols were quantified. It was found that organic particles can produce ROS upon interaction with water which can be enhanced in the presence of iron ions by Fenton-like reactions. The concentration EPFRs determined in size-distributed particles collected in urban and semi-urban locations could reflect the different type of aerosols sources in the locations investigated.

Further research is needed to understand which precursors, atmospheric processes and conditions can lead to the formation, accumulation and chemical stabilization of EPFRs and organic hydroperoxides. In this respect, temperature and light severely affect the final concentration of these species. For example, although organic hydroperoxide can be produced by photochemical oxidation, they are also thermo- and photolabile.

The combined effect of organic hydroperoxides, EPFR and transition metals in pure water, surrogate lung lining fluid in *in vitro* and *in vivo* experiments should also be investigated. Upon particle deposition in the respiratory tract, the interplay of these species could trigger catalytic cycles involving anti-oxidants which could generate a positive feedback in the production of ROS. The EPR-STICK developed and presented in this thesis can be a powerful tool to investigate such types of radical reactions. The toolbox provide a more tight working interface between spin-trapping EPR experiments and kinetic modeling of radical reactions.

4. Bibliography

Andriantsitohaina, R., Duluc, L., García-Rodríguez, J. C., Gil-del Valle, L., Guevara-Garcia, M., Simard, G., Soleti, R., Su, D.-F., Velásquez-Pérez, L., Wilson, J. X., and Laher, I.: Systems biology of antioxidants, Clinical Science (London, England: 1979), 123, 173–192, doi:10.1042/CS20110643, 2012.

Apel, K. and Hirt, H.: Reactive Oxygen Species: Metabolism, Oxidative Stress, and Signal Transduction, Annual Review of Plant Biology, 55, 373–399, doi:10.1146/annurev.arplant.55.031903.141701, 2004.

Arangio, A. M., Slade, J. H., Berkemeier, T., Pöschl, U., Knopf, D. A., and Shiraiwa, M.: Multiphase Chemical Kinetics of OH Radical Uptake by Molecular Organic Markers of Biomass Burning Aerosols: Humidity and Temperature Dependence, Surface Reaction, and Bulk Diffusion, The Journal of Physical Chemistry A, 119, 4533–4544, doi:10.1021/jp510489z, 2015.

Arangio, A. M., Tong, H., Socorro, J., Pöschl, U., and Shiraiwa, M.: Quantification of environmentally persistent free radicals and reactive oxygen species in atmospheric aerosol particles, Atmospheric Chemistry and Physics, 16, 13 105–13 119, doi:10.5194/acp-16-13105-2016, 2016.

Ayres, J. G., Borm, P., Cassee, F. R., Castranova, V., Donaldson, K., Ghio, A., Harrison, R. M., Hider, R., Kelly, F., Kooter, I. M., Marano, F., Maynard, R. L., Mudway, I., Nel, A., Sioutas, C., Smith, S., Baeza-Squiban, A., Cho, A., Duggan, S., and Froines, J.: Evaluating the Toxicity of Airborne Particulate Matter and Nanoparticles by Measuring Oxidative Stress Potential—A Workshop Report and Consensus Statement, Inhalation Toxicology, 20, 75–99, doi:10.1080/08958370701665517, 2008.

Bedard, K. and Krause, K.-H.: The NOX family of ROS-generating NADPH oxidases: physiology and pathophysiology, Physiological Reviews, 87, 245–313, doi:10.1152/physrev.00044.2005, 2007.

Berkemeier, T., Huisman, A. J., Ammann, M., Shiraiwa, M., Koop, T., and Pöschl, U.: Kinetic regimes and limiting cases of gas uptake and heterogeneous reactions in atmospheric aerosols and clouds: a general classification scheme, Atmospheric Chemistry and Physics, 13, 6663–6686, doi:10.5194/acp-13-6663-2013, 2013.

Bongaarts, J.: Development: Slow down population growth, Nature, 530, 409–412, doi:10.1038/530409a, 2016.

Borrowman, C. K., Zhou, S., Burrow, T. E., and Abbatt, J. P. D.: Formation of environmentally persistent free radicals from the heterogeneous reaction of ozone and polycyclic aromatic compounds, Phys. Chem. Chem. Phys., 18, 205–212, doi:10.1039/C5CP05606C, 2016.

Bährle, C., Custodis, V., Jeschke, G., van Bokhoven, J., and Vogel, F.: In situ Observation of Radicals and Molecular Products During Lignin Pyrolysis, ChemSusChem, 7, 2022–2029, doi:10.1002/cssc.201400079, 2014.

Carmichael, A. J., Makino, K., and Riesz, P.: Quantitative Aspects of ESR and Spin Trapping of Hydroxyl Radicals and Hydrogen Atoms in Gamma-Irradiated Aqueous Solutions, Radiation Research, 100, 222, doi:10.2307/3576343, 1984.

Cheresh, P., Kim, S.-J., Tulasiram, S., and Kamp, D. W.: Oxidative stress and pulmonary fibrosis, Biochimica et Biophysica Acta (BBA) - Molecular Basis of Disease, 1832, 1028–1040, doi:10.1016/j.bbadis.2012.11.021, 2013.

Church, D. F.: Spin Trapping Organic Radicals, Analytical Chemistry, 66, 419A–427A, doi:10.1021/ac00079a002, 1994.

Cohen, J., Screen, J. A., Furtado, J. C., Barlow, M., Whittleston, D., Coumou, D., Francis, J., Dethloff, K., Entekhabi, D., Overland, J., and Jones, J.: Recent Arctic amplification and extreme mid-latitude weather, Nature Geoscience, 7, 627–637, doi:10.1038/ngeo2234, 2014.

Crutzen, P. J.: Geology of mankind, Nature, 415, 23–23, doi:10.1038/415023a, 2002.

Dellinger, B., Pryor, W. A., Cueto, B., Squadrito, G. L., and Deutsch, W. A.: The role of combustion-generated radicals in the toxicity of PM2.5, Proceedings of the Combustion Institute, 28, 2675–2681, doi:10.1016/S0082-0784(00)80687-6, 2000.

Dellinger, B., Pryor, W. A., Cueto, R., Squadrito, G. L., Hegde, V., and Deutsch, W. A.: Role of Free Radicals in the Toxicity of Airborne Fine Particulate Matter, Chemical Research in Toxicology, 14, 1371–1377, doi:10.1021/tx010050x, 2001.

Dusek, U., Frank, G. P., Hildebrandt, L., Curtius, J., Schneider, J., Walter, S., Chand, D., Drewnick, F., Hings, S., Jung, D., Borrmann, S., and Andreae, M. O.: Size Matters More Than Chemistry for Cloud-Nucleating Ability of Aerosol Particles, Science, 312, 1375–1378, doi:10.1126/science.1125261, 2006.

Eaton, G. R., Eaton, S. S., Barr, D. P., and Weber, R. T.: Quantitative EPR, Springer, Wien; New York, oCLC: 663098006, 2010.

Ehlers, E. and Krafft, T., eds.: Earth system science in the Anthropocene, Springer, Berlin ; New York, 2006.

Fields, S.: Global Nitrogen: Cycling out of Control, National Institute of Environmental Health Sciences, Brogan & Partners, 112, A557–A563, 2004.

Finkel, T. and Holbrook, N. J.: Oxidants, oxidative stress and the biology of ageing, Nature, 408, 239–247, doi:10.1038/35041687, 2000.

Finlayson-Pitts, B. J. and Pitts, J. N.: Chemistry of the upper and lower atmosphere: theory, experiments, and applications, Academic Press, San Diego, 2000.

Fox, J. E., Gulledge, J., Engelhaupt, E., Burow, M. E., and McLachlan, J. A.: Pesticides reduce symbiotic efficiency of nitrogen-fixing rhizobia and host plants, Proceedings of the National Academy of Sciences, 104, 10 282–10 287, doi:10.1073/pnas.0611710104, 2007.

Foyer, C. H. and Noctor, G.: Redox homeostasis and antioxidant signaling: a metabolic interface between stress perception and physiological responses, The Plant Cell, 17, 1866–1875, doi:10.1105/tpc.105.033589, 2005.

Gehling, W. and Dellinger, B.: Environmentally Persistent Free Radicals and Their Lifetimes in PM $_{2.5}$, Environmental Science & Technology, 47, 8172–8178, doi:10.1021/es401767m, 2013.

Gehling, W., Khachatryan, L., and Dellinger, B.: Hydroxyl Radical Generation from Environmentally Persistent Free Radicals (EPFRs) in PM $_{2.5}$, Environmental Science & Technology, 48, 4266–4272, doi:10.1021/es401770y, 2014.

George, I. J. and Abbatt, J. P. D.: Heterogeneous oxidation of atmospheric aerosol particles by gas-phase radicals, Nature Chemistry, 2, 713–722, doi:10.1038/nchem.806, 2010.

Gilardoni, S., Massoli, P., Paglione, M., Giulianelli, L., Carbone, C., Rinaldi, M., Decesari, S., Sandrini, S., Costabile, F., Gobbi, G. P., Pietrogrande, M. C., Visentin, M., Scotto, F., Fuzzi, S., and Facchini, M. C.: Direct observation of aqueous secondary organic aerosol from biomass-burning emissions, Proceedings of the National Academy of Sciences, 113, 10 013–10 018, doi:10.1073/pnas.1602212113, 2016.

Janzen, E. G.: A Critical Review of Spin Trapping in Biological Systems, in: Free Radicals in Biology, pp. 115–154, Elsevier, 1980.

Jimenez, J. L., Canagaratna, M. R., Donahue, N. M., Prevot, A. S. H., Zhang, Q., Kroll, J. H., DeCarlo, P. F., Allan, J. D., Coe, H., Ng, N. L., Aiken, A. C., Docherty, K. S., Ulbrich, I. M., Grieshop, A. P., Robinson, A. L., Duplissy, J., Smith, J. D., Wilson, K. R., Lanz, V. A., Hueglin, C., Sun, Y. L., Tian, J., Laaksonen, A., Raatikainen, T., Rautiainen, J., Vaattovaara, P., Ehn, M., Kulmala, M., Tomlinson, J. M., Collins, D. R., Cubison, M. J., E., Dunlea, J., Huffman, J. A., Onasch, T. B., Alfarra, M. R., Williams, P. I., Bower, K., Kondo, Y., Schneider, J., Drewnick, F., Borrmann, S., Weimer, S., Demerjian, K.,

Salcedo, D., Cottrell, L., Griffin, R., Takami, A., Miyoshi, T., Hatakeyama, S., Shimono, A., Sun, J. Y., Zhang, Y. M., Dzepina, K., Kimmel, J. R., Sueper, D., Jayne, J. T., Herndon, S. C., Trimborn, A. M., Williams, L. R., Wood, E. C., Middlebrook, A. M., Kolb, C. E., Baltensperger, U., and Worsnop, D. R.: Evolution of Organic Aerosols in the Atmosphere, Science, 326, 1525–1529, doi:10.1126/science.1180353, 2009.

Kareiva, P., Watts, S., McDonald, R., and Boucher, T.: Domesticated Nature: Shaping Landscapes and Ecosystems for Human Welfare, Science, 316, 1866–1869, doi:10.1126/science.1140170, 2007.

Konaka, R., Kawai, M., Noda, H., Kohno, M., and Niwa, R.: Synthesis and evaluation of DMPO-type spin traps, Free Radical Research, 23, 15–25, 1995.

Koop, T., Bookhold, J., Shiraiwa, M., and Pöschl, U.: Glass transition and phase state of organic compounds: dependency on molecular properties and implications for secondary organic aerosols in the atmosphere, Physical Chemistry Chemical Physics, 13, 19 238, doi:10.1039/c1cp22617g, 2011.

Krapf, M., El Haddad, I., Bruns, E., Molteni, U., Daellenbach, K., Prévôt, A., Baltensperger, U., and Dommen, J.: Labile Peroxides in Secondary Organic Aerosol, Chem, 1, 603–616, doi:10.1016/j.chempr.2016.09.007, 2016.

Kroll, J. H., Lim, C. Y., Kessler, S. H., and Wilson, K. R.: Heterogeneous Oxidation of Atmospheric Organic Aerosol: Kinetics of Changes to the Amount and Oxidation State of Particle-Phase Organic Carbon, The Journal of Physical Chemistry A, 119, 10 767–10 783, doi:10.1021/acs.jpca.5b06946, 2015.

Krzyzanowski, M., Apte, J. S., Bonjour, S. P., Brauer, M., Cohen, A. J., and Prüss-Ustun, A. M.: Air Pollution in the Mega-cities, Current Environmental Health Reports, 1, 185–191, doi:10.1007/s40572-014-0019-7, 2014.

Lakey, P. S. J., Berkemeier, T., Tong, H., Arangio, A. M., Lucas, K., Pöschl, U., and Shiraiwa, M.: Chemical exposure-response relationship between air pollutants and reactive oxygen species in the human respiratory tract, Scientific Reports, 6, 32 916, doi:10.1038/srep32916, 2016.

Lambeth, J. D.: NOX enzymes and the biology of reactive oxygen, Nature Reviews. Immunology, 4, 181–189, doi:10.1038/nri1312, 2004.

Lehmann, J., Coumou, D., and Frieler, K.: Increased record-breaking precipitation events under global warming, Climatic Change, 132, 501–515, doi:10.1007/s10584-015-1434-y, 2015.

Lelieveld, J., Evans, J. S., Fnais, M., Giannadaki, D., and Pozzer, A.: The contribution of outdoor air pollution sources to premature mortality on a global scale, Nature, 525, 367–371, doi:10.1038/nature15371, 2015.

Levy, H.: Normal atmosphere: large radical and formaldehyde concentrations predicted, Science (New York, N.Y.), 173, 141–143, doi:10.1126/science.173.3992.141, 1971.

Lin, G., Sillman, S., Penner, J. E., and Ito, A.: Global modeling of SOA: the use of different mechanisms for aqueous-phase formation, Atmospheric Chemistry and Physics, 14, 5451–5475, doi:10.5194/acp-14-5451-2014, 2014.

Lomnicki, S., Truong, H., Vejerano, E., and Dellinger, B.: Copper oxide-based model of persistent free radical formation on combustion-derived particulate matter, Environmental Science & Technology, 42, 4982–4988, 2008.

Mahowald, N., Ward, D. S., Kloster, S., Flanner, M. G., Heald, C. L., Heavens, N. G., Hess, P. G., Lamarque, J.-F., and Chuang, P. Y.: Aerosol Impacts on Climate and Biogeochemistry, Annual Review of Environment and Resources, 36, 45–74, doi:10.1146/annurev-environ-042009-094507, 2011.

Maskos, Z. and Dellinger, B.: Radicals from the Oxidative Pyrolysis of Tobacco, Energy & Fuels, 22, 1675–1679, doi:10.1021/ef7006694, 2008.

McMichael, A. J.: Population health in the Anthropocene: Gains, losses and emerging trends, The Anthropocene Review, 1, 44–56, doi:10.1177/2053019613514035, 2014.

Medwedeff, W. G. and Roe, G. H.: Trends and variability in the global dataset of glacier mass balance, Climate Dynamics, doi:10.1007/s00382-016-3253-x, 2016.

Miraldo, A., Li, S., Borregaard, M. K., Florez-Rodriguez, A., Gopalakrishnan, S., Rizvanovic, M., Wang, Z., Rahbek, C., Marske, K. A., and Nogues-Bravo, D.: An Anthropocene map of genetic diversity, Science, 353, 1532–1535, doi:10.1126/science.aaf4381, 2016.

Monastersky, R.: Anthropocene: The human age, Nature, 519, 144–147, doi:10.1038/519144a, 2015.

Montzka, S. A., Krol, M., Dlugokencky, E., Hall, B., Jockel, P., and Lelieveld, J.: Small Interannual Variability of Global Atmospheric Hydroxyl, Science, 331, 67–69, doi:10.1126/science.1197640, 2011.

Mutzel, A., Poulain, L., Berndt, T., Iinuma, Y., Rodigast, M., Böge, O., Richters, S., Spindler, G., Sipilä, M., Jokinen, T., Kulmala, M., and Herrmann, H.: Highly Oxidized Multifunctional Organic Compounds Observed in Tropospheric Particles: A Field and Laboratory Study, Environmental Science & Technology, 49, 7754–7761, doi:10.1021/acs.est.5b00885, 2015.

Peng, R. D., Dominici, F., Pastor-Barriuso, R., Zeger, S. L., and Samet, J. M.: Seasonal analyses of air pollution and mortality in 100 US cities, American Journal of Epidemiology, 161, 585–594, doi:10.1093/aje/kwi075, 2005.

Perkins, M.: Spin Trapping, in: Advances in Physical Organic Chemistry, vol. 17, pp. 1–64, Elsevier, 1980.

Population Fund, ed.: Unleashing the potential of urban growth, no. 2007 in State of world population, UNFPA, New York, NY, oCLC: 253959030, 2007.

Pöschl, U.: Atmospheric Aerosols: Composition, Transformation, Climate and Health Effects, Angewandte Chemie International Edition, 44, 7520–7540, doi:10.1002/anie.200501122, 2005.

Pöschl, U. and Shiraiwa, M.: Multiphase Chemistry at the Atmosphere–Biosphere Interface Influencing Climate and Public Health in the Anthropocene, Chemical Reviews, 115, 4440–4475, doi:10.1021/cr500487s, 2015.

Pöschl, U., Rudich, Y., and Ammann, M.: Kinetic model framework for aerosol and cloud surface chemistry and gas-particle interactions – Part 1: General equations, parameters, and terminology, Atmospheric Chemistry and Physics, 7, 5989–6023, doi:10.5194/acp-7-5989-2007, 2007.

Qiu, J.: Megacities pose serious health challenge, Nature, doi:10.1038/nature.2012.11495, 2012.

Ray, P. D., Huang, B.-W., and Tsuji, Y.: Reactive oxygen species (ROS) homeostasis and redox regulation in cellular signaling, Cellular Signalling, 24, 981–990, doi:10.1016/j.cellsig.2012.01.008, 2012.

Ruddiman, W. F.: The Anthropocene, Annual Review of Earth and Planetary Sciences, 41, 45–68, doi:10.1146/annurev-earth-050212-123944, 2013.

Seinfeld, J. H. and Pandis, S. N.: Atmospheric chemistry and physics: from air pollution to climate change, Wiley, Hoboken, New Jersey, 3rd edition edn., oCLC: 946547332, 2016.

Shiraiwa, M., Ammann, M., Koop, T., and Poschl, U.: Gas uptake and chemical aging of semisolid organic aerosol particles, Proceedings of the National Academy of Sciences, 108, 11 003–11 008, doi:10.1073/pnas.1103045108, URL http://www.pnas.org/cgi/doi/10.1073/pnas.1103045108, 2011a.

Shiraiwa, M., Sosedova, Y., Rouvière, A., Yang, H., Zhang, Y., Abbatt, J. P. D., Ammann, M., and Pöschl, U.: The role of long-lived reactive oxygen intermediates in the reaction of ozone with aerosol particles, Nature Chemistry, 3, 291–295, doi:10.1038/nchem.988, 2011b.

Shiraiwa, M., Pfrang, C., Koop, T., and Pöschl, U.: Kinetic multi-layer model of gas-particle interactions in aerosols and clouds (KM-GAP): linking condensation, evaporation and chemical reactions of organics, oxidants and water, Atmospheric Chemistry and Physics, 12, 2777–2794, doi:10.5194/acp-12-2777-2012, 2012a.

Shiraiwa, M., Selzle, K., and Pöschl, U.: Hazardous components and health effects of atmospheric aerosol particles: reactive oxygen species, soot, polycyclic aromatic compounds and allergenic proteins, Free Radical Research, 46, 927–939, doi:10.3109/10715762.2012.663084, 2012b.

Slade, J. H., Thalman, R., Wang, J., and Knopf, D. A.: Chemical aging of single and multicomponent biomass burning aerosol surrogate particles by OH: implications for cloud condensation nucleus activity, Atmospheric Chemistry and Physics, 15, 10 183–10 201, doi:10.5194/acp-15-10183-2015, 2015.

Steffen, W., Broadgate, W., Deutsch, L., Gaffney, O., and Ludwig, C.: The trajectory of the Anthropocene: The Great Acceleration, The Anthropocene Review, 2, 81–98, doi:10.1177/2053019614564785, 2015.

Stocker, T., ed.: Climate change 2013: the physical science basis: Working Group I contribution to the Fifth assessment report of the Intergovernmental Panel on Climate Change, Cambridge University Press, New York, 2014.

Tong, H., Arangio, A. M., Lakey, P. S. J., Berkemeier, T., Liu, F., Kampf, C. J., Brune, W. H., Pöschl, U., and Shiraiwa, M.: Hydroxyl radicals from secondary organic aerosol decomposition in water, Atmospheric Chemistry and Physics, 16, 1761–1771, doi:10.5194/acp-16-1761-2016, 2016.

Turrens, J. F.: Mitochondrial formation of reactive oxygen species, The Journal of Physiology, 552, 335–344, doi:10.1113/jphysiol.2003.049478, 2003.

Urban, M. C.: Accelerating extinction risk from climate change, Science, 348, 571–573, doi:10.1126/science.aaa4984, 2015.

Venter, O., Sanderson, E. W., Magrach, A., Allan, J. R., Beher, J., Jones, K. R., Possingham, H. P., Laurance, W. F., Wood, P., Fekete, B. M., Levy, M. A., and Watson, J. E. M.: Sixteen years of change in the global terrestrial human footprint and implications for biodiversity conservation, Nature Communications, 7, 12 558, doi:10.1038/ncomms12558, 2016.

Weil, J. A., Bolton, J. R., and Wiley InterScience (Online service): Electron paramagnetic resonance: elementary theory and practical applications., Wiley-Interscience, Hoboken, N.J., oCLC: 87898611, 2007.

WHO: Ambient air pollution: A global assessment of exposure and burden of disease, WHO, Geneve, 2016.

Winterbourn, C. C.: Reconciling the chemistry and biology of reactive oxygen species, Nature Chemical Biology, 4, 278–286, doi:10.1038/nchembio.85, 2008.

World Meteorological Organization, ed.: Scientific assessment of ozone depletion: 2010: pursuant to Article 6 of the Montreal Protocol on Substances that Deplete the Ozone Layer, no. no. 52 in Global Ozone Research and Monitoring Project report, World Meterological Organization, Geneva, Switzerland, 2011.

Zalasiewicz, J., Waters, C. N., Ivar do Sul, J. A., Corcoran, P. L., Barnosky, A. D., Cearreta, A., Edgeworth, M., Galuszka, A., Jeandel, C., Leinfelder, R., McNeill, J., Steffen, W., Summerhayes, C., Wagreich, M., Williams, M., Wolfe, A. P., and Yonan, Y.: The geological cycle of plastics and their use as a stratigraphic indicator of the Anthropocene, Anthropocene, 13, 4–17, doi:10.1016/j.ancene.2016.01.002, 2016.

Zhao, H., Joseph, J., Zhang, H., Karoui, H., and Kalyanaraman, B.: Synthesis and biochemical applications of a solid cyclic nitrone spin trap: a relatively superior trap for detecting superoxide anions and glutathiyl radicals, Free Radical Biology & Medicine, 31, 599–606, 2001.

Ziemann, P. J. and Atkinson, R.: Kinetics, products, and mechanisms of secondary organic aerosol formation, Chemical Society Reviews, 41, 6582, doi:10.1039/c2cs35122f, 2012.

A. Personal List of Publications

A.1. Journal Articles

1. H. Tong, P. S. Lakey, A. M. Arangio, J. Socorro, C. Kampf, T. Berkemeier, W. H. Brune, J. Crowley, U. Pöschl, and M. Shiraiwa, Reactive oxygen species formed in aqueous mixtures of secondary organic aerosols and mineral dust influencing cloud chemistry and public health in the Anthropocene, ***Faraday Discuss.***, *submitted*

2. J. H. Slade, M. Shiraiwa, A. M. Arangio, H. Su, U. Pöschl, J. Wang, and D. A. Knopf, Cloud droplet activation through oxidation of organic aerosol influenced by temperature and particle phase state, ***J. Geophys. Res.***, *doi:*$10.1002/2016GL072424, 2017$

3. D. S. Macholdt, K. P. Jochum, C. Pöhlker, A. M. Arangio, J. D. Foerster, B. Stoll, U. Weis, B. Weber, M. Müller, M. Kappl, M. Shiraiwa, A. L. D. Kilcoyne, M. Weigand, D. Scholz, G. Haug, A. Al-Amri, and M. O. Andreae, Characterization and differentiation of rock varnish types from different environments by microanalytical techniques, ***Chem. Geol.***, *submitted*.

4. A. M. Arangio, H. Tong, J. Socorro, U. Pöschl, M. Shiraiwa, Quantification of environmentally persistent free radicals and reactive oxygen species in atmospheric aerosol particles, ***Atmos. Chem. Phys.***, $16, 13105 - 13119, 2016. doi : 10.5194/acp - 16 - 13105 - 2016$.

5. P. S. Lakey, T. Berkemeier, T. Haijie, A. M. Arangio, K. Lucas, U. Pöschl, M. Shiraiwa, Chemical exposure-response relationship between air pollutants and reactive oxygen species in the human respiratory tract, ***Sci. Rep.***, $6, 32916, 2016$.

6. H. Tong, A. M. Arangio, P. S. Lakey, T. Berkemeier, F. Liu, C. J. Kampf, W. H. Brune, U. Pöschl, M. Shiraiwa, Hydroxyl radicals from secondary organic aerosol decomposition in water, ***Atmos. Chem. Phys.***, $16, 1761 - 1771, 2016$.

7. A. M. Arangio, J. H. Slade, T. Berkemeier, U. Pöschl, D. A. Knopf, M. Shiraiwa, Multiphase chemical kinetics of OH radical uptake by molecular organic markers of biomass burning aerosols: Humidity and temperature dependence, surface reaction and bulk diffusion, ***J. Phys. Chem. A***, $119, 4533 - 4544, 2015$.

8. S. Monaco, A. M. Arangio, F. Soavi, M. Mastragostino, E. Palliard, S. Passerini: An electrochemical study of oxygen reduction in pyrrolidinium-based ionic liquids for lithium/oxygen batteries, ***Electrochem. Acta***, $83, 94 - 104, 2012$

Oral Presentation

1. A. M. Arangio, H. Tong, J. Socorro, U. Pöschl, M. Shiraiwa, Quantification of environmentally persistent free radicals and reactive oxygen species in atmospheric aerosol particles, European Aerosol Conference 2016, Tours, France.

Poster Presentation

1. A. M. Arangio, H. Tong, J. Socorro, U. Pöschl, M. Shiraiwa, Quantification of environmentally persistent free radicals and reactive oxygen species in atmospheric aerosol particles, European Aerosol Conference 2015, Milan, Italy.

2. A. M. Arangio, H. Tong, J. Socorro, U. Pöschl, M. Shiraiwa, Quantification of environmentally persistent free radicals and reactive oxygen species in atmospheric aerosol particles, 7th Summer School of the European Federation of EPR groups on Advanced EPR, Berlin, Germany.

3. A. M. Arangio, J. H. Slade, T. Berkemeier, U. Pöschl, D. A. Knopf, M. Shiraiwa, Multiphase chemical kinetics of OH radical uptake by molecular organic markers of biomass burning aerosols: Humidity and temperature dependence, surface reaction and bulk diffusion, Towards a molecular-level understanding of atmospheric aerosols 2014, Ascona, Switzerland.

4. A. M. Arangio, J. H. Slade, T. Berkemeier, U. Pöschl, D. A. Knopf, M. Shiraiwa, Multiphase chemical kinetics of OH radical uptake by molecular organic markers of biomass burning aerosols: Humidity and temperature dependence, surface reaction and bulk diffusion, European Geosciences Union general assembly 2014, Vienna, Austria.

5. A. M. Arangio, J. H. Slade, T. Berkemeier, U. Pöschl, D. A. Knopf, M. Shiraiwa, Multiphase chemical kinetics of OH radical uptake by molecular organic markers of biomass burning aerosols: Humidity and temperature dependence, surface reaction and bulk diffusion, Earth System Science 2014, Jena, Germany.

B. Selected List of Publications

1. A. M. Arangio, J. H. Slade, T. Berkemeier, U. Pöschl, D. A. Knopf, M. Shiraiwa, Multiphase chemical kinetics of OH radical uptake by molecular organic markers of biomass burning aerosols: Humidity and temperature dependence, surface reaction and bulk diffusion, ***J. Phys. Chem.*** A, $119, 4533 - 4544, 2015$.

2. H. Tong, A. M. Arangio, P. Lakey, T. Berkemeier, F. Liu, C. J. Kampf, W. H. Brune, U. Pöschl, M. Shiraiwa, Hydroxyl radicals from secondary organic aerosol decomposition in water, ***Atmos. Chem. Phys.***, $16, 1761 - 1771, 2016$.

3. A. M. Arangio, H. Tong, J. Socorro, U. Pöschl, M. Shiraiwa, Quantification of environmentally persistent free radicals and reactive oxygen species in atmospheric aerosol particles, ***Atmos. Chem. Phys.***, $16, 13105 - 13119, 2016. doi : 10.5194/acp - 16 - 13105 - 2016$.

4. A. M. Arangio, P. Lakey, H. Tong, T. Berkemeier, U. Pöschl, M. Shiraiwa, EPR-STICK, a software package for Electron Paramagnetic Resonance spectral processing, simulation and kinetic modeling of spin trapping experiments, *to be submitted*

5. A. M. Arangio and M. Shiraiwa, Comparison of Environmentally Persistent Free Radicals in Size Distributed Atmospheric Particles from different locations, *report*

B.1. Arangio et al., J. Phys. Chem. A, 2015

Multiphase Chemical Kinetics of OH Radical Uptake by Molecular Organic Markers of Biomass Burning Aerosols: Humidity and Temperature Dependence, Surface Reaction, and Bulk Diffusion

Andrea M. Arangio[1], Jonathan H. Slade[2], Thomas Berkemeier[1], Ulrich Pöschl[1], Daniel A. Knopf[2] and Manabu Shiraiwa[1]

1 Max Planck Institute for Chemistry, Multiphase Chemistry Department, Mainz, Germany
2 Institute for Terrestrial and Planetary Atmospheres, School of Marine and Atmospheric Science, Stony Brook University, Stony Brook, New York, United States

Journal of Physics Chemistry A, 119, 4533 – 4544, 2015.

Authors contributions.

MS, DK and UP designed research. JS and DK performed experiments and collected data. AA and TB performed parameters optimization. AA analyzed and performed kinetic modeling. All authors discussed the results. AA, UP, DK, and MS wrote the paper.

THE JOURNAL OF PHYSICAL CHEMISTRY A

Article

pubs.acs.org/JPCA

Multiphase Chemical Kinetics of OH Radical Uptake by Molecular Organic Markers of Biomass Burning Aerosols: Humidity and Temperature Dependence, Surface Reaction, and Bulk Diffusion

Andrea M. Arangio,[†] Jonathan H. Slade,[‡] Thomas Berkemeier,[†] Ulrich Pöschl,[†] Daniel A. Knopf,*[,‡] and Manabu Shiraiwa*[,†]

[†]Multiphase Chemistry Department, Max Planck Institute for Chemistry, D-55128 Mainz, Germany

[‡]Institute for Terrestrial and Planetary Atmospheres, School of Marine and Atmospheric Sciences, Stony Brook University, Stony Brook, New York 11794, United States

ABSTRACT: Multiphase reactions of OH radicals are among the most important pathways of chemical aging of organic aerosols in the atmosphere. Reactive uptake of OH by organic compounds has been observed in a number of studies, but the kinetics of mass transport and chemical reaction are still not fully understood. Here we apply the kinetic multilayer model of gas−particle interactions (KM-GAP) to experimental data from OH exposure studies of levoglucosan and abietic acid, which serve as surrogates and molecular markers of biomass burning aerosol (BBA). The model accounts for gas-phase diffusion within a cylindrical coated-wall flow tube, reversible adsorption of OH, surface-bulk exchange, bulk diffusion, and chemical reactions at the surface and in the bulk of the condensed phase. The nonlinear dependence of OH uptake coefficients on reactant concentrations and time can be reproduced by KM-GAP. We find that the bulk diffusion coefficient of the organic molecules is approximately 10^{-16} cm^2 s^{-1}, reflecting an amorphous semisolid state of the organic substrates. The OH uptake is governed by reaction at or near the surface and can be kinetically limited by surface-bulk exchange or bulk diffusion of the organic reactants. Estimates of the chemical half-life of levoglucosan in 200 nm particles in a biomass burning plume increase from 1 day at high relative humidity to 1 week under dry conditions. In BBA particles transported to the free troposphere, the chemical half-life of levoglucosan can exceed 1 month due to slow bulk diffusion in a glassy matrix at low temperature.

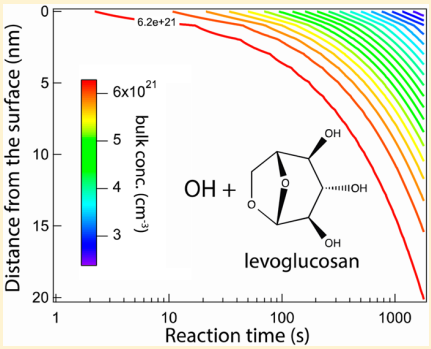

INTRODUCTION

Biomass burning is one of the largest sources of primary organic aerosols, black carbon,[1] and trace gases in the Earth's atmosphere with a source strength comparable to fossil fuel burning.[2−4] Biomass burning aerosol (BBA) has a significant impact on climate and public health. BBAs are ubiquitous and via pyro-convection can also reach the upper troposphere and lower stratosphere regions of the atmosphere.[5−9] They scatter or absorb solar radiation and can serve as cloud condensation nuclei and ice nuclei affecting cloud microphysical and radiative properties.[10,11] Black and brown carbon produced from incomplete combustion are important contributors to the radiative forcing,[12,13] and polycyclic aromatic hydrocarbons (PAHs) associated with BBA can cause adverse health effects such as oxidative stress.[14−16]

Several field campaigns and remote sensing studies have been performed to investigate the impact of biomass burning on local, regional, and global scales.[17−21] The contribution of biomass burning emissions to field-collected particles is typically evaluated by applying chemical receptor-based models, which utilize source-specific molecules, also termed biomolecular markers, found in the particles to identify the source and estimate aerosol source strength.[22] Levoglucosan (1,6-anhydro-β-D-glucopyranose, $C_6H_{10}O_5$) and abietic acid (1-phenanthrenecarboxylic acid, $C_{20}H_{30}O_2$) are produced during lignin and hemicellulose combustion and often used as molecular markers of biomass burning emission.[23−25]

Although levoglucosan and abietic acid are considered chemically stable in the atmosphere, several field campaigns on BBA emissions have shown large seasonal variations of levoglucosan concentration characterized by a strong levoglucosan depletion during summer compared to C/O ratio and K^+, which indicates the marker's degradation during transport.[26,27] This is supported by laboratory studies which have shown that levoglucosan and abietic acid can degrade by photooxidation[28] and heterogeneous reactions with OH[29−35] and NO_3 radicals.[36,37] The reaction rate of the marker depends on the gas-phase concentration of the oxidants[29] as well as relative humidity (RH).[35] Multiphase chemical processes alter the physical and chemical properties of the particles,[38−41] which in turn impact radiative and hygroscopic properties, cloud

Special Issue: Mario Molina Festschrift

Received: October 18, 2014
Revised: February 13, 2015
Published: February 16, 2015

DOI: 10.1021/jp510489z
J. Phys. Chem. A 2015, 119, 4533−4544

condensation nuclei and ice nuclei activities,[42−44] brown carbon formation,[45−47] and toxicity.[16,48] Multiphase oxidation of levoglucosan and abietic acid by OH can also lead to significant degradation.[29−33,35]

In experimental studies heterogeneous and multiphase chemical processes are often characterized by the uptake coefficient γ_{OH}, which is the ratio between the net flux of OH to the particle and the OH collision flux.[49] The γ_{OH} values experimentally derived for levoglucosan and abietic acid reacting with OH are in the range of 0.056−1.[29,35] Applying the kinetic multilayer model of gas−particle interactions in aerosols and clouds (KM-GAP),[50] we analyze new experimental data on the OH exposure of levoglucosan and abietic acid substrates under dry conditions and investigate the relative contributions of surface and bulk reactions to the overall OH uptake. KM-GAP allows us to estimate kinetic parameters such as surface accommodation coefficient, desorption time, reaction rate coefficients, bulk diffusion coefficients of both OH and organics, and the Henry's law coefficient of OH in the organic phase. Kinetic regimes and limiting cases[51,52] of the multiphase reactions of OH radicals were investigated by systematic sensitivity studies to the laboratory data. Finally, the chemical half-life of levoglucosan due to heterogeneous and multiphase reactions was estimated for atmospherically relevant gas-phase OH concentrations.

METHODS

Figure 1 shows a schematic of the KM-GAP model with multiple compartments and layers: gas phase, near-surface gas phase, sorption layer, surface layer, and a number of bulk layers. KM-GAP treats the following processes of mass transport and chemical reactions explicitly: gas-phase diffusion, surface adsorption and desorption, surface-bulk exchange, bulk diffusion, and chemical reactions at the surface and in the bulk.[50] Gas-phase diffusion flux and correction factor for a cylindrical flow tube are derived analogous to spherical particles as described in Pöschl et al. (2007)[49] and has been validated[53] against the numerical approach of Brown,[54] which had also been used to determine the experimental γ_{OH} values.[29] Surface and bulk layer thicknesses can change due to volatilization or condensation in response to mass transport, which eventually leads to particle growth or shrinkage. Mass transport fluxes between layers are based on the first-order approximation of Fick's diffusion equation using bulk diffusion coefficients.[50] The surface-bulk exchange is constrained by solubility of the compound in the bulk (e.g., by the Henry's law coefficient). For the simulation of coated-wall flow-tube experiments, the initial thickness of the organic film was taken to be 100 nm and described by 100 model layers. The exact number of model layers was relevant for the resolution of the bulk profile but not for the overall model result of OH uptake, which was determined by chemical reaction in the uppermost few nanometers of the organic film. Like in the determination of experimental γ_{OH} values,[29] the organic surface was assumed to be smooth. For the estimation of chemical half-lifes and the degraded fraction of biomass burning particles, we assumed spherical geometry of the particles.

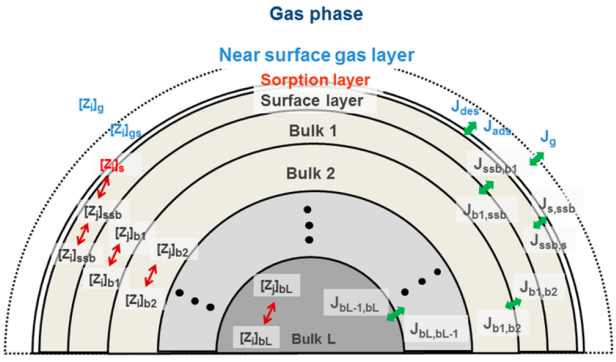

Figure 1. Schematics of the kinetic multilayer model of gas−particle interactions in aerosols and clouds (KM-GAP).[50] Concentrations of species Z_i and Z_j in the gas (g) and near-surface gas phase, at the sorption layer (s) and in the surface (ssb) and in the bulk (b) layers. J are the transport fluxes between each layer, including the gas-phase diffusion flux (J_g), the adsorption (J_{ads}) and desorption (J_{des}) fluxes, surface−bulk exchange fluxes ($J_{s,ssb}$, $J_{ssb,s}$), and bulk diffusion fluxes (J_b).

The reaction rates at the surface and in the bulk are described using a second-order dependence from the concentration of the reactants in each bulk layer. The reaction scheme for levoglucosan and abietic acid reacting with OH was proposed by Slade and Knopf.[29] Hydrogen abstraction from the substrate is the first and the limiting step for both levoglucosan and abietic acid, as also suggested by molecular dynamic simulations.[55] Two reaction products are considered in the model, one being volatile and the other nonvolatile. For simplicity, secondary reactions between OH and these products are not taken into account; these are usually slower than the primary reaction.[56] Self-reaction of OH on the surface is also neglected because the uptake coefficients reported for OH self-reaction are as low as 10^{-4}.[29,57]

The temporal evolution of the uptake coefficient, γ_{OH}, and the surface and bulk compositions were simulated by numerically solving the ordinary differential equations considering the mass balance of each layer. The physically well-constrained input parameters include thermal velocity of OH (T = 298 K; ω_{OH} = 6.1 × 10^4 cm s^{-1}), effective molecular diameter of OH (δ_{OH} = 0.30 nm), levoglucosan (LG; δ_{LG}= 0.69 nm), and abietic acid (AA; δ_{AA} = 0.78 nm).[37] The gas-phase diffusion coefficient of OH under experimental conditions was 185 cm^2 s^{-1}.[29] The concentration of levoglucosan for each bulk layer is 6.27 × 10^{21} cm^{-3} considering a densely packed system formed exclusively by levoglucosan molecules (molecular volume =1.59 × 10^{-22} cm^3).[37]

The kinetic input parameters include the surface accommodation coefficient of OH on a free substrate ($\alpha_{s,0}$), desorption lifetime (τ_d), second-order surface (k_{SLR}) and bulk (k_{BR}) reaction rate coefficients between OH and organics, Henry's law coefficient of OH ($K_{sol,cc}$) in the organic phase, and the bulk diffusion coefficients for OH and organics (D_{OH}, D_{org}), respectively. We assumed $\alpha_{s,0}$ = 1, as the measured maximum γ_{OH} for this reaction system is ∼0.9,[29,35] and $\alpha_{s,0}$ needs to be larger than γ_{OH} by definition.[49] This assumption is also consistent with molecular dynamic simulations of OH[58] and our previous study on kinetic modeling and experiments of ozonolysis on organic surfaces.[48] Moreover, sensitivity studies showed that the modeled γ_{OH} is insensitive to $\alpha_{s,0}$ as long as $\alpha_{s,0}$ >∼0.5. Other parameters are less constrained and used as fitting parameters in this study.

To fit the experimental data, we varied the kinetic parameters in KM-GAP using a global optimization method that utilizes a uniformly sampled Monte Carlo search to seed a genetic algorithm (MCGA method). The genetic algorithm (Matlab

DOI: 10.1021/jp510489z
J. Phys. Chem. A 2015, 119, 4533−4544

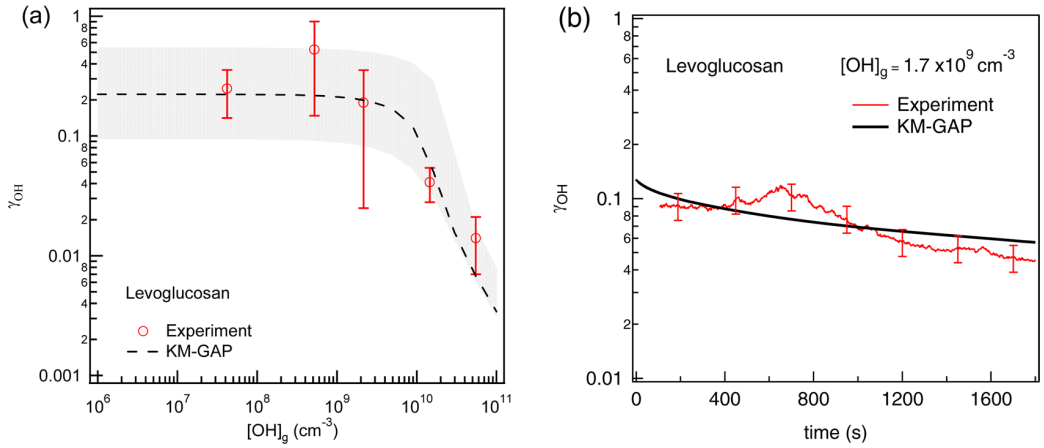

Figure 2. OH uptake coefficient (γ_{OH}) for levoglucosan measured (red) and modeled (black) by KM-GAP. (a) γ_{OH} as a function of gas-phase OH concentration. The shaded area represents model simulations with different sets of kinetic parameters determined by the Monte Carlo genetic algorithm method. (b) Temporal evolution of γ_{OH} with gas-phase OH concentration of 1.7×10^9 cm^{-3}.

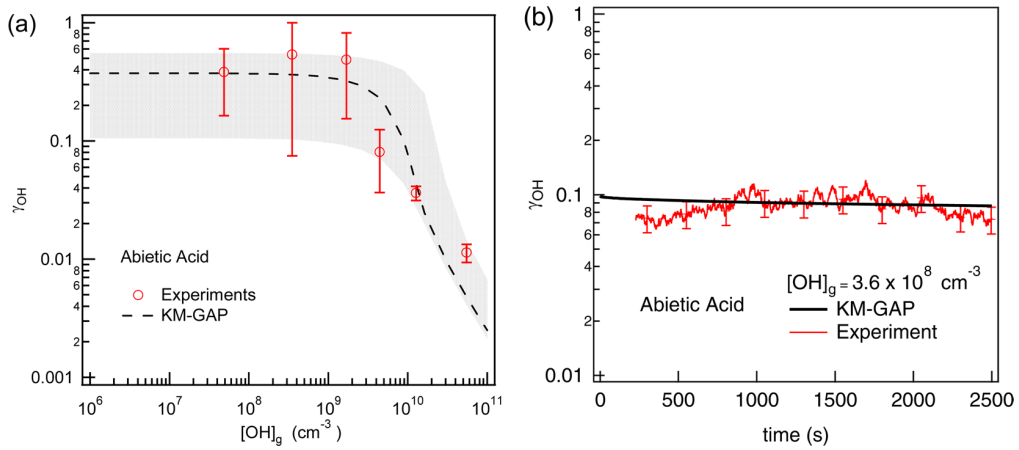

Figure 3. OH uptake coefficient (γ_{OH}) for abietic acid measured (red) and modeled (black) by KM-GAP. (a) γ_{OH} as a function of gas-phase OH concentration. The shaded area represents model simulations with different sets of kinetic parameters determined by the Monte Carlo genetic algorithm method. (b) Temporal evolution of γ_{OH} with gas-phase OH concentration of 3.6×10^8 cm^{-3}.

software) was terminated when the correlation between experimental data and model output converged into an optimum. Since the optimization of the kinetic parameters to the experimental data was not unique in all kinetic parameters, repeated execution of the MCGA method yields a range of kinetic parameters, which can be used to describe the experimental data. For each parameter a plausible range of variation was chosen based on previous kinetic studies.[37,48,50,51,59,60] The upper limit of k_{BR} is given by the rate coefficient of a diffusion-controlled reaction which can be estimated from the bulk diffusion coefficients and effective molecular radii of the reactants:[61]

$$k_{BR,max} = 4\pi(D_{OH} + D_{org})(r_{OH} + r_{org})$$

Assuming $r_{OH} + r_{org} \approx r_{org} \approx 10^{-7}$ cm, we obtain $k_{BR,max} \approx 10^{-11}$ cm^3 s^{-1} for a liquid matrix with $D_{OH} + D_{org} \approx D_{OH} \approx 10^{-5}$ cm^2 s^{-1} and $k_{BR,max} \approx 10^{-14}$ cm^3 s^{-1} for a semisolid matrix with $D_{OH} + D_{org} \approx D_{OH} \approx 10^{-8}$ cm^2 s^{-1}. Earlier studies have reported a range of 3.1×10^{-13} to 1.1×10^{-11} cm^3 s^{-1} for the bulk reaction rate coefficient of OH and levoglucosan in the liquid phase,[28,30,32,33] but no literature values are available for semisolid or solid phases. Assuming that the kinetics of diffusion and reaction at the surface are similar to the bulk, a rough estimate for the upper limit of the surface reaction rate coefficient can be obtained by dividing the maximum bulk rate coefficient through the sum of the effective molecular radii of the reactants ($\sim 10^{-7}$ cm), yielding $k_{SLR,max} \sim 10^{-4}$ cm^2 s^{-1}. Note, however, that the maximum rates of surface diffusion and reaction may substantially deviate from the bulk-derived estimates depending on the reaction system and conditions.[62,63]

Levoglucosan and abietic acid substrates were exposed under dry conditions to OH in the presence of O_2 using a coated-wall flow-tube reactor coupled to a chemical ionization mass spectrometer as described in detail previously.[29] In brief, OH radicals were produced via a microwave discharge of H_2 in a He carrier flow followed by reaction with O_2 in a movable halocarbon wax-coated glass injector.[57] OH was detected as OH^- following chemical ionization by SF_6^-. OH radical concentrations in these experiments varied from $\sim 10^8$ to 10^9 molecules cm^{-3}, representing, within an order of magnitude, concentrations measured in fresh biomass burning plumes.[64] The organic substrates were exposed to OH radicals for about ~40 min at about 5.5 hPa. The residence time for OH over the exposed substrate ranged from 0.08 to 1.25 ms. Uptake

DOI: 10.1021/jp510489z
J. Phys. Chem. A 2015, 119, 4533−4544

coefficients were derived experimentally as described in detail previously[36] and corrected for gas-phase diffusion to the flow reactor walls by application of the Brown formalism.[54]

RESULTS AND DISCUSSION

Figures 2a and 3a show γ_{OH} as a function of gas-phase OH concentration, $[OH]_g$, for levoglucosan and abietic acid, respectively. γ_{OH} for levoglucosan and abietic acid stays constant at ~0.3 when $[OH]_g$ is below ~10^9 cm^{-3}. Above this concentration, γ_{OH} decreases to ~0.01 at $[OH]_g$ = 10^{11} cm^{-3}. The temporal evolution of γ_{OH} for levoglucosan and abietic acid at $[OH]_g$ = 1.7 × 10^9 cm^{-3} and 3.6 × 10^8 cm^{-3}, respectively, are shown in Figures 2b and 3b, respectively. For levoglucosan, γ_{OH} shows a slight decrease from ~0.1 to ~0.06 during the reaction time of 1800 s. The slight increase of the uptake coefficient after ~500 s is within the range of experimental uncertainties (±17%). For abietic acid, γ_{OH} is stable at ~0.09. As demonstrated by the black lines in Figures 2 and 3, both the time and concentration dependence of γ_{OH} can be reproduced by KM-GAP.

Figure 4 shows the distribution of kinetic parameter values obtained by the MCGA method for levoglucosan and abietic acid. The bulk diffusivities of the organic molecules (D_{org}) are the most tightly constrained parameters, which are found to be ~2 × 10^{-16} cm^2 s^{-1} for levoglucosan and ~9 × 10^{-17} cm^2 s^{-1} for abietic acid. It reflects the semisolid nature of the compounds under these experimental conditions as also reported in previous studies[59,65−67] and discussed later with regard to atmospheric implications. Note that the bulk diffusivities derived from the MCGA fitting to the chemical kinetics data are characteristic for the near-surface-bulk region where reactions mainly occur in the investigated systems and diffusivity might be enhanced relative to the inner bulk material.[68] The estimated D_{org} is about 4 orders of magnitude higher than D_{org} assumed in our previous work investigating NO_3 uptake by levoglucosan and abietic acid, in which D_{org} was less well constrained.[37] The MCGA estimates for D_{OH} in levoglucosan and abietic acid range from 10^{-11} to 10^{-8} cm^2 s^{-1}. Price et al.[66] measured the bulk diffusivity of water in levoglucosan as ~10^{-10} cm^2 s^{-1} at 20% RH; we adopt this value for further simulations based on the analogy of gas-phase diffusivity between OH and H_2O.[69]

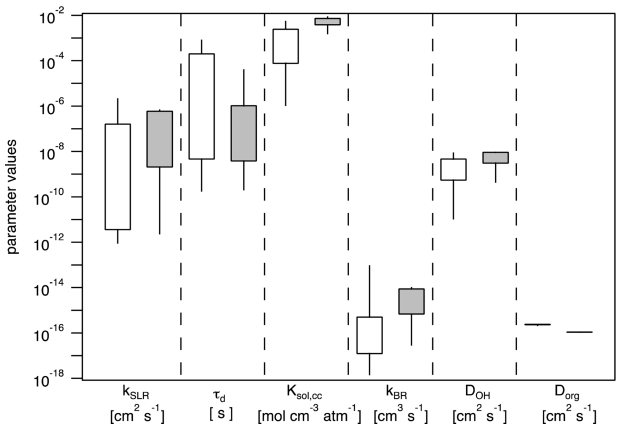

Figure 4. Kinetic parameters for multiphase chemical reactions of OH with levoglucosan (white) and abietic acid (gray) determined by the MCGA method of fitting the experimental data with the KM-GAP model. The ranges of parameters are depicted as a box−whisker plot (the percentiles of 10, 25, 75, and 90% are shown).

For the Henry's law coefficient of OH in the organic phase we obtain a range of 10^{-5}−10^{-3} mol cm^{-3} atm^{-1}, which is at least 1 order of magnitude smaller than that in water.[70−72] The bulk reaction rate coefficient, k_{BR}, is not well constrained with the current experimental data set. Sensitivity analyses indicate that the k_{BR} value does not play a critical role under these experimental conditions and therefore cannot be pinned down by fitting to the experimental data. k_{SLR} and τ_d are found to be mutually interdependent and exhibit a tight inverse correlation as shown in Figure 5. Different combinations of k_{SLR} and τ_d can be chosen due to the wide range of values spanning 7 orders of magnitude. Molecular dynamic simulations[58] suggest that τ_d should be on the order of nanoseconds; if τ_d = 10 ns, then k_{SLR} is constrained to ~10^{-8} cm^2 s^{-1}. This result is consistent with the combination of k_{SLR} ~10^{-10} cm^2 s^{-1} and τ_d ~10 ns used to model the NO_3 uptake by the same organic species in an earlier study,[37] because OH is more reactive than NO_3.

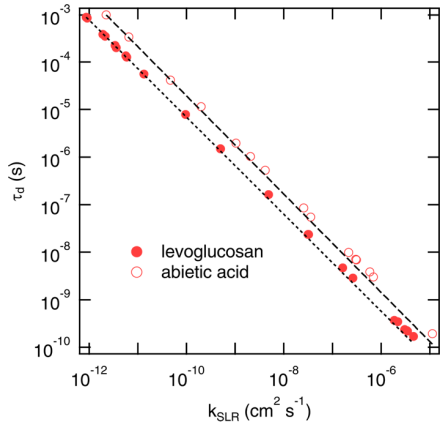

Figure 5. Correlation between desorption lifetime of OH_3 (τ_d) and second-order surface reaction rate coefficients (k_{SLR}) between OH_3 and levoglucosan (solid circles) or abietic acid (open circles) determined by the MCGA method of fitting the experimental data with the KM-GAP model. The black lines are linear fits in a log−log plot.

In evaluating the potential impacts of secondary chemistry on γ_{OH}, we consider reactions between OH and nonvolatile oxidation products applying k_{BR} 2 orders of magnitude smaller than k_{BR} for OH and levoglucosan. The results show that effects of secondary chemistry on γ_{OH} is negligible over the experimental exposure time for $[OH]_g$ < 10^{10} cm^{-3}, while secondary chemistry can affect γ_{OH} for $[OH]_g$ > 10^{10} cm^{-3} by up to 50% only in long exposure time. As k_{BR} for secondary chemistry cannot be constrained well with the current data set, we do not include secondary chemistry for further simulations, although secondary chemistry can be important for the long-term evolution of the condensed phase.[56,73]

Figure 6a shows the temporal evolution of γ_{OH} simulated by KM-GAP, when levoglucosan is exposed to five different OH concentrations (5 × 10^6 to 5 × 10^{10} cm^{-3}). For identification of the limiting step for the overall OH uptake, we determine kinetic regimes and limiting cases of the system. Note that the behavior and sensitivity of levoglucosan and abietic acid are very similar; thus, the analysis of only levoglucosan is shown.

DOI: 10.1021/jp510489z
J. Phys. Chem. A 2015, 119, 4533−4544

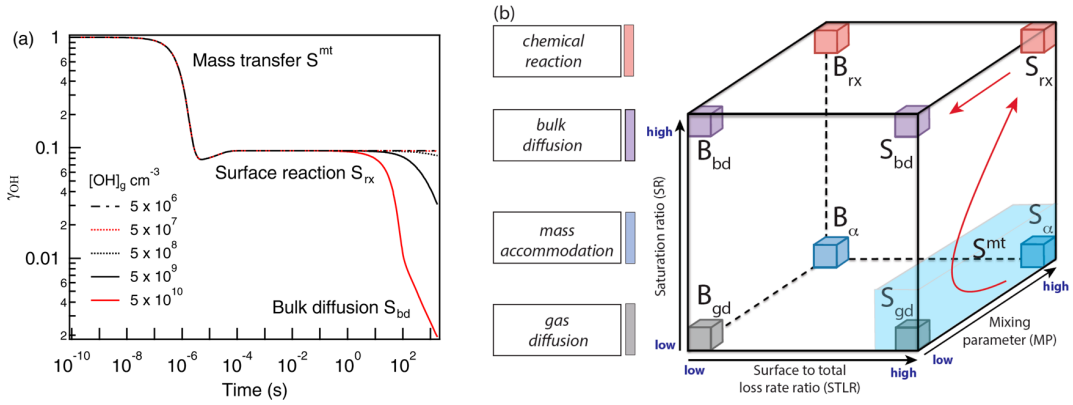

Figure 6. (a) Temporal evolution of OH uptake coefficient (γ_{OH}) for levoglucosan at different OH concentrations. OH uptake is initially limited by mass transfer (S^{mt}) of OH until ~10^{-6} s and then limited by surface reaction (S_{rx}) and the bulk-to-surface transport of levoglucosan (S_{bd}) depending on OH gas-phase concentration. (b) Kinetic regimes and limiting cases of OH uptake are mapped onto the axes of a cube representing reaction location, saturation ratio, and mixing parameter.[51] The red arrows represent evolution of the kinetic regimes: $S^{mt} \rightarrow S_{rx} \rightarrow S_{bd}$.

The cases of limiting behavior arise from the following three criteria that are fundamental to reactive gas uptake:[51,52]

(a) Surface-to-total loss rate ratio (STLR) distinguishes the reaction location between the particle surface (STLR ≈ 1) and the bulk (STLR ≈ 0).

(b) Saturation ratio (SR) determines the abundance of OH at the particle surface or in the bulk. SR ≈ 1 indicates the system is adequately supplied with OH, and SR ≈ 0 indicates the system is deprived of OH and is mass transfer limited.

(c) Mixing parameter (MP) reveals the heterogeneity of the system. MP ≈ 1 indicates the system is well-mixed, and MP ≈ 0 indicates that a strong concentration gradient exists due to diffusion limitation.

The kinetic regimes and limiting cases defined by these criteria can be visualized on a "kinetic cube", in which each axis corresponds to one of the three classification parameters,[51] as shown in Figure 6b. The symbols "S" and "B" indicate the predominant reaction location: particle surface and particle bulk, respectively. A subscript denotes the rate-limiting process for gas uptake: "rx" indicates chemical reaction; "bd" indicates bulk diffusion; "α" indicates mass accommodation; "gd" indicates gas-phase diffusion.

Figure 7 shows the evolution of these criteria at $[OH]_g = 5 \times 10^{10}$ cm^{-3}, and Table 1 summarizes the values for these three criteria for three different time regimes. At any simulated OH concentration, STLR is close to 1 at any simulation time, indicating that the reaction mainly takes place at the particle surface and the system is in the surface reaction regime (S). At the beginning of the uptake process up to ~10^{-6} s, SR at the particle surface (surface saturation ratio; SSR) is very low, indicating that the surface is deprived of OH. γ_{OH} is equal to the surface accommodation coefficient and gas-phase diffusion correction factor (i.e., the ratio of gas-phase concentration at the near-surface gas phase to that far from the surface) is 1 at the very beginning and reduced to ~0.3, implying that mass transfer is the limiting step (S^{mt}) for initial OH uptake.

As shown in Figure 7, SSR becomes ~0.9 after ~10^{-6} s, indicating that the adsorption–desorption equilibrium is established and the surface is close to saturation by OH radicals with respect to a Langmuir adsorption isotherm. Note that the actual surface coverage of OH stays as low as 10^{-6}. The surface mixing parameter of organics (SMP_Y; the ratio of the actual surface concentration to the maximum possible surface

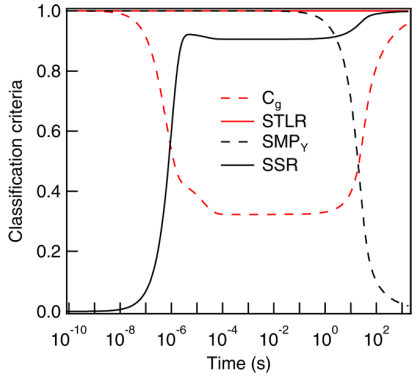

Figure 7. Temporal evolution of criterion parameters for determination of kinetic regimes and limiting cases for multiphase reactions of levoglucosan with $[OH]_g$ of 5×10^{10} cm^{-3}: Surface-to-total loss rate ratio (STLR), gas-phase diffusion correction factor (C_g), surface saturation ratio (SSR), and surface mixing parameter (SMP).

Table 1. Assignment of Kinetic Regimes and Limiting Cases for Multiphase Chemical Reactions of OH with Levoglucosan

	<10^{-6} s	10^{-6}–1 s	1–10^3 s
STLR	~1	~1	~1
SSR	~0	~0.9	~0.9–1
SMP_Y	~1	~1	~0.02–1
kinetic regimes	S^{mt}	S_{rx}	S_{rx} (low $[OH]_g$) S_{bd} (high $[OH]_g$)

concentration) is ~1, showing that bulk-to-surface transport of organics is sufficiently fast without kinetic limitation by bulk diffusion. In this case, the overall OH uptake is mainly limited by surface reaction (S_{rx}), and also partly by gas-phase diffusion as C_g is still ~0.3. In case of low $[OH]_g$ with <~10^8 cm^{-3}, SMP_Y stays at ~1 and γ_{OH} stays at ~0.1 over the entire simulation time.

At high OH concentration $[OH]_g \geq 10^9$ cm^{-3}, SMP_Y decreases to ~0.02, and γ_{OH} decreases substantially after ~1 s. In such a case, the surface reaction is limited by bulk diffusion of organics from the bulk to the surface (S_{bd}). At $[OH]_g = 5 \times 10^{10}$ cm^{-3}, the surface loss rate of levoglucosan is about 4 orders of magnitude higher than that at $[OH]_g = 5 \times 10^6$ cm^{-3}.

DOI: 10.1021/jp510489z
J. Phys. Chem. A 2015, 119, 4533–4544

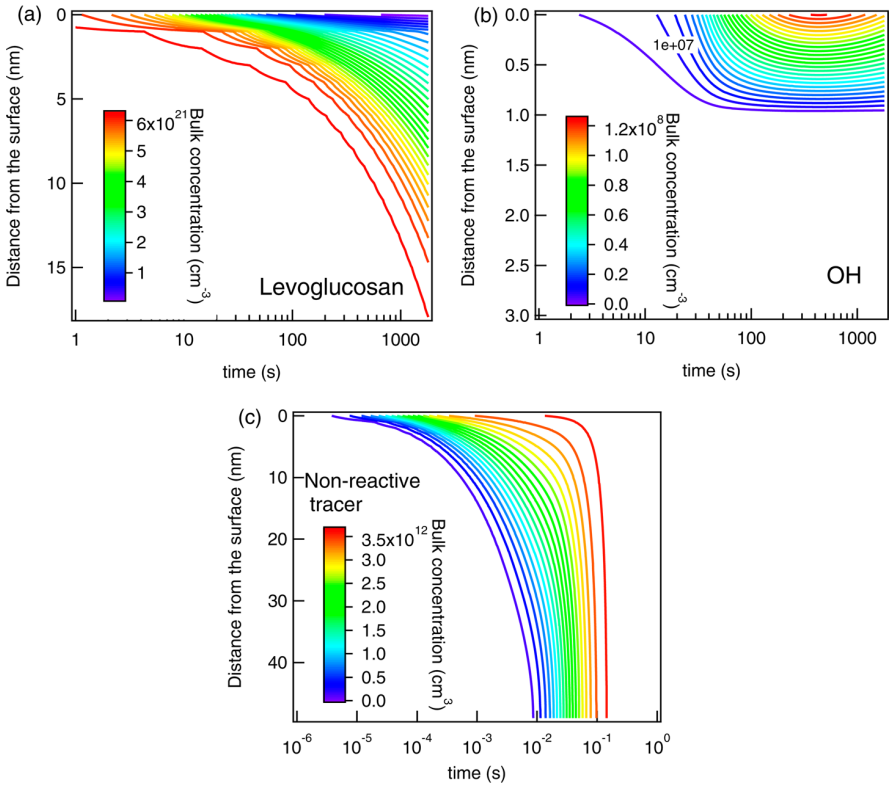

Figure 8. Evolution of the bulk concentration profile of (a) levoglucosan and (b) OH as a response to OH exposure of 5×10^{10} cm^{-3}. (c) Evolution of the bulk concentration profile of nonreactive tracer in the absence of chemical reactions but the same diffusivity as OH.

As the surface loss rate is larger than the diffusion flux of organics to the surface, levoglucosan at the surface is depleted followed by evaporation of volatile reaction products (e.g., glucic acid or 2-hydroxypropanedial).[29] Consequently, a strong concentration gradient of levoglucosan in the bulk develops after ~10 s, as shown in Figure 8a. Up to ~10 s, the bulk is free of OH radicals as most of them reacted away at the surface (Figure 8b). After ~10 s when levoglucosan is depleted at the surface, OH starts to diffuse into the near-surface bulk.

Note that constraining the reaction zone to the near-surface bulk is the result of the interplay between the diffusion and reaction of both levoglucosan and OH. The diffusivity of OH alone, neglecting reaction, would allow significant penetration into the bulk as demonstrated by the very fast incorporation into the bulk of an unreactive tracer with the same diffusion coefficient as OH (Figure 8c).

In summary, the temporal evolution of the limiting cases is depicted by arrows on the kinetic cube in Figure 6b: $S^{mt} \rightarrow S_{rx} \rightarrow S_{bd}$. For confirmation of the identified kinetic regimes and limiting cases and identification of the sensitive kinetic parameters, we conduct a sensitivity analysis by varying each kinetic parameter by 1 order of magnitude. Sensitivity of an input parameter λ_i on the modeled uptake coefficient, γ_{OH}, can be expressed through its normalized sensitivity coefficient $S^n(\lambda_i)$ defined as follows:[51]

$$S^n(\lambda_i) = \frac{\Delta \ln \gamma_{OH}}{\Delta \ln \lambda_i} \quad (1)$$

$S^n(\lambda_i)$ is derived by applying two different $[OH]_g$ (1×10^{10} cm^{-3} and 5×10^6 cm^{-3}) for the reaction time 0.01 and 1800 s: at 0.01 s the limiting case is expected to be S_{rx}; at 1800 s it is expected to be S_{rx} at low $[OH]_g$ and S_{bd} at high $[OH]_g$ (see Figure 4a).

Table 2 shows the results of such calculations. $S^n(\lambda_i)$ for k_{BR}, $K_{sol,cc}$, and D_{OH} are practically zero, indicating OH uptake is insensitive to these bulk-process-related parameters at both high and low $[OH]_g$. k_{SLR}, τ_d, and $\alpha_{s,0}$ are the most sensitive parameters, confirming that the OH uptake is dominated by surface processes. $S^n(k_{SLR})$ and $S^n(\tau_d)$ values are similar, showing that both parameters regulating surface reaction rates are equally important. At high OH concentrations in the S_{bd} region, $S^n(k_{SLR})$, $S^n(\tau_d)$, and $S^n(\alpha_{s,0})$ are about zero. γ_{OH} is sensitive to D_{org} only at high OH concentration and after a long

Table 2. Sensitivity Analysis Coefficient for Low $[OH]_g = 5 \times 10^6$ cm^{-3} and High $[OH]_g = 1 \times 10^{10}$ cm^{-3} Exposure Simulations[a]

	S^n							
	$[OH]_g = 5 \times 10^6$ cm^{-3}				$[OH]_g = 1 \times 10^{10}$ cm^{-3}			
	$t = 10^{-2}$ s		$t = 1.8 \times 10^3$ s		$t = 10^{-2}$ s		$t = 1.8 \times 10^3$ s	
	↑	↓	↑	↓	↑	↓	↑	↓
$\alpha_{s,0}$		1		1		1		0.01
τ_d	0.63	0.93	0.63	0.94	0.63	0.93	0	0.01
k_{slr}	0.63	0.94	0.63	0.94	0.63	0.93	0	0.01
k_{BR}	0	0	0	0	0	0	0	0
$K_{sol,cc}$	0	0	0	0	0	0	0	0
D_{OH}	0	0	0	0	0	0	0	0
D_{org}	0	0	0	0	0	0	0.49	0.50

[a] ↑ and ↓ denote an increase and a decrease of each parameter by 1 order of magnitude, respectively.

DOI: 10.1021/jp510489z
J. Phys. Chem. A 2015, 119, 4533−4544

exposure time, confirming that the OH uptake is limited by the bulk diffusivity of levoglucosan. OH uptake by abietic acid shows very similar sensitivity.

The reduction of γ_{OH} upon increase of gas-phase OH concentrations (Figures 2a and 3a) is a typical behavior of the so-called Langmuir−Hinshelwood mechanism, in which an adsorbed molecule reacts with organics by surface reaction. This is in contrast to the Eley−Rideal mechanism, in which a single kinetic step of collision and reaction occurs between gaseous species and surface molecules.[49] OH has been considered to undergo Eley−Rideal mechanism due to its high reactivity, but our findings are consistent with recent studies[29,41,74−76] suggesting that OH follows Langmuir−Hinshelwood behavior. Reduction of γ_{OH} at high gas-phase concentration is associated with saturation of gaseous species at the surface, which is caused by relatively slower surface reaction rates in the case of less reactive gas species such as ozone.[48,77,78] In the case of OH, accumulation at the surface (e.g., SSR ≈ 1; see Figure 7) is due to reduced surface reaction rates limited by bulk diffusion of levoglucosan or abietic acid.

■ ATMOSPHERIC IMPLICATION

We estimate the chemical half-life, $t_{1/2}$, of levoglucosan and abietic acid by multiphase chemical reactions of OH radicals for a range of ambient RH and temperature. $t_{1/2}$ is defined as the time after which the number of organic molecules in the condensed phase has decreased to half of its initial value. We consider a pure levoglucosan or abietic acid particle with a diameter of 200 nm. $t_{1/2}$ for abietic acid is found to be ∼30% longer than that for levoglucosan, and we focus our analysis on levoglucosan. $[OH]_g$ ranges from 10^6 cm^{-3} in typical pristine environments to ∼10^8 cm^{-3} in the fresh biomass burning plumes.[5] We consider two scenarios representing dry conditions and cloud processing occurring in the boundary layer at 25 °C. At dry conditions, the same kinetic parameters set for the simulations reported in Figure 2 are used. Under high RH, levoglucosan undergoes a moisture-induced phase transition transforming from an amorphous semisolid to a liquid phase.[65] For the cloud processing scenario, bulk diffusion coefficients of OH and levoglucosan are increased to 10^{-5} and 10^{-7} cm^2 s^{-1}, respectively, and the Henry's law coefficient of OH in water is used (2.5×10^{-2} mol cm^{-3} atm^{-1}).[71] $k_{BR} = 1.8 \times 10^{-12}$ cm^3 s^{-1} is used as reported by Zhao et al.[28] Other parameters are kept the same as for dry conditions to explore and characterize the effects of bulk diffusion and OH solubility on the multiphase reactions of BBA.

Biomass burning is often associated with strong convection, and the plume can reach the midtroposphere and possibly also upper troposphere and lower stratosphere.[6−8,79] We simulate $t_{1/2}$ under lower temperatures of 10 and 0 °C. The glass transition temperature (T_g) of levoglucosan is determined to be ∼283 ± 17 K,[67] at which levoglucosan undergoes glass transition with a viscosity exceeding ∼10^{12} Pa s, corresponding to bulk diffusivity (D_{LG}) < ∼10^{-20} cm^2 s^{-1} based on the Stokes−Einstein relation. A recent study shows that the Stokes−Einstein relation may break down close to T_g.[80] We assume that $D_{LG} = 10^{-18}$ cm^2 s^{-1} at 10 °C and 10^{-20} cm^2 s^{-1} below 0 °C. The temperature dependence of bulk diffusivity of H_2O in levoglucosan can be estimated using a semiempirical parametrization developed by Berkemeier et al.[81] based on a Vogel−Fulcher−Tammann approach. Figure 9 shows the estimated D_w with uncertainty reflecting the uncertainty of the input parameter T_g. Considering D_{OH} should be slightly larger than D_w, we use the upper estimate of D_w for calculations. $t_{1/2}$ at 10 and below 0 °C are simulated using the estimated bulk diffusivity and keeping all other parameters the same. Note that a decrease of the reaction rate coefficients with decreasing temperature may increase $t_{1/2}$ further; thus our estimates can be regarded as lower limits.

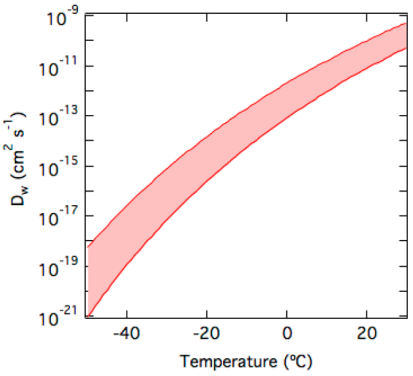

Figure 9. Diffusion coefficient of H_2O as a function of temperature estimated using a parametrization[81] based on a Vogel−Fulcher−Tammann approach.

Figure 10a shows $t_{1/2}$ for levoglucosan simulated as a function of gas-phase OH concentration for different temperatures and humidity. At dry conditions $t_{1/2}$ is more than 37 days for $[OH]_g$ of ∼3×10^6 cm^{-3} and $t_{1/2}$ decreases to more than 1 week for biomass burning plume conditions with $[OH]_g > 10^7$ cm^{-3}. Under cloud processing conditions at 25 °C, $t_{1/2}$ is ∼9 days at $[OH]_g \sim 3 \times 10^6$ cm^{-3} and less than 3 days in a biomass burning plume with $[OH]_g > 10^7$ cm^{-3}, due to the absence of kinetic limitations of mass transport in the particle phase with the high bulk diffusivity of levoglucosan and OH and high OH water solubility. At low temperatures $t_{1/2}$ increases substantially to about 1 month at 10 °C and can be over a year below 0 °C. Below T_g, $t_{1/2}$ stays almost constant as levoglucosan is practically degraded only at the surface and levoglucosan in the bulk is shielded well in a glassy matrix.

This behavior is consistent with the results of previous studies reporting the importance of the particle phase state for the chemical aging of aerosols.[35,37,59,82] For levoglucosan films, Lai et al.[33] observed a decrease of reactivity upon increase of relative humidity which may be a consequence of the blocking surface reactive sites by adsorbed water molecules.[35,65] The estimated chemical half-life is comparable with previously reported *e*-folding time of levoglucosan under dry and humid conditions[29,31,35] and in aqueous solution,[28,32,34] ranging from 1 day to more than a month depending on ambient relative humidity and gas-phase OH concentration.

Levoglucosan is widely used as a molecular marker of biomass burning in source apportionment studies with the assumption that the marker is stable up to 1 week during its transportation in the atmosphere.[22,83] Figure 10b shows the degraded fraction of levoglucosan contained in a 200 nm diameter particle upon exposure to a range of OH concentrations for 1 week under cloud processing and dry conditions at 10 and 0 °C. The calculations indicate that 12% of levoglucosan is degraded under ambient OH concentrations of 3×10^6 cm^{-3} under dry conditions at 25 °C. The degraded fraction reaches more than 40% under cloud processing. If the plume stays in the boundary layer and lower troposphere, about 30−50% of levoglucosan may be degraded after 1 week of OH

DOI: 10.1021/jp510489z
J. Phys. Chem. A 2015, 119, 4533−4544

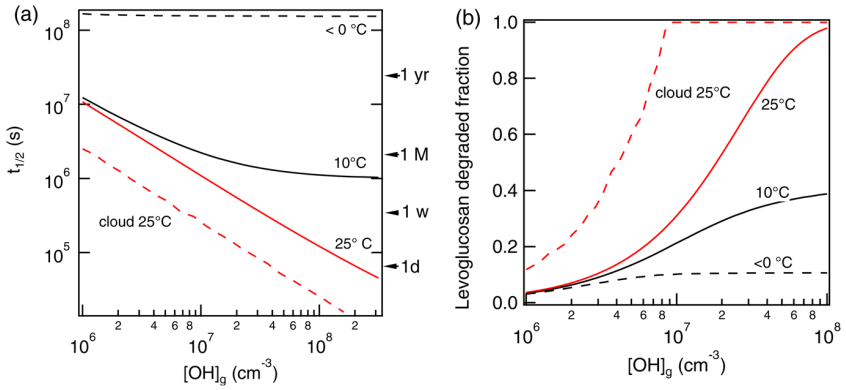

Figure 10. (a) Chemical half-life of levoglucosan in a particle with 200 nm diameter for different environmental conditions: at 25 °C under dry (solid red line) and cloud conditions (dashed red line), and at 10 °C (solid black line) and below 0 °C (dashed black line) under dry conditions. (b) Degraded fraction of levoglucosan after 1 week exposure at different OH concentrations at 25 °C under dry (solid red line) and cloud conditions (dashed red line), and at 10 °C (solid black line) and below 0 °C (dashed black line) under dry conditions.

exposure. Most of levoglucosan may be depleted particularly under high OH concentrations and humid conditions. In the case of strong plume convection reaching higher altitudes and thus lower temperatures, up to ∼30% and ∼10% of levoglucosan may be degraded at 10 and 0 °C, respectively. This estimation is consistent with aircraft observations, finding a large amount of biomass burning aerosol even in the highly aged plumes in the midtroposphere and upper troposphere.[8,79,84]

Note that levoglucosan and abietic acid are reactive toward other oxidants such as O_3 and NO_3.[36,37,85] Moreover, they are semivolatile and partition to the gas phase, where it can be degraded by gas-phase reactions with various oxidants.[86−88] BBAs consist of a mixture of organic and inorganic compounds possibly multiphase in nature,[83,89] potentially shielding organics from oxidants thereby impacting the degradation kinetics as has been shown previously in the case of O_3 oxidation.[90−92] For comprehensive understanding of chemical aging of biomass burning markers, partitioning and gas-phase and multiphase oxidation should be accounted for in models.[93−96] For the reasons listed previously, the chemical half-life estimated in this work is considered as an upper limit. Nevertheless, the simulation results suggest that the air mass history (RH and temperature) play a crucial role in source apportionment studies applying levoglucosan and abietic acid as molecular markers. Aerosol apportionment studies may account for degradation of these markers using estimates derived here and apply additional markers, such as, e.g., CH_3CN,[97] to improve prediction of aerosol source strengths.

■ CONCLUSION

We have applied the kinetic multilayer model to coated-wall flow-tube experiments for OH exposure to levoglucosan and abietic acid, which serve as surrogates and molecular markers of biomass burning aerosols. The bulk diffusion coefficient of OH in the organic material is estimated to be $\sim 10^{-10}$ cm^2 s^{-1}, and diffusivity of levoglucosan and abietic acid to be $\sim 10^{-16}$ cm^2 s^{-1}, characteristic of an amorphous semisolid state. The sensitivity studies reveal that OH uptake is dominated by surface reactions at ambient relevant OH concentrations ($<10^7$ cm^{-3}) but can be limited by the surface-bulk exchange and bulk diffusion upon increase of OH gas-phase concentration. We assessed that it can take 1 week to degrade 50% of the molecules contained in 200 nm sized particles by OH under dry conditions, while it takes only several days upon liquefaction under cloud processing. If a biomass burning plume is transported to the midtroposphere or upper troposphere by convection, the chemical half-life of the organic compounds can be more than a month due to slow bulk diffusion as a consequence of low temperatures. The findings demonstrate that multiphase chemical aging of condensed-phase organic material by OH depends strongly on environmental conditions such as RH and temperature. This has important implications for source apportionment studies but also for the evolution of organic aerosol in the atmosphere in general, and as such for aerosol radiative properties and aerosol cloud formation potential.

Though this study is unique in its kind and allows for a much improved fundamental understanding of the underlying molecular processes governing the OH reactive uptake and multiphase kinetics, it is not complete and many points still have to be addressed in future studies to better resolve the involved mechanisms and to yield a more accurate prediction of the atmospheric evolution of organic aerosol. From this combined experimental and modeling study, we can conclude and suggest the following key points that warrant further investigation into the nature of multiphase kinetics.

1. Temperature and RH Effect. The troposphere experiences large variations in temperature and RH. Most of the troposphere exhibits temperatures lower than 273 K, i.e., much lower than temperatures typically applied in experimental kinetics studies involving organic aerosol. Also, RH varies significantly within the troposphere from a few percent to saturation in clouds. Organic aerosols exhibit various phase states (liquid, semisolid, or amorphous solid) depending on temperature and RH, undergoing moisture-induced or temperature-induced glass transition.[98] Clearly, this has subsequent effects on the multiphase kinetics of atmospheric trace gases due to changes in oxidant and organics diffusivity.[35,59,82,92,99,100] Frozen or solid organic substrates typically exhibit a much lower uptake than their liquid counterparts.[39,91,101,102] Moreover, multicomponent mixtures of inorganic and organic species can undergo liquid−liquid phase transition in response to changes in RH.[103−105] These complex processes result in a wide range of multiphase kinetics for varying temperature and RH for the same particle system. These processes not only impact the chemical aging of organic aerosol but also formation

DOI: 10.1021/jp510489z
J. Phys. Chem. A 2015, 119, 4533−4544

and partitioning of SOA[60,106] and cloud formation potential.[43,81,107]

2. Volatilization and Subsequent Gas-Phase Chemistry. OH oxidation of organic substrates can lead to volatilization.[29,57,108,109] Volatilized products can further react with OH in the gas phase, providing an additional sink for OH, making kinetics simulations of flow tube and chamber experiments more challenging. This may also be crucial for estimates of the atmospheric OH budget in a biomass burning plume. Gas-phase reactions may yield semivolatile and low-volatile oxidation products that can recondense on particulate matter.[40] Experiments should aim to measure gas-phase composition during kinetic experiments to place upper/lower limits on the contribution of gas-phase reaction kinetics to overall OH loss. The kinetic flux model[50] as applied here can be a useful tool to investigate such aspects.

3. Interplay of Gas Uptake and Bulk Diffusion. This study indicates that diffusion of substrate molecules can play a crucial role in the overall uptake kinetics even for an amorphous semisolid organic substrate. Substrate diffusion was also found to be important in ozonolysis of polycyclic aromatic hydrocarbons coated by amorphous semisolid SOA coatings.[100] Diffusion processes in the bulk can occur in parallel to surface reaction and reversible adsorption. In this study we have demonstrated different dominating regimes depending on OH gas-phase concentration for which the uptake can be limited by surface reaction or by bulk-to-surface transport, the latter being strongly dependent on substrate diffusivity. It can be expected that these regimes will vary in response to changes in organic phase state due to changes in RH and temperature making prediction of these multiphase chemical kinetics involving atmospheric organic aerosol even more complicated. Our findings challenge the application of simple Langmuir–Hinshelwood and Eley–Rideal mechanisms to organic substrates. Novel experimental approaches that can deconvolute surface processes from bulk processes or application of combined experimental and modeling techniques are necessary to improve our understanding of the chemical aging processes of organic aerosols.

AUTHOR INFORMATION

Corresponding Authors

*(M.S.) E-mail: m.shiraiwa@mpic.de.

*(D.A.K.) E-mail: daniel.knopf@stonybrook.edu.

Notes

The authors declare no competing financial interest.

ACKNOWLEDGMENTS

We thank two anonymous reviewers for useful comments. A.M.A., T.B., U.P., and M.S. acknowledge support by the Pan-European Gas-AeroSOls-climate interaction Study (No. 265148, PEGASOS). J.H.S. and D.A.K. acknowledge support by the National Science Foundation, Grant AGS-0846255. T. B. was supported by the Max Planck Graduate Center with the Johannes Gutenberg-Universität Mainz (MPGC).

REFERENCES

(1) Bond, T. C.; Doherty, S. J.; Fahey, D. W.; Forster, P. M.; Berntsen, T.; DeAngelo, B. J.; Flanner, M. G.; Ghan, S.; Karcher, B.; Koch, D.; Kinne, S.; Kondo, Y.; Quinn, P. K.; Sarofim, M. C.; Schultz, M. G.; Schulz, M.; Venkataraman, C.; Zhang, H.; Zhang, S.; Bellouin, N.; Guttikunda, S. K.; Hopke, P. K.; Jacobson, M. Z.; Kaiser, J. W.; Klimont, Z.; Lohmann, U.; Schwarz, J. P.; Shindell, D.; Storelvmo, T.; Warren, S. G.; Zender, C. S. Bounding the role of black carbon in the climate system: A scientific assessment. *J. Geophys. Res.: Atmos.* **2013**, *118* (11), 5380–5552.

(2) Crutzen, P. J.; Andreae, M. O. Biomass burning in the tropics: Impact on atmospheric chemistry and biogeochemical cycles. *Science* **1990**, *250* (4988), 1669–1678.

(3) Andreae, M. O.; Merlet, P. Emission of trace gases and aerosols from biomass burning. *Global Biogeochem. Cycles* **2001**, *15* (4), 955–966.

(4) Janhäll, S.; Andreae, M. O.; Pöschl, U. Biomass burning aerosol emissions from vegetation fires: Particle number and mass emission factors and size distributions. *Atmos. Chem. Phys.* **2010**, *10*, 1427–1439.

(5) Hobbs, P. V.; Sinha, P.; Yokelson, R. J.; Christian, T. J.; Blake, D. R.; Gao, S.; Kirchstetter, T. W.; Novakov, T.; Pilewskie, P. Evolution of gases and particles from a savanna fire in South Africa. *J. Geophys. Res.: Atmos.* **2003**, *108* (D13), No. 8485.

(6) Jost, H. J.; Drdla, K.; Stohl, A.; Pfister, L.; Loewenstein, M.; Lopez, J. P.; Hudson, P. K.; Murphy, D. M.; Cziczo, D. J.; Fromm, M.; Bui, T. P.; Dean-Day, J.; Gerbig, C.; Mahoney, M. J.; Richard, E. C.; Spichtinger, N.; Pittman, J. V.; Weinstock, E. M.; Wilson, J. C.; Xueref, I. In-situ observations of mid-latitude forest fire plumes deep in the stratosphere. *Geophys. Res. Lett.* **2004**, *31* (11), No. L11101.

(7) Fromm, M.; Lindsey, D. T.; Servranckx, R.; Yue, G.; Trickl, T.; Sica, R.; Doucet, P.; Godin-Beekmann, S. E. The Untold Story of Pyrocumulonimbus. *Bull. Am. Meteorol. Soc.* **2010**, *91* (9), 1193–1209.

(8) Hudson, P. K.; Murphy, D. M.; Cziczo, D. J.; Thomson, D. S.; de Gouw, J. A.; Warneke, C.; Holloway, J.; Jost, J. R.; Hubler, G. Biomass-burning particle measurements: Characteristic composition and chemical processing. *J. Geophys. Res.: Atmos.* **2004**, *109* (D23), No. D23S27.

(9) Andreae, M. O.; Rosenfeld, D.; Artaxo, P.; Costa, A. A.; Frank, G. P.; Longo, K. M.; Silva-Dias, M. A. F. Smoking rain clouds over the Amazon. *Science* **2004**, *303* (5662), 1337–1342.

(10) Vakkari, V.; Kerminen, V. M.; Beukes, J. P.; Tiitta, P.; van Zyl, P. G.; Josipovic, M.; Venter, A. D.; Jaars, K.; Worsnop, D. R.; Kulmala, M.; Laakso, L. Rapid changes in biomass burning aerosols by atmospheric oxidation. *Geophys. Res. Lett.* **2014**, *41* (7), 2644–2651.

(11) Shantz, N. C.; Gultepe, I.; Andrews, E.; Zelenyuk, A.; Earle, M. E.; Macdonald, A. M.; Liu, P. S. K.; Leaitch, W. R. Optical, physical, and chemical properties of springtime aerosol over Barrow Alaska in 2008. *Int. J. Climatol.* **2014**, *34* (10), 3125–3138.

(12) Stocker, T. F., Qin, D., Plattner, G.-K., Tignor, M., Allen, S. K., Boschung, J., Nauels, A., Xia, Y., Bex, V., Midgley, P. M., Eds. *Climate change 2013: The physical science basis*, Working Group I Contribution to the Fifth IPCC Assessment Report; Intergovernmental Panel on Climate Change: Bern, Switzerland, 2013.

(13) Ramanathan, V.; Carmichael, G. Global and regional climate changes due to black carbon. *Nat. Geosci.* **2008**, *1* (4), 221–227.

(14) de Oliveira Alves, N.; Matos Loureiro, A. L.; Dos Santos, F. C.; Nascimento, K. H.; Dallacort, R.; de Castro Vasconcellos, P.; de Souza Hacon, S.; Artaxo, P.; de Medeiros, S. R. Genotoxicity and composition of particulate matter from biomass burning in the eastern Brazilian Amazon region. *Ecotoxicol. Environ. Saf.* **2011**, *74* (5), 1427–33.

(15) de Oliveira Alves, N.; de Souza Hacon, S.; de Oliveira Galvao, M. F.; Simoes Peixotoc, M.; Artaxo, P.; de Castro Vasconcellos, P.; de Medeiros, S. R. Genetic damage of organic matter in the Brazilian Amazon: A comparative study between intense and moderate biomass burning. *Environ. Res.* **2014**, *130*, 51–58.

(16) Shiraiwa, M.; Selzle, K.; Pöschl, U. Hazardous components and health effects of atmospheric aerosol particles: Reactive oxygen species, soot, polycyclic aromatic compounds and allergenic proteins. *Free Radical Res.* **2012**, *46* (8), 927–939.

(17) Okoshi, R.; Rasheed, A.; Reddy, G. C.; McCrowey, C. J.; Curtis, D. B. Size and mass distributions of ground-level sub-micrometer biomass burning aerosol from small wildfires. *Atmos. Environ.* **2014**, *89*, 392–402.

DOI: 10.1021/jp510489z
J. Phys. Chem. A 2015, 119, 4533–4544

(18) Ichoku, C.; Kahn, R.; Chin, M. Satellite contributions to the quantitative characterization of biomass burning for climate modeling. *Atmos. Res.* **2012**, *111*, 1−28.
(19) Sang, X.; Zhang, Z.; Chan, C.; Engling, G. Source categories and contribution of biomass smoke to organic aerosol over the southeastern Tibetan Plateau. *Atmos. Environ.* **2013**, *78*, 113−123.
(20) Viana, M.; Reche, C.; Amato, F.; Alastuey, A.; Querol, X.; Moreno, T.; Lucarelli, F.; Nava, S.; Calzolai, G.; Chiari, M.; Rico, M. Evidence of biomass burning aerosols in the Barcelona urban environment during winter time. *Atmos. Environ.* **2013**, *72*, 81−88.
(21) Capes, G.; Johnson, B.; McFiggans, G.; Williams, P. I.; Haywood, J.; Coe, H. Aging of biomass burning aerosols over West Africa: Aircraft measurements of chemical composition, microphysical properties, and emission ratios. *J. Geophys. Res.* **2008**, *113*, No. D00C15.
(22) Robinson, A. L.; Subramanian, R.; Donahue, N. M.; Bernardo-Bricker, A.; Rogge, W. F. Source apportionment of molecular markers and organic aerosol. 2. Biomass smoke. *Environ. Sci. Technol.* **2006**, *40* (24), 7811−7819.
(23) Simoneit, B. R. T.; Schauer, J. J.; Nolte, C. G.; Oros, D. R.; Elias, V. O.; Fraser, M. P.; Rogge, W. F.; Cass, G. R. Levoglucosan, a tracer for cellulose in biomass burning and atmospheric particles. *Atmos. Environ.* **1999**, *33*, 173−182.
(24) Fraser, M. P.; Lakshmanan, K. Using levoglucosan as a molecular marker for the long-range transport of biomass combustion aerosols. *Environ. Sci. Technol.* **2000**, *34* (21), 4560−4564.
(25) Hu, Q. H.; Xie, Z. Q.; Wang, X. M.; Kang, H.; Zhang, P. Levoglucosan indicates high levels of biomass burning aerosols over oceans from the Arctic to Antarctic. *Sci. Rep.* **2013**, *3*, No. 3119.
(26) Mochida, M.; Kawamura, K.; Fu, P. Q.; Takemura, T. Seasonal variation of levoglucosan in aerosols over the western North Pacific and its assessment as a biomass-burning tracer. *Atmos. Environ.* **2010**, *44* (29), 3511−3518.
(27) Saarikoski, S.; Timonen, H.; Saarnio, K.; Aurela, M.; Järvi, L.; Keronen, P.; Kerminen, V. M.; Hillamo, R. Sources of organic carbon in fine particulate matter in northern European urban air. *Atmos. Chem. Phys.* **2008**, *8* (20), 6281−6295.
(28) Zhao, R.; Mungall, E. L.; Lee, A. K. Y.; Aljawhary, D.; Abbatt, J. P. D. Aqueous-phase photooxidation of levoglucosan—A mechanistic study using aerosol time of flight chemical ionization mass spectrometry (Aerosol-ToF-CIMS). *Atmos. Chem. Phys.* **2014**, *14*, 9695−9706.
(29) Slade, J. H.; Knopf, D. A. Heterogeneous OH oxidation of biomass burning organic aerosol surrogate compounds: Assessment of volatilisation products and the role of OH concentration on the reactive uptake kinetics. *Phys. Chem. Chem. Phys.* **2013**, *15* (16), 5898−5915.
(30) Hennigan, C. J.; Sullivan, A. P.; Collett, J. L.; Robinson, A. L. Levoglucosan stability in biomass burning particles exposed to hydroxyl radicals. *Geophys. Res. Lett.* **2010**, *37*, No. L09806.
(31) Kessler, S. H.; Smith, J. D.; Che, D. L.; Worsnop, D. R.; Wilson, K. R.; Kroll, J. H. Chemical sinks of organic aerosol: Kinetics and products of the heterogeneous oxidation of erythritol and levoglucosan. *Environ. Sci. Technol.* **2010**, *44* (18), 7005−10.
(32) Hoffmann, D.; T, A.; Iinuma, Y.; Herrmann, H. Atmospheric Stability of Levoglucosan: A Detailed Laboratory and Modeling Study. *Environ. Sci. Technol.* **2010**, *44* (2), 694−699.
(33) Lai, C.; Liu, Y.; Ma, J.; Ma, Q.; He, H. Degradation kinetics of levoglucosan initiated by hydroxyl radical under different environmental conditions. *Atmos. Environ.* **2014**, *91*, 32−39.
(34) Teraji, T.; Arakaki, T. Bimolecular Rate Constants between Levoglucosan and Hydroxyl Radical: Effects of pH and Temperature. *Chem. Lett.* **2010**, *39* (8), 900−901.
(35) Slade, J. H.; Knopf, D. A. Multiphase OH oxidation kinetics of organic aerosol: The role of particle phase state and relative humidity. *Geophys. Res. Lett.* **2014**, *41* (14), 5297−5306.
(36) Knopf, D. A.; Forrester, S. M.; Slade, J. H. Heterogeneous oxidation kinetics of organic biomass burning aerosol surrogates by O_3, NO_2, N_2O_5, and NO_3. *Phys. Chem. Chem. Phys.* **2011**, *13* (47), 21050−21062.
(37) Shiraiwa, M.; Pöschl, U.; Knopf, D. A. Multiphase chemical kinetics of NO_3 radicals reacting with organic aerosol components from biomass burning. *Environ. Sci. Technol.* **2012**, *46* (12), 6630−6636.
(38) Pöschl, U. Atmospheric aerosols: Composition, transformation, climate and health effects. *Angew. Chem., Int. Ed.* **2005**, *44* (46), 7520−7540.
(39) Rudich, Y.; Donahue, N. M.; Mentel, T. F. Aging of organic aerosol: Bridging the gap between laboratory and field studies. *Annu. Rev. Phys. Chem.* **2007**, *58*, 321−352.
(40) Jimenez, J. L.; Canagaratna, M. R.; Donahue, N. M.; Prevot, A. S.; Zhang, Q.; Kroll, J. H.; DeCarlo, P. F.; Allan, J. D.; Coe, H.; Ng, N. L.; Aiken, A. C.; Docherty, K. S.; Ulbrich, I. M.; Grieshop, A. P.; Robinson, A. L.; Duplissy, J.; Smith, J. D.; Wilson, K. R.; Lanz, V. A.; Hueglin, C.; Sun, Y. L.; Tian, J.; Laaksonen, A.; Raatikainen, T.; Rautiainen, J.; Vaattovaara, P.; Ehn, M.; Kulmala, M.; Tomlinson, J. M.; Collins, D. R.; Cubison, M. J.; Dunlea, E. J.; Huffman, J. A.; Onasch, T. B.; Alfarra, M. R.; Williams, P. I.; Bower, K.; Kondo, Y.; Schneider, J.; Drewnick, F.; Borrmann, S.; Weimer, S.; Demerjian, K.; Salcedo, D.; Cottrell, L.; Griffin, R.; Takami, A.; Miyoshi, T.; Hatakeyama, S.; Shimono, A.; Sun, J. Y.; Zhang, Y. M.; Dzepina, K.; Kimmel, J. R.; Sueper, D.; Jayne, J. T.; Herndon, S. C.; Trimborn, A. M.; Williams, L. R.; Wood, E. C.; Middlebrook, A. M.; Kolb, C. E.; Baltensperger, U.; Worsnop, D. R. Evolution of organic aerosols in the atmosphere. *Science* **2009**, *326* (5959), 1525−9.
(41) George, I. J.; Abbatt, J. P. Heterogeneous oxidation of atmospheric aerosol particles by gas-phase radicals. *Nat. Chem.* **2010**, *2* (9), 713−722.
(42) Petters, M. D.; Prenni, A. J.; Kreidenweis, S. M.; DeMott, P. J.; Matsunaga, A.; Lim, Y. B.; Ziemann, P. J. Chemical aging and the hydrophobic-to-hydrophilic conversion of carbonaceous aerosol. *Geophys. Res. Lett.* **2006**, *33* (24), No. L24806.
(43) Wang, B.; Knopf, D. A. Heterogeneous ice nucleation on particles composed of humic-like substances impacted by O_3. *J. Geophys. Res.* **2011**, *116* (D3), No. D03205.
(44) Wang, B. B.; Laskin, A.; Roedel, T.; Gilles, M. K.; Moffet, R. C.; Tivanski, A. V.; Knopf, D. A. Heterogeneous ice nucleation and water uptake by field-collected atmospheric particles below 273 K. *J. Geophys. Res.: Atmos.* **2012**, *117* (D21), No. D00V19.
(45) Zhang, X.; Lin, Y. H.; Surratt, J. D.; Weber, R. J. Sources, composition and absorption Angstrom exponent of light-absorbing organic components in aerosol extracts from the Los Angeles Basin. *Environ. Sci. Technol.* **2013**, *47* (8), 3685−3693.
(46) Flores, J. M.; Washenfelder, R. A.; Adler, G.; Lee, H. J.; Segev, L.; Laskin, J.; Laskin, A.; Nizkorodov, S. A.; Brown, S. S.; Rudich, Y. Complex refractive indices in the near-ultraviolet spectral region of biogenic secondary organic aerosol aged with ammonia. *Phys. Chem. Chem. Phys.* **2014**, *16* (22), 10629−10642.
(47) Liu, J.; Scheuer, E.; Dibb, J.; Ziemba, L. D.; Thornhill, K. L.; Anderson, B. E.; Wisthaler, A.; Mikoviny, T.; Devi, J. J.; Bergin, M.; Weber, R. J. Brown carbon in the continental troposphere. *Geophys. Res. Lett.* **2014**, *41* (6), 2191−2195.
(48) Shiraiwa, M.; Sosedova, Y.; Rouviere, A.; Yang, H.; Zhang, Y.; Abbatt, J. P.; Ammann, M.; Pöschl, U. The role of long-lived reactive oxygen intermediates in the reaction of ozone with aerosol particles. *Nat. Chem.* **2011**, *3* (4), 291−295.
(49) Pöschl, U.; Rudich, Y.; Ammann, M. Kinetic model framework for aerosol and cloud surface chemistry and gas-particle interactions—Part 1: General equations, parameters, and terminology. *Atmos. Chem. Phys.* **2007**, *7*, 5989−6023.
(50) Shiraiwa, M.; Pfrang, C.; Koop, T.; Pöschl, U. Kinetic multi-layer model of gas-particle interactions in aerosols and clouds (KM-GAP): Linking condensation, evaporation and chemical reactions of organics, oxidants and water. *Atmos. Chem. Phys.* **2012**, *12* (5), 2777−2794.
(51) Berkemeier, T.; Huisman, A. J.; Ammann, M.; Shiraiwa, M.; Koop, T.; Pöschl, U. Kinetic regimes and limiting cases of gas uptake

DOI: 10.1021/jp510489z
J. Phys. Chem. A 2015, 119, 4533−4544

and heterogeneous reactions in atmospheric aerosols and clouds: A general classification scheme. *Atmos. Chem. Phys.* **2013**, *13* (14), 6663−6686.
(52) Shiraiwa, M.; Berkemeier, T.; Schilling-Fahnestock, K. A.; Seinfeld, J. H.; Pöschl, U. Molecular corridors and kinetic regimes in the multiphase chemical evolution of secondary organic aerosol. *Atmos. Chem. Phys.* **2014**, *14* (16), 8323−8341.
(53) Knopf, D. A.; Pöschl, U.; Shiraiwa, M. Flow and Flux-Based Analytical Solution of Gas-Phase Diffusion Correction for Tubular Flow Reactors with an Absorbing or Reactive Wall Surface. *Anal. Chem.*, **2015**, under review.
(54) Brown, R. L. Tubolar Flow Reactors with First-Order Kinetics. *J. Res. Natl. Bur. Stand.* **1978**, *83* (1), 1−8.
(55) Bai, J.; Sun, X.; Zhang, C.; Xu, Y.; Qi, C. The OH-initiated atmospheric reaction mechanism and kinetics for levoglucosan emitted in biomass burning. *Chemosphere* **2013**, *93* (9), 2004−2010.
(56) Houle, F. A.; Hinsberg, W. D.; Wilson, K. R. Oxidation of a model alkane aerosol by OH radical: The emergent nature of reactive uptake. *Phys. Chem. Chem. Phys.* **2015**, *17* (6), 4412−4423.
(57) Bertram, A. K.; Ivanov, A. V.; Hunter, M.; Molina, L. T.; Molina, M. J. The reaction probability of OH on organic surfaces of tropospheric interest. *J. Phys. Chem. A* **2001**, *105* (41), 9415−9421.
(58) Vieceli, J.; Roeselova, M.; Potter, N.; Dang, L. X.; Garrett, B. C.; Tobias, D. J. Molecular dynamics simulations of atmospheric oxidants at the air-water interface: Solvation and accommodation of OH and O_3. *J. Phys. Chem. B* **2005**, *109* (33), 15876−15892.
(59) Shiraiwa, M.; Ammann, M.; Koop, T.; Pöschl, U. Gas uptake and chemical aging of semisolid organic aerosol particles. *Proc. Natl. Acad. Sci. U. S. A.* **2011**, *108* (27), 11003−11008.
(60) Shiraiwa, M.; Yee, L. D.; Schilling, K. A.; Loza, C. L.; Craven, J. S.; Zuend, A.; Ziemann, P. J.; Seinfeld, J. H. Size distribution dynamics reveal particle-phase chemistry in organic aerosol formation. *Proc. Natl. Acad. Sci. U. S. A.* **2013**, *110* (29), 11746−11750.
(61) Atkins, P. W. *Physical Chemistry*; Oxford University Press: Oxford, U.K., 1998.
(62) Mak, C. H.; Brand, J. L.; Koehler, B. G.; George, S. M. Coverage dependence of the surface diffusion coefficient for hydrogen on Ru (001). *Surf. Sci.* **1987**, *191* (1), 108−120.
(63) Seebauer, E. G.; Allen, C. E. Estimating surface diffusion coefficients. *Prog. Surf. Sci.* **1995**, *49* (3), 265−330.
(64) Yokelson, R. J.; Crounse, J. D.; DeCarlo, P. F.; Karl, T.; Urbanski, S.; Atlas, E.; Campos, T.; Shinozuka, Y.; Kapustin, V.; Clarke, A. D.; Weinheimer, A.; Knapp, D. J.; Montzka, D. D.; Holloway, J.; Weibring, P.; Flocke, F.; Zheng, W.; Toohey, D.; Wennberg, P. O.; Wiedinmyer, C.; Mauldin, L.; Fried, A.; Richter, D.; Walega, J.; Jimenez, J. L.; Adachi, K.; Buseck, P. R.; Hall, S. R.; Shetter, R. Emissions from biomass burning in the Yucatan. *Atmos. Chem. Phys.* **2009**, *9* (15), 5785−5812.
(65) Mikhailov, E.; Vlasenko, S.; Martin, S. T.; Koop, T.; Pöschl, U. Amorphous and crystalline aerosol particles interacting with water vapor: Conceptual framework and experimental evidence for restructuring, phase transitions and kinetic limitations. *Atmos. Chem. Phys.* **2009**, *9*, 9491−9522.
(66) Price, H. C.; Murray, B. J.; Mattsson, J.; O'Sullivan, D.; Wilson, T. W.; Baustian, K. J.; Benning, L. G. Quantifying water diffusion in high-viscosity and glassy aqueous solutions using a Raman isotope tracer method. *Atmos. Chem. Phys.* **2014**, *14* (8), 3817−3830.
(67) Zobrist, B.; Marcolli, C.; Pedernera, D. A.; Koop, T. Do atmospheric aerosols form glasses? *Atmos. Chem. Phys.* **2008**, *8* (17), 5221−5244.
(68) Ediger, M. D.; Forrest, J. A. Dynamics near Free Surfaces and the Glass Transition in Thin Polymer Films: A View to the Future. *Macromolecules* **2014**, *47* (2), 471−478.
(69) Ivanov, A. V.; Trakhtenberg, S.; Bertram, A. K.; Gershenzon, Y. M.; Molina, M. J. OH, HO_2, and ozone gaseous diffusion coefficients. *J. Phys. Chem. A* **2007**, *111* (9), 1632−1637.
(70) Hanson, D. R.; Burkholder, J. B.; Howard, C. J.; Ravishankara, A. R. Measurement of hydroxyl and hydroperoxy radical uptake coefficients on water and sulfuric acid surfaces. *J. Phys. Chem.* **1992**, *96* (12), 4979−4985.
(71) Lelieveld, J.; Crutzen, P. J. The role of clouds in tropospheric photochemistry. *J. Atmos. Chem.* **1991**, *12* (3), 229−267.
(72) Jacob, D. J. Chemistry of OH in Remote Clouds and Its Role in the Production of Formic-Acid and Peroxymonosulfate. *J. Geophys. Res.: Atmos.* **1986**, *91* (D9), 9807−9826.
(73) Wiegel, A. A.; Wilson, K. R.; Hinsberg, W. D.; Houle, F. A. Stochastic methods for aerosol chemistry: A compact molecular description of functionalization and fragmentation in the heterogeneous oxidation of squalane aerosol by OH radicals. *Phys. Chem. Chem. Phys.* **2015**, *17* (6), 4398−4411.
(74) Enami, S.; Hoffmann, M. R.; Colussi, A. J. In situ mass spectrometric detection of interfacial intermediates in the oxidation of RCOOH(aq) by gas-phase OH-radicals. *J. Phys. Chem. A* **2014**, *118* (23), 4130−4137.
(75) Bagot, P. A. J.; Waring, C.; Costen, M. L.; McKendrick, K. G. Dynamics of Inelastic Scattering of OH Radicals from Reactive and Inert Liquid Surfaces. *J. Phys. Chem. C* **2008**, *112* (29), 10868−10877.
(76) Vlasenko, A.; George, I. J.; Abbatt, J. P. Formation of volatile organic compounds in the heterogeneous oxidation of condensed-phase organic films by gas-phase OH. *J. Phys. Chem. A* **2008**, *112* (7), 1552−1560.
(77) Pöschl, U.; Letzel, T.; Schauer, C.; Niessner, R. Interaction of Ozone and Water Vapor with Spark Discharge Soot Aerosol Particles Coated with Benzo[*a*]pyrene: O_3 and H_2O Adsorption, Benzo[*a*]-pyrene Degradation, and Atmospheric Implications. *J. Phys. Chem. A* **2001**, *105* (16), 4029−4041.
(78) Shiraiwa, M.; Garland, R. M.; Pöschl, U. Kinetic double-layer model of aerosol surface chemistry and gas-particle interactions (K2-SURF): Degradation of polycyclic aromatic hydrocarbons exposed to O_3, NO_2, H_2O, OH and NO_3. *Atmos. Chem. Phys.* **2009**, *9* (24), 9571−9586.
(79) Murphy, D. M.; Cziczo, D. J.; Hudson, P. K.; Thomson, D. S. Carbonaceous material in aerosol particles in the lower stratosphere and tropopause region. *J. Geophys. Res.: Atmos.* **2007**, *112* (D4), No. D04203.
(80) Power, R. M.; Simpson, S. H.; Reid, J. P.; Hudson, A. J. The transition from liquid to solid-like behaviour in ultrahigh viscosity aerosol particles. *Chem. Sci.* **2013**, *4* (6), 2597−2604.
(81) Berkemeier, T.; Shiraiwa, M.; Pöschl, U.; Koop, T. Competition between water uptake and ice nucleation by glassy organic aerosol particles. *Atmos. Chem. Phys.* **2014**, *14*, 12513−12531.
(82) Kuwata, M.; Martin, S. T. Phase of atmospheric secondary organic material affects its reactivity. *Proc. Natl. Acad. Sci. U. S. A.* **2012**, *109* (43), 17354−17359.
(83) Simoneit, B. R. T. Biomass burning—A review of organic tracers for smoke from incomplete combustion. *Appl. Geochem.* **2002**, *17* (3), 129−162.
(84) Cubison, M. J.; Ortega, A. M.; Hayes, P. L.; Farmer, D. K.; Day, D.; Lechner, M. J.; Brune, W. H.; Apel, E.; Diskin, G. S.; Fisher, J. A.; Fuelberg, H. E.; Hecobian, A.; Knapp, D. J.; Mikoviny, T.; Riemer, D.; Sachse, G. W.; Sessions, W.; Weber, R. J.; Weinheimer, A. J.; Wisthaler, A.; Jimenez, J. L. Effects of aging on organic aerosol from open biomass burning smoke in aircraft and laboratory studies. *Atmos. Chem. Phys.* **2011**, *11* (23), 12049−12064.
(85) Gross, S.; Iannone, R.; Xiao, S.; Bertram, A. K. Reactive uptake studies of NO_3 and N_2O_5 on alkenoic acid, alkanoate, and polyalcohol substrates to probe nighttime aerosol chemistry. *Phys. Chem. Chem. Phys.* **2009**, *11* (36), 7792−7803.
(86) Oja, V.; Suuberg, E. M. Vapor Pressures and Enthalpies of Sublimation of D-Glucose, D-Xylose, Cellobiose, and Levoglucosan. *J. Chem. Eng. Data* **1999**, *44* (1), 26−29.
(87) Xie, M.; Hannigan, M. P.; Barsanti, K. C. Gas/particle partitioning of 2-methyltetrols and levoglucosan at an urban site in Denver. *Environ. Sci. Technol.* **2014**, *48* (5), 2835−2842.
(88) May, A. A.; Saleh, R.; Hennigan, C. J.; Donahue, N. M.; Robinson, A. L. Volatility of organic molecular markers used for source

DOI: 10.1021/jp510489z
J. Phys. Chem. A 2015, 119, 4533−4544

apportionment analysis: Measurements and implications for atmospheric lifetime. *Environ. Sci. Technol.* **2012**, *46* (22), 12435−12444.
(89) Iinuma, Y.; Brüggemann, E.; Gnauk, T.; Müller, K.; Andreae, M. O.; Helas, G.; Parmar, R.; Herrmann, H. Source characterization of biomass burning particles: The combustion of selected European conifers, African hardwood, savanna grass, and German and Indonesian peat. *J. Geophys. Res.: Atmos.* **2007**, *112* (D8), No. D08209.
(90) Ziemann, P. J. Aerosol products, mechanisms, and kinetics of heterogeneous reactions of ozone with oleic acid in pure and mixed particles. *Faraday Discuss.* **2005**, *130*, 469−490.
(91) Knopf, D. A.; Anthony, L. M.; Bertram, A. K. Reactive uptake of O_3 by multicomponent and multiphase mixtures containing oleic acid. *J. Phys. Chem. A* **2005**, *109* (25), 5579−5589.
(92) Pfrang, C.; Shiraiwa, M.; Pöschl, U. Chemical ageing and transformation of diffusivity in semi-solid multi-component organic aerosol particles. *Atmos. Chem. Phys.* **2011**, *11* (14), 7343−7354.
(93) Springmann, M.; Knopf, D. A.; Riemer, N. Detailed heterogeneous chemistry in an urban plume box model: Reversible co-adsorption of O_3, NO_2, and H_2O on soot coated with benzo[*a*]-pyrene. *Atmos. Chem. Phys.* **2009**, *9* (19), 7461−7479.
(94) Kaiser, J. C.; Riemer, N.; Knopf, D. A. Detailed heterogeneous oxidation of soot surfaces in a particle-resolved aerosol model. *Atmos. Chem. Phys.* **2011**, *11* (9), 4505−4520.
(95) Zaveri, R. A.; Easter, R. C.; Schilling, J. E.; Seinfeld, J. H. Modeling kinetic partitioning of secondary organic aerosol and size distribution dynamics: Representing effects of volatility, phase state, and particle-phase reaction. *Atmos. Chem. Phys.* **2014** *14*, 5153−5181.
(96) Roldin, P.; Eriksson, A. C.; Nordin, E. Z.; Hermansson, E.; Mogensen, D.; Rusanen, A.; Boy, M.; Swietlicki, E.; Svenningsson, B.; Zelenyuk, A.; Pagels, J. Modelling non-equilibrium secondary organic aerosol formation and evaporation with the aerosol dynamics, gas- and particle-phase chemistry kinetic multilayer model ADCHAM. *Atmos. Chem. Phys.* **2014**, *14*, 7953−7993.
(97) de Gouw, J. A.; Warneke, C.; Parrish, D. D.; Holloway, J. S.; Trainer, M.; Fehsenfeld, F. C. Emission sources and ocean uptake of acetonitrile (CH_3CN) in the atmposhere. *J. Geophys. Res.* **2003**, *108* (D11), No. 4329.
(98) Koop, T.; Bookhold, J.; Shiraiwa, M.; Poschl, U. Glass transition and phase state of organic compounds: Dependency on molecular properties and implications for secondary organic aerosols in the atmosphere. *Phys. Chem. Chem. Phys.* **2011**, *13* (43), 19238−19255.
(99) Shiraiwa, M.; Pfrang, C.; Pöschl, U. Kinetic multi-layer model of aerosol surface and bulk chemistry (KM-SUB): The influence of interfacial transport and bulk diffusion on the oxidation of oleic acid by ozone. *Atmos. Chem. Phys.* **2010**, *10* (8), 3673−3691.
(100) Zhou, S.; Shiraiwa, M.; McWhinney, R. D.; Pöschl, U.; Abbatt, J. P. Kinetic limitations in gas-particle reactions arising from slow diffusion in secondary organic aerosol. *Faraday Discuss.* **2013**, *165*, 391−406.
(101) de Gouw, J. A.; Lovejoy, E. R. Reactive uptake of ozone by liquid organic compounds. *Geophys. Res. Lett.* **1998**, *25* (6), 931−934.
(102) Moise, T.; Talukdar, R. K.; Frost, G. J.; Fox, R. W.; Rudich, Y. Reactive uptake of NO_3 by liquid and frozen organics. *J. Geophys. Res.: Atmos.* **2002**, *107* (D2), No. 4014.
(103) Krieger, U. K.; Marcolli, C.; Reid, J. P. Exploring the complexity of aerosol particle properties and processes using single particle techniques. *Chem. Soc. Rev.* **2012**, *41* (19), 6631−6662.
(104) You, Y.; Renbaum-Wolff, L.; Carreras-Sospedra, M.; Hanna, S. J.; Hiranuma, N.; Kamal, S.; Smith, M. L.; Zhang, X.; Weber, R. J.; Shilling, J. E.; Dabdub, D.; Martin, S. T.; Bertram, A. K. Images reveal that atmospheric particles can undergo liquid-liquid phase separations. *Proc. Natl. Acad. Sci. U. S. A.* **2012**, *109* (33), 13188−13193.
(105) Shiraiwa, M.; Zuend, A.; Bertram, A. K.; Seinfeld, J. H. Gas-particle partitioning of atmospheric aerosols: Interplay of physical state, non-ideal mixing and morphology. *Phys. Chem. Chem. Phys.* **2013**, *15* (27), 11441−11453.
(106) Perraud, V.; Bruns, E. A.; Ezell, M. J.; Johnson, S. N.; Yu, Y.; Alexander, M. L.; Zelenyuk, A.; Imre, D.; Chang, W. L.; Dabdub, D.; Pankow, J. F.; Finlayson-Pitts, B. J. Nonequilibrium atmospheric secondary organic aerosol formation and growth. *Proc. Natl. Acad. Sci. U. S. A.* **2012**, *109* (8), 2836−2841.
(107) Wang, B. B.; Lambe, A. T.; Massoli, P.; Onasch, T. B.; Davidovits, P.; Worsnop, D. R.; Knopf, D. A. The deposition ice nucleation and immersion freezing potential of amorphous secondary organic aerosol: Pathways for ice and mixed-phase cloud formation. *J. Geophys. Res.: Atmos.* **2012**, *117* (D16), No. D16209.
(108) Molina, M. J.; Ivanov, A. V.; Trakhtenberg, S.; Molina, L. T. Atmospheric evolution of organic aerosol. *Geophys. Res. Lett.* **2004**, *31* (22), No. L22104.
(109) McNeill, V. F.; Yatavelli, R. L. N.; Thornton, J. A.; Stipe, C. B.; Landgrebe, O. Heterogeneous OH oxidation of palmitic acid in single component and internally mixed aerosol particles: Vaporization and the role of particle phase. *Atmos. Chem. Phys.* **2008**, *8* (17), 5465−5476.

DOI: 10.1021/jp510489z
J. Phys. Chem. A 2015, 119, 4533−4544

B.2. Tong et al., Atmos. Chem. Phys., 2016

Hydroxyl radicals from secondary organic aerosol decomposition in water

Haijie Tong[1], Andrea M. Arangio[1], Pascale J. Lakey[1], Thomas Berkemeier[1], Fobang Liu[1], Chistopher J. Kampf[1,2], William H. Brune[3], Ulrich Pöschl[1], and Manabu Shiraiwa[1]

1 Max Planck Institute for Chemistry, Multiphase Chemistry Department, Mainz, Germany
2 Institute for Inorganic and Analytical Chemistry, Johannes Gutemberg University Mainz, Mainz, Germany
3 Department of Meteorology, Pennsylvania State University, University Park, United State

Atmospheric Chemistry and Physics, 16, 1716 – 1771, 2016.

Authors contributions.

HT, AA, and MS designed research. HT, AA and FL performed experiments and collected data. PL and TB performed kinetic modeling. All authors discussed the results. HT, UP, and MS wrote the paper.

Atmos. Chem. Phys., 16, 1761–1771, 2016
www.atmos-chem-phys.net/16/1761/2016/
doi:10.5194/acp-16-1761-2016

Atmospheric Chemistry and Physics Open Access EGU

Hydroxyl radicals from secondary organic aerosol decomposition in water

Haijie Tong[1], Andrea M. Arangio[1], Pascale S. J. Lakey[1], Thomas Berkemeier[1], Fobang Liu[1], Christopher J. Kampf[1,2], William H. Brune[3], Ulrich Pöschl[1], and Manabu Shiraiwa[1]

[1]Multiphase Chemistry Department, Max Planck Institute for Chemistry, Mainz, Germany
[2]Institute for Inorganic and Analytical Chemistry, Johannes Gutenberg University Mainz, Mainz, Germany
[3]Department of Meteorology, Pennsylvania State University, University Park, PA 16802, USA

Correspondence to: Manabu Shiraiwa (m.shiraiwa@mpic.de)

Received: 22 October 2015 – Published in Atmos. Chem. Phys. Discuss.: 3 November 2015
Revised: 29 January 2016 – Accepted: 2 February 2016 – Published: 15 February 2016

Abstract. We found that ambient and laboratory-generated secondary organic aerosols (SOA) form substantial amounts of OH radicals upon interaction with liquid water, which can be explained by the decomposition of organic hydroperoxides. The molar OH yield from SOA formed by ozonolysis of terpenes (α-pinene, β-pinene, limonene) is $\sim$0.1 % upon extraction with pure water and increases to $\sim$1.5 % in the presence of Fe^{2+} ions due to Fenton-like reactions. Upon extraction of SOA samples from OH photooxidation of isoprene, we also detected OH yields of around $\sim$0.1 %, which increases upon addition of Fe^{2+}. Our findings imply that the chemical reactivity and aging of SOA particles is strongly enhanced upon interaction with water and iron. In cloud droplets under dark conditions, SOA decomposition can compete with the classical H_2O_2 Fenton reaction as the source of OH radicals. Also in the human respiratory tract, the inhalation and deposition of SOA particles may lead to a substantial release of OH radicals, which may contribute to oxidative stress and play an important role in the adverse health effects of atmospheric aerosols.

1 Introduction

Secondary organic aerosols (SOA) account for a major fraction of fine air particulate matter and have a strong influence on climate and public health (Jimenez et al., 2009; Pöschl et al., 2010; Huang et al., 2014). Formation of SOA is triggered by oxidation of volatile organic compounds followed by condensation of semi-volatile oxidation products (Hallquist et al., 2009; Donahue et al., 2012). Recently, it has been shown that extremely low volatility organic compounds contribute significantly to SOA growth (Ehn et al., 2014; Jokinen et al., 2015; Mentel et al., 2015).

Particle phase chemistry and cloud processing are also efficient pathways for SOA formation and aging (Kalberer et al., 2004; Herrmann et al., 2005; Ervens et al., 2011; Shiraiwa et al., 2013). Evolution of SOA is one of the largest uncertainties in the current understanding of air quality, climate and public health (Kanakidou et al., 2005; Solomon, 2007). With regard to SOA health effects, substantial amounts of reactive oxygen species including organic radicals are detected in ambient and laboratory-generated SOA (Venkatachari and Hopke, 2008; Chen and Hopke, 2010; Chen et al., 2010; Fuller et al., 2014). Despite intensive research, multiphase chemical reactions of SOA in the atmosphere and upon interaction with the human respiratory tract are not well understood (Pöschl and Shiraiwa, 2015).

OH radicals in atmospheric droplets originate from the uptake of gaseous OH radicals (Jacob, 1986; Arakaki et al., 2013) as well as photolysis of ozone (Anglada et al., 2014). A recent study has shown that SOA can form OH radicals in the aqueous phase under light conditions (Badali et al., 2015). Under dark conditions, Fenton reactions between H_2O_2 and iron ions have been regarded as the main source of OH radicals so far (Herrmann et al., 2005). In this study, we found that OH radicals are formed by decomposition of SOA upon interactions of water and iron ions under dark conditions.

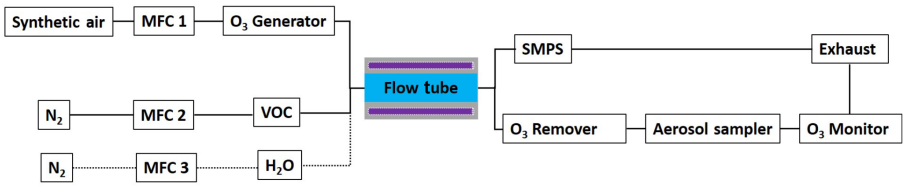

Figure 1. Schematics of the experimental setup for generation and collection of SOA particles.

2 Methods

2.1 SOA formation and particle collection

Figure 1 shows the experimental setup for generation of secondary organic aerosols (SOA). O_3 was used as oxidant for oxidation of α-pinene, β-pinene and limonene, and OH radicals were used for naphthalene. O_3 was generated via synthetic air (Westfalen AG, 1.8–2.1 L min^{-1}) passing through a 185 nm UV light (O_3 generator, L.O.T.-Oriel GmbH & Co. KG). The typical ozone concentrations were 600 ppb for α-pinene, β-pinene and limonene, and 1200 ppb for naphthalene. A total of 1 mL of α-pinene (98 %, Sigma Aldrich), β-pinene (99 %, Sigma Aldrich) or limonene (99 %, Sigma Aldrich) was kept in a 1.5 mL amber glass vial (VWR International GmbH), and 5–10 g of naphthalene crystals (99.6 %, Alfa Aesar GmbH & Co. KG) was put in a 100 mL glass bottle (DURAN Group GmbH) as SOA precursor sources. A total of 1 bar and 50–150 ccm min^{-1} N_2 (99.999 %, Westfalen AG) flow was passed through these sources, and the evaporated volatile organic compound (VOC) vapours were introduced into a 7 L quartz flow tube reactor for gas-phase oxidation reaction with O_3 or OH radicals with a reaction time of $\sim$ 3 min. SOA by α-pinene, β-pinene and limonene were generated under dark and dry conditions. The flow tube reactor is surrounded by four UV lights (wavelength of 254 nm, LightTech Lamp Technology Ltd.), which were turned on to generate OH radicals by photolysis of ozone and water vapour. The relative humidity in the flow tube was 30 % for generating naphthalene SOA, and other experiments were conducted under dry conditions. Isoprene SOA was produced in a potential aerosol mass (PAM) chamber through the reaction of gas phase OH radicals and isoprene. The detailed information about this chamber has been described elsewhere (Kang et al., 2007; Lambe et al., 2011), and the SOA generated by the PAM chamber have been shown to be similar to SOA generated in large environmental chambers (Bruns et al., 2015; Lambe et al., 2015) and the atmosphere (Ortega et al., 2015) in terms of oxidation state and chemical composition. Briefly the isoprene vapour was taken into the chamber by N_2 gas with an estimated concentration of tens of parts per million (ppm). Ozone concentration in the PAM was 6–15 ppm, and relative humidity was 30–40 %.

Number concentration and size distribution of the generated SOA particles were characterized using a scanning mobility particle sizer (SMPS, GRIMM Aerosol Technik GmbH & Co. KG). The typical size of the SOA ranged from 50 to 400 nm. The median diameters of the mass size distribution were 100–200 nm. MnO_2 (copper mesh covered with MnO_2 from ANSYCO Analytische Systeme und Componenten GmbH fixed in Gelman filter) and charcoal (4–8 mesh, Sigma Aldrich) denuders were used to remove unreacted O_3 before the collection of SOA particles on a filter. SOA was collected on 47 mm Omnipore Teflon filters (100 nm pore size, Merck Chemicals GmbH). The concentration of O_3 was monitored after an ozone denuder with an ozone analyser (typically 0–20 ppb, model 49i, Thermo Fisher Scientific Inc.). Two silica gel (2–4 mm, Carl Roth GmbH & Co. KG) denuders were used to dry the naphthalene SOA before collection.

Blank tests confirmed that no radicals were produced without SOA particles on a filter. Condensation of water vapour on a filter during SOA collection was negligible. A Teflon filter with particle loading was weighed using a XSE105DU balance with accuracy of $\pm$20 µg. It was then immersed into a 0.5–1 mL 10 mM BMPO water solution and stirred with a vortex shaker (Heidolph Reax 1) for 2–7 min for particle extraction. A typical extraction efficiency of $>$ 70 % in weight can be obtained with 7 min extraction time. After extraction, the filter was dried under 2–3 bar N_2 for $\sim$ 10 min and the filter was weighed. The weight difference was regarded as the weight of extracted particles. The final SOA concentration depends on the extraction time, and the average molar mass of SOA was assumed to be 200 g mol^{-1} in calculating SOA concentrations. The pH of SOA solutions was in the range of 4.8–6.4.

A micro-orifice uniform deposit impactor (MOUDI, 110-R mode, MSP Corporation) was used for collection of ambient particles on the roof of the Max Planck Institute for Chemistry (Mainz, Germany) in 24 h time resolution with a flow rate of 30 L min^{-1} from 17:30 UTC + 1 4 June 2015 to 17:30 5 June 2015 and from 17:30 7 June 2015 to 17:30 8 June 2015. Particles within the diameter range of 180–320 nm, which is the size range dominated by organic aerosols in Mainz (Faber et al., 2013), were used for further analysis. The mass loading of these two samples on filters were $\sim$ 70 and 80 µg, respectively. Teflon filters of 47 mm diameter (100 nm pore size, Merck Chemicals GmbH) were

used to collect the roof particles. Filters were cleaned with pure ethanol and ultra-pure water and dried by nitrogen gas before sampling and weighing. The extraction procedure is the same as that for laboratory SOA, and the field particle extracts were concentrated with a N_2 flux to obtain high signal-to-noise ratio spectra. Concentrations of field particles in water extracts for EPR measurements were $\sim 0.3\,g\,L^{-1}$, which is of the same order of magnitude as extracts of laboratory-generated SOA.

2.2 CW-EPR

Continuous-wave electron paramagnetic resonance (CW-EPR) spectroscopy (EMXplus-10/12, Bruker, Germany) was applied for detection of radicals. A total of 15–30 µL sample solutions were kept in a 50 µL capacity micropipette and inserted into a highly sensitive cavity (E4119001 HS-W1) for analysis. The set of EPR parameters used for this study was as follows: a modulation frequency of 100 kHz; a modulation amplitude of 0.6 or 1; microwave power of 2.149 mW (20 dB) or 21.17 mW (10 dB); a receiver gain of 40 dB; a time constant of 0.01 ms; and a magnetic field scan of 100 G. After the SOA extraction, the samples were immediately analysed by an EPR.

The spin trap 5-*tert*-butoxycarbonyl-5-methyl-1-pyrroline-N-oxide (BMPO, high purity, Enzo Life Sciences GmbH) was used as a trapping agent of OH radicals. Compared to other spin-trapping agents such as 5, 5-dimethyl-1-pyrroline N-oxide (DMPO), BMPO has the following advantages: high purity and stability in the crystalline phase; highly distinguishable EPR spectra for different structure of the trapped radicals; and spectra with high signal-to-noise ratio. Buffer solutions are often used in the spin-trapping technique, but they were not used in this study to avoid changing the real acidity environment of SOA solutions. A BMPO concentration of 10 mM was used. No significant difference was observed among 10, 20, 30, 40 and 50 mM BMPO solutions, confirming that a BMPO concentration of 10 mM is sufficient to achieve the maximum trapping efficiency. The influence of the BMPO concentration on the aqueous phase OH radical trapping efficiency for β-pinene SOA was investigated as shown in Fig. S3. Further blank tests confirmed that H_2O_2 (30 %, Sigma Aldrich), Fe^{2+} and Fe^{3+} ($Fe_2O_{12}S_3 \cdot xH_2O$, 97 %, Sigma Aldrich) do not induce OH radical formation when each of them is mixed with BMPO in water (Fig. S4).

The spin-counting method was applied for quantification of OH radicals using the embedded subroutine of the Bruker Xenon software (Weber, 2012). For better quantification of detected radicals, the spin-fitting method (Bruker Xenon software, chapter 13; Weber, 2012) was used to increase the signal-to-noise ratio especially for low radical concentrations. The required parameters are hyperfine splitting parameters for OH radicals, which were taken from Zhao et al. (2001). Spectral simulations for radical adducts were

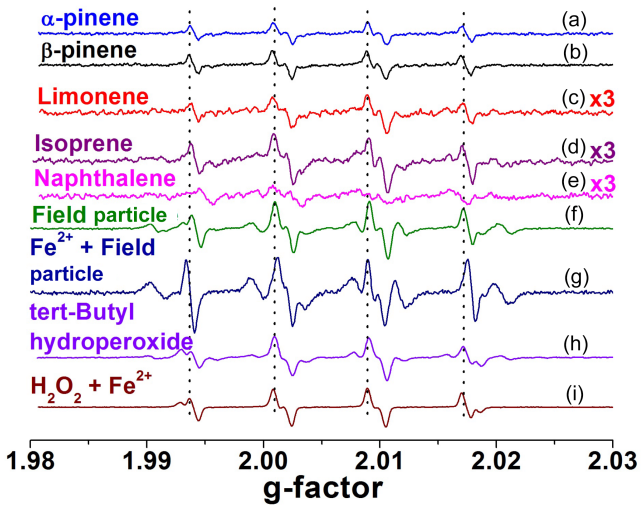

Figure 2. EPR spectra of sample solutions mixed with the spin-trapping agent BMPO: (a) α-pinene SOA, (b) β-pinene SOA, (c) limonene SOA, (d) isoprene SOA, (e) naphthalene SOA, (f) 180–320 nm size field particles, (g) 180–320 nm size field particles mixed with Fe^{2+}, (h) *tert*-butyl hydroperoxide solution and (i) H_2O_2 solution with Fe^{2+}. The four peaks (dotted lines) are characteristic of BMPO-OH adducts.

carried out using the Matlab-based computational package Easyspin (Stoll and Schweiger, 2006). A global optimization (genetic algorithm) was conducted to obtain parameters for simulating the EPR spectrum. The parameter set was further optimized using the particle swarm method within the Easyspin program. The function "garlic" for cw EPR spectra in isotropic and fast motion regimes was chosen for simulation. The hyperfine splitting constants for simulation were taken from the Zhu et al. (2009).

2.3 LC-MS/MS

The SOA extracts mixed with spin-trapping agent BMPO were also analysed with a nanoHPLC-chip-MS/MS system (Agilent), which consists of a nano pump (G2226A) with four-channel micro-vacuum degasser (G1379B), a microfluidic chip cube with electrospray ionization (ESI) source (G4240-62010) interfaced to a Q-TOF mass spectrometer (6540; nominal mass resolution 30 000 at a scan rate of $5\,s^{-1}$), a capillary pump (G1376A) with degasser (G1379B), and an auto-sampler with thermostat (G1377A). All modules were controlled by Mass Hunter software (Rev. B.05.01, Agilent). Eluents used were 3 % (v/v) acetone nitrile (Chromasolv, Sigma, Seelze, Germany) in water / formic acid (0.1 % v/v, Chromasolv, Sigma, Seelze, Germany) (Eluent A) and 3 % water / formic acid (0.1 % v/v) in acetone nitrile (Eluent B). The flow rate was 400 nL min^{-1} with a gradient program that starting with 3 % B for 3 min followed by a 36 min step that raised eluent B to 60 %. Further, eluent B was increased to 80 % at 40 min and returned to initial condi-

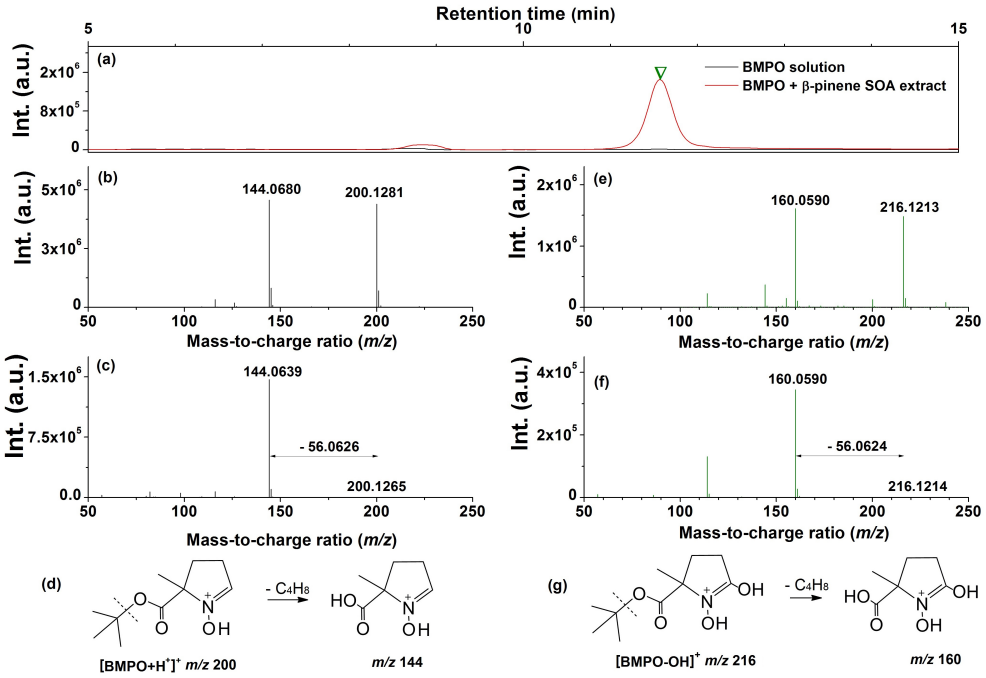

Figure 3. LC-MS/MS analysis. **(a)** LC-MS chromatogram of aqueous BMPO solution (black line) and BMPO mixed with β-pinene SOA water extracts (red line). The downward triangle indicates the retention time of m/z 216 (BMPO-OH). **(b)** MS spectrum of $[\mathrm{BMPO}+\mathrm{H}^+]^+$ with nominal m/z 200. **(c)** MS^2 spectrum of m/z 200, with the characteristic fragment ion m/z 144.0639 ($[\mathrm{BMPO}+\mathrm{H}^+]^+ - m/z$ 56.0626). **(d)** Proposed fragmentation pathway for m/z 200. The most abundant fragment ion present in **(c)** corresponds to the loss of $\mathrm{C_4H_8}$ from $[\mathrm{BMPO}+\mathrm{H}^+]^+$. **(e)** MS spectrum of $[\mathrm{BMPO\text{-}OH}]^+$ with m/z 216. **(f)** The MS^2 spectrum of m/z 216, with the characteristic fragment ion m/z 160.0590 ($[\mathrm{BMPO\text{-}OH}]^+ - m/z$ 56.0624). **(g)** Proposed fragmentation pathway for m/z 216. The observed loss of $\mathrm{C_4H_8}$ is characteristic of the fragmentation of the *t*-butoxycarbonyl function of BMPO.

tions within 0.1 min, followed by column re-equilibration for 9.9 min before the next run. The ESI-Q-TOF instrument was operated in the positive ionization mode (ESI+) with an ionization voltage of 1900 V. Fragmentation of protonated ions was conducted using the automatic MS/MS mode. Spectra were recorded over the mass range of m/z 100–3000. Data analysis was performed using the qualitative data analysis software (Rev. B. 06.00, Agilent).

2.4 Kinetic modelling

The chemical reactions used to describe the BMPO/SOA/Fe^{2+}/H_2O system, including Fenton-like reactions, are listed along with their rate coefficients in Table S1. From this set of 25 reactions, 16 were optimized using the MCGA method and parameter ranges are given in Table S1 to illustrate the uncertainty arising from global optimization. For all other parameters reference values were taken from the literature, which remained fixed during optimization. Kinetic rate coefficients of a large set of chemical reactions were determined using a uniformly sampled Monte Carlo search seeding a genetic algorithm (MCGA method; Berkemeier et al., 2013; Arangio et al., 2015) as the global optimization method. This algorithm optimizes the correlation between a kinetic model and experimental data in order to constrain the input parameters of the model. Genetic algorithms mimic processes known from natural evolution and offer mechanisms such as crossover and mutation to avoid convergence towards local minima. In the kinetic model, ROOH represents all organic hydroperoxides without resolving individual structures. This is a simplification, which is necessary for the kinetic modelling but seems to return consistent results.

3 Results and discussion

Figure 2 indicates that EPR spectra of laboratory generated SOA by α-pinene (spectrum a), β-pinene (spectrum b), limonene (spectrum c) and isoprene (spectrum d) SOA were composed of four major peaks, whereas naphthalene SOA (spectrum e) exhibited no significant signals. These four peaks were also found for field samples (spectrum f) and became more prominent in the presence of Fe^{2+} (spectrum g). In addition, the same splitting was also observed in a solution of *tert*-butyl hydroperoxide (spectrum h). Four-line signals generated by hyperfine splittings are characteristic of BMPO-trapped OH radicals in water solution,

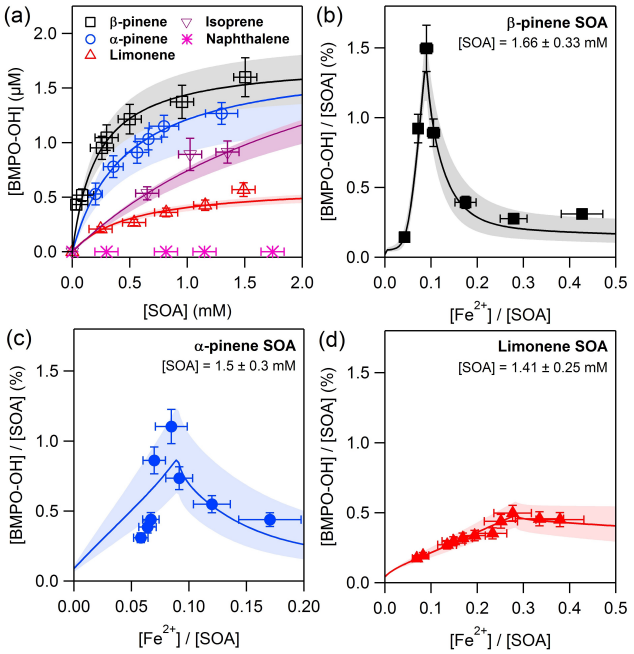

Figure 4. OH formation efficiency by SOA. **(a)** Concentrations of OH radicals formed in water extracts of SOA of β-pinene (black), α-pinene (blue), limonene (red), isoprene (purple) and naphthalene (pink) as a function of SOA concentrations in the aqueous phase. The formation efficiency of OH (molar concentration ratio of OH to SOA: [BMPO-OH] / [SOA], in %) in iron containing SOA water extracts against molar concentration ratios of $FeSO_4$ and SOA ($[Fe^{2+}]$ / [SOA]) by **(b)** β-pinene, **(c)** α-pinene and **(d)** limonene. The markers are experimental data, and the solid curves with shaded area are modelled with uncertainty.

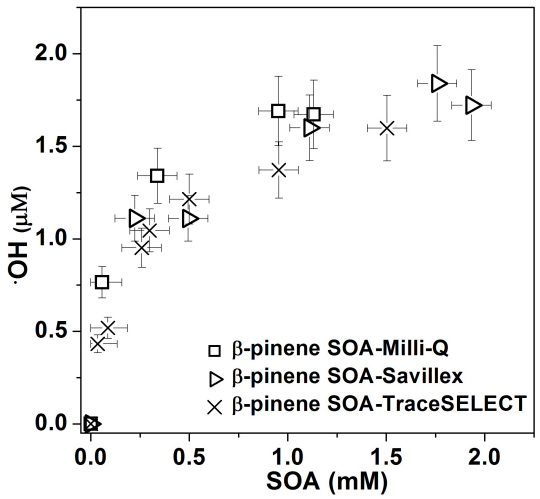

Figure 5. OH yield of β-pinene SOA in three different kinds of pure water: Milli-Q (squares), Savillex (triangles) and TraceSELECT (Sigma, crosses).

as shown in the spectrum (spectrum i) for solutions of H_2O_2 and Fe^{2+}, generating OH via the Fenton reaction ($Fe^{2+} + H_2O_2 \rightarrow Fe^{3+} + OH^- + {}^{\bullet}OH$ (Zhao et al., 2001).

Figure 3 shows LC-MS chromatograms of the BMPO-OH adduct (m/z 216.121) for aqueous BMPO solutions (black line) and for BMPO in aqueous β-pinene SOA extract (red line). A strong peak is observed at a retention time of 11.6 min for BMPO in aqueous β-pinene SOA extract, but not for the aqueous BMPO solution, which served as a blank. Confirmation of the BMPO structure for m/z 216.121 was achieved by comparing MS^2 spectra of $[BMPO + H^+]^+$ (m/z 200.126) from the aqueous standard and m/z 216.121. In both cases the loss of a characteristic fragment with a mass of 56.062 Da is observed (panel c and f), which corresponds to the loss of C_4H_8 from the t-butoxycarbonyl function of BMPO. The above LC-MS/MS analysis confirms the presence of OH radicals in β-pinene SOA extracts observed by EPR shown in Fig. 2.

The EPR and LC-MS/MS observations provide strong evidence that OH radicals are generated in water extracts of SOA by α-pinene, β-pinene, limonene and isoprene as well as field fine particles, which can be enhanced by Fe^{2+}. Note that additional hyperfine splitting is observed for monoterpene and isoprene SOA and especially for field samples, indicating the presence of organic radicals. Figure 4a shows that the amount of OH radicals trapped by BMPO increases as the SOA concentration increases in the aqueous phase. The OH yield from β-pinene SOA is the highest generating ~ 1.5 μM of OH radicals at 1.5 mM SOA concentration, followed by α-pinene, isoprene and limonene SOA. Naphthalene SOA has a negligible yield of OH radicals.

For assessment of potential interferences from trace amounts of impurities such as transition metals in water, the OH yield was also measured in water with three different purity grades – Milli-Q water (18.2 M, Thermo Scientific™ Barnstead™ GenPure™ xCAD Plus ultrapure water system), TraceSELECT® Ultra ACS reagent water (Sigma Aldrich) and Savillex water (DST-1000 Acid Purification System) – which results in excellent agreement (Fig. 5) confirming that OH radicals can be formed in the absence of transition metals.

Ambient particulate matter is often associated with iron ions, which play an important role in aerosol chemistry via Fenton-like reactions (Deguillaume et al., 2005). To investigate the effects of transition metals on OH formation by SOA, different concentrations of Fe^{2+} were added in SOA water extracts. Figure 4b–d show the OH formation efficiency (molar concentration ratio of OH and SOA: [BMPO-OH] / [SOA], in %) of β-pinene, α-pinene and limonene SOA as a function of molar concentration ratio of $FeSO_4$ to SOA ($[Fe^{2+}]$ / [SOA]). The OH formation efficiency reaches maximum values of 1.5 % for β-pinene SOA, 1.1 % for α-pinene SOA and 0.5 % for limonene. Different behaviours in OH formation efficiency of limonene compared to α-pinene and β-pinene may be induced by different organic hydroperoxide concentrations and different R subgroup structure of

ROOH. This order is the same as the order of the relative contribution of organic peroxides in these types of SOA (Docherty et al., 2005). For isoprene SOA, the first results of ongoing experiments indicate a significant increase of OH yield with increasing Fe^{2+} concentrations. The EPR spectra of the isoprene SOA show a dependence on the oxidant concentration level in the PAM chamber. The more complex behaviour of the isoprene SOA from OH photooxidation is under investigation and will be presented in a follow-up study.

The observed formation of OH radicals is most likely due to hydrolysis and thermal decomposition of organic hydroperoxides (ROOH), which account for the predominant fraction of terpene SOA (Docherty et al., 2005; Epstein et al., 2014) as well as in rain water (Hellpointner and Gäb, 1989), but they have little contribution for naphthalene SOA (Kautzman et al., 2010). ROOH are formed via multigenerational gas-phase oxidation and autoxidation, introducing multiple hydroperoxy functional groups forming extremely low volatility organic compounds (Crounse et al., 2013; Ehn et al., 2014). Due to the low binding energy of the O–O bond induced by the electron-donating R group, ROOH are well-known to undergo thermal homolytic cleavage ($ROOH \rightarrow RO^{\bullet} + {}^{\bullet}OH$; Nam et al., 2000). In the presence of Fe^{2+}, it has been reported that decomposition of ROOH can be enhanced mainly via Fenton-like reactions leading to heterolytic cleavage of the O–O bond in the following two ways depending on the pH and reaction environments: $ROOH + Fe^{2+} \rightarrow RO^{\bullet} + OH^{-} + Fe^{3+}$ or $ROOH + Fe^{2+} \rightarrow RO^{-} + {}^{\bullet}OH + Fe^{3+}$ (Goldstein and Meyerstein, 1999; Deguillaume et al., 2005). Note that homolytic cleavage can be catalysed by iron ions (Foster and Caradonna, 2003). The formed alkoxy radicals ($RO^{\bullet}$) were trapped by BMPO and found to increase as the Fe^{2+} concentration increases (Fig. 6). The formation of organic radicals in α-pinene and limonene SOA has been also detected in the previous studies (Pavlovic and Hopke, 2010; Chen et al., 2011). As shown in Fig. 4, the chemical box model including the above three ROOH decomposition pathways reproduces experimental data very well, strongly suggesting that the source of OH radicals is decomposition of ROOH. The decrease of OH radical production with increasing Fe^{2+} concentration is supposedly induced by reaction of the BMPO-OH adduct with Fe^{2+} (Yamazaki and Piette, 1990) (see also Supplement).

It has been suggested that hydrogen peroxide (H_2O_2) can be generated from α- and β-pinene SOA in water, but the mass yield of H_2O_2 is $\sim 0.2\,\%$ (Wang et al., 2011). In the presence of Fe^{2+}, H_2O_2 can yield OH radicals via the Fenton reaction, and the formation efficiency of BMPO-OH adduct by mixtures of H_2O_2 with Fe^{2+} was measured to be $\sim 0.6\,\%$ (Fig. S2). Thus, the potential contribution of generated H_2O_2 to OH yields in β- and α-pinene SOA extracts is much lower than the observed OH radicals. Moreover, the OH yield was not affected, even if β-pinene SOA was dried under a N_2 flow before the water extraction to evaporate particle-phase H_2O_2. Hence it is clear that the H_2O_2 in SOA should not be the dominant source of OH radicals observed in this study.

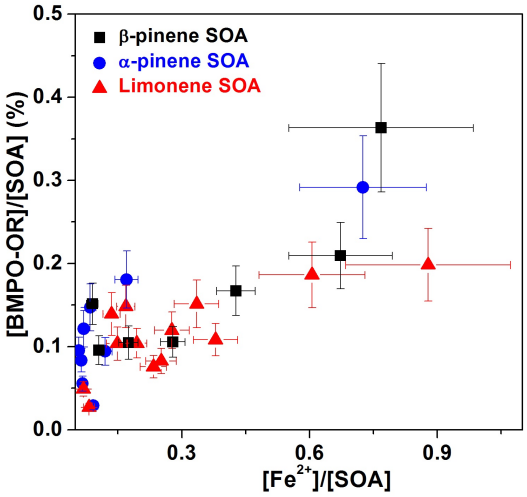

Figure 6. Formation efficiency of organic radicals. Molar concentration ratio of organic radicals to SOA ([BMPO-OR] / [SOA], in %) in mixtures of Fe^{2+} and SOA solutions.

4 Implications

The implications of this finding are illustrated in Figs. 7 and 8. The orange area in Fig. 7a shows OH production rate by Fenton reactions between Fe^{2+} and H_2O_2 forming OH radicals as a function of H_2O_2 concentration with typical dissolved iron concentrations in cloud droplets of 0.1–2.5 µM (Deguillaume et al., 2005). The green area shows the OH production rate by SOA decomposition in cloud or fog droplets, which ranges of ~ 0.01–$100\,nM\,s^{-1}$ depending on SOA precursors and the Fe^{2+} and SOA concentrations (see Supplement). It clearly shows that SOA decomposition is comparably important to the Fenton reaction in most conditions and that SOA can be the main source of OH radicals at low concentrations of H_2O_2 and Fe^{2+}. Water-soluble gases such as aldehydes taken up by deliquesced particles may undergo reactions in the presence of OH radicals to form low-volatility products, including organic acids, peroxides, peroxyhemiacetals and oligomers (Lim et al., 2010; Ervens et al., 2011; Liu et al., 2012; Ervens, 2015; Lim and Turpin, 2015; McNeill, 2015). Thus, the formed OH radicals would promote chemical aging of SOA especially in the presence of iron ions (e.g. SOA-coated mineral dust particles) (Chu et al., 2014) and may also induce aqueous-phase oxidation of sulfur dioxide forming sulfuric acid (Harris et al., 2013).

Recent studies have shown that OH radicals can trigger autoxidation reactions in the gas phase, generating highly oxidized and extremely low volatility compounds (Crounse et al., 2013; Ehn et al., 2014). In addition, it has been shown that some radicals can be long-lived in the condensed phase

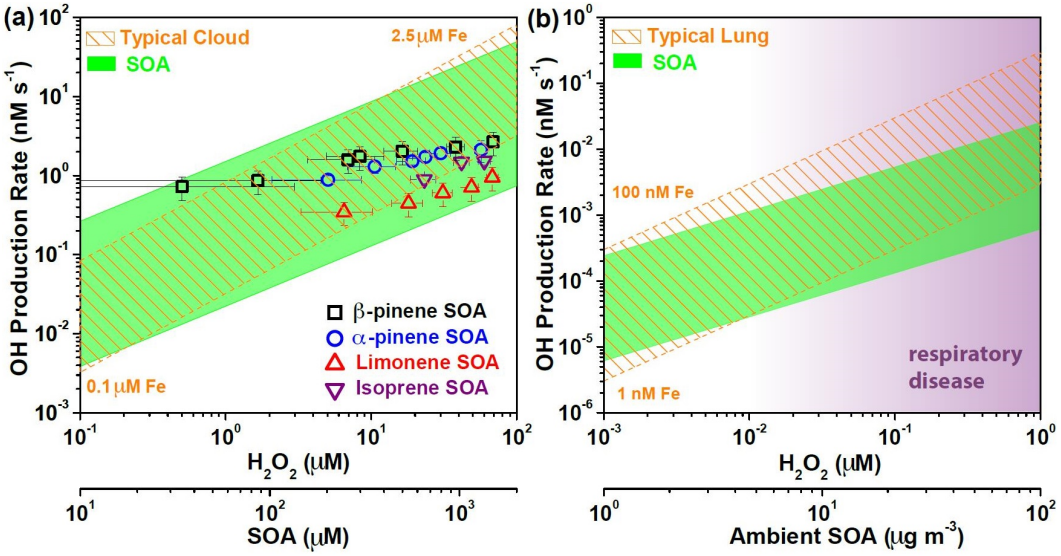

Figure 7. OH production rate in cloud droplets and lung lining fluid. **(a)** The OH production rate in cloud droplets by SOA decomposition compared to the classical Fenton reaction. The data points were measured in the absence of Fe^{2+} for different precursors of β-pinene (black squares), α-pinene (blue circles), limonene (red upward triangles) and isoprene (purple downward triangles). The shaded green area represents the possible range in the presence of iron as a function of SOA concentration in the aqueous phase, which is based on the minimum and maximum OH radical production efficiency of SOA in Fig. 4. The dashed lines represent OH production rates due to the Fenton reaction from H_2O_2 with typical dissolved iron concentrations ($Fe^{2+}:Fe^{3+}=1:1$) of 0.1 and 2.5 µM. **(b)** The OH production rate in lung lining fluid by SOA decomposition as a function of ambient SOA concentrations, and by the classical Fenton reaction as a function of H_2O_2 concentrations with typical dissolved iron concentrations ($Fe^{2+}:Fe^{3+}=1:1$) of 100 and 1 nM. The purple shaded area represents patients with respiratory disease exhibiting high H_2O_2 concentrations in the bronchoalveolar lavage (Corradi et al., 2008).

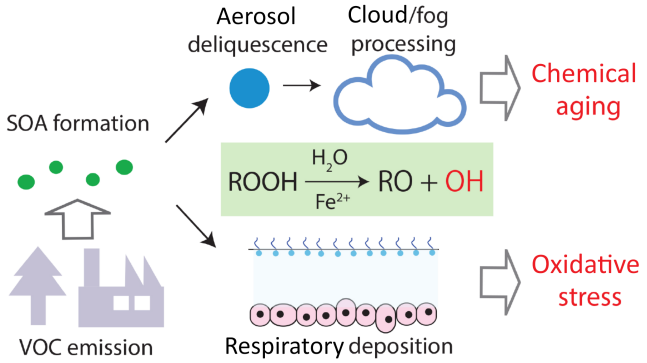

Figure 8. Implications of OH formation by SOA. Formation of OH radicals upon decomposition of organic hydroperoxides (ROOH) in secondary organic aerosol leads to rapid chemical aging of SOA particles upon deliquescence and cloud or fog processing in the atmosphere as well as oxidative stress upon inhalation and deposition in the human respiratory tract. Mixing and Fenton-like reactions of iron with ROOH from SOA can occur both in atmospheric particles and in the lung lining fluid.

(Shiraiwa et al., 2011b; Gehling and Dellinger, 2013) by interacting with transition metals (Truong et al., 2010). We hypothesize that OH radicals formed from SOA decomposition could also trigger autoxidation in the condensed phase. Such a self-amplification cycle of SOA formation and aging may be relevant for example in the Amazon, where cloud and fog processing are important pathways forming a high fraction of SOA with high O : C ratio, resulting in an enhancement of cloud condensation nuclei activity of particles (Pöschl et al., 2010; Pöhlker et al., 2012). Organic peroxides are often used as the agent of the vulcanization processes to initiate the radical polymerization by forming free radicals, which abstract hydrogen atoms from the elastomer molecules converting them into radicals that undergo oligomerization to form elastic polymer or rubber. Similar processes might also occur in SOA particles ("SOA vulcanization"), which may contribute to formation of dimers and oligomers observed in SOA particles (Kalberer et al., 2004) possibly leading to the occurrence of an amorphous solid state (Virtanen et al., 2010; Koop et al., 2011; Shiraiwa et al., 2011a; Renbaum-Wolff et al., 2013; Kidd et al., 2014).

In indoor air, terpenes are commonly found at higher concentrations than in the ambient air due to their widespread use as solvents and odorants in cleaning products and air fresheners (Weschler, 2011). Depending on precursor concentrations, the SOA concentration in indoor air can reach up to 30 µg m^{-3} with the highest contribution from limonene SOA (Waring, 2014). To evaluate potential adverse health effects by SOA deposition into the lungs, we estimated the OH production rate by SOA within the lung lining fluid (LLF) as

a function of ambient SOA concentration considering breathing and deposition rates (see Supplement) (Fig. 7b). The pH of lung lining fluid for healthy people is about 7.4. Our recent experiments have shown that the formation of OH radicals was increased by $\sim 20\,\%$ at a pH of 7.4 in a phosphate-buffered saline solution. Thus, the OH production rate by SOA decomposition shown in Fig. 7b may represent the lower limit. We intend to investigate pH effects on OH formation in detail in follow-up studies.

Figure 7b also shows the OH production rate by the Fenton reaction with typical iron (Gutteridge et al., 1996) and H_2O_2 concentrations in the LLF (Corradi et al., 2008). Patients with respiratory diseases are reported to have high H_2O_2 concentrations in the bronchoalveolar lavage (Corradi et al., 2008) (as shown in shaded purple area), and the Fenton reaction may be the main source of OH radicals for such patients. However, for healthy people with low H_2O_2 and Fe^{2+} concentrations, SOA decomposition can be more important than the Fenton process under high ambient or indoor SOA concentrations. Excess concentrations of reactive oxygen species including hydrogen peroxide, OH radicals (and potentially also organic radicals) are shown to cause oxidative stress to human lung fibroblasts, alveolar cells and tissues (Pöschl and Shiraiwa, 2015). Thus, in polluted indoor or urban megacities with high SOA concentration such as in Beijing, SOA particles may play a critical role in adverse aerosol health effects.

The Supplement related to this article is available online at doi:10.5194/acp-16-1761-2016-supplement.

Acknowledgements. This work was funded by the Max Planck Society. C. J. Kampf acknowledges financial support by the German Research Foundation (DFG project KA 4008/1-1).

The article processing charges for this open-access publication were covered by the Max Planck Society.

Edited by: F. Keutsch

References

Anglada, J. M., Martins-Costa, M., Ruiz-López, M. F., and Francisco, J. S.: Spectroscopic signatures of ozone at the air–water interface and photochemistry implications, P. Natl. Acad. Sci. USA, 111, 11618–11623, 2014.

Arakaki, T., Anastasio, C., Kuroki, Y., Nakajima, H., Okada, K., Kotani, Y., Handa, D., Azechi, S., Kimura, T., and Tsuhako, A.: A general scavenging rate constant for reaction of hydroxyl radical with organic carbon in atmospheric waters, Environ. Sci. Technol., 47, 8196–8203, 2013.

Arangio, A. M., Slade, J. H., Berkemeier, T., Pöschl, U., Knopf, D. A., and Shiraiwa, M.: Multiphase Chemical Kinetics of OH Radical Uptake by Molecular Organic Markers of Biomass Burning Aerosols: Humidity and Temperature Dependence, Surface Reaction, and Bulk Diffusion, J. Phys. Chem. A, 119, 4533–4544, 2015.

Badali, K. M., Zhou, S., Aljawhary, D., Antiñolo, M., Chen, W. J., Lok, A., Mungall, E., Wong, J. P. S., Zhao, R., and Abbatt, J. P. D.: Formation of hydroxyl radicals from photolysis of secondary organic aerosol material, Atmos. Chem. Phys., 15, 7831–7840, doi:10.5194/acp-15-7831-2015, 2015.

Berkemeier, T., Huisman, A. J., Ammann, M., Shiraiwa, M., Koop, T., and Pöschl, U.: Kinetic regimes and limiting cases of gas uptake and heterogeneous reactions in atmospheric aerosols and clouds: a general classification scheme, Atmos. Chem. Phys., 13, 6663–6686, doi:10.5194/acp-13-6663-2013, 2013.

Bruns, E. A., El Haddad, I., Keller, A., Klein, F., Kumar, N. K., Pieber, S. M., Corbin, J. C., Slowik, J. G., Brune, W. H., Baltensperger, U., and Prévôt, A. S. H.: Inter-comparison of laboratory smog chamber and flow reactor systems on organic aerosol yield and composition, Atmos. Meas. Tech., 8, 2315–2332, doi:10.5194/amt-8-2315-2015, 2015.

Chen, X. and Hopke, P.: A chamber study of secondary organic aerosol formation by limonene ozonolysis, Indoor air, 20, 320–328, 2010.

Chen, X., Hopke, P. K., and Carter, W. P.: Secondary organic aerosol from ozonolysis of biogenic volatile organic compounds: chamber studies of particle and reactive oxygen species formation, Environ. Sci. Technol., 45, 276–282, 2010.

Chen, X., Hopke, P. K., and Carter, W. P. L.: Secondary Organic Aerosol from Ozonolysis of Biogenic Volatile Organic Compounds: Chamber Studies of Particle and Reactive Oxygen Species Formation, Environ. Sci. Technol., 45, 276–282, 2011.

Chu, B., Liu, Y., Li, J., Takekawa, H., Liggio, J., Li, S.-M., Jiang, J., Hao, J., and He, H.: Decreasing effect and mechanism of $FeSO_4$ seed particles on secondary organic aerosol in α-pinene photooxidation, Environ. Pollut., 193, 88–93, 2014.

Corradi, M., Pignatti, P., Brunetti, G., Goldoni, M., Caglieri, A., Nava, S., Moscato, G., and Balbi, B.: Comparison between exhaled and bronchoalveolar lavage levels of hydrogen peroxide in patients with diffuse interstitial lung diseases, Acta Biomed., 79, 73–78, 2008.

Crounse, J. D., Nielsen, L. B., Jørgensen, S., Kjaergaard, H. G., and Wennberg, P. O.: Autoxidation of organic compounds in the atmosphere, J. Phys. Chem. Lett., 4, 3513–3520, 2013.

Deguillaume, L., Leriche, M., Desboeufs, K., Mailhot, G., George, C., and Chaumerliac, N.: Transition Metals in Atmospheric Liquid Phases: Sources, Reactivity, and Sensitive Parameters, Chem. Rev., 105, 3388–3431, 2005.

Docherty, K. S., Wu, W., Lim, Y. B., and Ziemann, P. J.: Contributions of organic peroxides to secondary aerosol formed from reactions of monoterpenes with O_3, Environ. Sci. Technol., 39, 4049–4059, 2005.

Donahue, N. M., Henry, K. M., Mentel, T. F., Kiendler-Scharr, A., Spindler, C., Bohn, B., Brauers, T., Dorn, H. P., Fuchs, H., Tillmann, R., Wahner, A., Saathoff, H., Naumann, K.-H., Möhler, O., Leisner, T., Müller, L., Reinnig, M.-C., Hoffmann, T., Salo, K., Hallquist, M., Frosch, M., Bilde, M., Tritscher, T., Barmet, P., Praplan, A. P., DeCarlo, P. F., Dommen, J., Prévôt, A. S. H., and

Baltensperger, U.: Aging of biogenic secondary organic aerosol via gas-phase OH radical reactions, P. Natl. Acad. Sci. USA, 109, 13503–13508, 2012.

Ehn, M., Thornton, J. A., Kleist, E., Sipila, M., Junninen, H., Pullinen, I., Springer, M., Rubach, F., Tillmann, R., Lee, B., Lopez-Hilfiker, F., Andres, S., Acir, I.-H., Rissanen, M., Jokinen, T., Schobesberger, S., Kangasluoma, J., Kontkanen, J., Nieminen, T., Kurten, T., Nielsen, L. B., Jorgensen, S., Kjaergaard, H. G., Canagaratna, M., Dal Maso, M., Berndt, T., Petaja, T., Wahner, A., Kerminen, V.-M., Kulmala, M., Worsnop, D. R., Wildt, J., and Mentel, T. F.: A large source of low-volatility secondary organic aerosol, Nature, 506, 476–479, 2014.

Epstein, S. A., Blair, S. L., and Nizkorodov, S. A.: Direct photolysis of α-pinene ozonolysis secondary organic aerosol: effect on particle mass and peroxide content, Environ. Sci. Technol., 48, 11251–11258, 2014.

Ervens, B.: Modeling the Processing of Aerosol and Trace Gases in Clouds and Fogs, Chem. Rev., 115, 4157–4198, 2015.

Ervens, B., Turpin, B. J., and Weber, R. J.: Secondary organic aerosol formation in cloud droplets and aqueous particles (aqSOA): a review of laboratory, field and model studies, Atmos. Chem. Phys., 11, 11069–11102, doi:10.5194/acp-11-11069-2011, 2011.

Faber, P., Drewnick, F., Veres, P. R., Williams, J., and Borrmann, S.: Anthropogenic sources of aerosol particles in a football stadium: Real-time characterization of emissions from cigarette smoking, cooking, hand flares, and color smoke bombs by high-resolution aerosol mass spectrometry, Atmos. Environ., 77, 1043–1051, 2013.

Foster, T. L. and Caradonna, J. P.: Fe^{2+}-catalyzed heterolytic ROOH bond cleavage and substrate oxidation: A functional synthetic non-heme iron monooxygenase system, J. Am. Chem. Soc., 125, 3678–3679, 2003.

Fuller, S., Wragg, F., Nutter, J., and Kalberer, M.: Comparison of on-line and off-line methods to quantify reactive oxygen species (ROS) in atmospheric aerosols, Atmos. Environ., 92, 97–103, 2014.

Gehling, W. and Dellinger, B.: Environmentally Persistent Free Radicals and Their Lifetimes in $PM_{2.5}$, Environ. Sci. Technol., 47, 8172–8178, 2013.

Goldstein, S. and Meyerstein, D.: Comments on the mechanism of the "Fenton-like" reaction, Acc. Chem. Res., 32, 547–550, 1999.

Gutteridge, J. M. C., Mumby, S., Quinlan, G. J., Chung, K. F., and Evans, T. W.: Pro-oxidant iron is present in human pulmonary epithelial lining fluid: implications for oxidative stress in the lung, Biochem. Biophys. Res. Commun., 220, 1024–1027, 1996.

Hallquist, M., Wenger, J. C., Baltensperger, U., Rudich, Y., Simpson, D., Claeys, M., Dommen, J., Donahue, N. M., George, C., Goldstein, A. H., Hamilton, J. F., Herrmann, H., Hoffmann, T., Iinuma, Y., Jang, M., Jenkin, M. E., Jimenez, J. L., Kiendler-Scharr, A., Maenhaut, W., McFiggans, G., Mentel, Th. F., Monod, A., Prévôt, A. S. H., Seinfeld, J. H., Surratt, J. D., Szmigielski, R., and Wildt, J.: The formation, properties and impact of secondary organic aerosol: current and emerging issues, Atmos. Chem. Phys., 9, 5155–5236, doi:10.5194/acp-9-5155-2009, 2009.

Harris, E., Sinha, B., van Pinxteren, D., Tilgner, A., Fomba, K. W., Schneider, J., Roth, A., Gnauk, T., Fahlbusch, B., Mertes, S., Lee, T., Collett, J., Foley, S., Borrmann, S., Hoppe, P., and Herrmann, H.: Enhanced Role of Transition Metal Ion Catalysis During In-Cloud Oxidation of SO_2, Science, 340, 727–730, 2013.

Hellpointner, E. and Gäb, S.: Detection of methyl, hydroxymethyl and hydroxyethyl hydroperoxides in air and precipitation, Nature, 337, 631–634, 1989.

Herrmann, H., Tilgner, A., Barzaghi, P., Majdik, Z., Gligorovski, S., Poulain, L., and Monod, A.: Towards a more detailed description of tropospheric aqueous phase organic chemistry: CAPRAM 3.0, Atmos. Environ., 39, 4351–4363, 2005.

Huang, R.-J., Zhang, Y., Bozzetti, C., Ho, K.-F., Cao, J.-J., Han, Y., Daellenbach, K. R., Slowik, J. G., Platt, S. M., Canonaco, F., Zotter, P., Wolf, R., Pieber, S. M., Bruns, E. A., Crippa, M., Ciarelli, G., Piazzalunga, A., Schwikowski, M., Abbaszade, G., Schnelle-Kreis, J., Zimmermann, R., An, Z., Szidat, S., Baltensperger, U., Haddad, I. E., and Prevot, A. S. H.: High secondary aerosol contribution to particulate pollution during haze events in China, Nature, 514, 218–222, 2014.

Jacob, D. J.: Chemistry of OH in remote clouds and its role in the production of formic acid and peroxymonosulfate, J. Geophys. Res.-Atmos., 91, 9807–9826, 1986.

Jimenez, J. L., Canagaratna, M. R., Donahue, N. M., Prevot, A. S. H., Zhang, Q., Kroll, J. H., DeCarlo, P. F., Allan, J. D., Coe, H., Ng, N. L., Aiken, A. C., Docherty, K. S., Ulbrich, I. M., Grieshop, A. P., Robinson, A. L., Duplissy, J., Smith, J. D., Wilson, K. R., Lanz, V. A., Hueglin, C., Sun, Y. L., Tian, J., Laaksonen, A., Raatikainen, T., Rautiainen, J., Vaattovaara, P., Ehn, M., Kulmala, M., Tomlinson, J. M., Collins, D. R., Cubison, M. J., Dunlea, E. J., Huffman, J. A., Onasch, T. B., Alfarra, M. R., Williams, P. I., Bower, K., Kondo, Y., Schneider, J., Drewnick, F., Borrmann, S., Weimer, S., Demerjian, K., Salcedo, D., Cottrell, L., Griffin, R., Takami, A., Miyoshi, T., Hatakeyama, S., Shimono, A., Sun, J. Y., Zhang, Y. M., Dzepina, K., Kimmel, J. R., Sueper, D., Jayne, J. T., Herndon, S. C., Trimborn, A. M., Williams, L. R., Wood, E. C., Middlebrook, A. M., Kolb, C. E., Baltensperger, U., and Worsnop, D. R.: Evolution of organic aerosols in the atmosphere, Science, 326, 1525–1529, 2009.

Jokinen, T., Berndt, T., Makkonen, R., Kerminen, V.-M., Junninen, H., Paasonen, P., Stratmann, F., Herrmann, H., Guenther, A. B., Worsnop, D. R., Kulmala, M., Ehn, M., and Sipilä, M.: Production of extremely low volatile organic compounds from biogenic emissions: Measured yields and atmospheric implications, P. Natl. Acad. Sci. USA, 112, 7123–7128, 2015.

Kalberer, M., Paulsen, D., Sax, M., Steinbacher, M., Dommen, J., Prevot, A., Fisseha, R., Weingartner, E., Frankevich, V., and Zenobi, R.: Identification of polymers as major components of atmospheric organic aerosols, Science, 303, 1659–1662, 2004.

Kanakidou, M., Seinfeld, J. H., Pandis, S. N., Barnes, I., Dentener, F. J., Facchini, M. C., Van Dingenen, R., Ervens, B., Nenes, A., Nielsen, C. J., Swietlicki, E., Putaud, J. P., Balkanski, Y., Fuzzi, S., Horth, J., Moortgat, G. K., Winterhalter, R., Myhre, C. E. L., Tsigaridis, K., Vignati, E., Stephanou, E. G., and Wilson, J.: Organic aerosol and global climate modelling: a review, Atmos. Chem. Phys., 5, 1053–1123, doi:10.5194/acp-5-1053-2005, 2005.

Kang, E., Root, M. J., Toohey, D. W., and Brune, W. H.: Introducing the concept of Potential Aerosol Mass (PAM), Atmos. Chem. Phys., 7, 5727–5744, doi:10.5194/acp-7-5727-2007, 2007.

Kautzman, K. E., Surratt, J. D., Chan, M. N., Chan, A. W. H., Hersey, S. P., Chhabra, P. S., Dalleska, N. F., Wennberg, P. O.,

Flagan, R. C., and Seinfeld, J. H.: Chemical Composition of Gas- and Aerosol-Phase Products from the Photooxidation of Naphthalene, J. Phys. Chem. A, 114, 913–934, 2010.

Kidd, C., Perraud, V., Wingen, L. M., and Finlayson-Pitts, B. J.: Integrating phase and composition of secondary organic aerosol from the ozonolysis of alpha-pinene, P. Natl. Acad. Sci. USA, 111, 7552–7557, 2014.

Koop, T., Bookhold, J., Shiraiwa, M., and Pöschl, U.: Glass transition and phase state of organic compounds: dependency on molecular properties and implications for secondary organic aerosols in the atmosphere, Phys. Chem. Chem. Phys., 13, 19238–19255, 2011.

Lambe, A. T., Ahern, A. T., Williams, L. R., Slowik, J. G., Wong, J. P. S., Abbatt, J. P. D., Brune, W. H., Ng, N. L., Wright, J. P., Croasdale, D. R., Worsnop, D. R., Davidovits, P., and Onasch, T. B.: Characterization of aerosol photooxidation flow reactors: heterogeneous oxidation, secondary organic aerosol formation and cloud condensation nuclei activity measurements, Atmos. Meas. Tech., 4, 445–461, doi:10.5194/amt-4-445-2011, 2011.

Lambe, A. T., Chhabra, P. S., Onasch, T. B., Brune, W. H., Hunter, J. F., Kroll, J. H., Cummings, M. J., Brogan, J. F., Parmar, Y., Worsnop, D. R., Kolb, C. E., and Davidovits, P.: Effect of oxidant concentration, exposure time, and seed particles on secondary organic aerosol chemical composition and yield, Atmos. Chem. Phys., 15, 3063–3075, doi:10.5194/acp-15-3063-2015, 2015.

Lim, Y. B. and Turpin, B. J.: Laboratory evidence of organic peroxide and peroxyhemiacetal formation in the aqueous phase and implications for aqueous OH, Atmos. Chem. Phys., 15, 12867–12877, doi:10.5194/acp-15-12867-2015, 2015.

Lim, Y. B., Tan, Y., Perri, M. J., Seitzinger, S. P., and Turpin, B. J.: Aqueous chemistry and its role in secondary organic aerosol (SOA) formation, Atmos. Chem. Phys., 10, 10521–10539, doi:10.5194/acp-10-10521-2010, 2010.

Liu, Y., Monod, A., Tritscher, T., Praplan, A. P., DeCarlo, P. F., Temime-Roussel, B., Quivet, E., Marchand, N., Dommen, J., and Baltensperger, U.: Aqueous phase processing of secondary organic aerosol from isoprene photooxidation, Atmos. Chem. Phys., 12, 5879–5895, doi:10.5194/acp-12-5879-2012, 2012.

McNeill, V. F.: Aqueous organic chemistry in the atmosphere: Sources and chemical processing of organic aerosols, Environ. Sci. Technol., 49, 1237–1244, 2015.

Mentel, T. F., Springer, M., Ehn, M., Kleist, E., Pullinen, I., Kurtén, T., Rissanen, M., Wahner, A., and Wildt, J.: Formation of highly oxidized multifunctional compounds: autoxidation of peroxy radicals formed in the ozonolysis of alkenes – deduced from structure–product relationships, Atmos. Chem. Phys., 15, 6745–6765, doi:10.5194/acp-15-6745-2015, 2015.

Nam, W., Han, H. J., Oh, S.-Y., Lee, Y. J., Choi, M.-H., Han, S.-Y., Kim, C., Woo, S. K., and Shin, W.: New insights into the mechanisms of OO bond cleavage of hydrogen peroxide and tert-alkyl hydroperoxides by iron (III) porphyrin complexes, J. Am. Chem. Soc., 122, 8677–8684, 2000.

Ortega, A. M., Hayes, P. L., Peng, Z., Palm, B. B., Hu, W., Day, D. A., Li, R., Cubison, M. J., Brune, W. H., Graus, M., Warneke, C., Gilman, J. B., Kuster, W. C., de Gouw, J. A., and Jimenez, J. L.: Real-time measurements of secondary organic aerosol formation and aging from ambient air in an oxidation flow reactor in the Los Angeles area, Atmos. Chem. Phys. Discuss., 15, 21907–21958, doi:10.5194/acpd-15-21907-2015, 2015.

Pavlovic, J. and Hopke, P. K.: Detection of radical species formed by the ozonolysis of α-pinene, J. Atmos. Chem., 66, 137–155, 2010.

Pöhlker, C., Wiedemann, K. T., Sinha, B., Shiraiwa, M., Gunthe, S. S., Smith, M., Su, H., Artaxo, P., Chen, Q., Cheng, Y., Elbert, W., Gilles, M. K., Kilcoyne, A. L. D., Moffet, R. C., Weigand, M., Martin, S. T., Pöschl, U., and Andreae, M. O.: Biogenic potassium salt particles as seeds for secondary organic aerosol in the Amazon, Science, 337, 1075–1078, 2012.

Pöschl, U. and Shiraiwa, M.: Multiphase Chemistry at the Atmosphere–Biosphere Interface Influencing Climate and Public Health in the Anthropocene, Chem. Rev., 115, 4440–4475, 2015.

Pöschl, U., Martin, S. T., Sinha, B., Chen, Q., Gunthe, S. S., Huffman, J. A., Borrmann, S., Farmer, D. K., Garland, R. M., Helas, G., Jimenez, J. L., King, S. M., Manzi, A., Mikhailov, E., Pauliquevis, T., Petters, M. D., Prenni, A. J., Roldin, P., Rose, D., Schneider, J., Su, H., Zorn, S. R., Artaxo, P., and Andreae, M. O.: Rainforest Aerosols as Biogenic Nuclei of Clouds and Precipitation in the Amazon, Science, 329, 1513–1516, 2010.

Renbaum-Wolff, L., Grayson, J. W., Bateman, A. P., Kuwata, K., Sellier, M., Murray, B. J., Schilling, J. E., Martin, S. T., and Bertram, A. K.: Viscosity of α-pinene secondary organic material and implications for particle growth and reactivity, P. Natl. Acad. Sci. USA, 110, 8014–8019, 2013.

Shiraiwa, M., Ammann, M., Koop, T., and Pöschl, U.: Gas uptake and chemical aging of semisolid organic aerosol particles, P. Natl. Acad. Sci. USA, 108, 11003–11008, 2011a.

Shiraiwa, M., Sosedova, Y., Rouvière, A., Yang, H., Zhang, Y., Abbatt, J. P., Ammann, M., and Pöschl, U.: The role of long-lived reactive oxygen intermediates in the reaction of ozone with aerosol particles, Nat. Chem., 3, 291–295, 2011b.

Shiraiwa, M., Yee, L. D., Schilling, K. A., Loza, C. L., Craven, J. S., Zuend, A., Ziemann, P. J., and Seinfeld, J. H.: Size distribution dynamics reveal particle-phase chemistry in organic aerosol formation, P. Natl. Acad. Sci. USA, 110, 11746–11750, 2013.

Solomon, S.: Climate change 2007-the physical science basis: Working group I contribution to the fourth assessment report of the IPCC, Cambridge University Press, Cambridge, 2007.

Stoll, S. and Schweiger, A.: EasySpin, a comprehensive software package for spectral simulation and analysis in EPR, J. Magn. Reson., 178, 42–55, 2006.

Truong, H., Lomnicki, S., and Dellinger, B.: Potential for misidentification of environmentally persistent free radicals as molecular pollutants in particulate matter, Environ. Sci. Technol., 44, 1933–1939, 2010.

Venkatachari, P. and Hopke, P. K.: Development and evaluation of a particle-bound reactive oxygen species generator, J. Aerosol. Sci., 39, 168–174, 2008.

Virtanen, A., Joutsensaari, J., Koop, T., Kannosto, J., YliPirilä, P., Leskinen, J., Mäkelä, J. M., Holopainen, J. K., Pöschl, U., Kulmala, M., Worsnop, D. R., and Laaksonen, A.: An amorphous solid state of biogenic secondary organic aerosol particles, Nature, 467, 824–827, 2010.

Wang, Y., Kim, H., and Paulson, S. E.: Hydrogen peroxide generation from alpha- and beta-pinene and toluene secondary organic aerosols, Atmos. Environ., 45, 3149–3156, 2011.

Waring, M. S.: Secondary organic aerosol in residences: predicting its fraction of fine particle mass and determinants of formation strength, Indoor Air, 24, 376–389, 2014.

Weber, R. T.: Xenon Data Processing Reference, Bruker BioSpin Corporation: Billerica, MA USA, chapter 14, 1–24, 2012.

Weschler, C. J.: Chemistry in indoor environments: 20 years of research, Indoor Air, 21, 205–218, 2011.

Yamazaki, I. and Piette, L. H.: ESR spin-trapping studies on the reaction of Fe^{2+} ions with H_2O_2-reactive species in oxygen toxicity in biology, J. Biol. Chem., 265, 13589–13594, 1990.

Zhao, H., Joseph, J., Zhang, H., Karoui, H., and Kalyanaraman, B.: Synthesis and biochemical applications of a solid cyclic nitrone spin trap: a relatively superior trap for detecting superoxide anions and glutathiyl radicals, Free Radic. Biol. Med., 31, 599–606, 2001.

Zhu, B.-Z., Shan, G.-Q., Huang, C.-H., Kalyanaraman, B., Mao, L., and Du, Y.-G.: Metal-independent decomposition of hydroperoxides by halogenated quinones: Detection and identification of a quinone ketoxy radical, P. Natl. Acad. Sci. USA, 106, 11466–11471, 2009.

Supplement of Atmos. Chem. Phys., 16, 1761–1771, 2016
http://www.atmos-chem-phys.net/16/1761/2016/
doi:10.5194/acp-16-1761-2016-supplement

Atmospheric Chemistry and Physics Open Access EGU

Supplement of

Hydroxyl radicals from secondary organic aerosol decomposition in water

H. Tong et al.

Correspondence to: Manabu Shiraiwa (m.shiraiwa@mpic.de)

EPR experiments

The spin counting method was applied for quantification of OH radicals using the embedded subroutine of the Bruker Xenon software (Weber, 2012). Briefly, peaks and a baseline of spectra were selected, followed by double integration of the peak intensity. Spin concentrations were calculated through the following equation (Eaton et al., 2010):

$$\mathrm{DI} = \mathrm{c} \cdot [G_R \cdot C_t \cdot \mathrm{n}] \cdot \left[\frac{\sqrt{P} \cdot B_m \cdot Q \cdot n_B \cdot S \cdot (S+1) \cdot n_S}{f(B_1, B_m)}\right]$$

where c = constant determined by a standard sample with known number of spins, G_R = Receiver gain, C_t = Conversion time, n = Number of scans, P = Microwave power (W), B_m = Modulation amplitude (Gauss), Q = Quality factor of resonator, n_B = Boltzmann factor for temperature dependence, S = Total electron spin, n_s = Number of spins, $f(B_1, B_m)$ = Spatial distribution of the microwave field and the modulation field, experienced by the sample. We calibrated this method using the stable radical TEMPOL and obtained a difference < 5% between the calculated and measured concentrations, confirming the reliability of the spin counting method. The absolute detection limit of number of spins in an EPR cavity (~20 μL) is estimated to be ~1012 spins, which translates to a detection limit of spin concentration of ~100 nM under our experimental conditions.

The error bars in x-axis in Fig. 4 to 7 are based on uncertainties in SOA mass measurements in the balance. The same procedure was also applied to blank filters by immersing them into 10 mM BMPO and 0.5 mM Fe^{2+} ($FeSO_4 \cdot 7H_2O$, ≥ 99%, Sigma Aldrich) solutions, confirming that very little BMPO or iron residues would stick to filters upon extraction. Extractions and EPR measurements were conducted under dark conditions to avoid interferences due to photolysis. 16 ml glass vials with PTFE closure from VWR International GmbH were used. All the vials have been rinsed for 5-10 times with 10 mL fresh Milli-Q water each time and dried under ultrapure dry nitrogen gas (99.999%, Westfalen AG) before SOA extraction. Power free gloves (Carl Roth GmbH + Co.KG) and lab coat were used to avoid particles deposition from human body. Vials were used only once to avoid residue contaminations. Experiments were repeated with vials from different sets and there were no differences in the experimental results. In addition, the experimental results were fully consistent when the vials made from different materials (glass or polystyrene 15 ml conical tubes (VWR

International GmbH)) were used. Particle concentrations in the laboratory were less than ~ 400 m^{-3} and we spent <3 s for opening and closing the vial caps to avoid contamination from deposition of particles into the samples. The filters were cleaned three times with 2-3 mL pure ethanol (ACS grade, VWR International S. A.S.) each time and dried with ultrapure dry nitrogen gas before SOA collection. The filter holder were cleaned with pure ethanol and Milli-Q water and dried with ultrapure dry nitrogen before experiment. OH radicals were not observed in different concentrations of hydrogen peroxide (TraceSELECT® Ultra, for ultratrace analysis) mixed with BMPO by an EPR. Thus, contaminations of transition metals during our handling procedure for particle extraction and analysis are negligible.

One example that includes the original and fitted spectra for BMPO/˙OH adduct of β-pinene SOA and cumene hydroperoxide is shown in Fig. S1. The final root mean square deviation of the fitting was ~0.03, indicating a very good agreement between the experimental and simulated spectra. Five different radicals (BMPO-CH_3, t-BuO-BMPO, BMPO-OCH_3, and two isomers for BMPO-OH adduct) were found to coexist in tert-Butyl hydroperoxide solution. Good agreement between the fitted and measured spectrum confirms the dominance of OH radicals. The residual of the spectra can be regarded as trapped organic radicals.

Considering that the BMPO-OH adduct is stable over ~30 minutes, we have scanned samples over 50 times in ~20 min to elevate the signal to noise ratio of EPR spectra. The decay of DMPO-OH in water leads to uncertainty of ~11 % in quantification of trapped OH radicals. OH radicals in SOA water extracts were quantified using the spin counting method by removing interferences from organic radicals with the spin fitting method (see Methods and Fig. S1).

To investigate the role of water in the formation of OH radicals, ethanol (ACS grade, VWR International S. A.S.) was used as solvent. As shown in Fig. S5 c, BMPO-OH adducts were also observed in β-pinene SOA (E) and tert-Butyl hydroperoxide (F) in ethanol. These observations clearly show that OH radicals can be generated in the absence of water. Note that β-pinene SOA (Fig. 2B) and tert-Butyl hydroperoxide (Fig. 2G) yielded stronger OH signals in water compared to in ethanol. Additional experiments have shown that the OH formation efficiency of β-pinene SOA and tert-Butyl hydroperoxide in water increased by ~30% at 310 K compared to at a room temperature of

295 K. These results indicate that the source of OH radicals may be a combination of hydrolysis and thermal decomposition by organic hydroperoxides(Choe and Min, 2005).

Fig. S5 shows EPR spectra of mixtures of BMPO and cumene hydroperoxide (80%, Sigma Aldrich) with and without Fe^{2+}. The formation of OH and organic radicals upon decomposition of cumene hydroperoxide is clearly observed (A), which is substantially enhanced in the presence of Fe^{2+} due to Fenton-like reactions (B) (Chevallier., 2004). This is in agreement with previous observations of OH radicals generated by organic hydroperoxides in water (Guo et al., 2003). In contrast, no significant signals were observed for Di-tert-butyl peroxide solutions with and without Fe^{2+} (Fig. S5). These observations suggest that the source of OH radicals is organic hydroperoxides (ROOH), but not organic peroxides (ROOR).

Kinetic Modelling

The modelling result is in agreement with the experimental observations of trapping OH with the BMPO spin trap shown in Fig. S2 for H_2O_2. The aqueous phase chemistry is dominated by the reaction between Fe^{2+} and H_2O_2 (R8) and subsequent trapping of OH by BMPO (R14). The predominant loss channel for the BMPO-OH adduct is oxidation by Fe^{3+} (R17). The same strategy is applied for modelling the dissociation of organic hydroperoxides (ROOH) in the absence and presence of Fe^{2+} in extracts of secondary organic aerosol (SOA). We assume that the reactions (1), (8), (10) and (12) for H_2O_2 also apply for ROOH as reactions (19) – (22). Additionally, thermal decomposition of ROOH is included, which dominates dissociation and hence OH production in the absence of Fe^{2+} (Fig. 4a). Reaction with organic molecules ("SOA") is a significant loss pathway for OH in our experiments. Since the initial concentration of BMPO was the same for all experiments, the ratio of SOA and BMPO varies between the different experiments. Hence, at higher SOA concentrations (Fig. 4a), a larger fraction of OH will react with organic molecules instead of BMPO, leading to the observed non-linear increase of the BMPO-OH signal. In the presence of Fe^{2+}, the Fenton-like reactions (19) and (20) lead to a much faster decomposition of ROOH. At higher Fe^{2+} concentrations however, the BMPO-OH adduct is effectively removed (Yamazaki and Piette, 1990) and the measured concentrations significantly reduced (Fig. 4b - d). Destruction of BMPO-OH can

be viewed as iron-catalysed reactions, as Fe^{2+} is constantly recovered in the presence of peroxides. Hence, at high $[Fe^{2+}]$/[SOA], destruction dominates over production. Such behaviour is more prominent for α–pinene and β–pinene SOA, due to higher concentrations of organic hydroperoxides. For limonene SOA, the OH production increased rather gradually with lower abundance of organic hydroperoxides, leading in return to a less prominent destruction of the BMPO-OH adducts by Fe^{2+}.

OH production rate in clouds and lung lining fluid

The OH production rate in cloud water due to Fenton reactions has been calculated. Typical dissolvable iron concentrations (Fe^{2+} and Fe^{3+} with a molar ratio of 1:1) and H_2O_2 concentrations in clouds ('Typical cloud' in Fig. 7a) were set to be 0.1 to 2.5 μM (Deguillaume et al., 2005) and 0.1 to 100 μM, respectively(Herrmann et al., 2015). A typical cloud water pH of 6 was assumed with a k_8 value of 1.1×10^{-18} cm^3 s^{-1} (Bataineh et al., 2012).

For estimation of the OH production rate in lung lining fluid by Fenton reactions, a typical iron concentration range of between 1 to 100 nM was used with Fe^{2+} to Fe^{3+} molar ratio of 1:1 (Hunter et al., 2013). It should be noted that there is a background concentration of iron within the LLF but this is not included during calculations as these iron ions are associated with ferritin and therefore unavailable for Fenton reactions (Ghio et al., 2006; Ghio, 2009). Additionally, typical H_2O_2 concentrations range of 0.001 to 1 μM in the LLF were chosen (Corradi et al., 2008). A pH value of 7 in the LLF (which is typical in healthy people (Paget-Brown et al., 2006)) was assumed and therefore k_8 in Table S1 would be expected to be 9.8×10^{-18} cm^3 s^{-1} (Bataineh et al., 2012), which lies within the range determined by global optimization.

In order to convert ambient concentration of SOA (μg m^{-3}) into an OH production rate in the LLF (P_{OH}, nM s^{-1}) the following equation was used: P_{OH} = (Ambient SOA concentration × breathing rate × PM deposition rate × R_{OH}) / total LLF volume, where ambient SOA concentrations ranged from 1 to 100 μg m^{-3}. R_{OH} is the OH formation efficiency of SOA in aqueous phase (Fig. 4). The breathing rate was assumed to be 230 cm^3 s^{-1}, the PM deposition rate was assumed to be 45% (Sarangapani and Wexler, 2000) and the total ELF volume was set to 25 ml (Walters, 2002).

Table S1. Equations and parameters used in the kinetic model.

Reaction number	Equation	Rate coefficient / $cm^3\ s^{-1}$	Reference
1	$H_2O_2 + OH \rightarrow H_2O + HO_2$	$k_1 = 5.5 \times 10^{-14}$	Christensen, et al.(Christensen et al., 1982)
2	$OH + OH \rightarrow H_2O_2$	$k_2 = 8.6 \times 10^{-12}$	Sehested, et al.(Sehested et al., 1968)
3	$OH + HO_2 \rightarrow H_2O + O_2$	$k_3 = 1.2 \times 10^{-11}$	Sehested, et al.(Sehested et al., 1968)
4	$HO_2 + HO_2 \rightarrow H_2O_2 + O_2$	$k_4 = 1.4 \times 10^{-15}$	Rush and Bielski(Rush and Bielski, 1985)
5	$H_2O_2 + HO_2 \rightarrow H_2O + O_2 + OH$	$k_5 = 5.0 \times 10^{-21}$	Koppenol et al. (1978)
6	$HO_2 + O_2^- \rightarrow H_2O_2 + OH^- + O_2$	$k_6 = 1.6 \times 10^{-13}$	Rush and Bielski(Rush and Bielski, 1985)
7	$H^+ + O_2^- \rightarrow HO_2$	$k_7 = 8.0 \times 10^{-11}$	Divišek and Kastening(Divišek and Kastening, 1975)
8	$Fe^{2+} + H_2O_2 \rightarrow Fe^{3+} + OH^- + OH$	$k_8 = 1.0 – 6.0 \times 10^{-17}$	
9	$Fe^{2+} + OH \rightarrow Fe^{3+} + OH^-$	$k_9 = 0.01 – 1.0 \times 10^{-11}$	Stuglik and Zagorski(Stuglik and PawełZagórski, 1981)
10	$Fe^{3+} + H_2O_2 \rightarrow Fe^{2+} + HO_2 + H^+$	$k_{10} < 1.0 \times 10^{-20}$	
11	$Fe^{3+} + HO_2 \rightarrow Fe^{2+} + O_2 + H^+$	$k_{11} = 3.3 \times 10^{-18}$	Rush and Bielski(Rush and Bielski, 1985)
12	$Fe^{2+} + H_2O_2 \rightarrow Fe^{4+}O^{2+} + H_2O$	$k_{12} = 0.5 - 8 \times 10^{-17}$	
13	$Fe^{4+} + Fe^{2+} \rightarrow 2Fe^{3+}$	$k_{13} = 10^{-19} – 10^{-16}$	
14	BMPO + OH → BMPO-OH	$k_{14} = 0.06 - 6.0 \times 10^{-12}$	
15	BMPO-OH → Product	$k_{15} = 0.02 - 2.0 \times 10^{-4}$	

16	BMPO-OH + Fe^{2+} → Product + Fe^{3+}	k_{16} = 0.1 - 1.0 × 10^{-19}
17	BMPO-OH + Fe^{3+} → Product + Fe^{2+}	k_{17} < 1.0 × 10^{-20}
18	BMPO-OH + Fe^{4+} → Product + Fe^{3+}	k_{18} = 1 - 8.0 × 10^{-18}
19	Fe^{2+} + ROOH → Fe^{3+} + RO^- + OH	k_{19} = k_8
20	Fe^{2+} + ROOH → Fe^{3+} + RO + OH^-	k_{20} < 1.0× 10^{-20}
21	Fe^{3+} + ROOH → Fe^{2+} + RO_2 + H^+	k_{21} =k_{10}
22	OH + ROOH → ROH + HO_2	k_{22} = k_1
23	ROOH → RO + OH	k_{23} = 0.1 – 4 × 10^{-5}
24	SOA + OH → SOA’	k_{24} = 0.3 – 2.0 × 10^{-12}
25	BMPO-OH + OH → Product	k_{25} = 0.1 – 8.0 × 10^{-12}

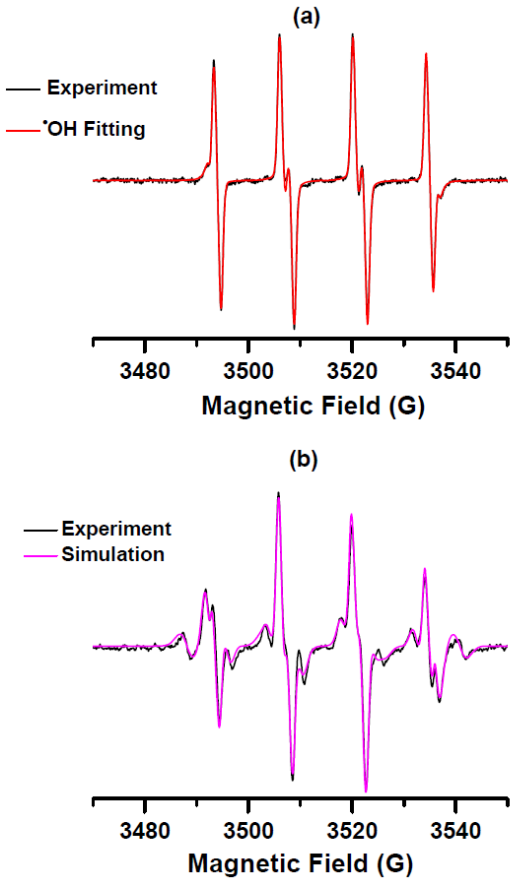

Figure S1. Measured, fitted and simulated EPR spectra. (a) Measured (black) and fitted (red) EPR spectra of water extracts of β-pinene SOA mixed with BMPO. (b) Measured (black) and simulated (pink) EPR spectra of a solution of tert-Butyl hydroperoxide mixed with BMPO.

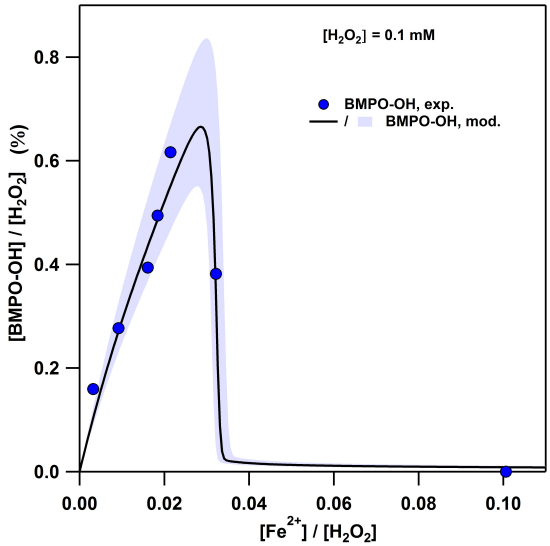

Figure S2. OH formation efficiency in H_2O_2/Fe^{2+} solutions. The concentrations of H_2O_2 and BMPO were 0.1 mM and 10 mM, respectively. The solid curve with shaded area is modelled with uncertainty.

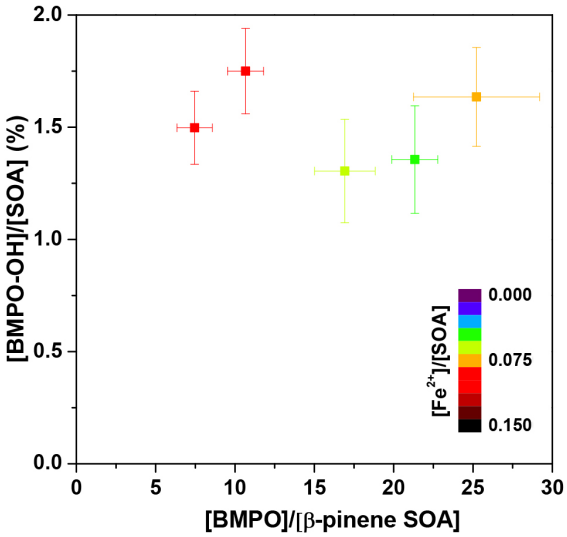

Figure S3. OH formation efficiency of β-pinene SOA/Fe^{2+} solutions as a function of BMPO concentration. The markers are colour coded with the molar ration of Fe^{2+} to SOA ([BMPO-OH]/[β-pinene SOA]).

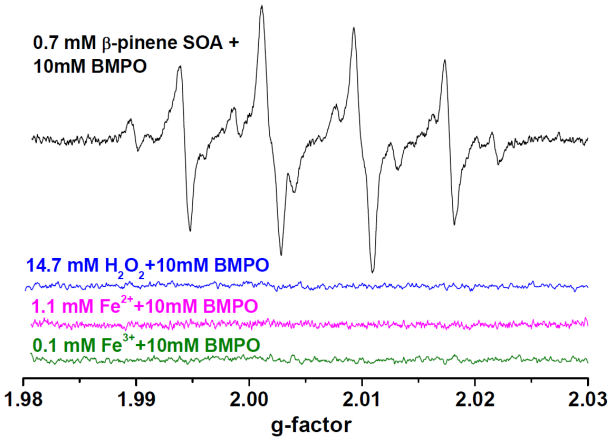

Figure S4. EPR spectra of BMPO mixtures. BMPO adducts with a 0.7 mM β-pinene SOA extracts (black line). Blank spectra of BMPO mixed with 14.7 mM H_2O_2 (blue line), 1.1 mM Fe^{2+} (pink line), and 0.1 mM Fe^{3+} (olive line) solutions. The BMPO concentration is 10 mM for all the samples.

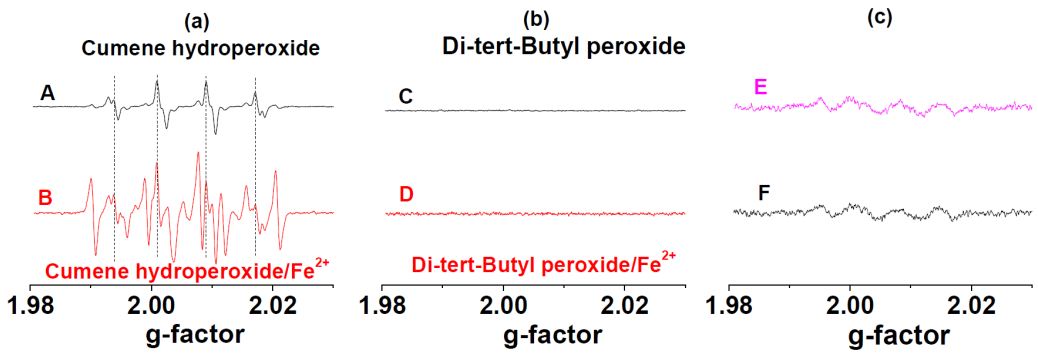

Figure S5. EPR spectra of various samples. EPR spectra of 15 mM cumene hydroperoxide solution in the absence of Fe^{2+} (A) and in the presence of 1.5 mM Fe^{2+} (B). EPR spectra of 15 mM Di-tert-Butyl peroxide solution in the absence of Fe^{2+} (C) and in the presence of 1.5 mM Fe^{2+}. EPR spectra of β-pinene SOA (E) and tert-Butyl hydroperoxide (F) in ethanol.

Supplementary references.

Bataineh, H., Pestovsky, O., and Bakac, A.: pH-induced mechanistic changeover from hydroxyl radicals to iron (IV) in the Fenton reaction, Chem. Sci., 3, 1594-1599, 2012.

Chevallier., E.: "Fenton-like" reactions of methylhydroperoxide and ethylhydroperoxide with Fe2+ in liquid aerosols under tropospheric conditions, Atmos. Environ., 38, 921, 2004.

Choe, E., and Min, D. B.: Chemistry and reactions of reactive oxygen species in foods, J. Food. Sci., 70, R142-R159, 2005.

Christensen, H., Sehested, K., and Corfitzen, H.: Reactions of hydroxyl radicals with hydrogen peroxide at ambient and elevated temperatures, J. Phys. Chem., 86, 1588-1590, 1982.

Corradi, M., Pignatti, P., Brunetti, G., Goldoni, M., Caglieri, A., Nava, S., Moscato, G., and Balbi, B.: Comparison between exhaled and bronchoalveolar lavage levels of hydrogen peroxide in patients with diffuse interstitial lung diseases, Acta Biomed, 79, 73-78, 2008.

Deguillaume, L., Leriche, M., Desboeufs, K., Mailhot, G., George, C., and Chaumerliac, N.: Transition Metals in Atmospheric Liquid Phases: Sources, Reactivity, and Sensitive Parameters, Chem. Rev., 105, 3388-3431, 2005.

Divišek, J., and Kastening, B.: Electrochemical generation and reactivity of the superoxide ion in aqueous solutions, J. Electroanal. Chem., 65, 603-621, 1975.

Eaton, G. R., Eaton, S. S., Barr, D. P., and Weber, R. T.: Quantitative EPR, Springer Science & Business Media, 2010.

Ghio, A. J., Turi, J. L., Yang, F., Garrick, L. M., and Garrick, M. D.: Iron homeostasis in the lung, Biol. Res., 39, 67-77, 2006.

Ghio, A. J.: Disruption of iron homeostasis and lung disease, Biochimica et Biophysica Acta (BBA) - General Subjects, 1790, 731-739, 2009.

Guo, Q., Qian, S. Y., and Mason, R. P.: Separation and identification of DMPO adducts of oxygen-centered radicals formed from organic hydroperoxides by HPLC-ESR, ESI-MS and MS/MS, J. Am. Soc. Mass Spectrom., 14, 862-871, 2003.

Herrmann, H., Schaefer, T., Tilgner, A., Styler, S. A., Weller, C., Teich, M., and Otto, T.: Tropospheric Aqueous-Phase Chemistry: Kinetics, Mechanisms, and Its Coupling to a Changing Gas Phase, Chem. Rev., 115, 4259-4334, 2015.

Hunter, R. C., Asfour, F., Dingemans, J., Osuna, B. L., Samad, T., Malfroot, A., Cornelis, P., and Newman, D. K.: Ferrous iron is a significant component of bioavailable iron in cystic fibrosis airways, MBio, 4, e00557-00513, 2013.

Koppenol, W. H., Butler, J., and Leeuwen, J. W. v.: The Haber‐Weiss cycle, Photochem. Photobiol., 28, 655-658, 1978.

Paget-Brown, A. O., Ngaintrakulpanit, L., Smith, A., Bunyan, D., Hom, S., Nguyen, A., and Hunt, J. F.: Normative data for pH of exhaled breath condensate, Chest, 129, 426-430, 2006.

Rush, J. D., and Bielski, B. H. J.: Pulse radiolytic studies of the reaction of perhydroxyl/superoxide O_2^- with iron(II)/iron(III) ions. The reactivity of HO_2/O_2^- with ferric ions and its implication on the occurrence of the Haber-Weiss reaction, J. Phys. Chem., 89, 5062-5066, 1985.

Sarangapani, R., and Wexler, A. S.: The role of dispersion in particle deposition in human airways, Toxicol. Sci., 54, 229-236, 2000.

Sehested, K., Rasmussen, O. L., and Fricke, H.: Rate constants of OH with HO_2,O_2^-, and $H_2O_2^+$ from hydrogen peroxide formation in pulse-irradiated oxygenated water, J. Phys. Chem., 72, 626-631, 1968.

Stuglik, Z., and PawełZagórski, Z.: Pulse radiolysis of neutral iron (II) solutions: oxidation of ferrous ions by OH radicals, Radiat. Phys. Chem., 17, 229-233, 1981.

Walters, D. V.: Lung lining liquid–The hidden depths, Neonatology, 81, 2-5, 2002.

Weber, R. T.: Xenon Data Processing Reference 2012.

Yamazaki, I., and Piette, L. H.: ESR spin-trapping studies on the reaction of Fe^{2+} ions with H_2O_2-reactive species in oxygen toxicity in biology, J. Biol. Chem., 265, 13589-13594, 1990.

B.3. Arangio et al., Atmos. Chem. Phys., 2016

Quantification of environmentally persistent free radicals and reactive oxygen species in atmospheric aerosol particles

Andrea M. Arangio[1], Haijie Tong[1], Joanna Socorro[1], Ulrich Pöschl[1] and Manabu Shiraiwa[1,2]

1 Max Planck Institute for Chemistry, Multiphase Chemistry Department, Mainz, Germany
2 Department of Chemistry, University of California, Irvine, CA, United State

Atmospheric Chemistry and Physics, 16, 13105 – 13119, 2016.

Authors contributions.

AA, HT and MS designed research. AA performed sampling, EPR analysis, spectra fitting and simulation. JS performed LC/MS/MS analysis. All authors discussed the results. AA and MS wrote the paper.

Atmos. Chem. Phys., 16, 13105–13119, 2016
www.atmos-chem-phys.net/16/13105/2016/
doi:10.5194/acp-16-13105-2016

Atmospheric Chemistry and Physics
Open Access
EGU

Quantification of environmentally persistent free radicals and reactive oxygen species in atmospheric aerosol particles

Andrea M. Arangio[1], Haijie Tong[1], Joanna Socorro[1], Ulrich Pöschl[1], and Manabu Shiraiwa[1,2]

[1]Multiphase Chemistry Department, Max Planck Institute for Chemistry, Mainz, Germany
[2]Department of Chemistry, University of California, Irvine, CA, USA

Correspondence to: Manabu Shiraiwa (m.shiraiwa@uci.edu)

Received: 13 June 2016 – Published in Atmos. Chem. Phys. Discuss.: 20 June 2016
Revised: 4 October 2016 – Accepted: 12 October 2016 – Published: 26 October 2016

Abstract. Fine particulate matter plays a central role in the adverse health effects of air pollution. Inhalation and deposition of aerosol particles in the respiratory tract can lead to the release of reactive oxygen species (ROS), which may cause oxidative stress. In this study, we have detected and quantified a wide range of particle-associated radicals using electron paramagnetic resonance (EPR) spectroscopy. Ambient particle samples were collected using a cascade impactor at a semi-urban site in central Europe, Mainz, Germany, in May–June 2015. Concentrations of environmentally persistent free radicals (EPFR), most likely semiquinone radicals, were found to be in the range of (1–7) $\times 10^{11}$ spins μg^{-1} for particles in the accumulation mode, whereas coarse particles with a diameter larger than 1 µm did not contain substantial amounts of EPFR. Using a spin trapping technique followed by deconvolution of EPR spectra, we have also characterized and quantified ROS, including OH, superoxide (O_2^-) and carbon- and oxygen-centered organic radicals, which were formed upon extraction of the particle samples in water. Total ROS amounts of (0.1–3) $\times 10^{11}$ spins μg^{-1} were released by submicron particle samples and the relative contributions of OH, O_2^-, C-centered and O-centered organic radicals were ∼ 11–31, ∼ 2–8, ∼ 41–72 and ∼ 0–25 %, respectively, depending on particle sizes. OH was the dominant species for coarse particles. Based on comparisons of the EPR spectra of ambient particulate matter with those of mixtures of organic hydroperoxides, quinones and iron ions followed by chemical analysis using liquid chromatography mass spectrometry (LC-MS), we suggest that the particle-associated ROS were formed by decomposition of organic hydroperoxides interacting with transition metal ions and quinones contained in atmospheric humic-like substances (HULIS).

1 Introduction

Epidemiological studies have clearly shown positive correlations between respiratory diseases and ambient fine particulate matter (Pope and Dockery, 2006; Strak et al., 2012; West et al., 2016). A recent study has estimated that outdoor air pollution leads to 3.3 million premature deaths per year worldwide, which is mostly due to particular matter with a particle diameter less than 2.5 µm ($PM_{2.5}$) (Lelieveld et al., 2015). Plausible reasons include the cytotoxicity of ambient $PM_{2.5}$ and its ability to induce inflammatory responses by oxidative stress causing functional alterations of pulmonary epithelial cells (Nel, 2005; Gualtieri et al., 2009). Oxidative stress is mediated by reactive oxygen species (ROS), including OH, H_2O_2 and superoxide (O_2^-), as well as organic radicals (Pryor et al., 1995; Winterbourn, 2008; Birben et al., 2012; Pöschl and Shiraiwa, 2015). Upon PM deposition into the respiratory tract and interactions with lung antioxidants, H_2O_2 can be generated by redox-active components contained in $PM_{2.5}$ such as transition metals (Charrier et al., 2014; Fang et al., 2016), semiquinones (Kumagai et al., 1997; Cho et al., 2005; Khachatryan et al., 2011; McWhinney et al., 2013) and humic-like substances (Kumagai et al., 1997; Cho et al., 2005; Lin and Yu, 2011; Charrier et al., 2014; Dou et al., 2015; Fang et al., 2016; Verma et al., 2015a). H_2O_2 can be converted into highly reactive OH radicals via Fenton-like reactions with iron and copper ions (Charrier et al., 2014; Enami et al., 2014).

Ambient particles have been found to contain large amounts of ROS (mostly H_2O_2) in the particle phase (Hung and Wang, 2001; Venkatachari et al., 2005, 2007; Fuller et al., 2014). Substantial amounts of particle-bound ROS are

found on biogenic secondary organic aerosols (SOA) produced from the oxidation of α-pinene, linalool, and limonene (Chen and Hopke, 2010; Chen et al., 2011; Pavlovic and Hopke, 2011; Wang et al., 2011, 2012). Recently, Tong et al. (2016) have shown that terpene and isoprene SOA can form OH radicals upon interactions with liquid water and iron ions under dark conditions. This can be explained by the decomposition of organic hydroperoxides, which account for the predominant fraction of SOA mass and are generated via multigenerational oxidation and autoxidation (Docherty et al., 2005; Ziemann and Atkinson, 2012; Crounse et al., 2013; Ehn et al., 2014; Epstein et al., 2014; Badali et al., 2015).

In addition, $PM_{2.5}$ contains environmentally persistent free radicals (EPFR) that can be detected directly by electron paramagnetic resonance (EPR) spectroscopy (Dellinger et al., 2001; Khachatryan et al., 2011; Gehling and Dellinger, 2013). EPFR are stable radicals with an *e* folding lifetime exceeding one day (Gehling and Dellinger, 2013; Jia et al., 2016). The chemical nature of EPFR is remarkably similar to semiquinone radicals, which can be stabilized via electron transfer with transition metals in the particle phase (Truong et al., 2010; Vejerano et al., 2011; Gehling and Dellinger, 2013). EPFR are formed upon combustion and pyrolysis of organic matter (Dellinger et al., 2001, 2007). The formation of stable radicals can also be induced by heterogeneous and multiphase chemistry of organic aerosols. Heterogeneous ozonolysis of aerosol particles such as polycyclic aromatic hydrocarbons (PAH) and pollen proteins can lead to the formation of long-lived reactive oxygen intermediates (ROI) (Shiraiwa et al., 2011, 2012; Reinmuth-Selzle et al., 2014; Borrowman et al., 2015; Kampf et al., 2015; Berkemeier et al., 2016).

In this work, ambient particles with a diameter in the range of 56 nm to 3.2 µm were collected using a cascade impactor during May–July 2015 in Mainz, Germany. Size dependences of EPFR concentrations contained in ambient particles have been measured using an EPR spectrometer. Particles were also extracted in water containing a spin-trapping agent followed by EPR analysis to quantify the formation of various radical forms of ROS, including OH, superoxide (O_2^-) and carbon- and oxygen-centered organic radicals.

2 Methods

Ambient particles were collected using a micro-orifice uniform deposition impactor (MOUDI, 110-R, MSP Corporation) on the roof of the Max Planck Institute for Chemistry, Mainz, Germany (49.99° N, 8.23° E). The sampling was conducted every 24 h starting at 17:00 during 28 May–9 June 2015. Particles were collected with a sampling time of 48 h during 26–27 June and 18–19 July 2015 in order to collect sufficiently high mass loadings for all stages of different particle size ranges. The sampling was conducted with a flow rate of 30 L min^{-1} with the following nominal lower cut-off particle diameters: 56, 100, 180, 320, 560 nm, 1, and 1.8 µm. Note that transmission and bouncing effects might have caused mixing of particles exhibiting relatively different sizes on one stage, particularly for coarse particles (Gomes et al., 1990; Bateman et al., 2014). Particles were collected on 47 mm diameter Teflon filters (100 nm pore size, Merck Chemicals GmbH). Before sampling, each filter was cleaned and sonicated for 10 min with pure ethanol and ultra-pure water and dried with nitrogen gas before weighing. Teflon filters were weighed four times using a balance (Mettler Toledo XSE105DU) and mounted in the MOUDI. After sampling, each filter was conditioned for at least 1 h (22–23 °C and 40–50 % RH) and weighted four times before being folded and inserted in a 4 mm EPR tube. Particles were extracted by immersing the filter into a solution containing 350 µL of 20 mM 5-tert-Butoxycarbonyl-5-methyl-1-pyrroline-N-oxide (BMPO, high purity; Enzo Life Sciences, Inc.) and stirred with a vortex shaker (Heidolph Reax 1) for 7–9 min. BMPO is an efficient spin-trapping agent for OH, O_2^- and organic radicals (Zhao et al., 2001; Tong et al., 2016). Note that the trapping efficiency of O_2^- and organic radicals might be lower compared to OH radicals, as the recent study has reported that nitrone-based spin traps have the highest reactivity towards OH and somewhat lower reactivity towards organic radicals and superoxide (Sueishi et al., 2015). Extracts were dried for approximately 14–17 min under 1–3 bar flow to reduce the volume of the solution to 50 µL, and then 20 µL were used for EPR measurements.

A continuous-wave electron paramagnetic resonance (CW-EPR) X-band spectrometer (EMXplus-10/12; Bruker Corporation) was used for detection and quantification of stable radicals and ROS. Filters containing particles were folded and introduced into a 4 mm I.D. quartz tube and inserted directly into a high sensitivity cavity. EPR spectra were recorded at a room temperature of 23 °C by setting the following operating parameters: a modulation frequency of 100 kHz; a microwave frequency of 9.84 GHz, a microwave power of 2.149 mW (20 db), a modulation amplitude of 1.0 G, a sweep width of 110.0 G, a sweep time of 175 s, a receiver gain of 40 db, a time constant of 40.96 ms, a conversion time of 160 ms and a scan number of 6. Paramagnetic species are characterized based on their *g* factor values. Free electrons have a *g* factor value of 2.0023 and organic radicals have higher *g* factor values (2.0030–2.0060), depending on the number of oxygen atoms in the molecule (Dellinger et al., 2007).

The spin-counting method embedded in the Bruker software, Xenon, was used to quantify detected radicals. The spin-counting method was calibrated using a standard compound 4-hydroxy-2,2,6,6-tetramethylpiperidin-1-oxyl (TEMPOL). The detection limit of EPR was $\sim 1 \times 10^{10}$ spins µg^{-1}. Concentrations of EPFR and ROS are reported in the unit of spins µg^{-1}, which indicates the number

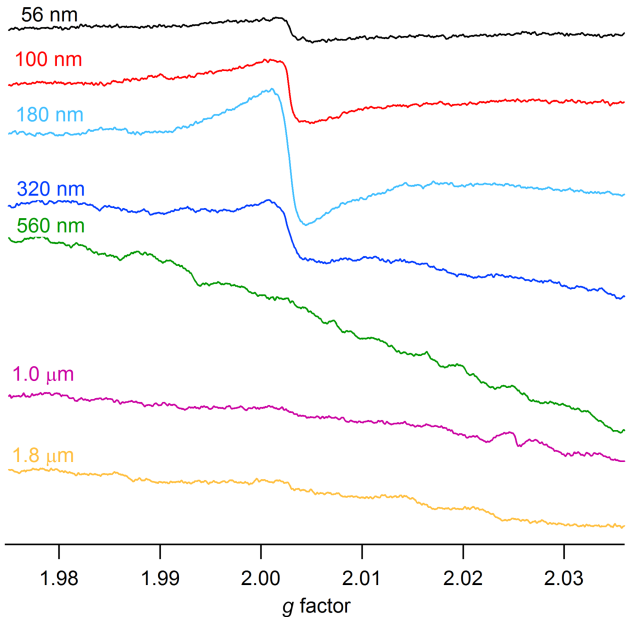

Figure 1. Electron paramagnetic resonance (EPR) spectra of atmospheric aerosol impactor samples with lower cut-off diameters in the range of 56 nm to 1.8 µm collected in Mainz, Germany, during 26–27 June, 2015.

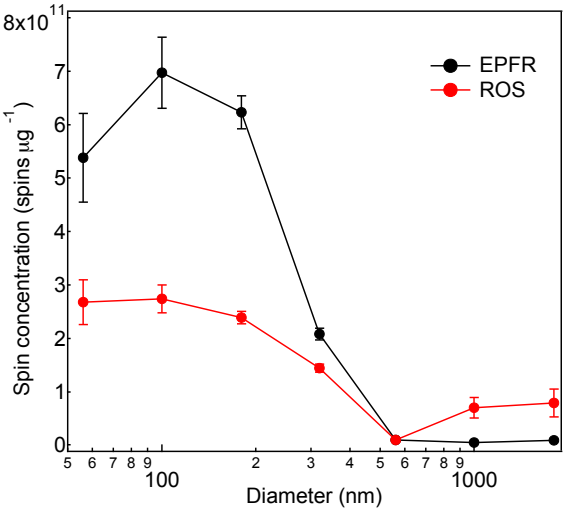

Figure 2. Concentrations (spins per microgram of particles) of environmentally persistent free radicals (EPFR) and radical forms of reactive oxygen species (ROS) in atmospheric aerosol samples plotted against particle diameter. The error bars represent standard errors based on uncertainties in the particle mass and signal integration of EPR spectra.

of spins (or radicals) per µg of particle mass. For better quantification and determination of the relative contributions of OH, O_2^-, carbon-centered and oxygen-centered organic radicals, EPR spectra were fitted and simulated using Xenon and the MATLAB-based computational package EasySpin (Stoll and Schweiger, 2006).

3 Results and discussion

3.1 Environmentally persistent free radicals

Figure 1 shows EPR spectra of ambient particles in the lower cut-off diameter range of 56 nm–1.8 µm. Fine particles, with lower cut-off diameters of 56–320 nm, show a single and unstructured peak with a g factor of ∼2.003 and with a peak to peak distance ($\Delta H_{p\text{-}p}$) ranging from 3 to 8 G. Such spectra are characteristic for EPFR, which have been attributed to semiquinone radicals (Dellinger et al., 2001, 2007; Vejerano et al., 2011; Bahrle et al., 2015). Particles with a diameter smaller than 56 nm and larger than 560 nm did not show significant signals, indicating the reduced amount of EPFR in these size ranges. EPR spectra for particles with the lower cut-off diameters of 56–320 nm for each sampling day are presented in Fig. A1 in the Appendix.

The black line in Fig. 2 shows the size distribution of EPFR concentrations. Particles with different sizes had different radical contents and particles with the lower cut-off diameter of 100 nm contained the highest EPFR concentrations of $7.0\,(\pm 0.7) \times 10^{11}$ spins µg^{-1}. High abundances of EPFR

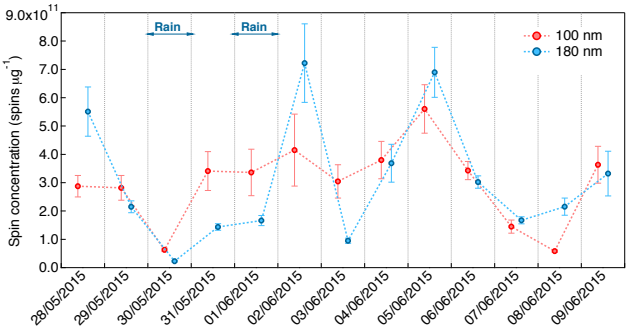

Figure 3. Temporal evolution of concentrations of environmentally persistent free radicals (EPFR) contained in atmospheric aerosol samples with lower cutoff diameters of 100 nm (red) and 180 nm (blue), measured in Mainz, Germany, during May–June 2015. The error bars represent standard errors based on uncertainties in the particle mass and signal integration of EPR spectra.

in particles in the accumulation mode is consistent with mass size distributions of combustion-generated particles, such as soot or black carbon, which typically have peak concentrations around 100–200 nm (Bond et al., 2013). This observation is in line with the fact that EPFR may often be associated with soot particles (Dellinger et al., 2007).

Figure 3 shows the temporal evolution of EPFR concentrations contained in particles with lower cut-off diameters of 100 and 180 nm. During the sampling period of 2 weeks, there were two rain events (on 30 May and 1 June 2015) and three sunny days (4–6 June 2015), and the other days were cloudy. The mass concentrations of particles within the di-

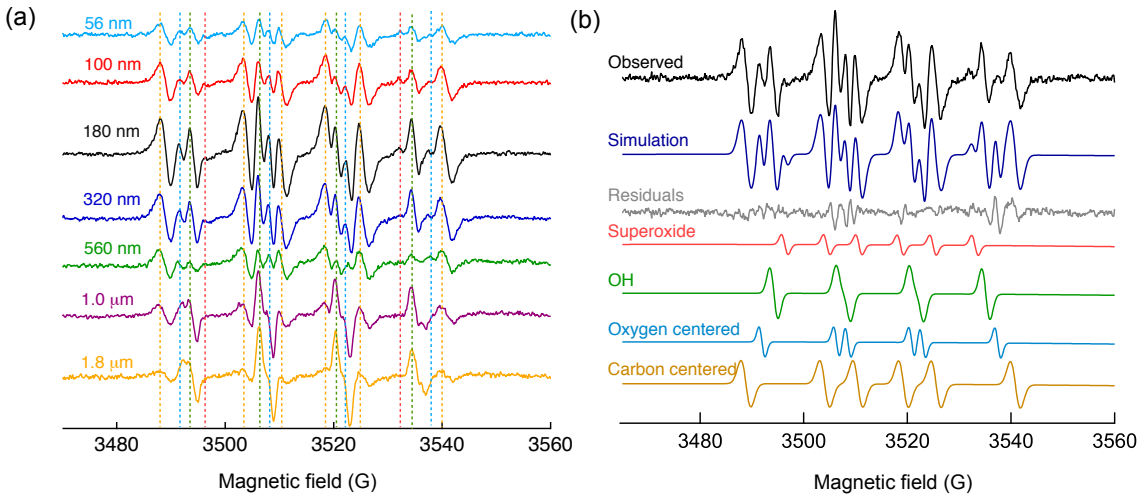

Figure 4. (a) Electron paramagnetic resonance (EPR) spectra of ambient aerosol impactor samples (Mainz, Germany; 26–27 June 2015) with lower cut-off diameters in the range of 56 nm to 1.8 µm extracted in water mixed with the spin-trapping agent BMPO. Dashed lines indicate the position of each peak for different types of trapped radicals of O_2^- (red), OH (green), carbon-centered (orange) and oxygen-centered organic radicals (light blue). **(b)** Simulation of the EPR spectrum of the atmospheric aerosol impactor sample with particle diameters in the range of 180–320 nm (lower to upper cut-off) by deconvolution into O_2^-, OH, O-centered and C-centered organic radicals (Blue is synthesis, grey is residual).

ameters of 56–560 nm were in the range of 3.9–12.8 µg m^{-3}. Maximum values of $\sim 7 \times 10^{11}$ spins µg^{-1} were reached during sunny days, indicating that photochemistry may be related to EPFR production. For example, heterogeneous reactions of photo-oxidants including O_3 and OH with soot or PAH may contribute to the formation of long-lived radicals (Shiraiwa et al., 2011; Borrowman et al., 2015). Radical concentrations were as low as 6.3×10^{10} spins µg^{-1} during rain events, most likely due to low production of EPFR and scavenging by precipitation.

The EPFR concentration contained in particles within the diameter of 56 nm–3.2 µm collected for 48 h during 26–27 June 2015 was $\sim 2.2 \times 10^{11}$ spins µg^{-1}. EPFR concentrations contained in particles within the diameter of 56–560 nm averaged over the entire measurement period was $2.0\,(\pm 1.3) \times 10^{11}$ spins µg^{-1}. Squadrito et al. (2001) determined the EPFR concentrations to be in the range of (1–10) $\times 10^{11}$ spins µg^{-1} in $PM_{2.5}$ sampled for 24 h in five different urban sites in the United States. Gehling et al. (2014) reported that the EPFR concentration was in the range of (7–55) $\times 10^{10}$ spins µg^{-1} at a site in Louisiana near heavy interstate traffic along a major industrial corridor of the Mississippi River. Shaltout et al. (2015) measured radical concentrations in the range of (2–6) $\times 10^{10}$ spins µg^{-1} in $PM_{2.5}$ collected in industrial-, residential- and traffic-dominated sites in Taif, Saudi Arabia. The EPFR concentrations measured in this work are comparable with these previous measurements.

3.2 Reactive oxygen species

Figure 4a shows EPR spectra of ambient particles with lower cut-off diameters of 56 nm–1.8 µm extracted in water with the spin-trapping agent BMPO. Each EPR spectrum is composed of several overlapped lines, originating from different radical forms of ROS. Dashed lines indicate the positions of each peak for each type of trapped ROS, including OH (green), superoxide (red), carbon-centered (orange) and oxygen-centered organic radicals (light blue). The relative abundance of these radicals was different for each size range, causing the EPR spectral features to be highly variable. For example, spectra from particles larger than 1.0 µm consist mainly of four peaks that are typical for OH radicals, whereas those for smaller particles contain more peaks indicating the presence of multiple radicals.

To estimate the relative amount of each type of ROS, the observed EPR spectra were fitted and simulated using the softwares EasySpin 5.0 and Xenon. Four types of radicals have been used to fit the spectra: BMPO-OH (hyperfine coupling constants of $a^N = 14.3$ G, $a_\beta^H = 12.7$ G, $a_\gamma^H = 0.61$ G), BMPO-OOH ($a^N = 14.3$ G, $a^H = 8.1$ G), BMPO-R ($a^N = 15.2$ G, $a^H = 21.6$ G) and BMPO-OR ($a^N = 14.5$ G, $a_\beta^H = 16.6$ G). As shown in Fig. 4b, the simulated EPR spectrum reproduced the observed spectrum very well with a small residual. The deconvolution of spectra allowed us to estimate the relative contribution of four types of ROS within each particle size range.

Figure 5 shows the relative contributions of OH (green), superoxide (red), carbon-centered (orange) and oxygen-centered (blue) organic radicals to the total radicals trapped

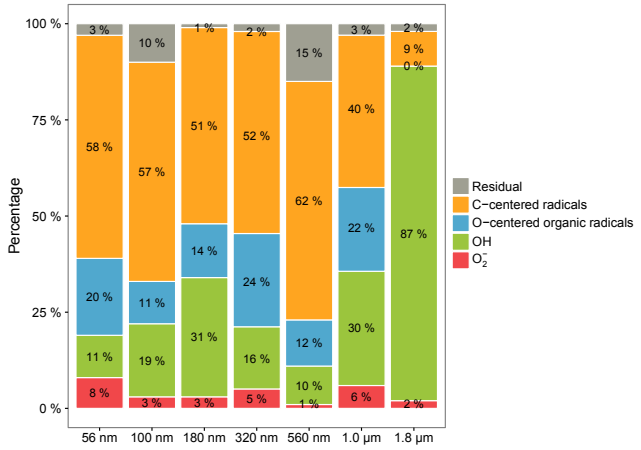

Figure 5. Relative amount of ROS in atmospheric aerosol impactor samples with lower cut-off diameters in the range of 50 nm–1.8 µm (Mainz, Germany; 26–27 June 2015) are as follows: O_2^- (red), OH (green), carbon-centered (orange), oxygen-centered organic radicals (blue) and residual (unidentified, grey).

by BMPO in water extracts of particles collected for 48 h during 26–27 June 2015. Carbon-centered radicals are the most abundant type of radicals, contributing ∼ 50–72 % of total ROS for PM_1. It decreases to 41 and 9 % for particles with lower cut-off diameters of 1 and 1.8 µm, respectively. The OH radical accounts for ∼ 11–31 % of total trapped radicals for PM_1, whereas OH was the dominant species for coarse particles with diameters of 1.8–3.2 µm. The least abundant radical for all size ranges was O_2^-, with contributions of ∼ 2–8 % and without any clear size dependence. The amount of oxygen-centered organic radicals ranges between 12 and 25 % in particles with a diameter below 1 µm and its contribution was negligible for coarse particles. Note that the contribution of oxygen-centered organic radicals for particles with a diameter of 1–1.8 µm might be attributed to the OH radical, since the hyperfine coupling constants for BMPO-OR for better fitting the spectrum for this size range needed to be changed slightly ($a^N = 13.5$ G, $a_\beta^H = 15.3$ G, $a_\gamma^H = 0.6$ G). These values are similar to constants of a second conformer of BMPO-OH.

The red line in Fig. 2 shows the size-dependent concentrations of radical forms of ROS (e.g., sum of OH, O_2^-, C- and O- centered organic radicals). Particles with the lower cut-off diameter of 100 nm have the highest ROS concentrations of $2.7\,(\pm 0.2) \times 10^{11}$ spins µg^{-1}. Concentrations are smaller for particles in the coarse mode with a diameter larger than 1 µm. This is consistent with previous studies, suggesting that particles in the accumulation mode are the most active in the ROS generation (Hung and Wang, 2001; Venkatachari et al., 2007; Saffari et al., 2013, 2014; Wang et al., 2013). The total concentration of radical forms of ROS was measured to be 1.2×10^{11} spins µg^{-1}. Note that O_2^- concentrations might be underestimated as the lifetime of the BMPO-OOH adduct is relatively short (∼ 23 min) (Ouari et al., 2011; Abbas et al., 2014).

Previous studies have measured redox activity and oxidative potential of PM by the dichlorofluorescein (DCFH) and dithiothreitol (DTT) assays. The DCFH assay is mostly sensitive to H_2O_2 and other peroxides. For example, Hung and Wang (2001) reported ROS concentrations as 1×10^{13} µg^{-1} in Taipei, Taiwan. This value is very similar to H_2O_2 concentrations contained in ambient $PM_{2.5}$, which has been quantified to be up to 1×10^{13} µg^{-1} in an urban environment in southern California using high-performance thin-layer chromatography (HPLC) fluorescence (Wang et al., 2012). The DTT assay is based on the decay of DTT due to redox reactions with PM components, reporting the oxidative potential of PM in moles of DTT consumed per unit of time and mass of PM. Verma et al. (2015a) and Fang et al. (2016) reported that $PM_{2.5}$ sampled in an urban environment in Atlanta, Georgia, USA, has a DTT activity in the range of 10–70 pmol min^{-1} µg^{-1}. Assuming an integration time of 20 min needed for the extraction of PM in this work, this value corresponds to $(1–8) \times 10^{14}$ µg^{-1} of DTT molecules consumed. Charrier et al. (2012) also reported that $PM_{2.5}$ sampled in an urban environment in Fresno, California, USA, has a DTT activity of 27–61 pmol min^{-1} µg^{-1}, corresponding to $(2–7) \times 10^{14}$ µg^{-1} of DTT molecules consumed in 20 min. Assuming that the consumption of one DTT molecule would correspond to the generation of one ROS molecule (e.g., H_2O_2), these values are about a few orders of magnitude higher than concentrations of radical forms of ROS measured in this study. This is reasonable as H_2O_2 is closed shell and much more stable than open-shell radical forms of ROS.

3.3 ROS formation mechanism

It has been shown that semiquinones and reduced transition metals including, Fe(II) and Cu(I), can react with O_2 to form O_2^-, which can be further converted into H_2O_2 (Gehling et al., 2014; Fang et al., 2016). Fenton-like reactions of H_2O_2 with Fe(II) or Cu(I) can lead to the formation of OH radicals (Winterbourn, 2008; Pöschl and Shiraiwa, 2015). OH radicals can also be generated by the decomposition of organic hydroperoxides (ROOH) contained in SOA, yielding RO radicals (Tong et al., 2016). Several studies have reported a metal-independent decomposition of hydroperoxides and organic hydroperoxides driven by substituted quinones producing RO radicals (Sanchez-Cruz et al., 2014; Huang et al., 2015). The presence of Fe(II) or quinones is suggested to enhance ROOH decomposition and the formation of RO and OH radicals (Zhu et al., 2007a, b, 2009; Sanchez-Cruz et al., 2014). Organic peroxides (ROOR) do not yield OH and RO radicals even in the presence of iron ions (Tong et al., 2016).

Based on these previous studies and considering that ambient particles may contain quinones, organic hydroperoxides and transition metals, the observed ROS formation may

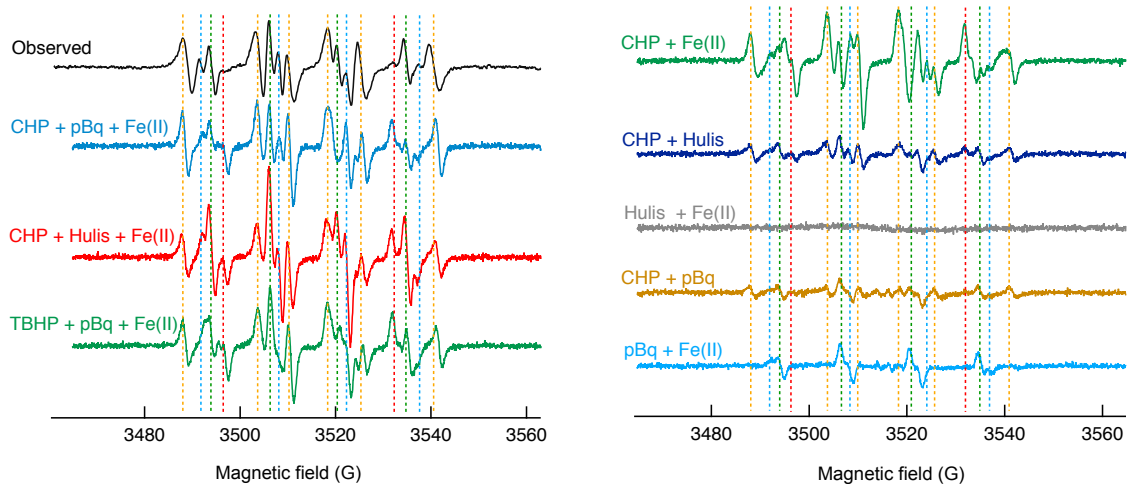

Figure 6. Electron paramagnetic resonance (EPR) spectra of atmospheric aerosol impactor sample with particle diameters in the range of 180–320 nm (lower to upper cut-off) extracted with water and BMPO (black) and of aqueous substance mixtures with the following ingredients: cumene hydroperoxide (CHP), p-benzoquinone (pBq) and Fe(II) (light blue) and t-butyl hydroperoxide (TBHP). The dashed vertical lines indicate the main peaks of BMPO adducts with O_2^- (red), OH (green), carbon- (light blown) and oxygen-centered organic radicals (light blue).

be caused by interactions of these chemical components. To further investigate this aspect, mixtures of organic hydroperoxides, quinones and Fe(II) were analyzed by EPR and liquid chromatography mass spectrometry (LC-MS). Two standard organic hydroperoxides, cumene hydroperoxide and tert-butyl hydroperoxide, were used. For quinones, p-benzoquinone and humic-like substances are used, as humic-like substance (HULIS) are known to contain substantial amounts of quinones (Verma et al., 2015b).

Figure 6 shows the comparison of EPR spectra of ambient particles with a diameter of 180–320 nm (black) sampled on 26 June 2015 (same as shown in Fig. 4) and the above mixtures of organic compounds. Panel a includes EPR spectra of mixtures of all three different components (ROOH, quinone, metal) and panel b presents mixtures of two different components. All three of the organic mixtures in panel a resemble the EPR spectrum of ambient particles by reproducing almost all of the peaks. In particular, the EPR spectrum of the mixture containing cumene hydroperoxide, humic acid and Fe(II) closely overlaps with the ambient particle EPR spectrum. Similarity of spectra between p-benzoquinone and HULIS suggests that the chemical nature of quinones and HULIS is very similar. Note that peaks related to the BMPO-OOH adduct at 3497 G and at 3530 G are more prominent in standard organic mixtures compared to ambient particles. This may be due to the relatively short lifetime of BMPO-OOH of $\sim$ 23 min (Zhao et al., 2001), which is comparable to the extraction and mixing time of BMPO with the atmospheric particles (21–28 min), during which BMPO-OOH may decay. The trapped radicals have been further characterized by LC-MS, confirming the presence of OH and semiquinone radicals as well as carbon- and oxygen-centered organic radicals, as detailed in Appendix A and Figs. A1 and A2.

EPR spectra of mixtures containing two compounds in panel b reproduce only a part of the observed peaks. These observations strongly suggest that the combination of these three chemical components play an important role in generating ROS species by atmospheric particles. The role of transition metals is crucial to enhance radical formation, most likely via Fenton-like reactions (Tong et al., 2016) and by participating in redox-cycling of quinones (Khachatryan and Dellinger, 2011), as intensities of EPR spectra without Fe(II) (CHP + HULIS, dark blue; CHP + pBq, orange) are small. Carbon-centered radicals may have multiple sources, such as the decomposition of the BMPO-OR adduct by scission of the carbon in β position, yielding for example CH_3 radicals (Zhu et al., 2007b; Huang et al., 2015), as detected by LC-MS (Fig. A2). They may also be generated by secondary reactions of non-trapped OH radicals with water-soluble organic compounds.

SOA particles, which may contain large amounts of organic hydroperoxides, account for a major fraction in PM_1 (Jimenez et al., 2009). SOA compounds may also coat coarse particles such as biological particles (Pöhlker et al., 2012). As shown in Fig. 2, semiquinones are mostly contained in submicron particles but not in coarse particles. Thus, the release of a variety of ROS species is most likely due to the interactions of organic hydroperoxides, semiquinones and transition metal ions, whereas the dominance of OH radicals in coarse particles may be due to the decomposition of organic hydroperoxides in the absence of semiquinones.

4 Conclusions and implications

In this study particle-associated environmentally persistent free radicals (EPFR) and radical forms of ROS have been quantified using electron paramagnetic resonance (EPR) spectroscopy. Average EPFR concentrations were measured to be $\sim 2 \times 10^{11}$ spins μg^{-1} in ambient particles collected in Mainz, Germany, in May–June 2015. The chemical identity of EPFR is likely to be semiquinone radicals based on the *g* factors observed by EPR spectroscopy. We found that particles with different sizes had different radical contents and particles with a diameter of 100–180 nm had the highest abundance of EPFR, whereas coarse particles did not contain EPFR. This is consistent with the size distribution of combustion particles, such as soot and humic-like substances (HULIS), which may contain substantial amounts of EPFR.

Reactive oxygen species (ROS) are formed upon extraction of particles into water. Particles with the diameter of 100–180 nm have released the highest ROS concentrations of $2.7\,(\pm 0.2) \times 10^{11}$ spins μg^{-1}. By deconvolution of the obtained EPR spectra, four types of radicals, including OH, O_2^-, carbon-centered and oxygen-centered organic radicals were quantified. The relative amounts of OH, O_2^-, C-centered and O-centered organic radicals in submicron particles were found to be $\sim$ 11–31, $\sim$ 2–8, $\sim$ 41–72 and $\sim$ 0–25 %, respectively, depending on the particle size. OH was the dominant species for coarse particles with a diameter larger than 1 µm. We suggest that the formation of these ROS species is due to the decomposition of organic hydroperoxides, which are a major component in SOA, interacting with semiquinones contained in soot or HULIS. ROS formation by Fenton-like reactions can be enhanced in the presence of iron ions.

These findings have significant implications for the chemical processing of organic aerosols in deliquesced particles and cloud water. The released OH radicals within particles or cloud droplets can oxidize other organic compounds, producing low-volatility products, including organic acids, peroxides and oligomers (Lim et al., 2010; McNeill et al., 2012; Ervens, 2015; Herrmann et al., 2015). Autoxidation in the condensed phase might be triggered by OH radicals forming highly oxidized compounds (Shiraiwa et al., 2014; Tong et al., 2016). High aqueous oxidant levels may cause fragmentation of organic compounds, resulting in an increased loss of carbon from the condensed phase (Daumit et al., 2016). The formed carbon- and oxygen-centered organic radicals are also expected to enhance chemical aging by participating in particle-phase chemistry involving aldehydes, carbonyls and organic peroxides (Ziemann and Atkinson, 2012), although the exact role and impact of formed organic radicals are still unclear and subject to further studies.

Previous studies have shown that redox-active components such as transition metals and quinones can induce ROS formation in surrogate lung lining fluid upon interactions with antioxidants (Charrier and Anastasio, 2011; Charrier et al., 2014). This study also implies that ROS can be formed in lung lining fluid upon inhalation and respiratory deposition of atmospheric aerosol particles. Even though some fractions of ROS may be scavenged by antioxidants contained in lung lining fluid, excess concentrations of ROS, including OH radicals, superoxide and also, potentially, carbon- and oxygen-centered organic radicals may cause oxidative stress to lung cells and tissues (Winterbourn, 2008; Pöschl and Shiraiwa, 2015; Tong et al., 2016). Recently, Lakey et al. (2016) have shown that fine particulate matter containing redox-active transition metals, quinones and secondary organic aerosols can increase ROS concentrations in the lung lining fluid to levels characteristic for respiratory diseases. ROS play a central role in chemical transformation of biomolecules, such as proteins and lipids, in lung fluid to form damage associated molecular patterns (DAMPs), which can trigger immune reactions causing inflammation through the tolling receptor radical cycle (Lucas and Maes, 2013). Due to the important implications of adverse aerosol health effects, further studies are warranted to characterize and quantify EPFR and ROS contained in atmospheric aerosol particles in various locations, including highly polluted regions such as East Asia and India.

5 Data availability

Data are available upon request by contacting M. Shiraiwa (m.shiraiwa@uci.edu).

Appendix A: LC-MS analysis of organic mixtures

Two solutions of mixtures of standard organic hydroperoxides and quinones were analyzed by liquid chromatography mass spectrometry (LC-MS). Solution (1) was the mixture of 200 µL of p-benzoquinone solution at a concentration of $0.2\,g\,L^{-1}$ (Reagent grade, $\geq 98\,\%$, Sigma-Aldrich) in water (trace SELECT® Ultra, ACS reagent, for ultratrace analysis, Sigma-Aldrich), 100 µL of Tert-Butyl hydroperoxide solution at a concentration of $8.9\,g\,L^{-1}$ (Luperox® TBH70X, 70 wt. in % H_2O, Sigma-Aldrich) in water, 2.5 µL of Iron (II) sulfate heptahydrate solution at $0.3\,g\,L^{-1}$ (reagentPlus®, $\geq 99\,\%$, Sigma-Aldrich) in water and 1 mg of 5-tert-Butoxycarbonyl-5-methyl-1-pyrroline-N-oxide (BMPO, high purity, Enzo Life Sciences, Inc.). Solution (2) was the same as solution (1) but without Iron (II) sulfate heptahydrate. These solutions were stirred with a vortex shaker (Heidolph Reax 1) for 5 min.

These solutions were analyzed using a 1260 Infinity Bio-inert Quaternary LC system with a quaternary pump (G5611A), a HiP sampler (G5667A) and an electrospray ionization (ESI) source interfaced to a Q-TOF mass spectrometer (6540 UHD Accurate-Mass Q-TOF, Agilent Technologies). All modules were controlled by MassHunter software (B.06.01, Agilent). The LC column was a Zorbax Extend-C18 Rapid Resolution HT (2.1×50 mm, 1.8 µm) with a column temperature of 30 °C. The mobile phases were 3 % (v/v) acetonitrile (HPLC Gradient Grade, Fisher Chemical) in water with formic acid (0.1 % v/v, LC-MS Chromasolv, Sigma-Aldrich) (Eluent A) and 3 % water in acetonitrile (Eluent B). The injection volume was 10 µL. The flow rate was $0.2\,mL\,min^{-1}$ with a gradient program that starting with 3 % B for 3 min followed by a 36 min steps that raised Eluent B to 60 %. Furthermore, Eluent B was increased to 80 % at 40 min and returned to initial conditions within 0.1 min, followed by column re-equilibration for 9.9 min before the next run.

The ESI-Q-TOF instrument was operated in the positive ionization mode (ESI+) with a gas temperature of 325 °C, 20 psig nebulizer, 4000 V capillary voltage and 90 V fragmental voltage. During the full spectrum MS mode, no collision energy was used in order to collect species as their molecular ions. During MS/MS analysis employed for the structure determination, the fragmentation of protonated ions was conducted using the target MS/MS mode with 20 V collision energy. Spectra were recorded over the mass range of m/z 50–1000. Data analysis was performed using qualitative data analysis software (B.06.00, Agilent). Blank solutions without BMPO were also prepared and analyzed. Background signals were subtracted from the MS spectrum.

Figure A2 shows LC-MS/MS mass spectra of the products formed from the reaction of tert-butyl hydroperoxide, p-benzoquinone and BMPO in the presence of iron (solution 1). Very similar results were obtained for solutions in the absence of iron (solution 2). BMPO adducts with radicals ·OH, $\cdot CH_3$ and $\cdot OCH_3$ were identified by LC-MS/MS. As shown in Fig. A2a.1, it was observed that ions at m/z 160.0596, 216.1221 and 238.1020 were major ions formed in the positive mode. These protonated ions represent the $[BMPO + OH–C_4H_8 + H]^+$, $[BMPO + OH + H]^+$ and $[BMPO + OH + Na + H]^+$ spin adducts, respectively. Figure A2a.2 displays the mass spectrum in the MS/MS mode for the fragmentation of the ion m/z 216.1221. Results confirmed the loss of the t-butoxycarbonyl function ($-C_4H_8$), which is a characteristic fragment of BMPO, to form the ion m/z 160.0585. The observed ion fragment m/z 114.0544, can be formed by the loss of CH_2O_2, as shown in Fig. A2a.3. In Fig. A2b.1, the spectrum showed the mass m/z 158.0804 and 214.1431 that can be attributed to the $[BMPO + CH_3 –C_4\,H_8 + H]^+$ and $[BMPO + CH_3 + H]^+$, respectively. The most abundant fragment ion (m/z 158.0803) in the MS/MS mode confirmed the formation of $BMPO + CH_3$ adduct, as shown in Fig. A2b.2. The peak m/z 112.0752 can be formed by the loss of CH_2O_2 (Fig. A2b.3). The spectrum in Fig. A2c.1 shows major peaks at m/z 174.0752, 230.1378 and 252.1198, corresponding to $[BMPO + OCH_3 –C_4H_8 + H]^+$, $[BMPO + OCH_3 + H]^+$ and $[BMPO + OCH_3 + Na + H]^+$, respectively. The formation of BMPO-OCH_3 was confirmed in MS/MS by the loss of the t-butoxycarbonyl functional group of BMPO to form the ion at m/z 174.0749 (panels c.2 and c.3).

In addition, the radicals $C_6H_5O_2\cdot$ or $\cdot C_6H_5O_2$ and $C_6H_9O_2\cdot$ or $\cdot C_6H_9O_2$ were detected, although it was not possible to determine whether the chemical structure represented carbon- or oxygen-centered organic radicals using the applied method. Figure A3a.1 shows the formation of protonated ions $[BMPO + C_6H_5O_2 + H]^+$ and $[BMPO + C_6H_5O_2 + Na+H]^+$ with m/z 308.1475 and 330.1298, respectively. The fragmentation in the MS/MS mode confirms the formation of $BMPO + C_6H_5O_2$ (m/z 252.0855) that corresponds to the loss of the characteristic t-butoxycarbonyl function as shown in Fig. A3a.2. The ion fragment observed m/z 128.0702, can be formed by the loss of C_5O_4 (Fig. A3a.3). Figure A3b.1 shows the ion m/z 312.1789, which can be attributed to the $BMPO + C_6H_9O_2$ spin adduct. Figure A3b.2 suggests that the fragmentation of m/z 312.1789 to 256.1166 by the loss of $-C_4H_8$ (Fig. A3b.3).

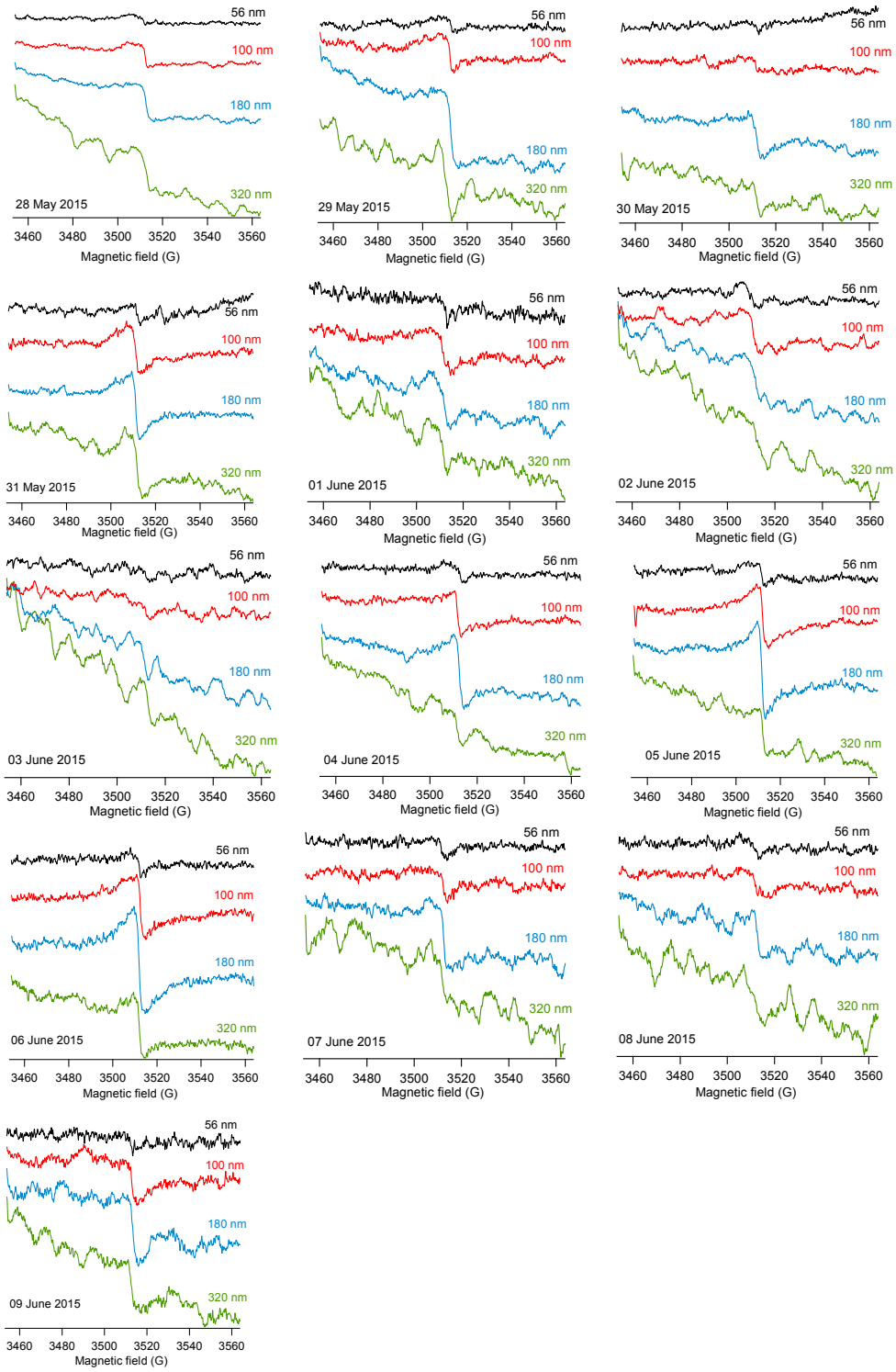

Figure A1. EPR spectra of atmospheric aerosol impactor samples with lower cut-off diameters of 56 nm (black), 100 nm (red), 180 nm (light blue) and 320 nm (green) for the measurement period during 28 May–9 June 2015.

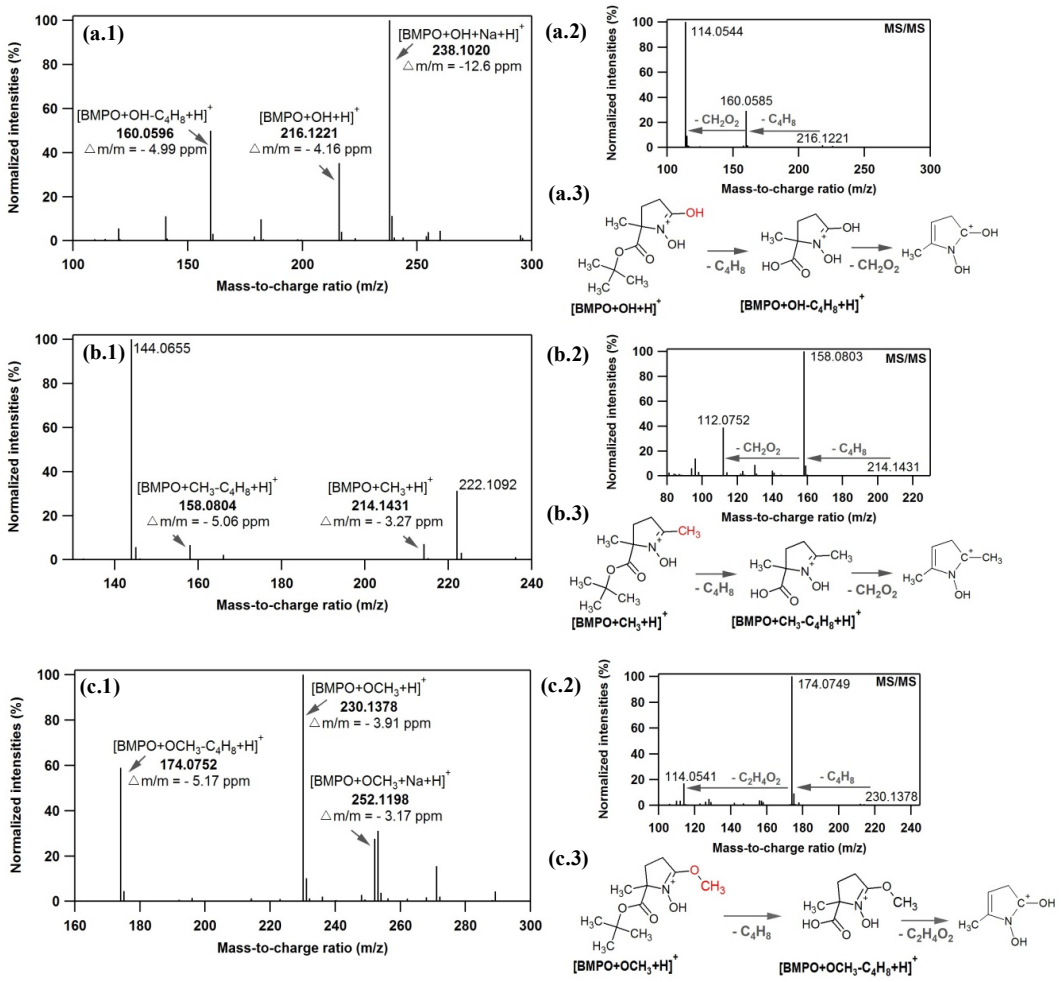

Figure A2. Mass spectra obtained with LC-MS/MS in the positive ionization mode from the mixture of tert-butyl hydroperoxide, p-benzoquinone and BMPO in the presence of iron (solution 1). MS spectra of **(a.1)** BMPO + OH, **(b.1)** BMPO + CH_3 and **(c.1)** BMPO + OCH_3. MS/MS spectra of **(a.2)** BMPO + OH, **(b.2)** BMPO + CH_3 and **(c.2)** BMPO + OCH_3. Proposed fragmentation pathways of **(a.3)** BMPO + OH, **(b.3)** BMPO + CH_3 and **(c.3)** BMPO + OCH_3.

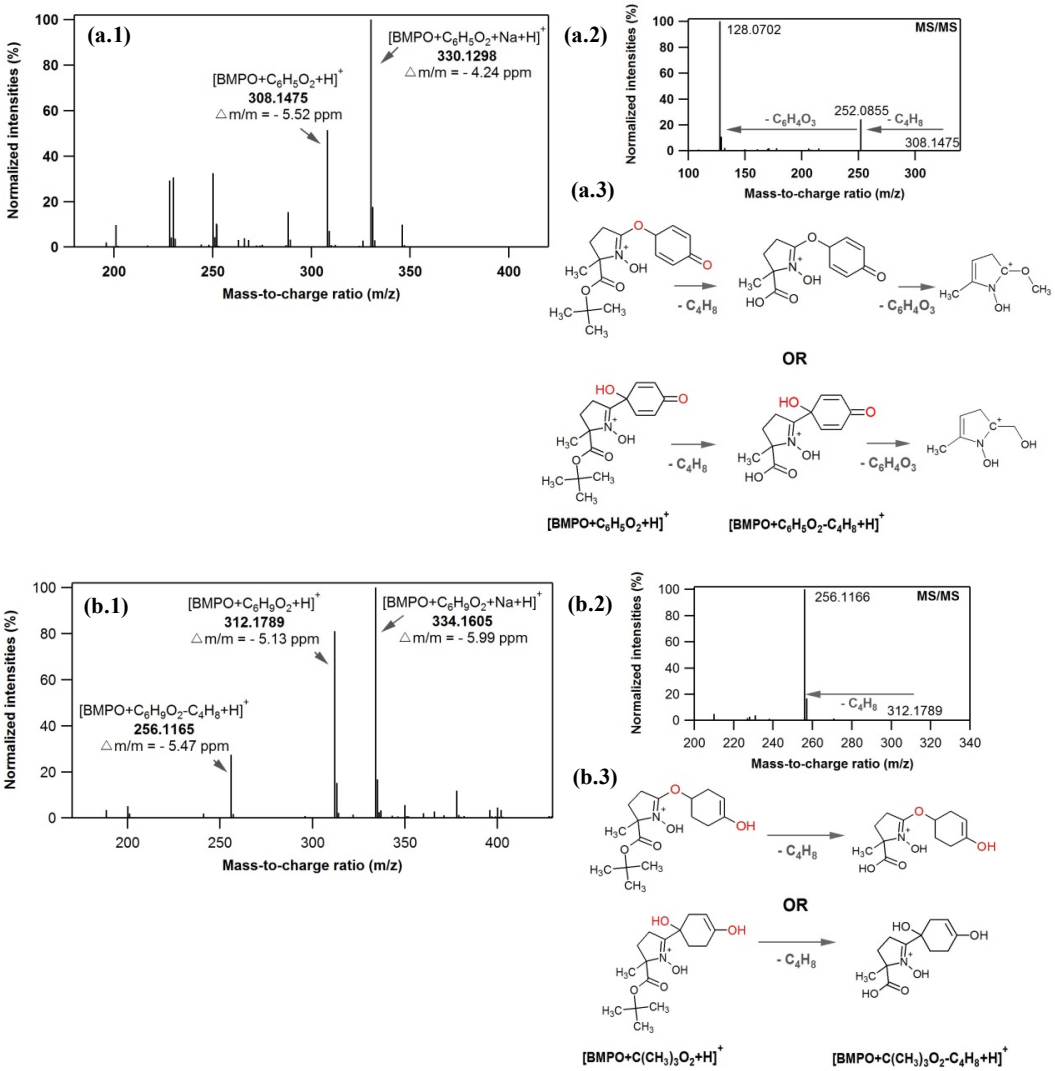

Figure A3. Mass spectra obtained with LC-MS/MS in the positive ionization mode for solution (1). MS spectra of **(a.1)** BMPO + $C_6H_5O_2$ and **(b.1)** BMPO + $C_6H_9O_2$. MS/MS spectra of **(a.2)** BMPO + $C_6H_5O_2$ and **(b.2)** BMPO + $C_6H_9O_2$. Proposed fragmentation pathways of **(a.3)** BMPO + $C_6H_5O_2$ and **(b.3)** BMPO + $C_6H_9O_2$.

Acknowledgements. This study is funded by the Max Planck Society. We thank Christopher Kampf and Fobang Liu for helping with LC-MS analysis and Pascale Lakey for helpful comments.

The article processing charges for this open-access publication were covered by the Max Planck Society.

Edited by: A. Kiendler-Scharr
Reviewed by: four anonymous referees

References

Abbas, K., Hardy, M., Poulhès, F., Karoui, H., Tordo, P., Ouari, O., and Peyrot, F.: Detection of superoxide production in stimulated and unstimulated living cells using new cyclic nitrone spin traps, Free Radical Biol. Med., 71, 281–290, 2014.

Badali, K. M., Zhou, S., Aljawhary, D., Antiñolo, M., Chen, W. J., Lok, A., Mungall, E., Wong, J. P. S., Zhao, R., and Abbatt, J. P. D.: Formation of hydroxyl radicals from photolysis of secondary organic aerosol material, Atmos. Chem. Phys., 15, 7831–7840, doi:10.5194/acp-15-7831-2015, 2015.

Bahrle, C., Nick, T. U., Bennati, M., Jeschke, G., and Vogel, F.: High-Field Electron Paramagnetic Resonance and Density Functional Theory Study of Stable Organic Radicals in Lignin: Influence of the Extraction Process, Botanical Origin, and Protonation Reactions on the Radical g Tensor, J. Phys. Chem. A, 119, 6475–6482, 2015.

Bateman, A. P., Belassein, H., and Martin, S. T.: Impactor Apparatus for the Study of Particle Rebound: Relative Humidity and Capillary Forces, Aerosol Sci. Technol., 48, 42–52, 2014.

Berkemeier, T., Steimer, S., Krieger, U. K., Peter, T., Pöschl, U., Ammann, M., and Shiraiwa, M.: Ozone uptake on glassy, semi-solid and liquid organic matter and the role of reactive oxygen intermediates in atmospheric aerosol chemistry, Phys. Chem. Chem. Phys., 18, 12662–12674, 2016.

Birben, E., Sahiner, U. M., Sackesen, C., Erzurum, S., and Kalayci, O.: Oxidative Stress and Antioxidant Defense, World Allergy Organization Journal, 5, 1–11, 2012.

Bond, T. C., Doherty, S. J., Fahey, D. W., Forster, P. M., Berntsen, T., DeAngelo, B. J., Flanner, M. G., Ghan, S., Karcher, B., Koch, D., Kinne, S., Kondo, Y., Quinn, P. K., Sarofim, M. C., Schultz, M. G., Schulz, M., Venkataraman, C., Zhang, H., Zhang, S., Bellouin, N., Guttikunda, S. K., Hopke, P. K., Jacobson, M. Z., Kaiser, J. W., Klimont, Z., Lohmann, U., Schwarz, J. P., Shindell, D., Storelvmo, T., Warren, S. G., and Zender, C. S.: Bounding the role of black carbon in the climate system: A scientific assessment, J. Geophys. Res.-Atmos., 118, 5380–5552, 2013.

Borrowman, C. K., Zhou, S., Burrow, T. E., and Abbatt, J. P.: Formation of environmentally persistent free radicals from the heterogeneous reaction of ozone and polycyclic aromatic compounds, Phys. Chem. Chem. Phys., 18, 205–212, 2015.

Charrier, J. G. and Anastasio, C.: Impacts of antioxidants on hydroxyl radical production from individual and mixed transition metals in a surrogate lung fluid, Atmos. Environ., 45, 7555–7562, 2011.

Charrier, J. G., McFall, A. S., Richards-Henderson, N. K., and Anastasio, C.: Hydrogen Peroxide Formation in a Surrogate Lung Fluid by Transition Metals and Quinones Present in Particulate Matter, Environ. Sci. Technol., 48, 7010–7017, 2014.

Chen, X. and Hopke, P. K.: A chamber study of secondary organic aerosol formation by limonene ozonolysis, Indoor Air, 20, 320–328, 2010.

Chen, X., Hopke, P. K., and Carter, W. P.: Secondary organic aerosol from ozonolysis of biogenic volatile organic compounds: chamber studies of particle and reactive oxygen species formation, Environ. Sci. Technol., 45, 276–282, 2011.

Cho, A. K., Sioutas, C., Miguel, A. H., Kumagai, Y., Schmitz, D. A., Singh, M., Eiguren-Fernandez, A., and Froines, J. R.: Redox activity of airborne particulate matter at different sites in the Los Angeles Basin, Environ. Res., 99, 40–47, 2005.

Crounse, J. D., Nielsen, L. B., Jørgensen, S., Kjaergaard, H. G., and Wennberg, P. O.: Autoxidation of organic compounds in the atmosphere, J. Phys. Chem. Lett., 4, 3513–3520, 2013.

Daumit, K. E., Carrasquillo, A. J., Sugrue, R. A., and Kroll, J. H.: Effects of Condensed-Phase Oxidants on Secondary Organic Aerosol Formation, J. Phys. Chem. A, 120, 1386–1394, 2016.

Dellinger, B., Pryor, W. A., Cueto, R., Squadrito, G. L., Hegde, V., and Deutsch, W. A.: Role of Free Radicals in the Toxicity of Airborne Fine Particulate Matter, Chem. Res. Toxicol., 14, 1371–1377, 2001.

Dellinger, B., Loninicki, S., Khachatryan, L., Maskos, Z., Hall, R. W., Adounkpe, J., McFerrin, C., and Truong, H.: Formation and stabilization of persistent free radicals, Proc. Combust. Inst., 31, 521–528, 2007.

Docherty, K. S., Wu, W., Lim, Y. B., and Ziemann, P. J.: Contributions of Organic Peroxides to Secondary Aerosol Formed from Reactions of Monoterpenes with O_3, Environ. Sci. Technol., 39, 4049–4059, 2005.

Dou, J., Lin, P., Kuang, B.-Y., and Yu, J. Z.: Reactive Oxygen Species Production Mediated by Humic-like Substances in Atmospheric Aerosols: Enhancement Effects by Pyridine, Imidazole, and Their Derivatives, Environ. Sci. Technol., 49, 6457–6465, 2015.

Ehn, M., Thornton, J. A., Kleist, E., Sipila, M., Junninen, H., Pullinen, I., Springer, M., Rubach, F., Tillmann, R., Lee, B., Lopez-Hilfiker, F., Andres, S., Acir, I.-H., Rissanen, M., Jokinen, T., Schobesberger, S., Kangasluoma, J., Kontkanen, J., Nieminen, T., Kurten, T., Nielsen, L. B., Jorgensen, S., Kjaergaard, H. G., Canagaratna, M., Dal Maso, M., Berndt, T., Petaja, T., Wahner, A., Kerminen, V.-M., Kulmala, M., Worsnop, D. R., Wildt, J., and Mentel, T. F.: A large source of low-volatility secondary organic aerosol, Nature, 506, 476–479, 2014.

Enami, S., Sakamoto, Y., and Colussi, A. J.: Fenton chemistry at aqueous interfaces, P. Natl. Acad. Sci. USA, 111, 623–628, 2014.

Epstein, S. A., Blair, S. L., and Nizkorodov, S. A.: Direct photolysis of α-pinene ozonolysis secondary organic aerosol: effect on particle mass and peroxide content, Environ. Sci. Technol., 48, 11251–11258, 2014.

Ervens, B.: Modeling the Processing of Aerosol and Trace Gases in Clouds and Fogs, Chem. Rev., 115, 4157–4198, 2015.

Fang, T., Verma, V., Bates, J. T., Abrams, J., Klein, M., Strickland, M. J., Sarnat, S. E., Chang, H. H., Mulholland, J. A., Tolbert, P. E., Russell, A. G., and Weber, R. J.: Oxidative potential of ambient water-soluble PM2.5 in the southeastern United States: contrasts in sources and health associations between ascorbic acid

(AA) and dithiothreitol (DTT) assays, Atmos. Chem. Phys., 16, 3865–3879, doi:10.5194/acp-16-3865-2016, 2016.

Fuller, S. J., Wragg, F. P. H., Nutter, J., and Kalberer, M.: Comparison of on-line and off-line methods to quantify reactive oxygen species (ROS) in atmospheric aerosols, Atmos. Environ., 92, 97–103, 2014.

Gehling, W. and Dellinger, B.: Environmentally Persistent Free Radicals and Their Lifetimes in $PM_{2.5}$, Environ. Sci. Technol., 47, 8172–8178, 2013.

Gehling, W., Khachatryan, L., and Dellinger, B.: Hydroxyl radical generation from environmentally persistent free radicals (EPFRs) in $PM_{2.5}$, Environ. Sci. Technol., 48, 4266–4272, 2014.

Gomes, L., Bergametti, G., Dulac, F., and Ezat, U.: Assessing the actual size distribution of atmospheric aerosols collected with a cascade impactor, J. Aerosol Sci., 21, 47–59, 1990.

Gualtieri, M., Mantecca, P., Corvaja, V., Longhin, E., Perrone, M. G., Bolzacchini, E., and Camatini, M.: Winter fine particulate matter from Milan induces morphological and functional alterations in human pulmonary epithelial cells (A549), Toxicol. Lett., 188, 52–62, 2009.

Herrmann, H., Schaefer, T., Tilgner, A., Styler, S. A., Weller, C., Teich, M., and Otto, T.: Tropospheric Aqueous-Phase Chemistry: Kinetics, Mechanisms, and Its Coupling to a Changing Gas Phase, Chem. Rev., 115, 4259–4334, 2015.

Huang, C. H., Ren, F. R., Shan, G. Q., Qin, H., Mao, L., and Zhu, B. Z.: Molecular mechanism of metal-independent decomposition of organic hydroperoxides by halogenated quinoid carcinogens and the potential biological implications, Chem. Res. Toxicol., 28, 831–837, 2015.

Hung, H.-F. and Wang, C.-S.: Experimental determination of reactive oxygen species in Taipei aerosols, J. Aerosol Sci., 32, 1201–1211, 2001.

Jia, H., Nulaji, G., Gao, H., Wang, F., Zhu, Y., and Wang, C.: Formation and Stabilization of Environmentally Persistent Free Radicals Induced by the Interaction of Anthracene with Fe(III)-Modified Clays, Environ. Sci. Technol., 50, 6310–6319, 2016.

Jimenez, J. L., Canagaratna, M. R., Donahue, N. M., Prevot, A. S. H., Zhang, Q., Kroll, J. H., DeCarlo, P. F., Allan, J. D., Coe, H., Ng, N. L., Aiken, A. C., Docherty, K. S., Ulbrich, I. M., Grieshop, A. P., Robinson, A. L., Duplissy, J., Smith, J. D., Wilson, K. R., Lanz, V. A., Hueglin, C., Sun, Y. L., Tian, J., Laaksonen, A., Raatikainen, T., Rautiainen, J., Vaattovaara, P., Ehn, M., Kulmala, M., Tomlinson, J. M., Collins, D. R., Cubison, M. J., Dunlea, E. J., Huffman, J. A., Onasch, T. B., Alfarra, M. R., Williams, P. I., Bower, K., Kondo, Y., Schneider, J., Drewnick, F., Borrmann, S., Weimer, S., Demerjian, K., Salcedo, D., Cottrell, L., Griffin, R., Takami, A., Miyoshi, T., Hatakeyama, S., Shimono, A., Sun, J. Y., Zhang, Y. M., Dzepina, K., Kimmel, J. R., Sueper, D., Jayne, J. T., Herndon, S. C., Trimborn, A. M., Williams, L. R., Wood, E. C., Middlebrook, A. M., Kolb, C. E., Baltensperger, U., and Worsnop, D. R.: Evolution of organic aerosols in the atmosphere, Science, 326, 1525–1529, 2009.

Kampf, C. J., Liu, F., Reinmuth-Selzle, K., Berkemeier, T., Meusel, H., Shiraiwa, M., and Pöschl, U.: Protein Cross-Linking and Oligomerization through Dityrosine Formation upon Exposure to Ozone, Environ. Sci. Technol., 49, 10859–10866, 2015.

Khachatryan, L. and Dellinger, B.: Environmentally Persistent Free Radicals (EPFRs)-2. Are Free Hydroxyl Radicals Generated in Aqueous Solutions?, Environ. Sci. Technol., 45, 9232–9239, 2011.

Khachatryan, L., Vejerano, E., Lomnicki, S., and Dellinger, B.: Environmentally Persistent Free Radicals (EPFRs), 1. Generation of Reactive Oxygen Species in Aqueous Solutions, Environ. Sci. Technol., 45, 8559–8566, 2011.

Kumagai, Y., Arimoto, T., Shinyashiki, M., Shimojo, N., Nakai, Y., Yoshikawa, T., and Sagai, M.: Generation of reactive oxygen species during interaction of diesel exhaust particle components with NADPH-cytochrome P450 reductase and involvement of the bioactivation in the DNA damage, Free Radical Biol. Med., 22, 479–487, 1997.

Lakey, P. S. J., Berkemeier, T., Tong, H., Arangio, A. M., Lucas, K., Pöschl, U., and Shiraiwa, M.: Chemical exposure-response relationship between air pollutants and reactive oxygen species in the human respiratory tract, Sci. Rep., 6, 32916, doi:10.1038/srep32916, 2016.

Lelieveld, J., Evans, J. S., Fnais, M., Giannadaki, D., and Pozzer, A.: The contribution of outdoor air pollution sources to premature mortality on a global scale, Nature, 525, 367–371, 2015.

Lim, Y. B., Tan, Y., Perri, M. J., Seitzinger, S. P., and Turpin, B. J.: Aqueous chemistry and its role in secondary organic aerosol (SOA) formation, Atmos. Chem. Phys., 10, 10521–10539, doi:10.5194/acp-10-10521-2010, 2010.

Lin, P. and Yu, J. Z.: Generation of Reactive Oxygen Species Mediated by Humic-like Substances in Atmospheric Aerosols, Environ. Sci. Technol., 45, 10362–10368, 2011.

Lucas, K. and Maes, M.: Role of the Toll Like Receptor (TLR) Radical Cycle in Chronic Inflammation: Possible Treatments Targeting the TLR4 Pathway, Mol. Neurobiol., 48, 190–204, 2013.

McNeill, V. F., Woo, J. L., Kim, D. D., Schwier, A. N., Wannell, N. J., Sumner, A. J., and Barakat, J. M.: Aqueous-phase secondary organic aerosol and organosulfate formation in atmospheric aerosols: A modeling study, Environ. Sci. Technol., 46, 8075–8081, 2012.

McWhinney, R. D., Zhou, S., and Abbatt, J. P. D.: Naphthalene SOA: redox activity and naphthoquinone gas-particle partitioning, Atmos. Chem. Phys., 13, 9731–9744, doi:10.5194/acp-13-9731-2013, 2013.

Nel, A.: Air pollution-related illness: Effects of particles, Science, 308, 804–806, 2005.

Ouari, O., Hardy, M., Karoui, H., and Tordo, P.: Recent developments and applications of the coupled EPR/Spin trapping technique (EPR/ST), in: Electron Paramagnetic Resonance, The Royal Society of Chemistry, 221 1–40, 2011.

Pavlovic, J. and Hopke, P. K.: Detection of radical species formed by the ozonolysis of α-pinene, J. Atmos. Chem., 66, 137–155, 2011.

Pöhlker, C., Wiedemann, K. T., Sinha, B., Shiraiwa, M., Gunthe, S. S., Smith, M., Su, H., Artaxo, P., Chen, Q., Cheng, Y., Elbert, W., Gilles, M. K., Kilcoyne, A. L. D., Moffet, R. C., Weigand, M., Martin, S. T., Pöschl, U., and Andreae, M. O.: Biogenic potassium salt particles as seeds for secondary organic aerosol in the Amazon, Science, 337, 1075–1078, 2012.

Pope, C. A. and Dockery, D. W.: Health effects of fine particulate air pollution: lines that connect, J. Air Waste Manag. Assoc., 56, 709–742, 2006.

Pöschl, U. and Shiraiwa, M.: Multiphase Chemistry at the Atmosphere–Biosphere Interface Influencing Climate and Pub-

lic Health in the Anthropocene, Chem. Rev., 115, 4440–4475, 2015.

Pryor, W. A., Squadrito, G. L., and Friedman, M.: The cascade mechanism to explain ozone toxicity – The role of lipid ozonation products, Free Radical Biol. Med., 19, 935–941, 1995.

Reinmuth-Selzle, K., Ackaert, C., Kampf, C. J., Samonig, M., Shiraiwa, M., Kofler, S., Yang, H., Gadermaier, G., Brandstetter, H., Huber, C. G., Duschl, A., Oostingh, G. J., and Pöschl, U.: Nitration of the birch pollen allergen Bet v 1.0101: Efficiency and site-selectivity of liquid and gaseous nitrating agents, J. Proteome Res., 13, 1570–1577, 2014.

Saffari, A., Daher, N., Shafer, M. M., Schauer, J. J., and Sioutas, C.: Seasonal and spatial variation in reactive oxygen species activity of quasi-ultrafine particles (PM0.25) in the Los Angeles metropolitan area and its association with chemical composition, Atmos. Environ., 79, 566–575, 2013.

Saffari, A., Daher, N., Shafer, M. M., Schauer, J. J., and Sioutas, C.: Global perspective on the oxidative potential of airborne particulate matter: a synthesis of research findings, Environ. Sci. Technol., 48, 7576–7583, 2014.

Sanchez-Cruz, P., Santos, A., Diaz, S., and Alegria, A. E.: Metal-independent reduction of hydrogen peroxide by semiquinones, Chem. Res. Toxicol., 27, 1380–1386, 2014.

Shaltout, A. A., Boman, J., Shehadeh, Z. F., Al-Malawi, D.-A. R., Hemeda, O. M., and Morsy, M. M.: Spectroscopic investigation of $PM_{2.5}$ collected at industrial, residential and traffic sites in Taif, Saudi Arabia, J. Aerosol Sci., 79, 97–108, 2015.

Shiraiwa, M., Sosedova, Y., Rouviere, A., Yang, H., Zhang, Y., Abbatt, J. P. D., Ammann, M., and Pöschl, U.: The role of long-lived reactive oxygen intermediates in the reaction of ozone with aerosol particles, Nature Chem., 3, 291–295, 2011.

Shiraiwa, M., Selzle, K., Yang, H., Sosedova, Y., Ammann, M., and Pöschl, U.: Multiphase chemical kinetics of the nitration of aerosolized protein by ozone and nitrogen dioxide, Environ. Sci. Technol., 46, 6672–6680, 2012.

Shiraiwa, M., Berkemeier, T., Schilling-Fahnestock, K. A., Seinfeld, J. H., and Pöschl, U.: Molecular corridors and kinetic regimes in the multiphase chemical evolution of secondary organic aerosol, Atmos. Chem. Phys., 14, 8323–8341, doi:10.5194/acp-14-8323-2014, 2014.

Squadrito, G. L., Cueto, R., Dellinger, B., and Pryor, W. A.: Quinoid redox cycling as a mechanism for sustained free radical generation by inhaled airborne particulate matter, Free Radical Biol. Med., 31, 1132–1138, 2001.

Stoll, S. and Schweiger, A.: EasySpin, a comprehensive software package for spectral simulation and analysis in EPR, J. Magn. Reson., 178, 42–55, 2006.

Strak, M., Janssen, N. A., Godri, K. J., Gosens, I., Mudway, I. S., Cassee, F. R., Lebret, E., Kelly, F. J., Harrison, R. M., Brunekreef, B., Steenhof, M., and Hoek, G.: Respiratory health effects of airborne particulate matter: the role of particle size, composition, and oxidative potential-the RAPTES project, Environ. Health Persp., 120, 1183–1189, 2012.

Sueishi, Y., Kamogawa, E., Nakamura, H., Ukai, M., Kunieda, M., Okada, T., Shimmei, M., and Kotake, Y.: Kinetic Evaluation of Spin Trapping Rate Constants of New CYPMPO-type Spin Traps for Superoxide and Other Free Radicals, Z. Phys. Chem., 229, 317–326, 2015.

Tong, H., Arangio, A. M., Lakey, P. S. J., Berkemeier, T., Liu, F., Kampf, C. J., Brune, W. H., Pöschl, U., and Shiraiwa, M.: Hydroxyl radicals from secondary organic aerosol decomposition in water, Atmos. Chem. Phys., 16, 1761–1771, doi:10.5194/acp-16-1761-2016, 2016.

Truong, H., Lomnicki, S., and Dellinger, B.: Potential for Misidentification of Environmentally Persistent Free Radicals as Molecular Pollutants in Particulate Matter, Environ. Sci. Technol., 44, 1933–1939, 2010.

Vejerano, E., Lomnicki, S., and Dellinger, B.: Formation and stabilization of combustion-generated environmentally persistent free radicals on an $Fe(III)_2O_3$/silica surface, Environ. Sci. Technol., 45, 589–594, 2011.

Venkatachari, P., Hopke, P. K., Grover, B. D., and Eatough, D. J.: Measurement of Particle-Bound Reactive Oxygen Species in Rubidoux Aerosols, J. Atmos. Chem., 50, 49–58, 2005.

Venkatachari, P., Hopke, P. K., Brune, W. H., Ren, X., Lesher, R., Mao, J., and Mitchell, M.: Characterization of Wintertime Reactive Oxygen Species Concentrations in Flushing, New York, Aerosol Sci. Tech., 41, 97–111, 2007.

Verma, V., Fang, T., Xu, L., Peltier, R. E., Russell, A. G., Ng, N. L., and Weber, R. J.: Organic Aerosols Associated with the Generation of Reactive Oxygen Species (ROS) by Water-Soluble $PM_{2.5}$, Environ. Sci. Technol., 49, 4646–4656, 2015a.

Verma, V., Wang, Y., El-Afifi, R., Fang, T., Rowland, J., Russell, A. G., and Weber, R. J.: Fractionating ambient humic-like substances (HULIS) for their reactive oxygen species activity – Assessing the importance of quinones and atmospheric aging, Atmos. Environ., 120, 351–359, 2015b.

Wang, D., Pakbin, P., Shafer, M. M., Antkiewicz, D., Schauer, J. J., and Sioutas, C.: Macrophage reactive oxygen species activity of water-soluble and water-insoluble fractions of ambient coarse, $PM_{2.5}$ and ultrafine particulate matter (PM) in Los Angeles, Atmos. Environ., 77, 301–310, 2013.

Wang, Y., Kim, H., and Paulson, S. E.: Hydrogen peroxide generation from alpha- and beta-pinene and toluene secondary organic aerosols, Atmos. Environ., 45, 3149–3156, 2011.

Wang, Y., Arellanes, C., and Paulson, S. E.: Hydrogen Peroxide Associated with Ambient Fine-Mode, Diesel, and Biodiesel Aerosol Particles in Southern California, Aerosol Sci. Technol., 46, 394–402, 2012.

West, J. J., Cohen, A., Dentener, F., Brunekreef, B., Zhu, T., Armstrong, B., Bell, M. L., Brauer, M., Carmichael, G., Costa, D. L., Dockery, D. W., Kleeman, M., Krzyzanowski, M., Künzli, N., Liousse, C., Lung, S.-C. C., Martin, R. V., Pöschl, U., Pope, C. A., Roberts, J. M., Russell, A. G., and Wiedinmyer, C.: "What We Breathe Impacts Our Health: Improving Understanding of the Link between Air Pollution and Health", Environ. Sci. Technol., 50, 4895–4904, 2016.

Winterbourn, C. C.: Reconciling the chemistry and biology of reactive oxygen species, Nature Chem. Biol., 4, 278–286, 2008.

Zhao, H., Joseph, J., Zhang, H., Karoui, H., and Kalyanaraman, B.: Synthesis and biochemical applications of a solid cyclic nitrone spin trap: a relatively superior trap for detecting superoxide anions and glutathiyl radicals, Free Radical Biol. Med., 31, 599–606, 2001.

Zhu, B. Z., Kalyanaraman, B., and Jiang, G. B.: Molecular mechanism for metal-independent production of hydroxyl radicals by

hydrogen peroxide and halogenated quinones, P. Natl. Acad. Sci. USA, 104, 17575–17578, 2007a.

Zhu, B. Z., Zhao, H. T., Kalyanaraman, B., Liu, J., Shan, G. Q., Du, Y. G., and Frei, B.: Mechanism of metal-independent decomposition of organic hydroperoxides and formation of alkoxyl radicals by halogenated quinones, P. Natl. Acad. Sci. USA, 104, 3698–3702, 2007b.

Zhu, B. Z., Shan, G. Q., Huang, C. H., Kalyanaraman, B., Mao, L., and Du, Y. G.: Metal-independent decomposition of hydroperoxides by halogenated quinones: detection and identification of a quinone ketoxy radical, P. Natl. Acad. Sci. USA, 106, 11466–11471, 2009.

Ziemann, P. J. and Atkinson, R.: Kinetics, products, and mechanisms of secondary organic aerosol formation, Chem. Soc. Rev., 41, 6582–6605, 2012.

B.4. Arangio et al., to be submitted

EPR-STICK, a software package for Electron Paramagnetic Resonance spectral processing, simulation and kinetic modeling of spin trapping experiment

Andrea M. Arangio[1], Pascale J. Lakey[1], Haijie Tong[1], Thomas Berkemeier[1], Ulrich Pöschl[1],and Manabu Shiraiwa[1,2]

1 Max Planck Institute for Chemistry, Multiphase Chemistry Department, Mainz, Germany
2 Department of Chemistry, University of California, Irvine, CA, United State

to be submitted.

Authors contributions.

AA, PL and MS designed research. AA performed Experiments, EPR analysis, spectra fitting and simulation. PL, AA and TB performed modeling and parameter optimization. All authors discussed the results. AA and MS wrote the manuscript.

1. Introduction

Free radicals, molecules, atoms and ions with unpaired electrons, are chemical species involved in many chemical transformations and processes in both biological systems and in the atmosphere [1, 2]. Direct detection of free radicals and their reactions are extremely challenging to accomplish due to their extremely high reactivity and their low concentration. Radical reactions typically occur in complex matrices and generate several types of radicals. Therefore, to investigate radical reactions requires sensitive and selective techniques for unambiguous detection, identification and quantification of the radicals involved. Optical techniques including IR, UV-vis, and fluorescence spectroscopies can be applied to detect radicals in simple gaseous matrix [3], but, for more complex matrices their applicability becomes difficult. Continuous wave Electron Paramagnetic Resonance (cw-EPR) spectroscopy is among a few techniques that permit to directly detect and quantify species with unpaired electrons even in complex matrices being sensitive to only paramagnetic species. In practice, EPR has severe limitations in many of its applications. Although EPR spectroscopy is highly sensitive (minimum detectable radical concentration is 10 nM [4]), at room temperature and in liquid solutions, radical concentrations are usually below the instrumental detection limit due to their short chemical life-time. Moreover, EPR is unable to unambiguously distinguish the types of free radical detected directly and therefore it is unable to resolve complex mixtures of free radicals. To overcome these problems two main solutions can be adopted: the Rapid Freeze-Quench (RFQ) technique and the spin-trapping technique. RFQ-EPR is usually applied to isolate enzymatic intermediates for a time scale of milliseconds [5 – 7] and it is useful mainly for qualitative studies. The spin trapping is a versatile, qualitative and quantitative technique that has been successfully applied to study free radicals reactions also involving Reactive Oxygen Species (ROS) in several fields [8 – 11]. The technique is an indirect analytical method based on the reaction between a target radical and a molecular probe containing a nitrone or nitroso functional group that produces long-lived nitroxide radicals upon reaction [10]. The nitroxide adducts formed by trapping the target radical accumulates in concentration until it can be detected

and quantified using conventional EPR at room temperature and in liquid solution. For nitrone-based spin traps, the radical adds directly to the carbon adjacent to the nitrogen of the nitrone group. Nuclei with nuclear magnetic moments eventually present in the vicinal positions to the nitroxide group generates peculiar magnetic properties, such as the hyperfine splitting; this causes the absorption EPR signal to have a precise pattern depending on the species trapped. Among others, 5,5-dimethyl-1-pyrroline N-oxide (DMPO) and 5-tert-butoxycarbonyl 5-methyl-1-pyrroline N-oxide (BMPO) are widely used spin-trap agents because of their higher redox stability compared to other nitrone based spin-traps. Moreover, they can form radical-adducts with several N-, S-, C- and O- centered radicals with very distinguishable EPR spectra, allowing the identification of a wide range of radical intermediates [11]. An advantage of using BMPO compared to DMPO is its ability to form a much more stable radical adduct with superoxide (BMPO/$^{\cdot}$OOH, $t_{1/2}$ = 23 min, DMPO/$^{\cdot}$OOH, $t_{1/2}$ = 45 s) with a higher signal-to-noise ratio compared to DMPO [11].

Although spin-trapping experiments are practically and conceptually rather easy to accomplish, interpretation and analysis of results remain a difficult task that could lead to erroneous and misleading conclusions. Radical reactions usually generate complex mixtures of radicals that are cumulatively trapped with different kinetics [12, 13] and generate intricate EPR spectra that evolve over time according the chemical stability of each radical adduct. Morever, in a spin trapping experiment, radical adducts concentrations should be determined once the steady-state concentrations for all radical-adducts has been reached. However, depending on the chemical environment and on the initial concentrations of reactants and the spin-trap agent, radical-adduct concentrations can be severely affected by secondary reactions. Indeed, free radicals and redox active transition metals can reduce the nitroxide radicals to the corresponding EPR-silent products, leading to underestimate the actual radical concentrations [14].

Simulation and fitting of experimental spectra are powerful tools used to gain more information about the system under investigation [15]. Complex EPR spectra resulting from a mixture of radical-adducts can be simulated to separate and eventually quantify singular

contributions. EasySpin is among the most commonly used toolbox to simulate and fit EPR spectra [16]. EasySpin allows a wide range of simulation and fitting options including scaling and least-squares fitting of experimental spectra with several optimization methods [17]. Despite its flexibility, EasySpin usage remains unpractical for inexperienced users and inefficient for expert users who want to carry out routine analysis on large experimental datasets. Moreover, with EasySpin it is not possible to perform radical quantifications and analyze the time evolution of EPR spectra which is crucial for kinetics studies and interpretation of spin-trapping experiments.

In this work we propose EPR-STICK (Electron Paramagnetic Resonance for Spin TrappIng Chemical Kinetics), a MATLAB toolbox, based on EasySpin, planned to facilitate the interpretation of spin trapping EPR experiments. The toolbox includes a user-friendly interface that allows users to easily process, fit and simulate experimental EPR spectra and includes modules for signal-to-noise optimization, baseline correction, spectrum integration for radical quantification and a kinetic module to study kinetics of radical reaction. To illustrate the applicability of EPR-STICK, experiments were carried out to investigate the kinetics of the spin trapping, the yield and efficiency of radical-adducts formed upon Fenton-like decomposition of tert-butyl-hydroperoxide catalyzed by iron ions in presence of BMPO. The kinetic parameters such as kinetic rate constant for radical production, trapping, and adduct decomposition reactions were determined by a global-optimization algorithm.

2. EPR-STICK description

EPR-STICK is a MATLAB toolbox which allows fast and easy EPR spectra processing, radical quantification, simulation, fitting and kinetic modeling of spin trapping EPR experimental data. Through a Graphic User Interface (GUI) users can perform the entire analysis directly in EPR-STICK or by using each functionality as a standalone tool.

2.1. Signal Processing and Quantification

Files containing instrumental parameters and 2D or 3D EPR spectra can be loaded and plotted directly in the GUI. The user can then easily smooth noisy spectra by applying filters, including a moving average, binomial, flat and Savitzky-Golay filter, which are already optimized to maximize the signal-to-noise ratio.

Before starting to quantify the number of radicals or to fit experimental EPR spectra, it is good practice to correct the spectral baseline. EPR-STICK includes both a simple and fast linear correction of the spectral baseline, perfect to be perform before fitting, and a more advanced and accurate module to correct the first integral of the spectrum. The advanced mode includes a polynomial baseline fitting to be applied on spectral region selected through the automatic peak recognition function or by manual selection in case high accuracy is requested.

After the baseline correction, single and double integrations operations can be easily applied to the entire spectrum to evaluate the double integral (DI), that is, the area underneath the first integral of the original EPR spectrum. DI is the key value for radical quantification being proportional to the absolute number of radicals in the sample. The two quantities are related by the following equation [18]:

$$\mathrm{DI} = c \cdot \left[G_R \cdot C_t \cdot n \right] \cdot \left[\frac{\sqrt{P} \cdot B_m \cdot Q \cdot n_B \cdot S \cdot (S+1) \cdot n_S}{f(B_1, B_m)} \right] \qquad (1)$$

where the *receiver gain* (G_R), *conversion time* (C_t), *number of scans* (n), *microwave power* (P), *modulation amplitude* (B_m), *quality factor* of the resonator (Q) and *spatial distribution of the microwave field and the modulation field* experienced by the sample ($f(B_1, B_m)$) are instrumental parameters and the *Boltzmann factor* for temperature dependence (n_B), *total electron spin* of the species in the sample (S) and the *total number of spins* (n_S) are experimental parameters.

Instrumental parameters c, G_R , C_t, n and $f(B_1, B_m)$ are usually held constant during an entire or even multiple experimental sessions and their product can be gathered together in a single

constant K determined by signal calibration. For spin-trapping experiments 4-hydroxy-2,2,6,6-tetramethylpiperidin-1-oxyl (TEMPOL) can be used as a standard as it is also a nitroxide-based stable radical with molecular structure and magnetic properties similar to radical-adducts formed by BMPO. For the calibration, users can choose the standard compound that better fits their experimental conditions. The relative calibration curve can then be stored in the toolbox. Equation 1 can be simplified as follows:

$$DI = K \cdot \sqrt{P} \cdot B_m \cdot Q \cdot n_B \cdot S \cdot (S + 1) \cdot n_S \qquad (2)$$

parameters P, B_m, Q, n_B and S are loaded in together with the EPR spectrum under investigation, for simplicity, we included them in a second constant $H = K \cdot \sqrt{P} \cdot B_m \cdot Q \cdot n_B \cdot S \cdot (S + 1)$. The relationship between DI and the number of spins is reduced to:

$$DI = H \cdot n_s \qquad (3)$$

it should be noted that calibration of the constant H are not necessary as it contains instrumental parameters that are loaded in the toolbox from the experimental file and are specific for the spectrum under analysis.

2.2. Simulation and fitting

EPR spectra simulations of radical-adducts are performed through the *garlic* function from EasySpin which computes isotropic and fast-motional cw-EPR spectra of radicals in solution [15]. The *garlic* function requires two inputs. The first input defines the experimental conditions and includes the resonance frequency and the magnetic field range swept. The second input defines the magnetic and spectral features of the spin system to simulate. It includes hyperfine coupling

constants of all magnetically active nuclei in the molecule (e.g. A_N, A_H, in MHz), g-factors (g), peak-to-peak distances (lwpp) and weights of contributions of each radical to the total spectrum (w).

The least-squares fitting of experimental spectra is carried out by tuning one or more magnetic and spectral parameters of each spin system. For this purpose the *esfit* function in EasySpin contains a wide range of optimization methods including global (Genetic Algorithm, Monte Carlo, Particle Swarm, Grid Search) and local (Simplex, Levenberg/Marquardt) optimization algorithms [16]. In spin-trapping experiments only a restricted number of radical-adducts are expected and a relatively small number of magnetic and spectral parameters needs to be optimized. Therefore, the fitting procedure in EPR-STICK is restricted to one local optimization algorithm and initial values of magnetic and spectral parameters of the radical-adducts are contrained. A local and editable library stores the literature values for magnetic and spectral parameters of the most common radical-adducts. These values are automatically loaded once EPR-STICK is launched. The user selects the most appropriate radical-adducts for fitting the experimental spectrum and the parameters to be optimized. The simplex optimization algorithm quickly finds the local minimum of the error function. The fitting procedure can be further constrained to optimize parameters of the same type but related to different radical-adducts (e.g. w_1 for adduct 1 and w_2 for adduct 2 are optimized together, but w_1 and g_1 are not). All parameters can be optimized in one single step by selecting the automatic procedure in which all g's, lwpp's and w's are optimized in sequence. In this case, at the end of the optimization of one group of parameters, the automatic procedure calculates the resulting root mean square of the standard deviation (RMSD) and evaluates the goodness of the fitting. The procedure will continue until the difference of the RMSDs of two sequential optimization steps is less than a tolerance value (default value 10^{-4}). Although the default fitting procedure is severely constrained, the user can also run the more flexible easyfit function in EasySpin. The concentration of each radical-adduct are then automatically evaluated by simulating and double integrating the corresponding EPR spectrum.

2.3. Kinetic model

Free radical concentrations estimated from spin-trapping experiments depend on trapping reactions, experimental conditions, chemical environment and the reaction time. The influence of each of these factors on spin-adduct concentrations can heavily affect the final concentration. A good strategy to keep under control secondary reactions consists in monitoring the time evolution of resulting EPR spectra. At each time step the spectrum can be fitted, and simulated to separate each single contributor to the total spectrum and finally, the concentration curve of each species can be plotted. The concentration evolution can be modeled in EPR-STICK through the kinetic module. Through this model users can explicitly study the radical and the trapping reaction involved in the system under investigation. The time evolution of the concentrations of each single radical-adduct can be simulated and information such as trapping efficiency and yield under user defined experimental conditions can be extrapolated. The kinetic module consists of a box model and requires as inputs the schema which can be as complex as the user requires and includes three parts: 1) a list of all species involved in the reaction mechanism and their initial concentrations; 2) a list of rate equations and rate constants; 3) a list of the loss and production terms for each species to be inserted in the differential equation. Once the reaction time has been assigned, differential equations are solved to evaluate the concentration of each reactant, intermediate and product at each time step. The user can then simulate the EPR spectrum at a selected time. The model output is plotted directly in the GUI according to the user instructions.

3. Experimental Materials and Method

Solutions of reactants were prepared by adding 10, 50, 100, 200 μL of 100mM of tert-butyl-hydroperoxide (Luperox® TBH70X, 70 wt. % H_2O, Sigma-Aldrich) and 1 μL of 1 mM iron sulfate heptahydrate (99.0%, Sigma-Aldrich) to milli-Q water containing 5-tert-butoxycarbonyl 5-methyl-

1-pyrroline N-oxide (BMPO) (>99%, Enzo Life Science) obtaining solutions with final volumes of 600 μL. The final concentrations of each reactant were 30 mM for BMPO, 1 μM for Fe(II) and 4, 8, 16, 33 mM for TBH. For each experiment fresh solutions of BMPO, iron and TBH were prepared. After mechanical stirring, 20 μL aliquots were immediately injected into 50 μL capillaries with 0.9 mm I.D. The capillary was inserted in a high sensitivity cavity of a continuous-wave electron paramagnetic resonance (CW-EPR) X-band spectrometer (EMXplus-10/12; Bruker Corporation). The resulting EPR spectrum was monitored for 30 min starting from the capillary insertion in the cavity by recording a total of 6 spectra. The time between mixing and inserting the capillary in the cavity (~ 2 min) was also monitored and added to the final experimental time. Each experiment was performed at room temperature (23 °C) and the EPR instrumental parameters were set as follows: modulation frequency of 100 kHz; microwave frequency of 9.866 GHz, microwave power of 13.44 mW (12 db), modulation amplitude of 1.0 G, sweep width of 100.0 G, sweep time of 50 s, receiver gain of 40 db, time constant of 0.01 ms, conversion time of 25.09 ms and scan number of 6 per each spectrum.

4. Results and discussion: Application

The black line in Figure 1 shows the EPR spectrum obtained at 30 min of reaction time for the solution containing 33 μM TBH, 1 μM Fe(II) and 30 mM BMPO. The experimental spectrum is composed of several overlapping lines originating from spin-adducts formed upon trapping of $^{\cdot}OH$ (blue), $O_2^{\cdot-}$ (orange), and carbon-centered (green) radicals. The simulated and fitted EPR spectrum (red) reproduced the experimental spectrum very well as shown by the small residuals (grey). The fitting was performed by applying the automatic procedure of EPR-STICK and consists of sequential optimizations of g-factor's, lwpp's and weight's of all radical-adducts by using the simplex algorithm with tolerance level of 10^{-4} for the RMSD.

Spectral and magnetic properties of each spin system resulting from the fitting were used to simulate singular EPR spectra and to evaluate the corresponding DI and radical-adduct

concentration. The error in the final concentrations was estimated from the area underneath the residual line obtained by subtraction of the first integral of the simulated spectrum from the first integral of the experimental spectrum. Using this methodology the error on the final concentration ranges from 12 to 20 % and includes the fitting error, baseline correction and spectral signal-to-noise.

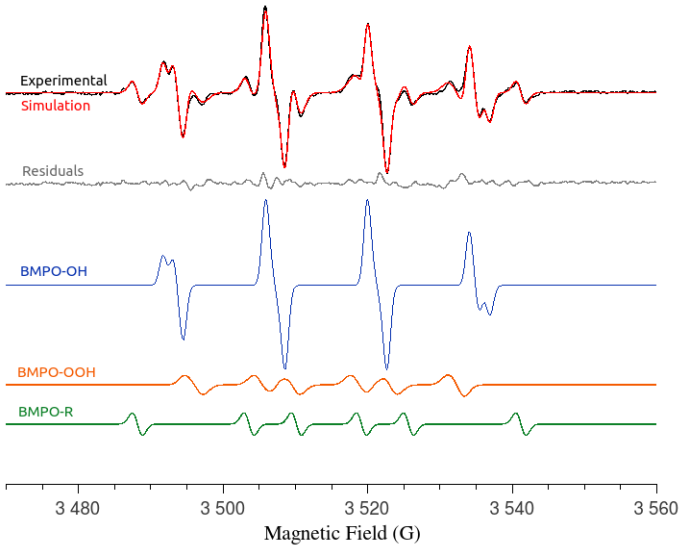

Figure 1: EPR spectrum (black) of reaction mixture containing 33 mM of TBH, 1 µM Fe(II) and 30 mM BMPO recorded at 30 min of reaction, the corresponding fitted spectrum (red) and the residual resulting from the fitting (grey). The trapped $^{\cdot}OH$ (blue), $O_2^{\cdot-}$ (orange) and carbon-centered radical (green) used in the fitting curve are also shown.

The fitting and deconvolution procedure described above was applied to all EPR spectra obtained from four different experiments where the TBH concentrations were 4, 8, 16, and 33 mM. The time evolution of concentrations for BMPO-OH (blue), BMPO-OOH (orange) and carbon-centered radicals, BMPO-R (green) resulting from each experiment are reported by the circles shown in Figure 2.

The time evolution of radical-adduct concentrations shown by the solid lines in Figure 2 were simulated by using the kinetic box model described in Section 2.3 and take into account the reactions reported in Table 1. Kinetic model parameters were estimated with the MonteCarlo and Genetic Algorithm (MCGA) global optimization procedure followed by a simplex optimization algorithm. This optimization procedure is described in Berkemeier et al. [19 - 21]. The resulting rate

constants are also reported in Table 1 together with the additional constrained and unconstrained kinetic parameters used in the model.

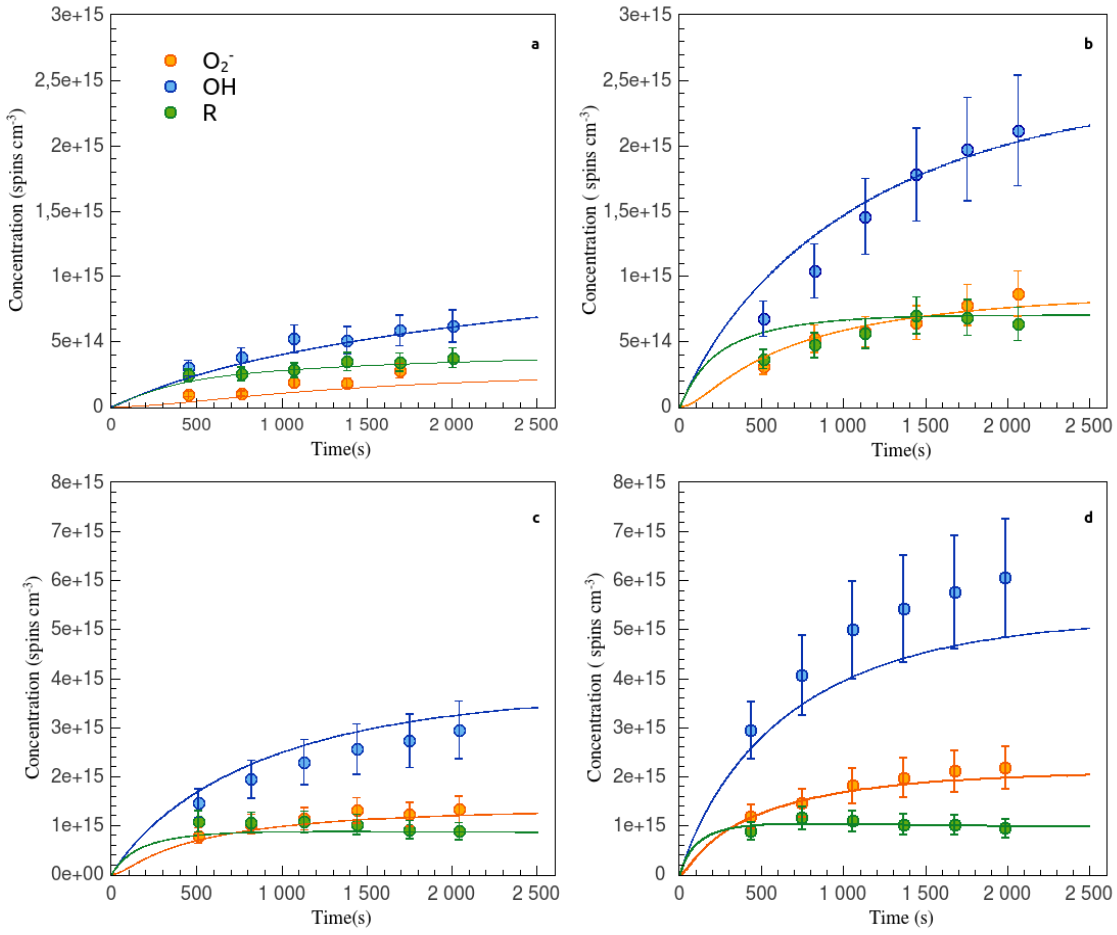

Figure 2: Time evolution of BMPO-OH (blue), BMPO-OOH (orange) and BMPO-R (green) concentrations obtained from reaction mixtures containing 1 µM Fe(II), 30 mM BMPO and 4 mM (a), 8 mM (b), 16 mM (c) and 33 mM (d). Circles are experimental data, solid lines are calculated from modelling.

The kinetic parameters resulting from fitting experimental data were further used to calculate the trapping efficiency and yield during experiments and in simulated conditions obtained by modify the initial concentration of BMPO. The trapping efficiency and yield are useful quantities for optimization of experimental conditions and evaluation of chemical stability of radical-adducts. Initial concentrations of reagents, the spin-trap and free radicals strongly affect the concentrations and stability of radical-adducts formed [22]. The trapping efficiency compares the fraction of radicals in the trapped form with the total concentration of radicals according to Equation 4:

$$\text{Efficiency}_{\text{radical-adduct}} = \frac{[adduct]}{[adduct]+[free\ radical]} \times 100 \qquad (4)$$

Equation 4 neglects reactions of free radicals with species other than the spin-trap agent. Considering a radical X and a second species Y, this assumption is valid as long as the quantity [BMPO] × k_{BMPO-X} > [Y] × k_{Y-X} × 10, to avoid to underestimate the efficiency by the 10%. At the working concentration of BMPO during the experiment this condition is held for all species. Figure 3 shows the time evolution of the trapping efficiency of ·OH (blue), $O_2^{\cdot-}$ (orange), and carbon-centered radical R (green). The reactant concentrations were 33 mM of TBH, 1 μM of Fe(II) and BMPO concentrations spanning from 30 μM to 300 mM. At reaction times in the millisecond scale and with the exception of BMPO-OH, radical-adduct concentrations are negligible compared to the concentrations of corresponding free radicals. As the reaction proceeds, the production of free radicals increases and the trapping reactions become effective. The efficiency increases with the production rate of the adduct which depends on the type of radical and the initial concentration of BMPO. The trapping efficiency for ·OH goes up to 100% almost instantaneously, whereas the trapping efficiency of $O_2^{\cdot-}$ and R· increase relatively slowly with time, with the R· trapping efficiency increasing faster than $O_2^{\cdot-}$. Both radical species are sensitive to the initial concentration of BMPO. The almost instantaneous increase of ·OH trapping efficiency reflects the fast and quantitative trapping reaction of the free radical even at low BMPO concentrations ($k_{BMPO+OH}$ = 8.0 × 10^{-11} cm^3 s^{-1}, k_{BMPO+R} = 1.6 × 10^{-15} cm^3 s^{-1}, $k_{BMPO+OOH}$ = 1.1 × 10^{-16} cm^3 s^{-1}). Once the trapping efficiency reaches a value of about 100%, free radical concentrations are negligible compared to radical-adduct concentrations. Although $O_2^{\cdot-}$ and R· reach efficiency values of 100% later than ·OH, they seem to still be fast within the experimental time scale, reaching 100% of efficiency in tenths of seconds and, at the latest, within the first 2 minutes for $O_2^{\cdot-}$ at a BMPO concentration of 30 μM. It worth noting that even though one tenth of second is not an issue in the experimental time scale, on the time scale of a radical reaction it can lead to an underestimation of the free radical concentration because of secondary reactions.

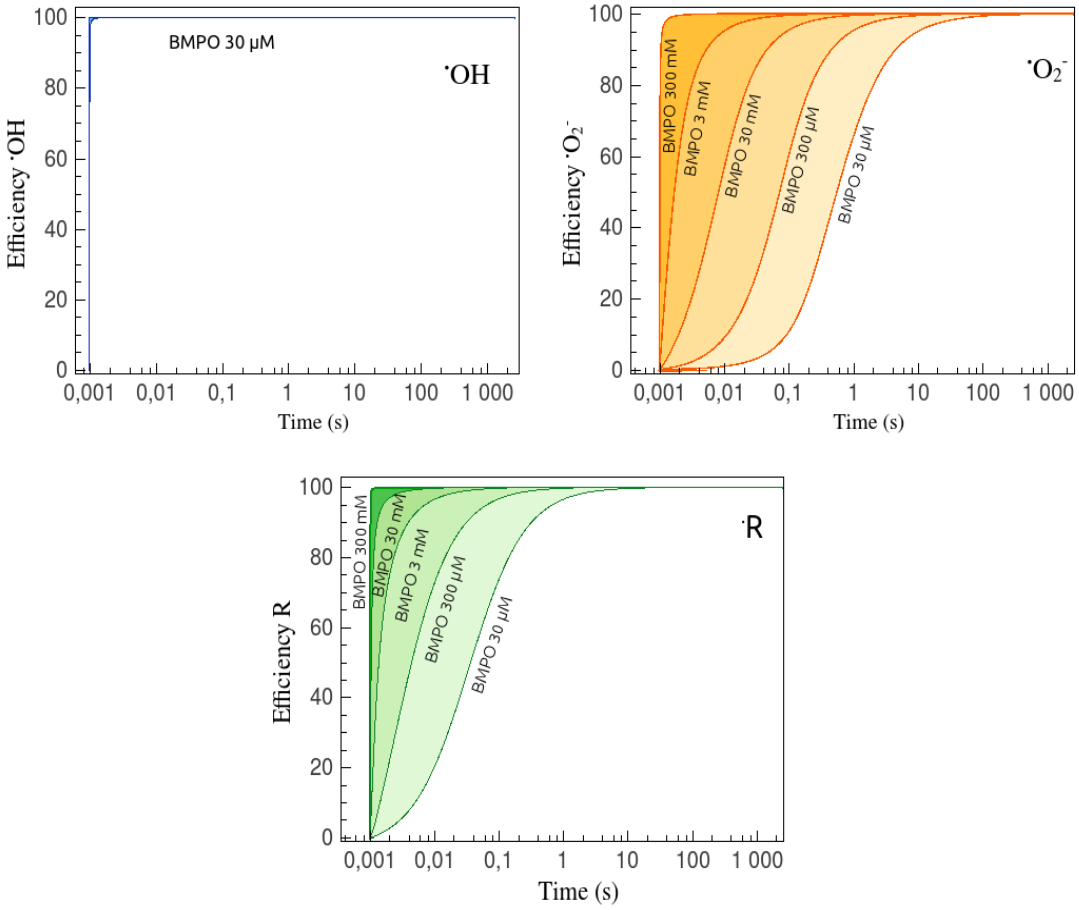

Figure 3: Model calculation of the time evolution of the efficiency for BMPO-OOH at TBH concentration of 33 mM, 1 µM Fe(II) and BMPO initial concentration ranging from 30 µM (light orange) to 300 mM (dark orange) .

Secondary reactions and decays of radical-adducts are not taken into account in the trapping efficiency as described in Equation 4. To take into account the impact of these reactions on the final radical-adducts concentrations the trapping yield η can be calculated as follow:

$$\eta = \frac{[adduct]_{actual}}{[adduct]_{theoretical\,max}} \times 100 \qquad (5)$$

where the numerator is the actual concentration of radical-adduct considering radical-adduct losses, whereas at the denominator is the maximum theoretical concentration of radical-adducts resulting when all radical-adduct losses are null. Figure 4 shows the time evolution of η for BMPO-OH (blue), BMPO-OOH (orange) and BMPO-R (green) adducts. The dark and light colored areas correspond to two regions of η where the TBH concentration was held constant at 33 mM (dark

areas) and 4 mM (light areas) and initial BMPO concentrations were varied between 30 µM (black line) and 300 mM (red line). Fe(II) concentration was held constant at 1 µM.

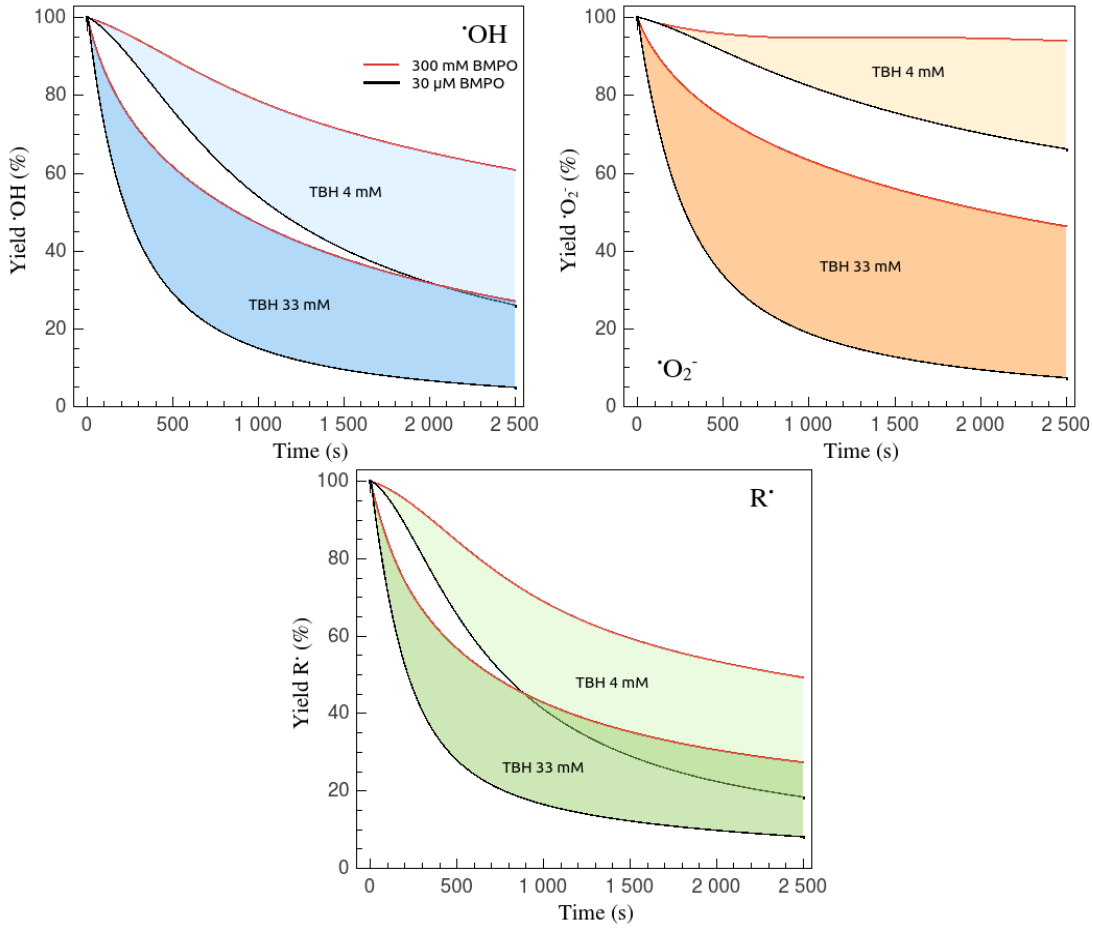

Figure 4: Time evolution of η for BMPO-OH (blue), BMPO-OOH (orange) and BMPO-R (green) from reaction mixtures containing 1 µM Fe(II), 4 mM (light colors) and 33 mM (dark colors) of TBH and initial concentration of BMPO in the range of 30µM (black) to 300 mM (red).

As defined above, η corresponds to the fraction of spin-adduct remaining after secondary reactions or decay take place and it depends on the difference in the initial concentration between the spin trap and TBH. At TBH concentrations of 33 mM and BMPO 30 µM (black lines below dark areas), η for all radical-adducts is about 25% after 10 min (600 s) and decreases down to 10% after 30 min (1800 s) of reaction. These values rises to 65 – 95 % at 10 min (600 s) and 30 – 75% at 30 min (1800 s) at 4 mM TBH concentration (black lines light areas). At BMPO concentrations of 300 mM, η reaches much higher values ranging from 60 to 95% after 10 min (600 s) of reaction and 40 an 95 % after 30 min (1800 s). This values confirm that at higher BMPO concentrations,

compared to TBH, a lower fraction of radical-adducts are destroyed over time. In the experiment described above, η never reaches 100% for all radical-adducts, even if 300 mM of BMPO are used. As reported in Table 1, there are two types of reactions that destroy radical-adducts, the reaction between adducts and free radicals and the reaction between adducts and iron. As BMPO concentrations increase, the contribution of radical-adduct losses due to the first type of reactions are weaker as less free radicals are available. At high BMPO concentrations, reactions of the second type are faster as radical-adducts concentrations increase. The reactions between radical-adducts and iron prevent η from reaching the 100%.

5. Conclusions

In this work we presented a new MATLAB toolbox which has been developed to simplify data processing, simulations and interpretations of spin-trapping EPR experiments. Combined with data processing, quantification, fitting and simulation tools, EPR-STICK has an additional kinetic module which allows users to study radical reaction mechanisms and to optimize experimental conditions. Trapping efficiency and yield can be evaluated and used to explore the trapping reactions and improve precision and accuracy of free-radical quantification by spin-trapping technique.

EPR-STICK has been applied to explore the kinetics of the trapping reaction of radicals formed during the TBH decomposition catalyzed by Fe(II) in the presence of the spin-trapping agent BMPO. The experimental spectra were processed to separate each radical-adduct contribution and estimate each radical concentration at each time step. To gain insights in the reaction mechanism, the experimental time evolution of all of the radical-adduct concentrations were simulated and fitted by using a global optimization procedure (MCGA). The resulting kinetic parameter were used to evaluate the trapping efficiency and yield. In the case study, we show that high BMPO concentrations are desirable for quantification purposes as all free radicals are almost instantaneously trapped and radical-adducts decompositions are minimized. However, very high

BMPO concentrations could accelerate radical-adduct decomposition due to reactions with species having constant concentrations over the reaction time (e.g. Fe^{2+} and Fe^{3+}).

Table 1: List of reactions and kinetic parameters optimized with MCGA and simplex algorithm.

Model reaction number	Reaction	Rate constant (s^{-1} or $cm^3\ s^{-1}$)	Reference and comment
3	$Fe^{2+} + O_2 \rightarrow O_2^- + Fe^{3+}$	4.8×10^{-22}	Determined from global optimization
4	$Fe^{2+} + O_2^- + 2H^+ \rightarrow Fe^{3+} + H_2O_2$	3.0×10^{-14}	20
5	$Fe^{2+} + H_2O_2 \rightarrow Fe^{3+} + OH^- + OH$	4.0×10^{-18}	20
6	$Fe^{2+} + OH \rightarrow Fe^{3+} + OH^-$	5.0×10^{-13}	24
7	$Fe^{3+} + H_2O_2 \rightarrow Fe^{2+} + HO_2 + H^+$	1.0×10^{-24}	25
8	$Fe^{3+} + HO_2 \rightarrow Fe^{2+} + O_2 + H^+$	3.0×10^{-18}	26
11	$H_2O_2 + OH \rightarrow H_2O + HO_2$	5.5×10^{-14}	27
12	$OH + OH \rightarrow H_2O_2$	8.6×10^{-12}	28
13	$OH + HO_2 \rightarrow H_2O + O_2$	1.2×10^{-11}	28
14	$HO_2 + HO_2 \rightarrow H_2O_2 + O_2$	1.4×10^{-15}	26
15	$H_2O_2 + HO_2 \rightarrow H_2O + O_2 + OH$	5×10^{-21}	29
16	$HO_2 + O_2^- \rightarrow H_2O_2 + OH^- + O_2$	1.7×10^{-13}	26
17	$O_2^- + OH \rightarrow O_2 + OH^-$	1.3×10^{-11}	30
18	$HO_2 \rightarrow Hplus + O_2^-$	2.3×10^{5}	31
19	$H^+ + O_2^- \rightarrow HO_2$	1×10^{-11}	32
23	$ROOH + Fe^{2+} \rightarrow OH + RO^- + Fe^{3+}$	1.0×10^{-24}	33
24	$ROOH + Fe^{2+} \rightarrow OH^- + RO + Fe^{3+}$	4.5×10^{-22}	Determined from global optimization
25	$RO \rightarrow R$	1.7×10^{5}	Determined from global optimization
26	$RH + OH \rightarrow R + H_2O$	1.0×10^{-15}	Determined from global optimization
27	$ROOH + HO_2 \rightarrow ROH + O_2 + OH$	5.0×10^{-21}	Assumed to be the same as for H_2O_2 (R15)
28	$ROOH + Fe^{3+} \rightarrow Fe^{2+} + HO_2 + H^+$	6.7×10^{-22}	Determined from global optimization
30	$ROOH + OH \rightarrow ROO + H_2O$	2.3×10^{-12}	Determined from global optimization
31	$R + O_2 \rightarrow ROO$	2.0×10^{-15}	Determined from global optimization
32	$ROO + OH^- \rightarrow RH + O_2^- + H_2O$	1.0×10^{-12}	Determined from global optimization
34	$ROO + HO_2 \rightarrow ROOH + O_2$	1.4×10^{-15}	34
35	$ROO + O_2^- + H+ \rightarrow ROOH + O_2$	1.5×10^{-13}	34
36	$BMPO + OH \rightarrow BMPO\text{-}OH$	8.0×10^{-11}	Determined from global optimization
37	$BMPO + O_2^- \rightarrow BMPO\text{-}OO^-$	1.1×10^{-16}	Determined from global optimization
38	$BMPO + HO_2 \rightarrow BMPO\text{-}OOH$	1.1×10^{-16}	Assumed to be the same as for O_2^- (R37)
39	$BMPO + RO \rightarrow BMPO\text{-}OR$	1.1×10^{-16}	Assumed to be the same as for O_2^- (R37)
40	$BMPO + R \rightarrow BMPO\text{-}R$	1.6×10^{-15}	Determined from global optimization
41	$ROO + ROO \rightarrow 2RO + O_2$	3.0×10^{-17}	Determined from global optimization
42	$ROO + BMPO \rightarrow BMPO\text{-}OOR$	1.1×10^{-16}	Assumed to be the same as for O_2^- (R37)
49	$BMPO\text{-}OOH \rightarrow Product$	1×10^{-4}	Determined from global optimization
50	$BMPO\text{-}O_2^- \rightarrow Product$	1×10^{-4}	Assumed to be the same as for OOH (R49)

51	BMPO-OOR → Product	1×10^{-4}	Assumed to be the same as for OOH (R49)
52	BMPO-R → Product	1×10^{-4}	Determined from global optimization
53	BMPO-OH → Product	1×10^{-4}	Assumed to be similar to R (R52)
54	BMPO-OR → Product	1×10^{-4}	Assumed to be similar to R (R52)
55	ROOH → RO + OH	5.8×10^{-7}	Determined from global optimization
56	BMPO-OOH + Fe^{3+} → Fe^{2+} + Product	1.0×10^{-19}	35
57	BMPO-O_2^- + Fe^{3+} → Fe^{2+} + Product	1.0×10^{-19}	Assumed to be the same as for OOH (R56)
58	BMPO-OOR + Fe^{3+} → Fe^{2+} + Product	1.0×10^{-19}	Assumed to be the same as for OOH (R56)
59	BMPO-R + Fe^{3+} → Fe^{2+} + Product	4.1×10^{-18}	Determined from global optimization
60	BMPO-OH + Fe^{3+} → Fe^{2+} + Product	1.9×10^{-18}	Determined from global optimization
61	BMPO-OR + Fe^{3+} → Fe^{2+} + Product	1.1×10^{-18}	Determined from global optimization
62	R + Fe^{2+} → Fe^{3+} + Product	2.1×10^{-11}	Determined from global optimization
63	R + Fe^{3+} → Fe^{2+} + Product	1.0×10^{-12}	36
64	RO_2 + Fe^{2+} → Fe^{3+} + Product	1.0×10^{-15}	37
65	RO_2 + Fe^{3+} → Fe^{2+} + Product	4.5×10^{-14}	37
66	R + R → Product	1.0×10^{-12}	38
67	OR + OR → Product	3.3×10^{-13}	39
68	RO_2 + RO_2 → Product	1.0×10^{-15}	40
69	RO_2 + HO_2 → Product	1.4×10^{-15}	40
70	All adducts + O_2^- → Product	4.1×10^{-16}	Close to the value for TEMPOL + O_2^- in 41
71	All adducts + OH → Product	1.0×10^{-11}	Close to the value for TEMPOL + OH in 42
72	All adducts + R → Product	5.5×10^{-14}	Determined from global optimization
73	All adducts + OR → Product	7.0×10^{-11}	Determined from global optimization
74	All adducts + OOR → Product	4.5×10^{-16}	Determined from global optimization

6. References

1. W.A. Pryor in *Free Radicals in* Biology, Vols. 1 and 2, Academic Press, New York 1976

2. U. Pöschl, and M. Shiraiwa: Multiphase Chemistry at the Atmosphere–Biosphere Interface Influencing Climate and Public Health in the Anthropocene, *Chem. Rev.*., 115(10), 4440 – 4475, 2015.

3. W. Hack: Detection methods for atoms and radicals in the gas-phase, *Int. Rev. Phys. Chem.*, 4, 165, 1985

4. D. F. Church: Spin Trapping Organic Radicals, *Anal. Chem.*, 66 (7), 419, 1994.

5. R. C. Bray: Sudden freezing as a technique for the study of rapid reactions, *Biochem. J.*, 81(1), 189 – 195, 1961.

3. D. P. Ballou, and G. A. Palmer: Practical rapid quenching instrument for the study of reaction mechanism by electron paramagnetic spectroscopy, *Anal. Chem.*, 46 (9), 1248 – 1253, 1974.

4. F. Nami, P. Gast, and E. J. J. Groenen: Rapid Freeze-Quench EPR Spectroscopy: Improved Collection of Frozen Particles, *Appl. Magn. Reson.*, 47, 643 – 653, 2016.

5. E. G. Janzen: Spin Trapping, *Acc. Chem. Res.*, 4 (1), 31 – 40, 1971

6. M. J. Perkins: Spin trapping in Advances in Physical Organic Chemistry (V. Gold and D. Bethall, Eds.), 17, 1-64. Academic Press, New York, 1980.

7. E. G. Janzen, A critical review of spin trapping in biological systems, *Free Radical in Biology* (W. A. Pryor, Ed.), Vol. IV, pp. 115-154. Academic Press, New York, 1980.

8. A. J. Carmichael, K. Makino and P. Riesz, Quantitative Aspects of ESR and Spin Trapping of Hydroxyl Radicals and Hydrogen Atoms in Gamma-Irradiated Aqueous Solutions, *Radiation Research*, 100, 2, 222-234, 1984.

9. G. M. Rosen, M. S. Cohen, B. E. Britigan, and S. Pou: Application of Spin Traps to Biological Systems, *Free Rad. Res. Comm.*, 9, 187.

10. R. Konaka, M. Kawai, H. Noda, M. Kohno, R. Niwa, Synthesis and evaluation of DMPO-type spin traps, Journal of Free Radical Research, 23 (1),15-25, 1995.

11. H. Zhao, J. Joseph, H. Zhang, H. Karoui, B. Kalyanaraman, Synthesis and biochemical applications of a solid cyclic nitrone spin trap: a relatively superior trap for detecting superoxide anions and glutathiyl radicals, *Free Radical Biology and Medicine,* 31(5), 599–606, 2001.

12. Y. Maeda, P. Schmid, D. Griller, K. U. Ingold, Solvent Effects on the Spin-trapping of Primary Alkyl Radicals, *J. C. S. Chem. Comm.*, 525, 1978

13. Y. Maeda, and K. U. Ingold, Kinetic Applications of Electron Paramagnetic Resonance Spectroscopy. 34. Rate Constants for Spin Trapping. 2. Secondary Alkyl Radicals, *J. Am. Chem. Soc.*, 101(17), 4976-4980, 1979.

14. S. Y. Qian, M. B. Kadiiska, Q. Guo, R. P. Mason, A novel protocol to identify and quantify all spin trapped free radicals from in vitro/in vivo interaction of HO and DMSO: LC/ESR, LC/MS, and dual spin trapping combinations, *Free Rad. Biol. Med.*, 38 (1), 125-135, 2005

15. A. M. Arangio, H. Tong, J. Socorro, U. Pöschl, and M. Shiraiwa: Quantification of environmentally persistent free radicals and reactive oxygen species in atmospheric aerosol particles, *Atmospheric Chemistry and Physics*, 16, 13105-13119, 2016.

16. S. Stoll, A. Schweiger, EasySpin, a comprehensive software package for spectral simulation and analysis in EPR, *Journal of Magnetic Resonance*, 178, 1, 42–55, 2006.

17. S. Stoll, Computational modeling and least-squares fitting of EPR spectra in: Sushil K. Misra (ed.), *Handbook of Multifrequency Electron Paramagnetic Resonance: Data and Techniques*, Wiley-VCH, 69-138, 2014.

18. G. R. Eaton, S. S. Eaton, D. P. Barr, R. T. Weber, *Quantitative EPR, a practitioner guide*, Springer-Verlag Vienna, 2010

19. A. M. Arangio, J. H. Slade, T. Berkemeier, U. Pöschl, D. A. Knopf, M. Shiraiwa, Multiphase Chemical Kinetics of OH Radical Uptake by Molecular Organic Markers of Biomass Burning Aerosols: Humidity and Temperature Dependence, Surface Reaction, and Bulk Diffusion, *The Journal of Physical Chemistry A*, 119(19), 4533-4544, 2015.

20. P. S. J. Lakey, T. Berkemeier, H. Tong, A. M. Arangio, K. Lucas, U. Pöschl, M. Shiraiwa, Chemical exposure-response relationship between air pollutants and reactive oxygen species in the human respiratory tract, *Scientific Reporti,* 6, 32916, 2016

21. T. Berkemeier, M. Ammann, U. K. Krieger, T. Peter, P. Spichtinger, U. Pöschl, M. Shiraiwa, A. J. Huisman: Technical Note: Monte-Carlo genetic algorithm (MCGA) for model analysis of multiphase chemical kinetics using multipe experimental data sets, *Atmos. Chem. Phys. Discuss.,* doi:10.5194/acp-2017-45, 2017.

22. J.M. Fontmorin, R.C. Burgos Castillo, W.Z. Tang, M. Sillanpää, Stability of 5,5-dimethyl-1-pyrroline-N-oxide as a spin-trap for quantification of hydroxyl radicals in processes based on Fenton reaction, *Water Research*, 99, 24 – 32, 2016.

23. P. S. J. Lakey, T. Berkemeier, H. Tong, A. M. Arangio, K. Lucas, U. Pöschl, M. Shiraiwa, Chemical exposure-response relationship between air pollutants and reactive oxygen species in the human respiratory tract, *Scientific Reporti,* 6, 32916, 2016

24. Z. Stuglik, Z. P. Zagorski, Pulse-radiolysis of neutral iron(II) solutions – Oxidation of ferrous ions by OH radicals, *Radiat. Phys. Chem.*, 17, 229-233, 1981.

25. S. Lewis, A. Lynch, L. Bachas, S. Hampson, L. Ormsbee, D. Bhattacharyya, Chelate-Modified Fenton Reaction for the Degradation of Trichloroethylene in Aqueous and Two-Phase Systems, *Environmental Engineering Science,* 26, 849-859, 2009.

26. J. D. Rush, B. H. Bielski, Pulse radiolytic studies of the reactions of HO_2/O_2^- with Fe(II)/Fe(III) ions- The reactivity of HO_2/O_2^- with ferric ions and its implication on the occurence of the Haber-Weiss reaction, *Journal of Physical Chemistry - U. S.*, 89, 5062 – 5066, 1985.

27. H. Christensen, K. Sehested, H. Corfitzen, Reactions of hydroxyl radicals with hydrogen peroxide at ambient and elevated temperatures, *Journal of Physical Chemistry - U. S.*, 86, 1588-1590, 1982.

28. K. Sehenstend, O. Rasmusse, H. Fricke, Rate constants of OH with HO_2, O_2^- and $H_2O_2^+$ from hydrogen peroxide formation in pulse irradiated oxygenated water, *Journal of Physical Chemistry - U. S.*, 72, 626, 1968

29. W. H. Koppenol, J. Butler, J. W. Vanleeuwen, The Haber-Weiss cycle, *Photochemistry and Photobiology*, 28, 655-660, 1978.

30. G. V. Buxton, C. L. Greenstock, W. P. Helman, A. B. Ross, Critical-review of rate constants for reactions of hydrated electrons, hydrogen-atoms and hydroxyl radicals ($\cdot OH/\cdot O^-$) in aqueous-solution, *Journal Physical Chemistry Reference Data*, 17, 513-886, 1988.

31. J. A. Thornton,L. Jaegle, V. F. McNeill, Assessing known pathways for HO_2 loss in aqueous atmospheric aerosols: Regional and global impacts on tropospheric oxidants, *Journal of Geophysical Reserch – Atmosphere*, 113, 2008.

32. J. Divišek, B. Kastening, Electrochemical generation and reactivity of the superoxide ion in aqueous solutions, *Journal of Electronanalytical Chemistry and Interface Electrochemistry*, 65, 603-621, 1975.

33. H. Tong, A. M. Arangio, P. S. J. Lakey, T. Berkemeier, F. Liu, C. J. Kampf, W. H. Brune, U. Pöschl, M. Shiraiwa, Hydroxyl radicals from secondary organic aerosol decomposition in water, *Atmospheric Chemistry and Physics*, 16, 1761-1771, 2016.

34. H. Hermann, A. Tilgner, P. Barzaghi, Z. Majdik, S. Gligorovski, L. Poulain, A. Monod, Towards a more detailed description of tropospheric aqueous phase organic chemistry: CAPRAM 3.0, *Atmospheric Environment*, 39(23-24), 4351-4363, 2005.

35. Y. Mizuta, T. Masumizu, M. Kohno, A. Mori, L. Packer, Kinetic analysis of the fenton reaction by ESR-Spin Trapping, *Biochemistry and Molecular Biology International*, 45(5), 1107-1120, 1997.

36. S. Croft, B. C. Gilbert, J. R. Lindsay Smith, A. C. Whitwood, An ESR Investigation of the Reactive Intermediate Generated in the Reaction Between Fe(II) and H_2O_2 in Aqueous Solution. Direct Evidence for the Formation of the Hydroxyl Radical, *Free Radical Research Communications*, 17(1), 21-39, 1992

37. P. Neta, R. E. Hule, A. B. Ross, Rate Constants for Reactions of Peroxyl Radicals in Fluid Solutions, *Journal Physical Chemistry Reference Data*, 19(2), 1990

38. M. Simic, P. Neta, E. Hayon, Pulse radiolysis study of alcohols in acqueous solution, 72(11). 3794-3800, 1969.

39. D. J. Carlsson, K. U. Ingold, Reactions of Alkoxy Radicals. IV. The Kinetics and Absolute Rate Constants for Some t-Butyl Hypochlorite Chlorinations, *Journal of the Americal Chemical Society*, 89(19), 4891-4894, 1967.

40. H. Herrmann, A. Reese, F. Wicktor, R. Zellner, A spectroscopic study of small organic peroxyl radicals (RO_2) in aqueous solution, *Journal of Molecular Structure*, 408 (409), 539-542, 1997.

41. M. C. Krishna, A. Russo, J. B. Mitchell, S. Goldstein, H. Dafni, A. Samuni, Do Nitroxide Antioxidants Act as Scavengers of O_2^- or as SOD mimics?, *The Journal of Biological Chemistry*, 271(42), 26026-26031, 1996.

42. A. Samuni, S. Goldstein, A. Russo, J. B. Mitchell, M. C. Krishna, P. Neta, Kinetics and Mechanism of Hydroxyl Radical and OH-Adduct Radical Reactions with Nitroxides and with Their Hydroxylamines, *Journal of American Chemical Society,* 124, 8719-8724, 2002.

B.5. Arangio et. al., in preparation

Comparison of Environmentally Persistent Free Radicals in Size Distributed Atmospheric Particles from different locations

in preparation.

Introduction

Environmentally Persistent Free Radicals (EPFR) are in a family of compounds with unpaired electrons that have an *e*-folding life time exceeding one day under atmospherically relevant conditions and are found in atmospheric particulate matters [1, 2]. The chemical nature of EPFR is remarkably similar to semiquinone radicals and several studies report EPFR formation from combustion and decomposition of aromatic compounds stabilized by metal oxides [3-5] and from pyrolysis of organic matter [6]. Other studies report the formation of stable organic radicals from heterogeneous processes such as the ozonolysis of Polycyclic Aromatic Hydrocarbons (PAH) [7, 8] suggesting that additional metal-free reaction paths, common in chemical aging processes of atmospheric aerosol, can also produce EPFRs.

During the last decades, EPFR have received considerable attention because of their ability to form reactive oxygen species (ROS) upon dissolution in water, ROS can induce oxidative stress associated with pulmonary diseases [9, 10]. The ability of EPFR to form ROS could also give rise to secondary chemistry in the particle phase that could explain the increase of secondary organic aerosol (SOA) mass observed from biomass-burning emission [11,12]. Therefore, EPFR concentrations in atmospheric particles gives additional information which is helpful in understanding and evaluating the impact of aerosols on public heath and aerosol evolution. Although EPFRs concentrations in atmospheric particulate matters with an aerodynamic diameter < 2.5 μm ($PM_{2.5}$) have already been measured in different urban sites [13, 14], EPFR concentrations in size segregated PM from megacities needs further investigation. Squadrito et al. [13] determined the EPFR concentrations to be in the range of (1–10) × 10^{11} spins μg^{-1} in $PM_{2.5}$ sampled for 24 h in five different urban sites in the United States, however, Arangio et al. [14] showed that particles in the size range of 56 – 320 nm have an average EPFR concentration of 2.2 ± 1.3 × 10^{11} spins μg^{-1}. Particles in the accumulation mode have the highest EPFR concentration of 7 ×

10^{11} spins μg^{-1}. Mass size distributions of soot or black carbon and SOA have typical diameter peak concentrations of around 100 – 200 nm [15], suggesting a potential relationship between EPFR, SOA and black carbon. To explore this potential relationship EPFR concentrations from different environments need to be determined. This study reports the size distribution and the time series of EPFR concentrations in atmospheric particles with size diameters between 100 nm and 320 nm sampled in Beijing (China), Nagoya (Japan), and Mainz (Germany). The data collected from each location are discussed and compared below.

Method

Ambient particles were collected using a micro-orifice uniform deposition impactor (MOUDI, 110-R, MSP Corporation) at a flow rate of 30 L min^{-1} with the following nominal lower cut-off particle diameters: 100, 180, 320 nm. The sampling periods and locations were the 28 May – 9 June 2015 in the Max Planck Institute for Chemistry, Mainz, Germany (49.99 N, 8.23 E), 1 – 10 January 2016 at the University of Chinese Academy of Science, Beijing, China (40.41 N, 116.76 E), 11 – 22 April 2016 at the department of Earth and Environmental Science, Nagoya University, Nagoya, Japan (35.15 N, 136.97 E). Particles were collected on 47 mm diameter Teflon filters (100 n pore size, Merk Chemicals GmbH) with a sampling time of 24 h for samples from Mainz and Nagoya and 12 h for samples from Beijing. Before sampling, each filter was cleaned and sonicated for 10 min in ultra-pure water and dried with nitrogen gas before weighing. Teflon filters were weighed four times using an analytical balance (Mettler Toledo XSE105DU) and mounted in the MOUDI.

A continuous-wave electron paramagnetic resonance (CW-EPR) X-band spectrometer (EMXplus-10/12; Bruker Corporation) was used to detect and quantify EPFR in particulate matter. Filters containing particles were folded and introduced into a 4 mm I.D. quartz tube and inserted directly into a high sensitivity cavity. EPR spectra for Mainz samples were

recorded at a room temperature of 23 °C whereas spectra for Beijing and Nagoya samples were recorded at a temperature of 100 K. All EPR spectra were recorded using the following instrumental parameters: modulation frequency, 100 kHz; microwave frequencies, 9.84 GHz for room temperature measurements, 9.43 GHz for 100 K measurements; microwave power, 2.143 mW (20 db), modulation amplitude, 1.0 G, sweep width, 110.0 G, sweep time, 175 s, receiver gain, 40 db, time constant, 40.96 ms, conversion time, 160 ms, and number of scans, 6. Paramagnetic species are characterized based on their *g* factor values, for free electrons the *g*-factor has a value of 2.0023 and for organic radicals higher *g*-factor values in the range of 2.0030 - 2.0060 are expected which depend on the number of oxygen atoms in the molecule [16].

Results and Discussion

Figure 1 shows the time evolution of the EPFR concentration in particles sampled in Beijing, Mainz and Nagoya. EPFR concentrations range from 6×10^{10} to 6×10^{13} spins μg^{-1} with the lowest value measured in Nagoya for particles with a lower cutoff size diameter of 320 nm and the highest value measured in Beijing for particles in the same size range. The EPFR concentrations measured are comparable with the values reported in the literature which range from 1×10^{11} to 2.2×10^{12} spins μg^{-1} for $PM_{2.5}$ [13, 14]. Often EPFR concentrations for Beijing samples exceeded the highest literature value, to our knowledge, this is the first time EPFR concentrations in size segregated particles are reported for this location. Particles with a lower cut-off diameter of 320 nm, collected in Nagoya and Mainz contain lower concentrations of EPFR compared to particles with a smaller size diameter. This trend is inverted for particles sampled in Beijing where particles with lower cut-off diameters of 100 nm have the lowest EPFR concentration.

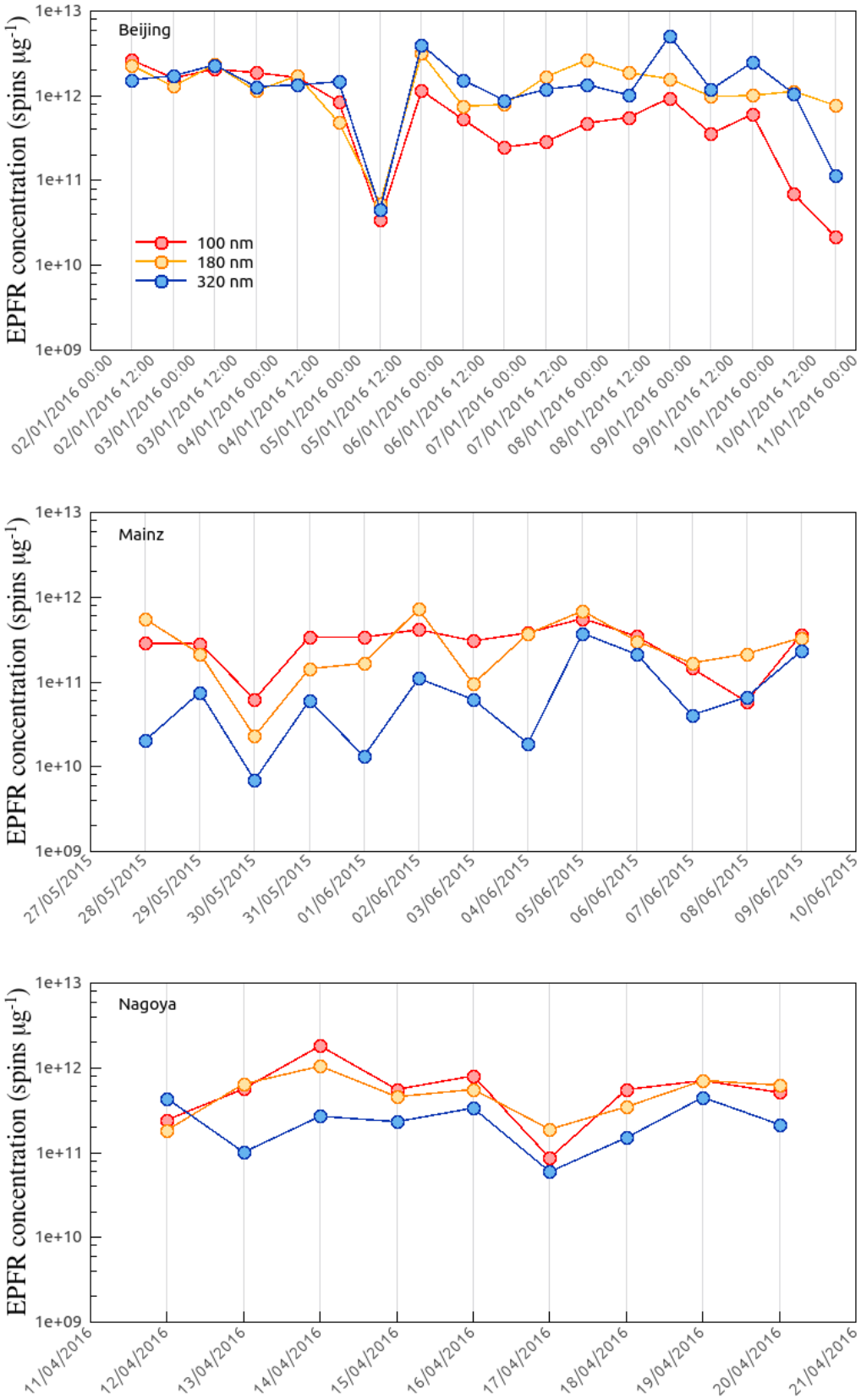

Figure 1: Temporal evolution of concentrations of environmentally persistent free radicals (EPFR) contained in atmospheric aerosol samples with lower cutoff diameters of 100 nm (red), 180 nm (yellow), 320 nm (blue), collected in Beijing, China in January 2016, Mainz, Germany, in May – June 2015, Nagoya, Japan, in April 2016.

Particles of all sizes have comparable EPFR concentration in the first five Beijing samples. These samples were collected during a haze event, which is typical in Beijing during the wintertime when the atmospheric stability combined with intense biomass combustion due to house heating causes aerosols to accumulate. The chemical evolution of particles during haze events in Beijing is characterized by intense aqueous-phase processing associated with the increased relative humidity [17]. Chemical processing together with particle coagulation can be the reason of the homogeneity for the EPFR concentration among particles with different size diameters collected between the 1st and the 5th of January 2016.

The box plot in Figure 2 summarizes the median and the range of EPFR concentrations in particles with different sizes collected in Beijing, Mainz and Nagoya. The average EPFR concentration in particles collected in Beijing is 1.3×10^{12} spins μg^{-1}, which is almost one order of magnitude higher than EPFR in the particles collected in Mainz and Nagoya for which the EPFR concentration was 2.3×10^{11} and 4.7×10^{11} spins μg^{-1} respectively. The difference is remarkably high for particles with lower cut-off sizes of 320 nm in which the EPFR concentrations were 1.6×10^{12} spins μg^{-1} in Beijing and 9.9×10^{10} and 2.5×10^{11} spins μg^{-1} in Mainz and Nagoya respectively. EPFR concentrations in 100 nm diameter particles are similar in all cases. Figure 2 also shows that the size distribution of the median EPFR concentrations tends to decrease with the increasing of particle sizes for Nagoya and Mainz samples but increases for Beijing samples.

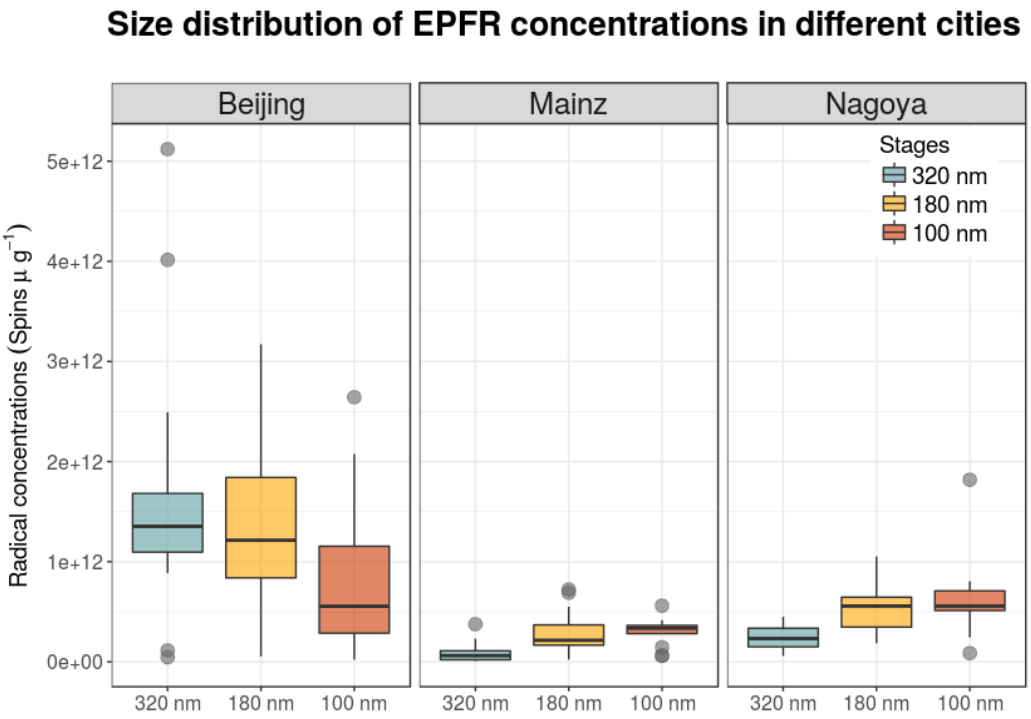

Figure 2: Comparison of average concentrations and standard deviations of environmentally persistent free radicals in atmospheric aerosol samples with lower cutoff diameters of 100 nm (red), 180 nm (yellow), 320 nm (blue), collected in Beijing (18 samples), China in January 2016, Mainz (13 samples), Germany, in May – June 2015, Nagoya (9 samples), Japan, in April 2016.

The differences in the size distribution of EPFR concentrations could be attributed to the types of emitting sources in the different locations. Domestic emissions of aerosols from biomass burning and coal combustions are the main sources of particles in Beijing during winter time [18]. Biomass burning sources produce particles in the accumulation mode that increase in size upon aging, reaching volume median diameters of 260-350 nm [19]. Oil combustion and traffic are instead the dominant sources of aerosol particles in Nagoya [20]. Size distributions of particles emitted by these sources typically have a peak in the Aitken mode in which particles have diameters on the order of tenths of nanometers [21]. Moreover, the peculiar meteorological conditions such as high relative humidity and atmospheric stability in Beijing during the sampling period, could also have facilitated coagulation processes that led to the growth of particles [17]. However, further research is necessary to confirm these hypothesis.

Conclusions

EPFR time series and its size distribution have been measured in this study for particles sampled in three different locations including Beijing (China), Nagoya (Japan) and Mainz (Germany). The average EPFR concentration contained in particles with size diameter range of 100 - 320 nm was 1.3×10^{12} spins μg^{-1} in Beijing which is almost one order of magnitude higher than average EPFR concentration in Mainz, 2.3×10^{11} spins μg^{-1}, and in Nagoya, 4.7×10^{11} spins μg^{-1}, reflecting heavy emissions from anthropogenic activities and biomass burning from house heating and coal combustion. EPFR concentrations were remarkably higher in 320 nm diameter particles collected in Beijing compared to the particle of the same size collected in Mainz and Nagoya. The results could be attributed to a different emission and processing pattern of aerosols between different locations. Particles in the accumulation mode are produced by biomass burning and coal combustions which are the main sources of particles in Beijing during winter time. Oil combustion and traffic are instead the dominant sources of aerosol particles in Nagoya which size distributions typically have a peak in the Aitken mode.

References

1. Gehling, W., and Dellinger, B.: Environmentally Persistent Free Radicals and Their Lifetimes in PM2.5, *Environ. Sci. Technol.*, 47, 8172-8178, 2013.

2. Jia, H., Nulaji, G., Gao, H., Wang, F., Zhu, Y., and Wang, C.: Formation and Stabilization of Environmentally Persistent Free Radicals Induced by the Interaction of Antracene with Fe(III)-Modified Clays, *Environ. Sci. Technol.*, 50, 6310 – 6319, 2016

3. Assaf, N. W., Altarawneh, M., Oluwoye, I., Radny, M., Lomnicki, S. M., and Dlugogorski, B. Z.: Formation of Environmentally Persistent Free Radicals on α-Al_2O_3, *Environ. Sci. Technol.*, 50, 11094 – 11102, 2016.

4. Truong, H., Lomnicki, S., and Dellinger, B.: Potential for Misidentification of Environmentally Persistent Free Radicals as Molecular Pollutant in Particulate Matter, *Environ. Sci. Technol.*, 44, 1933 – 1939, 2010.

5. Vejerano, E., Lomnicki, S., and Dellinger, B.: Formation and stabilization of combustion generated environmentally persistent free radicals on an $Fe(III)_2O_3$/silica surface, *Environ. Sci. Technol.*, 45, 589–594, 2011.

6. Bahrle, C., Nick, T. U., Bennati, M. , Jeschke, G., and Vogel, F.: High-Field Electron Paramagnetic Resonance and Density Functional Theory Study of Stable Organic Radicals in Lignin: Influence of the Extraction Process, Botanical Origin, and Protonation Reactions on the Radical g Tensor, *J. Phys. Chem. A,* 119, 6475 – 6482, 2015.

7. Shiraiwa, M., Sosedova, Y., Rouvière, A., Yang, H., Zhang, Y., Abbatt, J. P. D., Ammann, Pöschl, U.: The role of long-lived reactive oxygen intermediate in the reaction of ozone with aerosol particles, *Nat. Chem.,* 3, 291-295, 2011.

8. Borrowman, C. K., Zhou, S., Burrow, T. E., and Abbatt, J. P.: Formation of environmentally persistent free radicals from the heterogeneous reaction of ozone and polycyclic aromatic compounds, *Phys. Chem. Chem. Phys.,*18, 205 – 212, 2015.

9. Gehling, W., Khachatryan, L., and Dellinger, B.: Hydroxyl radical generation from environmentally persistent free radicals (EPFRs) in $PM_{2.5}$, *Environ. Sci. Technol.*, 48, 4266 – 4272, 2014.

10. Cheresh, P., Kim, S. J., Tulasiram, S., and Kamp, D.W.: Oxidative stress and pulmonary fibrosis, *Biochim. Biophys. Acta*, 7, 1028 – 1040, 2013.

11. Tong, H., Arangio, A. M., Lakey, P. S. J., Berkemeier, T., Liu, F., Kampf, C. J., Brune, W. H., Pöschl, U., and Shiraiwa, M.: Hydroxyl radicals from secondary organic aerosol decomposition in water, *Atmos. Chem. Phys.,* 16, 1761 – 1771, 2016.

12. Lin G., Sillman, S. Penner, J. E., and Ito, A.: Global modeling of SOA: the use of different mechanisms for aqueous-phase formation, Atmospheric Chemistry and Physics, *Atmos. Chem. Phys.*, 14, 5451-5475, 2014.

13. Squadrito, G. L., Cueto, R., Dellinger, B., and Pryor, W. A.: Quinoid redox cycling as a mechanism sustained free radical generation by inhaled airborne particulate matter, *Free Radical Biol. Med.,*178, 42 – 55, 2006.

14. Arangio A. M., Tong, H., Socorro, J., Pöschl, U., and Shiraiwa M.: Quantification of environmentally persistent free radicals and reactive oxygen species in atmospheric aerosol particle,
Atmos. Chem. Phys., 16, 13105 – 13119, 2016.

15. Bond, T. C., Doherty, S. J., Fahey, D. W., Forster, P. M., Berntsen, T., DeAngelo, B. J., Flanner, M. G., Ghan, S., Karcher, B., Koch, D., Kinne, S., Kondo, Y., Quinn, P. K., Sarofim, M. C., Schultz, M. G., Schulz, M., Venkataraman, C., Zhang, H., Zhang, S., Bellouin, N., Guttikunda, S. K., Hopke, P. K., Jacobson, M. Z., Kaiser, J. W., Klimont, Z., Lohmann, U., Schwarz, J. P., Shindell, D., Storelvmo, T., Warren, S. G., and Zender, C. S.: Bounding the role of black carbon in the climate system: A scientific assessment, *J. Geophys. Res.-Atmos.*, 118, 5380–5552, 2013

16. Dellinger, B., Lomnicki, S., Khachatryan, L., Maskos, Z., Hall, R. W., Adounkpe, J., McFerrin, C., and Troung, H.: Formation and stabilization of persistent free radicals, *Proc. Combust. Inst.*, 31, 521 – 528, 2007.

17. Sun, Y., Jiang, Q., Wang, Z., Fu, P., Li, J., Yang, T., and Yin, Y.: Investigation of the sources and evolution processes of severe haze pollution in Beijing in January 2013, *J. Geophys. Res.: Atmos.*, 119, 4380 – 4398, 2014.

18. Elser, M., Huang, R., Wolf, R., Slowik, J. G., Wang, Q., Canonaco, F., Li, G., Bozzetti, C., Daellenbach, K. R., Huang, Y., Zhang, R., Li, Z., Cao, J., Baltensperger, U., El-Haddad, I., Prévôt, A.S.H.: New insights into PM2.5 chemical composition and sources in two major cities in China during extreme haze events using aerosol mass spectrometry, *Atmos. Chem. Phys.*, 16, 3207-3225, 2016.

19. Reid, J. S., Koppmann, R., Eck, T. F., Eleuterio, D. P.,: A review of biomass burning emissions part-II: intensive physical properties of biomass burning particles, 5, 799-825, 2005.

20. Kamiya, Y., Iijima, A., Ikemori, F., Okuda, T., Ohura, T., Source apportionment of chlorinated polycyclic aromatic hydrocarbons associated with ambient particles in a Japanese megacity, *Scient. Rep.*, 6, 38358, 2016.

21. Geller, M., Sardar, S. B., Phuleria, H., Fine, P.M., Sioutas, C., Measurements of Particle Number and Mass Concentrations and Size Distributions in a Tunnel Environment, *Environ. Sci. Technol.* 39, 8653-8663.

Curriculum Vitae

Name : Andrea Mario Arangio

Date of birth : 11 January 1988

Place of birth : Enna, Italy

EDUCATION:

07/2013 – PRESENT **PhD student in Chemistry – Max Planck Institute for Chemistry, Mainz, Germany**
Secondary Organic aerosol and Oxidant Chemistry Group
Supervisor: Dr. Manabu Shiraiwa
Topic: Role of reactive oxygen species in multiphase chemistry of organic aerosols in the atmosphere.

05/2012-07/2012 **Visiting student – Electrochemical Energy Technology Institute (MEET), University of Münster, Germany**
EU project LABOHR for Li-air battery development
Supervisor: Prof. S. Passerini
Topic: design and fabrication of ad-hoc prototypes for systematic investigation of Li-air batteries.

09/2010 – 12/2012 **MSc in Chemistry – University of Bologna, Italy**
Photochemistry and Molecular Materials
Grade: 110/110 *summa cum laude*
Thesis: "Lithium-air battery with Ionic Liquids as electrolytes"
Supervisor: Prof. M. Mastragostino
Topics: Investigation of electrochemical techniques applied to energy storage systems.

09/2007-09/2010 **B.Sc. In Chemistry – University of Catania, Italy**
Grade: 110/110
Thesis: "Langmuir-Blodgett films of Dipalmitoylphosphatidylcholine and Polyethylene glycol on mica substrates"
Supervisor: Prof. G. Marletta
Topics: Chemical functionalization of solid surfaces.

09/2002– 07/2007 **Liceo Scientifico "P. Farinato" – Enna, Italy**
Key learnings : computer science, physic, math, chemistry, biology and earth science.